UNCLASSIFIED

AD NUMBER

AD828077

NEW LIMITATION CHANGE

TO

Approved for public release, distribution unlimited

FROM

Distribution authorized to U.S. Gov't. agencies and their contractors; Administrative/Operational Use; JAN 1968. Other requests shall be referred to Naval Air Systems Command, Washington, DC 20360.

AUTHORITY

USNASC notice, 4 Dec 1970

THIS PAGE IS UNCLASSIFIED

AD828077

HSER 4776
VOLUME I OF II

ENGINEERING REPORT

SHROUDED PROPELLER TEST PROGRAM METHOD DEVELOPMENT

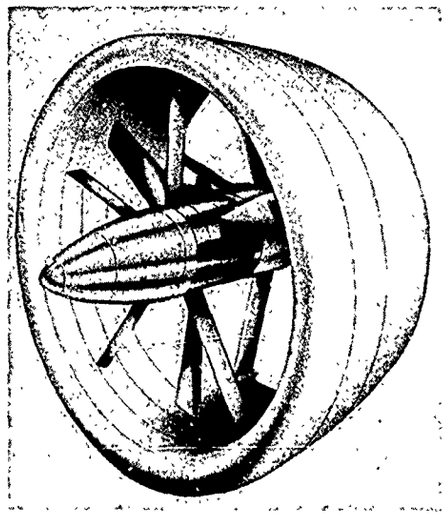

DDC
RECEIVED
MAR 12 1968
B

PHASE 3

CONTRACT NOw 64-0707-d

JANUARY, 1968

STATEMENT #2 UNCLASSIFIED

This document is subject to special export controls and each transmittal to foreign governments or foreign nationals may be made only with prior approval of Naval Air Systems Command Code (Air 604) Wash, D.C. 20360

Hamilton Standard DIVISION OF UNITED AIRCRAFT CORP UA

261

HSER 4776
VOLUME I OF II

ENGINEERING REPORT

SHROUDED PROPELLER TEST PROGRAM METHOD DEVELOPMENT

PREPARED BY: Rose Worobel
R. WOROBEL – SENIOR ANALYTICAL ENGINEER

A. A. Peracchio
A. A. PERACCHIO – SENIOR ANALYTICAL ENGINEER

APPROVED BY: Carl Rohrbach
C ROHRBACH – HEAD OF AERODYNAMICS & HYDRODYNAMICS

W Fortmann
W FORTMANN – CHIEF OF TECHNICAL STAFF

Al D. Croxall
A D CROXALL – CHIEF PROJECT ENGINEER

PHASE 3

CONTRACT NOw 64-0707-d
JANUARY, 1968

Hamilton Standard
DIVISION OF UNITED AIRCRAFT CORP

NUMBER OF PAGES: 235

ACKNOWLEDGEMENT

The authors wish to extend their sincere appreciation to Dr. D. E. Ordway, at the time associated with Therm Advanced Research, Incorporated, for his helpful suggestions and discussions.

SYNOPSIS OF SHROUDED PROPELLER TEST PROGRAM

A shrouded propeller test program was conducted under contract NOw-64-0707-d awarded to the Hamilton Standard Division of the United Aircraft Corporation by the Bureau of Naval Weapons in November of 1964. This program included both experimental and analytical phases.

The experimental phase of the program was conducted in the United Aircraft wind tunnel test facilities on a series of shroud-propeller models. This testing included the effects of varying the shroud parameters of lip shape, exit area ratio, propeller position, shroud chord length, and exterior shape, and propeller parameters such as planform distribution, number of blades, and tip clearance. Each of these parameters was tested over a wide range of propeller power loadings, tip speeds, and free-stream Mach numbers. These data were then presented in a manner in which the effect of variations of each geometric parameter on performance, pressure and velocity distributions could be separately evaluated. The results are reported in Hamilton Standard Report HSER 4348.

The analytical phase of the program involved the development of a shrouded propeller aerodynamic design and performance prediction method. This method, based on a theory which includes the interaction of shroud, propeller and centerbody induced flows, represents the propeller by a finite number of blades, and includes the influence of finite shroud and centerbody dimensions. The method has been computerized and substantiated by comparisons of calculations with the test data from the experimental phase. These efforts are reported in Hamilton Standard HSER 4776.

INDEX OF CONTENTS OF VOLUMES

Volume		Contents	No. of Pages
I	Method Develoment	Contains the Method Development and Analysis of the Comparisons of Calculations and Test.	235
II	Computer Program	Gives Detailed Instructions for Using the Computer Program as well as Sample Cases. It also Includes Fortran IV Listings of the Computer Programs.	129

CONTENTS

Section		Page
1.0	SUMMARY	1
2.0	INTRODUCTION	2
3.0	OBJECTIVES	3
4.0	CONCLUSIONS	4
5.0	RECOMMENDATIONS	6
6.0	DISCUSSION OF METHOD AND COMPUTER PROGRAM	7
	6.1 Mathematical Model	7
	6.1.1 Introduction	
	6.1.2 Formulation and Mathematical Solution for Zeroth Harmonic	
	6.2 Limiting Assumptions of Therm Advanced Research Model	13
	6.2.1 Introduction	
	6.2.2 Discussion of Zeroth Harmonic Assumption	
	6.2.3 Discussion of Incompressible Flow Assumption	
	6.2.4 Inclusion of Propeller Geometry	
	6.2.5 Discussion of Linearization Assumptions	
	6.2.5a Introduction	
	6.2.5b Representation of Shroud and Centerbody	
	6.2.5c Riegels Factor	
	6.2.5d Representation of Propeller and Wake	
	6.2.5e Discussion of Shroud Boundary Conditions	
	6.2.5f Summary of Linearization Assumptions	
	6.2.6 Summary of Limiting Assumptions	
	6.3 Shroud Thrust Calculation - Inviscid	55

CONTENTS

Section			Page
		6.3.1 Introduction	
		6.3.2 Shroud Thrust - Detailed Integration Method (Method 1)	
		6.3.3 Shroud Thrust Based on Momentum Theorem Using Propeller Circulation (Method 2)	
		6.3.4 Shroud Thrust Based on Momentum Theorem Using Propeller Thrust Coefficient (Method 3)	
		6.3.5 Evaluation of the Three Methods for Computing Shroud Thrust	
	6.4	Shroud Drag Prediction	65
		6.4.1 Introduction	
		6.4.2 Shroud Drag - No Pressure Gradient	
		6.4.3 Shroud Drag - With Pressure Gradient	
		6.4.4 Shroud Drag Evaluation	
	6.5	Thrust Coefficient Nomenclature	71
	6.6	Computer Program	71
		6.6.1 Introduction	
		6.6.2 Hamilton Standard Computer Deck H193	
		6.6.2a General Description	
		6.6.2b Inputs for Computer Program	
		6.6.2c Outputs from Computer Program	
		6.6.2d Computer Running Time	
7.0		COMPARISONS OF CALCULATIONS AND TEST	89
	7.1	Introduction	89
	7.2	Discussion of Test Data	89
	7.3	Performance Comparisons - Isolated Propeller	90
	7.4	Performance Comparisons - Shrouded Propeller	90
		7.4.1 Introduction	
		7.4.2 Shroud Pressure Distribution Comparisons	
		7.4.2a Power Coefficient	
		7.4.2b Area Ratio	
		7.4.2c Rotative Speed	
		7.4.2d Effect of Mach Number	
		7.4.2e Summary - Pressure Distribution Comparisons	

CONTENTS

Section		Page
	7.4.3 Propeller Performance Comparisons	
	7.4.3a Primary Parameters	
	7.4.3b Secondary Parameters	
	7.4.3c Comparison of Axial Velocity Distributions	
	7.4.3d Comparison of Propeller Thrust Derivatives	
	7.4.4 Shroud Net Thrust Comparisons	
	7.4.4a Primary Parameters	
	7.4.4b Secondary Parameters	
	7.4.4c Summary	
	7.4.5 Discussion of Centerbody Effects	
	7.5 Summary - Comparisons of Calculation and Test	163
8.0	EXTENSION TO STATIC	166
9.0	LIST OF SYMBOLS, SUBSCRIPTS AND SUPERSCRIPTS	170
10.0	REFERENCES	176
11.0	APPENDICES	179
	11.1 Incorporation of Centerbody into Therm Advanced Research Theory	180
	11.2 Application of Propeller Tip Correction	193
	11.3 Thrust Due to Distribution of Sources	204
	11.4 Shroud Thrust Based on Momentum Theorem	209
	11.5 Analysis of Higher Harmonics	218
	11.6 Discussion of Velocity Calculation in Propeller Plane	229
	11.7 Chi Integrals	233

ILLUSTRATIONS

Figure		Page
1	Definition of Propeller Fixed Coordinate System .	8
2	Propeller Velocity Diagram at Typical Station.	14
3	Pressure Coefficient Versus Azimuthal Angle.	20
4-7	Effect of Mach Number on Pressure Distribution.	23
8	Effect of Field Point Location on Shroud Pressure Coefficient.	29
9-10	Effect of Riegels Leading Edge Correction on Shroud Pressure Distribution.	33
11	Effect on Theoretical Performance of Using J'_0 or J'_2 in Equation (20).	37
12	Performance Comparison - Test and Theory - Effect of J_2 and Jo.	38
13	Effect of Jo and J_2 on Shroud Pressure Distribution.	39
14	Model for Tip Correction.	41
15	Effect of Goodman Tip Correction on Theoretical Performance.	42
16	Effect of Goodman Tip Correction - Performance Comparison of Test and Theory, J'_2 Used in Equation (20).	43
17	Effect of Goodman Tip Correction on Shroud Pressure Distribution.	44
18	Schematic Representation of Shroud Boundary Condition.	46
19	Discontinuous Velocities Along Shroud Camber Line.	48
20	Average Axial Induced Velocity at Shroud Reference Cylinder Versus Chordwise Location.	51

ILLUSTRATIONS

Figure		Page
21	Comparison of Geometric and Corrected Camber Line Slope.	52
22	Pressure Coefficient With and Without Boundary Condition Correction.	54
23	Forces on Shroud Vorticity and Source-Sink Distributions	57
24	Control Volume Around Shroud	61
25	Comparison of Net Thrust Calculation Methods	66
26	Input Requirements	74
27	Optional Printouts	77
28a	Sample Case for Defined Shroud and Propeller Geometry	78
28b	Sample Case for Defined Shroud and Propeller Circulation	83
28c	Sample Case for Shroud Alone	86
29	Hamilton Standard Shrouded Propeller Test - Shroud Shapes	91
30a	Shroud Thickness Ratio Distribution	92
30b	Shroud Camber Line Slope Distribution	93
31	Propeller Test Blades	94
32a	Model Blade Characteristics Common to All Blades	95
32b	Model Blade Characteristics	96
33	Nomenclature Coordination	97
34	Comparison of Calculations and Test for the Isolated Propeller 3WT	98

ILLUSTRATIONS

Figure		Page
35	Significant Shroud and Propeller Parameters	99
36a-36b	Effect of Power Coefficient on Pressure Distribution	101
37	Effect of Tip Speed on Pressure Coefficient	104
38-39	Effect of Corrections on Shroud Pressure Distribution	106
40	Correction to Shroud Camber Line Boundary Condition	108
41	Comparison of Geometric and Corrected Camber Line Slope	109
42	Shroud Vorticity Distribution Comparison	110
43	Comparison of Utilized and Actual Shroud Thickness Forms	113
44-47	Propeller Performance Comparisons of Calculation and Test - Effect of Mach Number	116
48	Effect of Area Ratio on the Computed Advance Ratio at the Propeller Plane	120
49	Propeller Performance Comparisons of Calculation and Test - Effect of Area Ratio	121
50	Propeller Performance Comparisons of Calculation and Test - Effect of Area Ratio	122
51	Propeller Performance Comparisons of Calculation and Test - Effect of Tip Speed	123
52	Propeller Performance Comparisons of Calculation and Test - Effect of Shroud External Shape	125

ILLUSTRATIONS

Figure		Page
53	Propeller Performance Comparisons of Calculation and Test - Effect of Shroud Lip Shape	126
54	Propeller Performance Comparisons of Calculation and Test - Effect of Shroud Length	127
55	Propeller Performance Comparisons of Calculation and Test - Effect of Propeller Position	128
56	Propeller Performance Comparisons of Calculation and Test - Effect of Propeller Planform	129
57	Propeller Performance Comparisons of Calculation and Test - Effect of Number of Blades	130
58	Propeller Performance Comparisons of Calculation and Test - Effect of Propeller Tip Clearance	132
59	Comparison of Calculation and Test of Radial Distribution of Propeller Plane Axial Velocities - Effect of Area Ratio	133
60	Comparison of Calculation and Test of Radial Distribution of Propeller Plane Axial Velocities - Effect of Propeller Planform	134
61	Comparison of Calculation and Test of Radial Distribution of Propeller Plane Axial Velocities - Effect of Number of Blades	135
62	Comparison of Calculation and Test of Radial Distribution of Propeller Plane Axial Velocities - Effect of Shroud Length	136

ILLUSTRATIONS

Figure		Page
63	Comparison of Calculation and Test of Radial Distribution of Propeller Plane Axial Velocities - Effect of RPM	137
64-68	Comparison of Calculation and Test for Radial Distribution of Propeller Elemental Thrust for B1-3WT	138
69-71	Shroud Performance Comparisons of Calculations and Test - Effect of Mach Number	145
72a-72b	Net Thrust Coefficient Versus Area Ratio	148
73	RMS Error Versus Mach Number	151
74	Shroud Performance Comparison of Calculation and Test - Effect of Propeller Tip Clearance	153
75	Shroud Performance Comparison of Calculation and Test - Effect of Propeller Planform	154
76	Shroud Performance Comparison of Calculation and Test - Effect of Propeller Position	155
77	Shroud Performance Comparison of Calculation and Test - Effect of Number of Blades	156
78	Shroud Performance Comparison of Calculation and Test - Effect of Shroud Lip Shape	157
79	Shroud Performance Comparison of Calculation and Test - Effect of Shroud Length	158

ILLUSTRATIONS

Figure		Page
80	Shroud Performance Comparison of Calculation and Test - Effect of Shroud External Shape	159
81	Sketch of Shroud Configurations B1, B4, B5	161
82	Performance Comparison of Calculation and Test - Effect of Centerbody on Area Ratio	162
83	Performance Comparison of Calculation and Test - Effect of Centerbody on Propeller Position	164
84	Pressure Coefficient Versus X/C	167
85	Percentage Error in Propeller Thrust versus V_a/V_o	169
A-1	Source-Sink Distribution Along Shroud Centerline.	181
A-2	Derivation of Relationship Between Body Shape and Source-Sink Distribution	186
A-3	Two-Dimensional Model	193
A-4	Placement of Wall Near Vortex Sheets	194
A-5	Goodman Tip Correction	195
A-6	Velocity Diagram for a Typical Blade Section	197
A-7	Average Velocity Diagram for a Given Propeller Radius	198

ILLUSTRATIONS

Figure		Page
A-8	Flow About Flat Plate Approximation	199
A-9	Ratio of Tip Correction to Tip Correction With No Wall	203
A-10	Force on Obstacle	204
A-11	Velocity Due to a Source	205
A-12	Force on a Source-Sink Distribution Due to External Sources and Sinks	206
A-13	Wake Model	209
A-14	Shroud Control Volume	212
A-15	Circulation Through the Cross Section of a Jet	214
A-16	Propeller and Wake Radius Diagram	215
A-17	Definition of Coordinate System	219
A-18	Definition of Variables in Biot-Savart Law	220
A-19	Approximate Function for Γ	225

1.0 SUMMARY

This report contains and summarizes a program conducted by Hamilton Standard for the development of an analytic shrouded propeller performance prediction method. The Therm Advanced Research, Inc. shrouded propeller theory was used as the basis of the method. Due to certain limitations in this basic theory, Hamilton Standard included propeller geometry, shroud drag, and the effect of centerbody. Furthermore, additional adjustments were made in an attempt to extend its applicability to lower velocities and to shrouds with greater thickness and camber than were considered in the basic theory. The method was computerized, and the computer program was then used in evaluating the computational procedure by comparisons with the test data obtained by Hamilton Standard in the United Aircraft wind tunnel test facility. In general, the method agreed well with test for Mach numbers greater than or equal to 0.20 for propeller performance and shroud surface pressure distributions. The net thrust (shroud plus propeller) comparisons were not as favorable, due to the simplifying assumptions in both the inviscid net thrust and shroud drag computations. The results show that further work is required to extend the theory to static conditions and to better define net thrust.

The wind tunnel tests were undertaken as Phase I and the method development as Phase III of contract NOw-64-0707-d awarded by the Bureau of Naval Weapons in November of 1964.

2.0 INTRODUCTION

Existing methods, based on momentum concepts, for the design and performance prediction of shrouded propellers are not able to account for shroud shape except in terms of shroud area ratio and therefore cannot be used to predict shroud pressure distributions. Also unaccounted for are the effects of propeller location, propeller tip clearance and centerbody geometry. Information on the effects of these variables is necessary for the design of shrouded propellers. The shroud pressure distribution is especially needed, since it enters directly into the prediction of the boundary layer separation characteristics of the shroud.

These shortcomings prompted Hamilton Standard to investigate treatments which included these effects, and led to the choice of the Therm Advanced Research, Inc. (T.A.R.) formulation as the basis for a shrouded propeller performance prediction method which has been programmed for digital computation.

The T.A.R. theory as formulated, however, contains certain assumptions which limit its applicability to high forward speeds and/or to thin shrouds of small camber. In addition, it does not permit specification of the propeller geometry and does not account for the effects of centerbody. Therefore, before it can be used as a performance prediction tool, and as part of its continuing development, methods for the removal of these shortcomings must be investigated and evaluated.

Mutual recognition of the need for the continued development of this method resulted in the Phase III portion of Navy Contracted NOw-64-0707-d, granted to the Hamilton Standard Division of the United Aircraft Corporation by Buweps. Under Phase III of this contract, the removal of the shortcomings discussed above are investigated. The resulting corrections to the the theory are incorporated into the computer program and the method validity checked by comparisons with the test data obtained from Phase I.

3.0 OBJECTIVES

1. Develop a practical design and performance prediction method for shrouded propellers based on the three-dimensional theory derived by Therm Advanced Research, Inc.

2. Investigate the feasibility of extending the method to include such effects as centerbody and shroud drag, and investigate the feasibility of extending the method to the static case.

3. Utilize the test data from Phase I to check out the method and tc provide empirical adjustments to the basic method as may be required.

4. Develop a computer program, describe the pertinent instructions for using the computer program, and present sample cases.

4.0 CONCLUSIONS

As a result of the reported investigations the following conclusions are drawn.

THEORETICAL

1. The effects of centerbody, propeller geometry, and shroud thrust and drag were added to the basic T.A.R. Theory.

2. Improvements to the representation of the propeller wake induced velocities, shroud boundary conditions, and shroud leading edge pressure distributions were incorporated.

COMPUTER PROGRAM

1. The improvements and additions to the theory have been incorporated into the program.

2. The program is a tool useful for parametric studies of shroud and propeller geometry variations due to ease of input manipulation and fast computing time.

3. The program is set up in a manner which readily permits additions and/or changes to any of its major sections.

METHOD EVALUATION

1. The velocity field, propeller performance, and thrust derivatives are well predicted for the range of velocities for which the theory is valid, i.e., for values of $\overline{V}_a/V_o \leq 1.35$, which corresponds for air to a Mach number of approximately .2 or greater. $\overline{V}_a$ is the average axial velocity at the propeller plane and V_o is the free stream velocity.

2. The shroud pressure distributions were well predicted for $\overline{V}_a/V_o \leq 1.35$, except in the leading edge region, where the agreement was fair. This region is weak because of the leading edge singularity inherent in the theory and the application of the approximate Riegels correction.

3. The net thrust (shroud plus propeller) comparisons of calculation and test are only fair for $\overline{V}_a/V_o \leq 1.35$. This is due to the limiting assumptions in both the inviscid net thrust and shroud drag computational procedures.

4. For $\overline{V}_a/V_o < 1.35$, the higher harmonics are not required in the computation of the shroud induced velocity, because their prime influence on performance is due to the direct contribution of the propeller which is properly accounted for by the Goldstein Theory.

4.0 (Continued)

5. The centerbody has an effect on performance which is properly predicted by the theory. The changes in performance due to changes in area ratio and propeller locations are not influenced by the detailed shape of the test centerbody, although there is an effect on the level of performance.

6. The corrections and additions to the theory resulted in better agreement between calculations and tests for $\bar{V}_a/V_0 \leq 1.35$.

7. The corrections and additions to the theory did not permit extension to low forward speed and static regimes since they were not all inclusive. In particular, the representations of the propeller wake, shroud thickness, and centerbody thickness were invalid for this regime.

5.0 RECOMMENDATIONS

Based on the reported investigations the following recommendations may be made.

USE OF EXISTING METHOD

1. For performance calculations in the static and low speed range, $\overline{V}_a/V_0 \geq 1.35$, use the Patterson method of Ref. 16 and 17 until a more rigorous method is developed.

2. Investigate the effect on performance and pressure distribution of the first order correction to the shroud boundary condition for a range of camber lines which differ from those used in this report.

METHOD IMPROVEMENT

1. Investigate methods for the improvement of the inviscid thrust calculation and shroud drag calculation by use of a more rigorous theoretical approach coupled with empirical corrections.

2. Improve the representation of the pressure distribution in the region of the leading edge by studying means for eliminating the singularity.

3. Investigate the use of the shroud surface instead of the shroud reference cylinder for the calculation of shroud surface pressure distribution.

EXTENSION TO STATIC

1. Develop the method for use in the static and low forward flight speed regime, using the T.A.R. static model of Ref. 18 as a starting point, and adding the effects of thickness, non-zero camber, variable propeller circulation, and a representation of the propeller wake incorporating self-induced distortion.

6.0 DISCUSSION OF METHOD AND COMPUTER PROGRAM

6.1 MATHEMATICAL MODEL

6.1.1 Introduction

The treatment of the incompressible flow field of shrouded propellers developed by Therm Advanced Research (T.A.R.) is the basis of the performance prediction method used throughout this study. A detailed description of their work is contained in Ref. 1 and 2. A brief description of the model is given so that the changes and additions incorporated during this contract will be easier to describe and understand. A propeller fixed coordinate system is used, and the shroud orientation in this system is shown in Fig. 1.

The theory as developed is a true three-dimensional theory. Its formulation is based on a lifting line representation of the blades of the propeller. As a result, azimuthal as well as radial and axial variations in flow properties are described. The mathematical complexities associated with such a model are, as may be expected, formidable. In addition, the prime performance parameters, such as shroud thrust, propeller thrust, and absorbed horsepower may be adequately represented by considering azimuthally averaged properties.

The azimuthal variations in the T.A.R. model are represented by expansion in a Fourier series over the angular variable, θ , which is defined in Fig. 1. It is shown in Ref. 1 that the equations defining the coefficients for each harmonic decouple, permitting separate evaluation. It is further shown that the solution for the zeroth harmonic, or azimuthal average, is exactly equivalent to a solution in which the propeller is represented by a non-uniformly loaded actuator disk.

The mathematical solution is much simpler for the zeroth harmonic than for the higher harmonics, and since, as noted above, azimuthally averaged properties (i.e., zeroth harmonic) may adequately define the performance parameters, only the zeroth harmonic has been incorporated into the method. Evaluation during the course of this program will then indicate whether the added complexity of incorporating the higher harmonics is necessary.

In the following, a brief description of the zeroth harmonic formulation and solution is given. For simplicity the zeroth harmonic is formulated by considering the actuator disk representation of the propeller directly, as opposed to the equivalent, but more complex, method of considering the zeroth harmonic of the finite bladed representation. Due to the exact equivalence of the two methods, the resulting equations are identical. The words zeroth harmonic and actuator disk will be used interchangeably, since the two are exactly equivalent.

DEFINITION OF PROPELLER FIXED COORDINATE SYSTEM

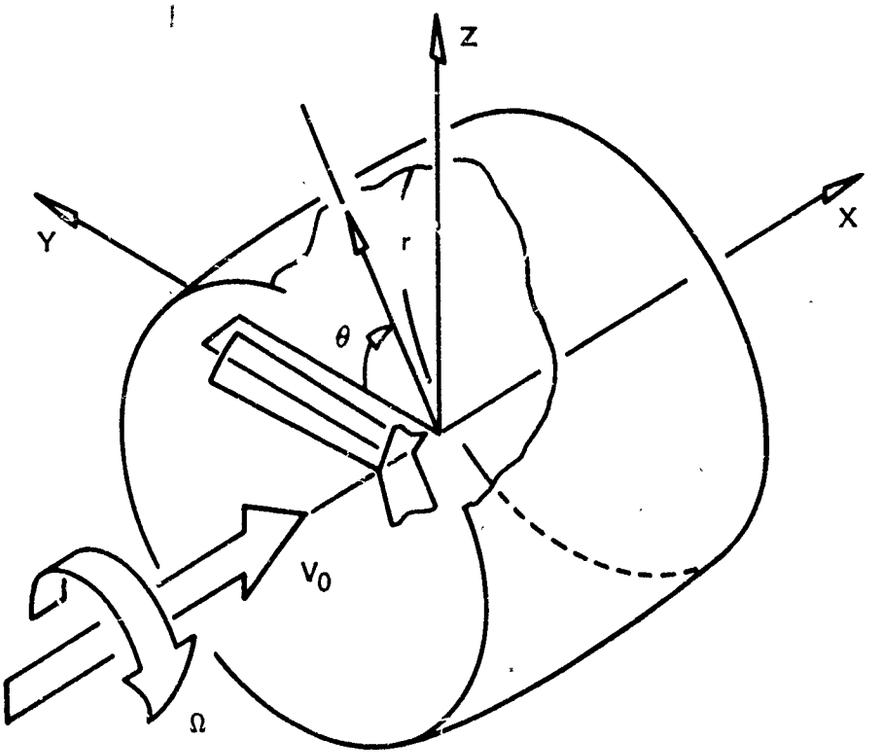

FIGURE 1.

6.1.2 Formulation of Mathematical Solution for Zeroth Harmonic

In the limit of the actuator disk representation of the propeller, there is no variation of flow properties with the angle Θ, so that all singularities used to represent the shroud, propeller, and wake system must have axisymmetric flow fields. Thus, the shroud camber line is represented by a distribution of vortex rings along the shroud reference cylinder. The shroud thickness form is represented by a distribution of source and sink rings along the reference cylinder. In the actuator disk limit the shroud sheds no wake, since there can be no azimuthal variation of vorticity along the shroud reference cylinder. The centerbody is represented by a line of three-dimensional sources and sinks distributed along the cylinder center line. The propeller in the limit of the zeroth harmonic is represented by an infinite number of bound blade vortices, oriented radially, whose strength varies radially in accordance with the propeller circulation distribution. This radial variation of propeller circulation gives rise to a propeller wake which is made up of an infinite number of helical filaments, set at the pitch corresponding to the ratio of free stream velocity to propeller tip speed.

Having described the mathematical singularities used to represent the various elements of the shrouded propeller, it is now necessary to specify their strengths. The source-sink distributions are obtained directly from the thickness forms, which for the shroud are defined relative to the shroud camber line. The shroud camber line is defined such that a normal at any point on the camber line, drawn from the upper surface to the lower surface, is bisected by the camber line. In this manner, the resulting thickness form is symmetrical. For reasons of mathematical tractability, the T.A.R. theory has been linearized by the assumption that the axial velocities induced by the various singularities are small compared to the free stream velocity. Consistent with this assumption, it is possible to show that the shroud source-sink distribution is proportional to the derivative of the thickness form with respect to chord, (See Ref. 3). The velocity field at any point can then be obtained by integration over the source-sink distribution.

The original T.A.R. theory did not include the effects of centerbody, which for practical shrouded propeller geometries could be significant. Therefore, Hamilton Standard, in conjunction with T.A.R., has incorporated centerbody effects into the theory and program. The details of the Hamilton Standard derivation are discussed in Appendix 11.1, and a brief description is given below. The centerbody is represented by a distribution of three-dimensional sources and sinks along the shroud centerline. Again, consistent with the linearization assumptions, application of continuity shows that the strength of this distribution is proportional to the derivative of the centerbody thickness form squared. Once the thickness form is specified, the velocity at any point in the flow field can be obtained by integration over the centerbody source-sink distribution.

The mathematical solution formulated by T.A.R. is such that the propeller radial circulation distribution is pre-specified, making it possible to use the theory to design a propeller geometry for the given distribution, but not to predict the distribution of

6.1.2 (Continued)

a given propeller geometry. This shortcoming was circumvented by use of an iterative procedure, described in paragraph 6.2.4. Once the propeller circulation distribution is specified, the circulation of the wake elements is also completely defined and the flow field due to the propeller and its wake can be obtained by use of the Biot-Savart law.

The only singularity distribution remaining to be specified is the vorticity distribution representing the shroud camber line. This distribution must be such that the boundary condition of no flow through the shroud wall be satisfied. Again, assuming that the induced axial velocity is small compared to V_o and that the slope of the camber line is small, this boundary condition becomes (See paragraph 6.2.5e for derivation):

$$\epsilon(X) = \frac{V_r\ (X)}{V_o} \tag{1}$$

where $\epsilon(X)$ = slope of the shroud camber line,

$V_r(X)$ = radial velocity along the mean camber line.

The radial velocity, $V_r(X)$, consists of contributions due to the propeller and its wake, the centerbody, the shroud thickness form, all of which are known within the synthesis of the T.A.R. analysis, and the unknown contribution due to the shroud vorticity. In terms of these velocities, the boundary condition Eq. (1) becomes

$$\left(\frac{V_r\ (X)}{V_o}\right)_{\substack{\text{Shroud}\\ \text{Vorticity}}} = \epsilon(X) - \left(\frac{V_r\ (X)}{V_o}\right)_{\substack{\text{Shroud}\\ \text{Thickness}}} - \left(\frac{V_r\ (X)}{V_o}\right)_{\substack{\text{Prop}\\ \text{Wake}}} - \left(\frac{V_r\ (X)}{V_o}\right)_{\text{Centerbody}} \tag{2}$$

where everything on the right hand side is known, but where the left hand side is known only in terms of the unknown shroud vorticity distribution. The relationship between $V_r(X)/V_o$ and the shroud vorticity distribution, $\gamma(X)$, is given by application of the Biot-Savart law to the ring vortices representing the shroud camber line, and results in a double integral over the shroud surface. A-priori integration over the azimuthal variable θ is permitted, since $\gamma(X)$ depends only on axial distance and not θ. This integration is expressible in terms of Legendre functions and reduces the double integral to the following single integral.

$$\left(\frac{V_r\ (\bar{X}_S)}{V_o}\right)_{\substack{\text{Shroud}\\ \text{Vorticity}}} = \int_{-\lambda}^{\lambda} \frac{\gamma(\bar{X}_V)}{V_o}\ \frac{\Delta\bar{X}_V}{2\pi}\ Q'_{1/2}\left(1 + \frac{\Delta\bar{X}_V^{\,2}}{2}\right) d\bar{X}_V \tag{3}$$

6.1.2 (Continued)

where

$Q'_{1/2}$ = derivative of Legendre function

$\bar{X}_V$ = X_V/R

X_V = position of shroud vortex ring

R = shroud reference cylinder radius

$\Delta\bar{X}_V$ = $\bar{X}_S - \bar{X}_V$

$\bar{X}_S$ = X_S/R

X_S = field point on shroud at which radial velocity is computed

C = shroud chord

λ = shroud chord/diameter ratio - C/2R

Substitution of Eq. (3) into Eq. (2) results in an integral equation for the unknown shroud vorticity distribution $\gamma(X_V)$, i.e.,

$$\int_{-\lambda}^{\lambda} \frac{\gamma(\bar{X}_V)}{V_o} \frac{\Delta\bar{X}_V}{2\pi} Q'_{1/2}\left(1 + \frac{\Delta\bar{X}_V}{2}^2\right) d\bar{X}_V = \epsilon(\bar{X}_S) - \frac{V_r(\bar{X}_S)}{V_o}\Big)_{\text{Shroud Thickness}} - \frac{V_r(\bar{X}_S)}{V_o}\Big)_{\text{Prop Wake}} - \frac{V_r(\bar{X}_S)}{V_o}\Big)_{\text{Center-body}} \quad (4)$$

It should be noted that due to symmetry considerations, the propeller bound vorticity, as represented by the actuator disk, does not induce a radial velocity at the shroud camber line, although the propeller wake does.

The T.A.R. mathematical solution of Eq. (4) for the zeroth harmonic is discussed in detail in Ref. 1 and 2. A brief description of the solution is given below. The evaluation of $\frac{V_r}{V_o}\Big)_{\text{prop wake}}$ in terms of propeller circulation is discussed in Appendix 11.7. Eq. (4) is solved by transformation to the Glauert variable ϕ, defined by $\bar{X} = -\lambda \cos\phi$ and expansion of $\gamma(\bar{X}_V)$ into the following Glauert series

$$\frac{\gamma(\phi_V)}{V_o} = \frac{b_{oo}}{2} \cot \phi_V + \sum_{\nu} \frac{b_{o\nu}}{2} \sin \nu \phi_V$$

where the summation on ν is carried out until the desired accuracy is obtained. Substitution of this expansion into Eq. (4), transformation of the variable of integration from $\bar{X}_V$ to the Glauert variable ϕ_V results in an integral equation in terms of the unknown constants $b_{o\nu}$.

6.1.2 (Continued)

The solution of this equation for the $b_{0\nu}$'s is based on an iteration procedure in which initial values for the $b_{0\nu}$'s are obtained by using a representation of the shroud vorticity distribution which neglects the curvature of the rings. This representation reduces the problem to that of classical thin airfoil theory. The initial values of the $b_{0\nu}$'s thus obtained are designated $b_{0\nu}^{2-D}$. The solution for the three-dimensional $b_{0\nu}$'s is complex and described fully in Ref. 2, along with the two-dimensional solution. The resulting expressions for the $b_{0\nu}$'s in terms of the $b_{0\nu}^{2-D}$ can be expressed concisely in matrix form as follows.

$$\left\{b_{0\nu}\right\} = \left[[I] + [P] + [P]^2 + \ldots [P]^j + \ldots\right]\left\{b_{0\nu}^{2-D}\right\}$$

Where the matrix [P] depends only on the shroud chord to diameter ratio and is tabulated in Ref. 2 for a range of λ's. Note that $[P]^j$ is defined as the self multiplication of [P] j times. The $([I] + [P] + \ldots [P]^j)$ matrix should be carried out to the point where the elements of $[P]^j$ are negligible compared to the sum of the previous terms, the power j of the last term representing the number of iterations necessary to obtain convergence.

The column matrix $\left\{b_{0\nu}^{2-D}\right\}$ is defined by the following set of equations in terms of the known radial velocities and camber on the right hand side of Eq. (4), and is the result of the classical thin airfoil solution mentioned above.

$$b_{00}^{2-D} = \frac{2}{\pi}\int_0^{\pi} \epsilon_e \, d\phi_s$$

$$b_{0\nu}^{2-D} = -\frac{4}{\pi}\int_0^{\pi} \epsilon_e \cos\nu\phi_s \, d\phi_s$$

where

$$\epsilon_e = 2\left\{\epsilon - \left(\frac{V_r}{V_0}\right)_{\substack{\text{Shroud}\\\text{Thickness}}} - \left(\frac{V_r}{V_0}\right)_{\substack{\text{Prop}\\\text{Wake}}} - \left(\frac{V_r}{V_0}\right)_{\substack{\text{Center-}\\\text{body}}}\right\}$$

The above paragraphs briefly described the formulation and T.A.R. mathematical solution for the zeroth harmonic. It is a linearized theory which accounts for the effects of shroud geometry, propeller circulation distribution, radius and location, and centerbody shape and location. Inherent in the linearized treatment of the problem are certain restrictions on the applicability of the method. These restrictions, and the attempts during this program to alleviate them will be the subject of the following paragraphs.

6.2 LIMITING ASSUMPTIONS OF THERM ADVANCED RESEARCH MODEL

6.2.1 Introduction

Due to practical considerations dictated by the need for mathematical tractability, certain simplifying assumptions to the mathematical model were necessary. These assumptions, which were discussed briefly in paragraph 6.1, manifest themselves as limitations on the applicability of the theory to certain regimes of operation. During the course of this contract, attempts were made to alleviate certain of these assumptions, in hopes of extending the applicability of the theory to a wider range of operating conditions. The nature of these attempts and their success or failure in improving the comparisons of test and theory are the subject of this section.

The following represent the major assumptions and the areas in which improvements to the theory were investigated.

1. Use of Zeroth Harmonic
2. Incompressible Flow
3. Input of Propeller Circulation Distribution
4. Linearization

The evaluation of these improvements is carried out at a Mach number of .3. The value is low enough to make compressibility effects small and yet high enough to satisfy the requirement that the perturbation velocities be small compared to V_o.

The effect of these corrections at the lower Mach numbers is considered in Section 7.0, where extensive comparisons of test and theory are made for the complete Mach number range.

6.2.2 Discussion of Zeroth Harmonic Assumption

Exclusion of the higher harmonics is dictated by the need for a mathematically tractable solution and computer program and in this sense is not a limitation of the theory (since the full theory as derived includes the effects of the higher harmonics). The validity of this assumption depends primarily on how well the theoretical and experimental performance results compare.

Consistent with the zeroth harmonic assumption is the representation of the propeller as an actuator disk. In evaluating the thrust and torque of the propeller, it is necessary to obtain the velocity diagram at each blade station. This diagram is shown in Fig. 2 for a typical radial position, with the induced velocity broken down into its various components. The shroud and centerbody induced velocity are obtained from

PROPELLER VELOCITY DIAGRAM AT TYPICAL STATION

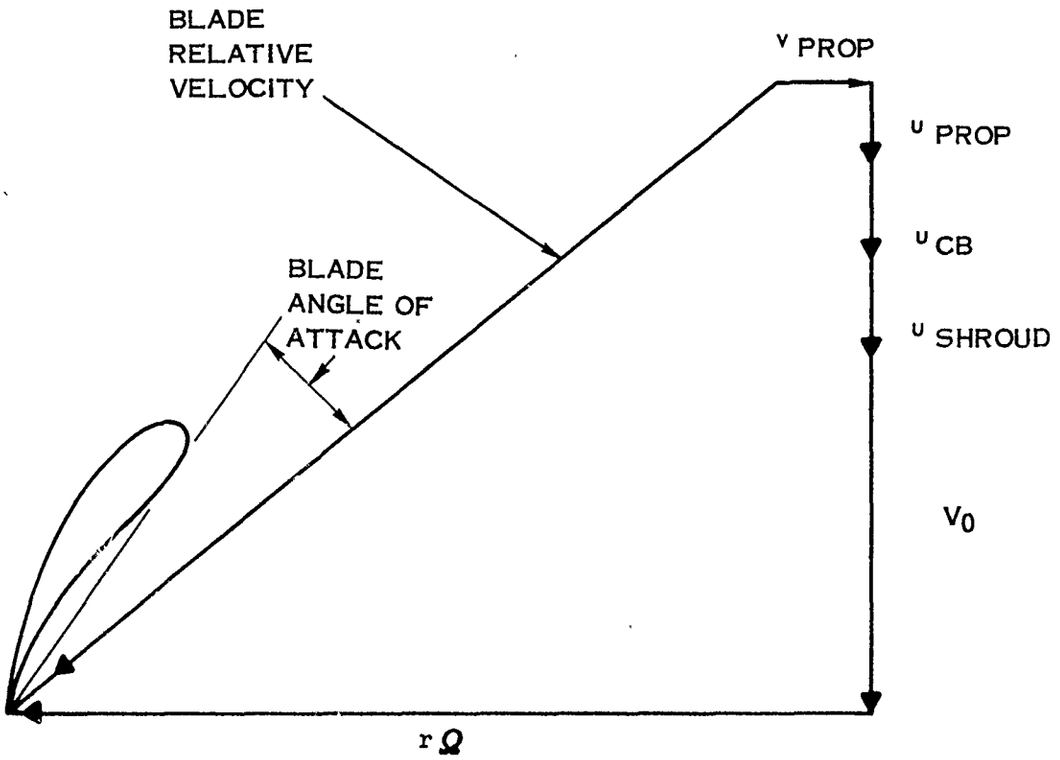

FIGURE 2.

6.2.2 (Continued)

the zeroth harmonic T.A.R. theory and are discussed in Appendix 11.6. However, instead of obtaining the propeller wake induced velocities from the actuator disk representation of the propeller, a partial accounting of the higher harmonic content of the propeller induced velocities is obtained by the use of the Goldstein three-dimensional representation of the propeller wake, (Ref. 4 & 5).

Hamilton Standard's experience with this method in the design and performance prediction of free air propellers in forward flight has shown that it accurately predicts the induced velocity field of the propeller wake.

A distinction should be made at this point to clarify the role of the propeller. Its influence on the velocity diagram is twofold. An indirect influence exists through the shroud vorticity distribution, which gives rise to the shroud induced velocity of Fig. 2. The propeller influence on shroud vorticity, and, therefore, shroud induced velocity, enters through Eq. (4), which is valid for the zeroth harmonic and requires the actuator disk representation for the propeller. The direct influence involves the induced velocity at the blade due to the propeller wake. This velocity is best represented by the three-dimensional Goldstein theory.

An estimate of the magnitude of the higher harmonics and, therefore, the validity of the above representations of the propeller induced velocity is afforded by the study of the pressure histories obtained during the test program. These data were obtained by two pressure transducers mounted in the shroud inner and outer surfaces just upstream of the propeller. The pressure fluctuations on the outer surface were small and indistinguishable for the most part from the inherent background noise signal. The inner surface fluctuations were much larger and resulted in usable traces. For purposes of estimating the magnitude of the higher harmonics, this inner signal, since it is closest to the propeller, represents the velocity field of most interest. The following discussion is, therefore, limited to consideration of the inner trace.

The velocity at the transducer consists of contributions from the propeller, its wake, and the remaining singularities used to define the shroud and centerbody. As discussed above, the direct contribution of the propeller wake to the velocity diagram as calculated by use of the Goldstein method accounts for the higher harmonics. The indirect effect, however, does not, since it manifests itself through the shroud induced velocity, which is based on the zeroth harmonic representation. The time history of the shroud induced velocity, or its equivalent shroud induced pressure, would be indicative of its harmonic content and, therefore, the validity of the zeroth harmonic representation. If the amplitude of the shroud induced pressure is small compared to the amplitude of the measured pressure, the major portion of the harmonic content is due to the propeller and wake, and as discussed above, is properly accounted for by use of the Goldstein method and the zeroth harmonic calculation for the shroud induced velocity. If not, inclusion of the higher harmonics is necessary for the calculation of

6.2.2 (Continued)

the shroud induced velocity.

An estimate of the harmonic content of the shroud induced velocity was made by subtracting the pressure contribution due to the propeller bound vorticity from the experimental pressure history. A complete accounting of the propeller contribution would also require the subtraction of the wake induced velocity. This entails the calculation, as a function of azimuthal angle, of the velocity field due to the propeller wake at the azial location of the pressure transducer, which is 0.075 shroud chord lengths upstream of the propeller disk. Methods for calculating this velocity were investigated and found to be formidable. In addition, the proximity of the transducer to the propeller bound vortex implies that much of the propeller induced azimuthal variation should be due to the bound vorticities. For these reasons, only the bound contributions were subtracted out since these could be evaluated with a reasonable amount of work. The derivation of the equations for the velocity field of the bound vortices is included in Appendix 11.5.

The relationship between the shroud surface pressure and velocity is given by Bernoulli's equation written for a coordinate system rotating with the propeller. This is shown in Eq. (5).

$$\frac{p - p_\infty}{q_o} = 1 + \frac{r^2 \Omega^2}{V_o^2} - \frac{w^2}{V_o^2} \qquad (5)$$

where w = velocity relative to a point in the propeller fixed coordinate system and contains no time varying quantities since, in this propeller fixed system, all the flow properties are steady. The time varying pressure field observed from a ground fixed coordinate system is equivalent to the azimuthal pressure variation observed in the propeller fixed system. Thus, the pressure histories obtained from the test program can be immediately converted to azimuthal pressure variations in the propeller fixed system. The following discussion is based on the use of a propeller fixed coordinate system. The velocity $\vec{w}$ can be written as follows, in terms of its various components

$$\vec{w} = (w_\theta + v_p)\,\vec{1}_\theta + (w_x + u_p)\,\vec{1}_x$$

where

v_p = tangential component of the propeller bound vortex velocity

u_p = axial component of the propeller bound vortex velocity

w_θ, w_x = velocity relative to blade exclusive of propeller bound vortex velocity

6.2.2 (Continued)

Its magnitude squared becomes

$$w^2 = (w_\theta + v_p)^2 + (w_x + u_p)^2$$

or

$$w^2 = w_\theta^2 + w_x^2 + 2 v_p w_\theta + 2 u_p w_x + u_p^2 + v_p^2 \quad (6)$$

Defining a total pressure coefficient C_p as $\frac{p-p_\infty}{q_o}$, Eq. (5) becomes

$$C_p = 1 + \frac{r^2 \Omega^2}{V_o^2} - \frac{w^2}{V_o^2} \quad (7)$$

It is this Cp that results from the pressure history obtained in the test program and is a known function of θ. A partial pressure coefficient can be defined in terms of w_θ^2 and w_x^2, the velocities due to everything but the propeller bound vorticity. Signifying this velocity and pressure coefficient by the subscript s, there results from Eq. (6):

$$w_s^2 = w^2 - (2v_p w_\theta + 2 u_p w_x + u_p^2 + v_p^2) \quad (8)$$

Eq. (7) can be solved for w^2 as follows

$$\frac{w^2}{V_o^2} = 1 + \frac{r^2 \Omega^2}{V_o^2} - C_p \quad (9)$$

Substituting Eq. (9) into Eq. (8), there results

$$\frac{w_s^2}{V_o^2} = 1 + \frac{r^2 \Omega^2}{V_o^2} - C_p - \left(\frac{2 v_p w_\theta}{V_o^2} + \frac{2 u_p w_x}{V_o^2} + \frac{u_p^2 + v_p^2}{V_o^2} \right) \quad (10)$$

From Eq. (7), C_{ps}, the partial pressure coefficient, becomes

$$C_{ps} = 1 + \frac{r^2 \Omega^2}{V_o^2} - \frac{w_s^2}{V_o^2} \quad (11)$$

6.2.2 (Continued)

Substituting Eq. (10) into Eq. (11), the equation for C_{ps} becomes

$$C_{ps} = C_p + \frac{2\, v_p\, w_\theta}{V_o^2} + \frac{2\, u_p\, w_x}{V_o^2} + \frac{u_p^2}{V_o^2} + \frac{v_p^2}{V_o^2} \qquad (12)$$

Now w_x and w_θ represent the velocity relative to the propeller fixed coordinate system. The velocity diagram below shows that w_x and w_θ are made up of components due to the axial free stream velocity, propeller rotative speed, and the velocities (u_e and v_e) induced by all singularities except the propeller bound vorticity.

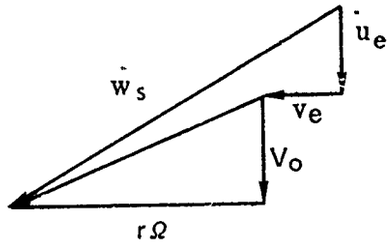

In terms of these components, w_x and w_θ become

$$w_x = V_o + u_e$$

$$w_\theta = r\Omega + v_e$$

Substituting these expressions for w_x and w_θ into Eq. (12) C_{ps} becomes

$$C_{ps} = C_p + \frac{2\, v_p r\, \Omega}{V_o^2} + \frac{2u_p\, V_o}{V_o^2} + \frac{2\, v_p\, v_e}{V_o^2} + \frac{2u_p\, u_e}{V_o^2} + \frac{u_p^2}{V_o^2} + \frac{v_p^2}{V_o^2} \qquad (13)$$

The quantities u_p, u_e, v_p, v_e represent the velocities induced by the singularities in the flow field, and are all small compared to V_o. The last 4 terms of Eq. (13) are therefore seen to be of second order compared to the remaining first order terms and can be neglected. Equation (13) thus reduces to Eq. (14)

6.2.2 (Continued)

$$C_{ps} = C_p + \frac{2\, v_p r\, \Omega}{V_o^2} + 2\, \frac{u_p}{V_o} \qquad (14)$$

which relates the partial pressure coefficient C_{ps} to quantities which are known either analytically or experimentally.

The pressure coefficient on the right hand side, C_p, is known from the test data, and the velocity components u_p, v_p due to the propeller bound vorticity are known analytically, as described in Appendix 11.5. Thus, everything on the right hand side is known as a function of azimuthal angle. The evaluation of Eq. (14) results in the azimuthal variation of the pressure coefficient based on all velocities except those due to the propeller bound vorticities, and should give a qualitative indication of the importance of the higher harmonics in evaluating the shroud induced portions of the velocity.

Eq. (14) was evaluated for the pressure history corresponding to run number 681-10 in Ref. 15. The operating condition was:

N	= 6502
J	= 1.276
C_P	= 0.428
$C_{T\ prop}$	= 0.249
M	= 0.3083

The total pressure coefficient is plotted in Fig. 3. Using the propeller circulation distribution computed for the above case, the velocities induced by the propeller bound vortex, u_p, v_p, were computed as outlined in Appendix 11.5. The partial pressure coefficient C_{ps} was then obtained from Eq. (14) and is also plotted on Fig. 3. The amplitude of the partial pressure coefficient is reduced by 54%, indicating that about half of the harmonic content is due to the propeller bound vorticity.

Inclusion of the wake induced velocity would lower the amplitude of the secondary pressure coefficient even further. Thus a large portion of the harmonic content is due directly to the propeller and is accounted for by the use of the three-dimensional Goldstein theory.

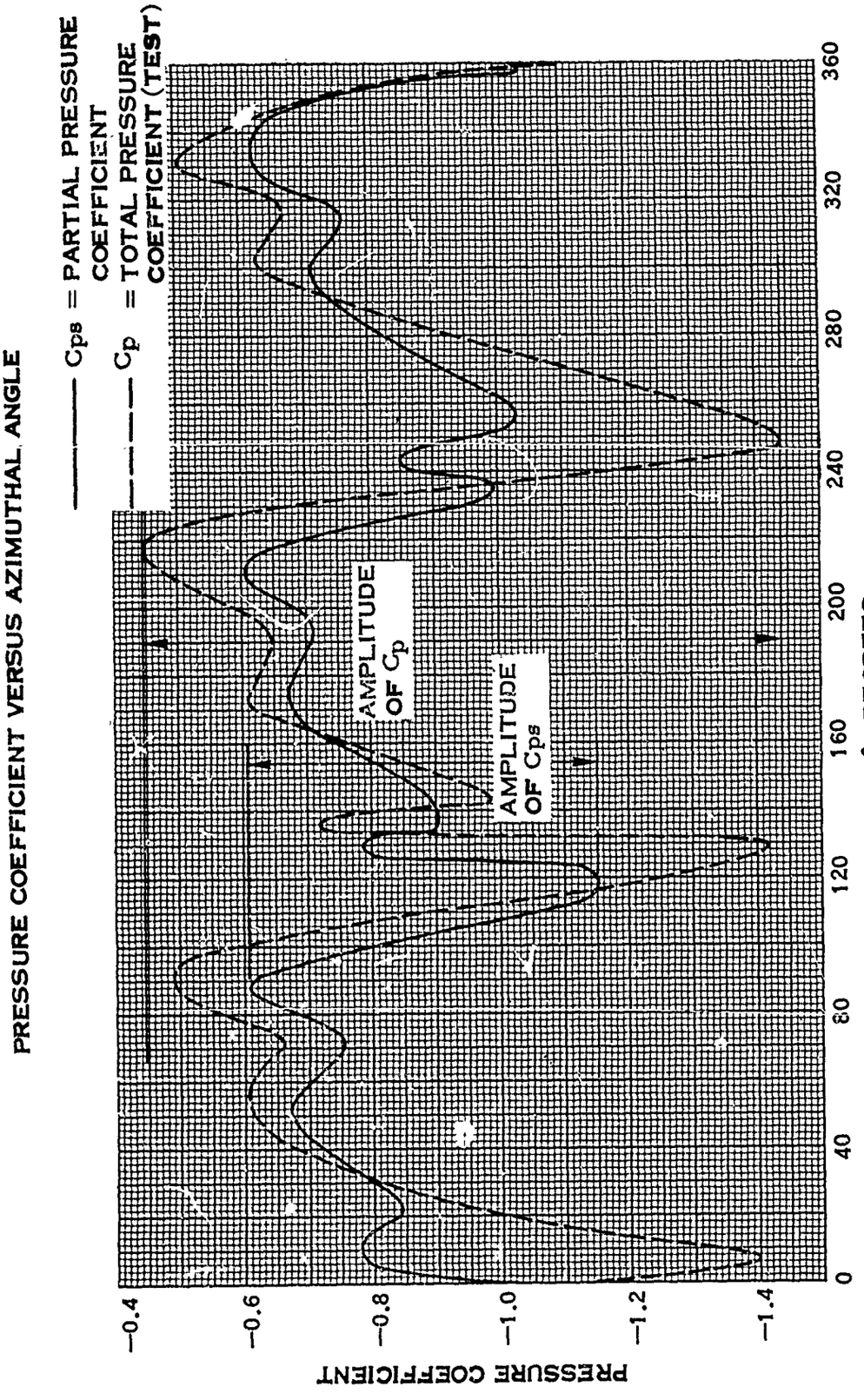
PRESSURE COEFFICIENT VERSUS AZIMUTHAL ANGLE
——— C_{ps} = PARTIAL PRESSURE COEFFICIENT
— — — C_p = TOTAL PRESSURE COEFFICIENT (TEST)
AMPLITUDE OF C_p
AMPLITUDE OF C_{ps}
PRESSURE COEFFICIENT
−0.4
−0.6
−0.8
−1.0
−1.2
−1.4
0
40
80
120
160
200
240
280
320
360
θ – DEGREES

FIGURE 3.

6.2.2 (Continued)

The excellent agreement exhibited in paragraph 7.4 between test and theory further indicates that the harmonic content of the shroud induced velocity, which is not accounted for by the theory, is small enough to have a negligible effect on performance.

In summary, it appears that the effects of the higher harmonics are due primarily to the direct contribution of the propeller. The indirect contribution which manifests itself through the shroud induced velocity appears to be secondary in nature. Thus, incorporation of the three-dimensional Goldstein analysis for the velocity field of the propeller accounts for a significant portion of the higher harmonics, results in an accurate performance prediction method, and eliminates the necessity of accounting for the higher harmonics in the shroud induced velocity calculation.

6.2.3 Discussion of Incompressible Flow Assumption

The assumption of incompressible flow is not severely limiting unless the free stream Mach number is high or the shroud area ratio and/or thickness form is large. For those cases where compressibility effects can be significant, a study of the applicability of the Karman-Tsien (K-T) correction to the flow field was undertaken. As derived, the K-T correction is applicable only to two-dimensional flow. Since the flow about the shroud is axisymmetric, the governing compressible flow equations must be written for a cylindrical coordinate system. The K-T correction, however, is based on use of the flow equations written for a two-dimensional Cartesian coordinate system. These equations are listed below in terms of the velocity potential ϕ, and speed of sound c,

$$\left(1 - \frac{\phi_r^2}{c^2}\right)\phi_{rr} + \left(1 - \frac{\phi_z^2}{c^2}\right)\phi_{zz} - \frac{2\phi_z\phi_r}{c^2}\phi_{zr} + \frac{\phi_r}{r} = 0$$

$$\left(1 - \frac{\phi_x^2}{c^2}\right)\phi_{xx} + \left(1 - \frac{\phi_z^2}{c^2}\right)\phi_{zz} - \frac{2\phi_x\phi_z}{c^2}\phi_{zx} = 0$$

where ϕ_r represents $\frac{\partial\phi}{\partial r}$, etc. Since ϕ_r, the radial velocity, is small, the two equations are seen to approach each other as r gets large. Thus, for flow about the shroud, where r tends to be large, the two equations are similar if ϕ_r is small and the K-T pressure correction may be applicable. Near the shroud centerline, where r is small, the equations differ and the K-T correction is definitely not applicable.

Comparison of theoretical and experimental shroud pressure distributions for the 1.1 and 1.3 area ratio shrouds for the .3 and .5 Mach number cases are shown in Fig. 4

6.2.3 (Continued)

through 7. The pressure coefficients in these figures has been corrected for the singularity in leading edge pressure due to the shroud camber line vorticity distribution by use of the Riegels factor, which will be discussed in paragraph 6.2.5c, but do not incorporate the K-T correction. The agreement of the incompressible theory with the test data is good for both Mach numbers.

The agreement on the outer surface for the .3 Mach number case is very good. At M = .5 the agreement is good except in the leading edge region. However, due to application of the Riegels correction, which at best is approximate, the resulting pressure distributions in the leading edge region cannot be expected to be highly accurate. Application of the K-T correction would improve the agreement in the leading edge region somewhat and worsen it from the quarter chord point to the trailing edge. On the inner surface, for $0. \leq \frac{X}{C} \leq .2$ the theory is seen to predict pressure coefficients which are more negative than the data, indicating over-estimation of the velocity magnitude. Application of the K-T correction would cause the pressure coefficients to become even more negative. It appears then, that the over-estimation of velocity by the incompressible T.A.R. theory in the leading edge region tends to compensate for the effects of compressibility. In view of these observations, coupled with the questionable applicability of the K-T correction to axisymmetric flow fields, no direct account will be made in the program for compressibility effects on the shroud pressure distribution.

The propeller velocity diagrams have not been corrected for the effects of compressibility because, as discussed above, the K-T correction becomes invalid as the inboard stations of the propeller are reached. In addition, it has been Hamilton Standard's experience that compressible propeller performance is well predicted by using the incompressible Goldstein solution with compressibility effects accounted for only in the airfoil data.

6.2.4 Inclusion of Propeller Geometry

The usefulness of an analytical prediction method for shrouded propellers depends in part on its ability to predict the performance of a given shroud and propeller geometry. The T.A.R. theory, as discussed in paragraph 6.1, requires that the propeller circulation distribution be specified. This approach permits the definition of the propeller geometry consistent with the specified circulation distribution but cannot predict the circulation of a propeller whose geometry is pre-defined.

To eliminate this shortcoming, Hamilton Standard has devised an iterative method which permits propeller geometry instead of circulation to be used as an input. The essence of the method is as follows.

a) The propeller geometry is defined, i.e., the blade angle, chord, and airfoil section are specified as functions of blade radius; the airfoil lift and drag characteristics are also specified.

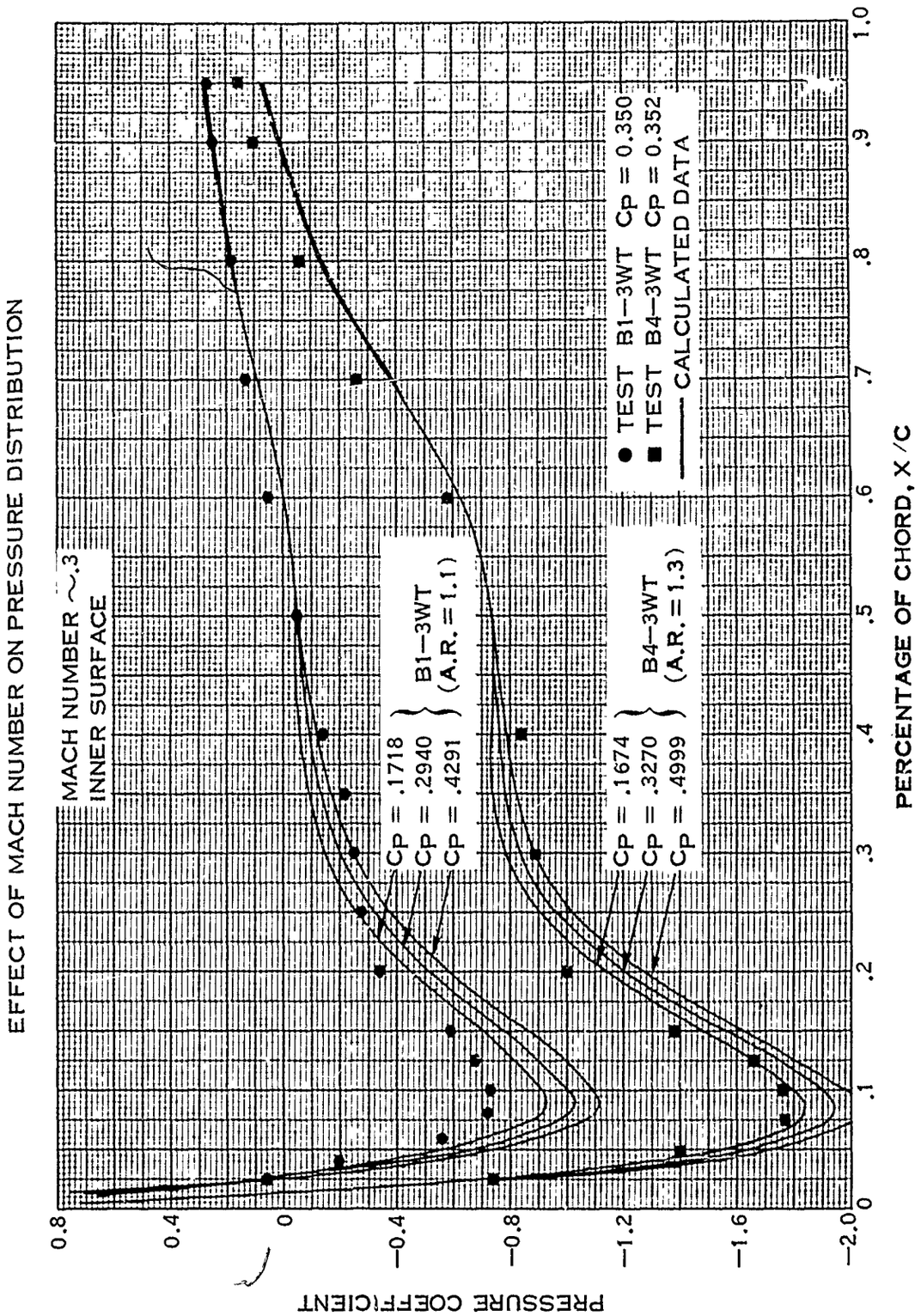
EFFECT OF MACH NUMBER ON PRESSURE DISTRIBUTION
MACH NUMBER ~.3
INNER SURFACE
Cp = .1718
Cp = .2940
Cp = .4291
B1–3WT (A.R. = 1.1)
Cp = .1674
Cp = .3270
Cp = .4999
B4–3WT (A.R. = 1.3)
● TEST B1–3WT Cp = 0.350
■ TEST B4–3WT Cp = 0.352
—— CALCULATED DATA
PRESSURE COEFFICIENT
0.8
0.4
0
−0.4
−0.8
−1.2
−1.6
−2.0
0
.1
.2
.3
.4
.5
.6
.7
.8
.9
1.0
PERCENTAGE OF CHORD, X/C

FIGURE 4.

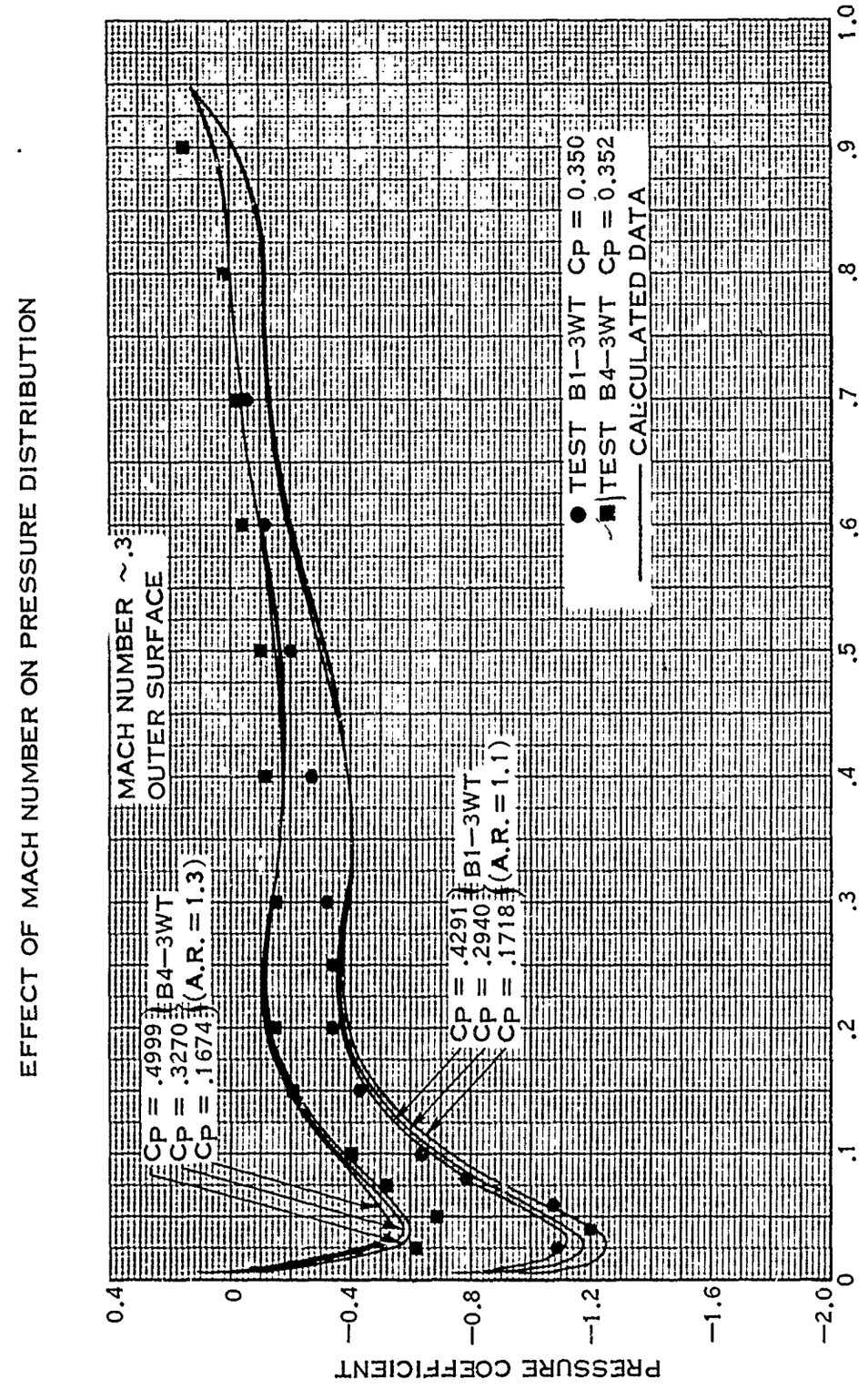
EFFECT OF MACH NUMBER ON PRESSURE DISTRIBUTION
MACH NUMBER ~.35
OUTER SURFACE
CP = .4999 B4—3WT (A.R. = 1.3)
CP = .3270
CP = .1674
CP = .4291 B1—3WT (A.R. = 1.1)
CP = .2940
CP = .1718
● TEST B1—3WT CP = 0.350
■ TEST B4—3WT CP = 0.352
—— CALCULATED DATA
PRESSURE COEFFICIENT
0.4
0
—0.4
—0.8
—1.2
—1.6
—2.0
0
.1
.2
.3
.4
.5
.6
.7
.8
.9
1.0
PERCENTAGE OF CHORD, X/C
B1—3WT
(A.R. = 1.1)

FIGURE 5.

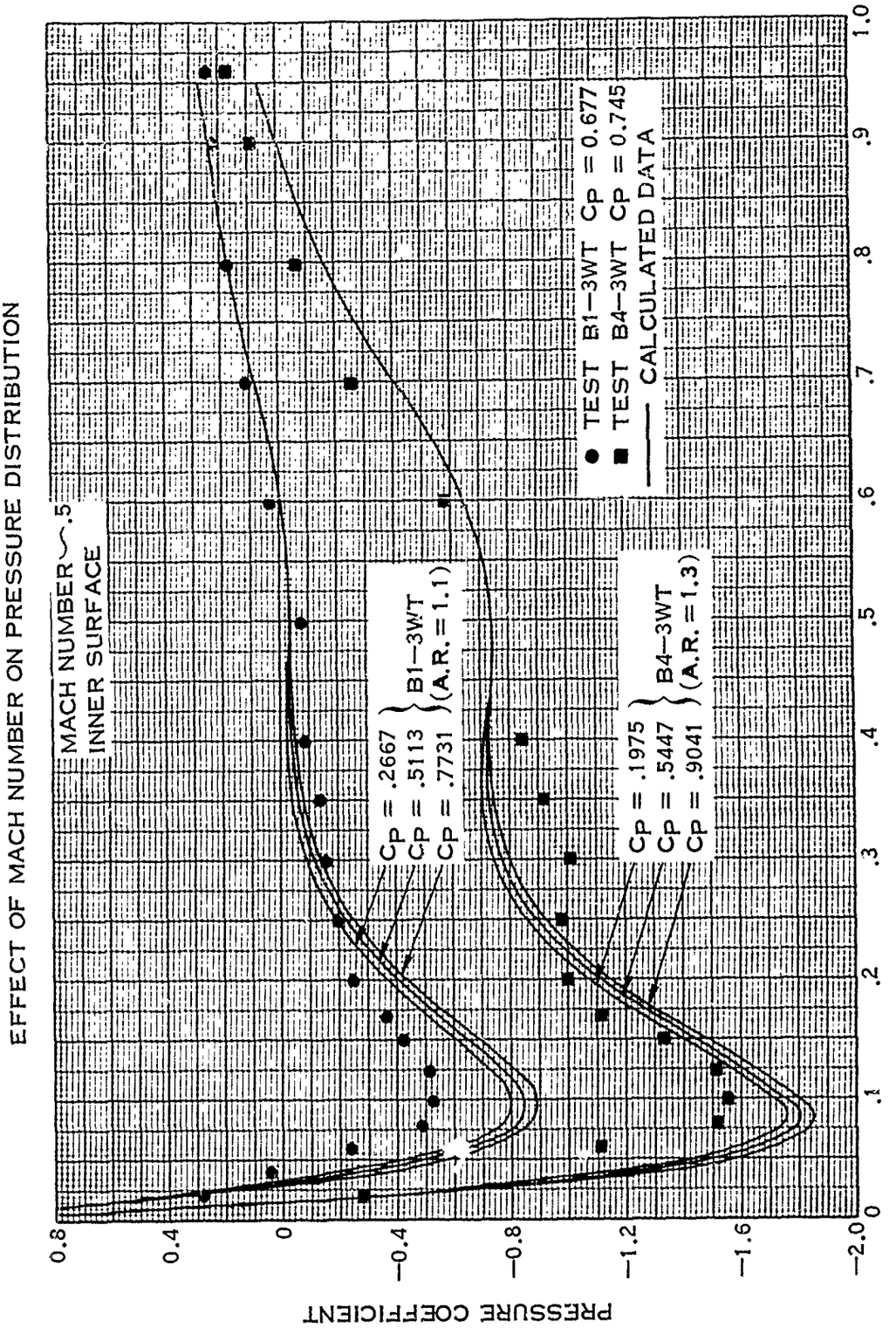
EFFECT OF MACH NUMBER ON PRESSURE DISTRIBUTION
MACH NUMBER ~.5
INNER SURFACE
● TEST B1—3WT Cp = 0.677
■ TEST B4—3WT Cp = 0.745
—— CALCULATED DATA
Cp = .2667
Cp = .5113
Cp = .7731
B1—3WT (A.R. = 1.1)
Cp = .1975
Cp = .5447
Cp = .9041
B4—3WT (A.R. = 1.3)
PRESSURE COEFFICIENT
0.8
0.4
0
−0.4
−0.8
−1.2
−1.6
−2.0
0
.1
.2
.3
.4
.5
.6
.7
.8
.9
1.0
PERCENTAGE OF CHORD, X/C

FIGURE 6.

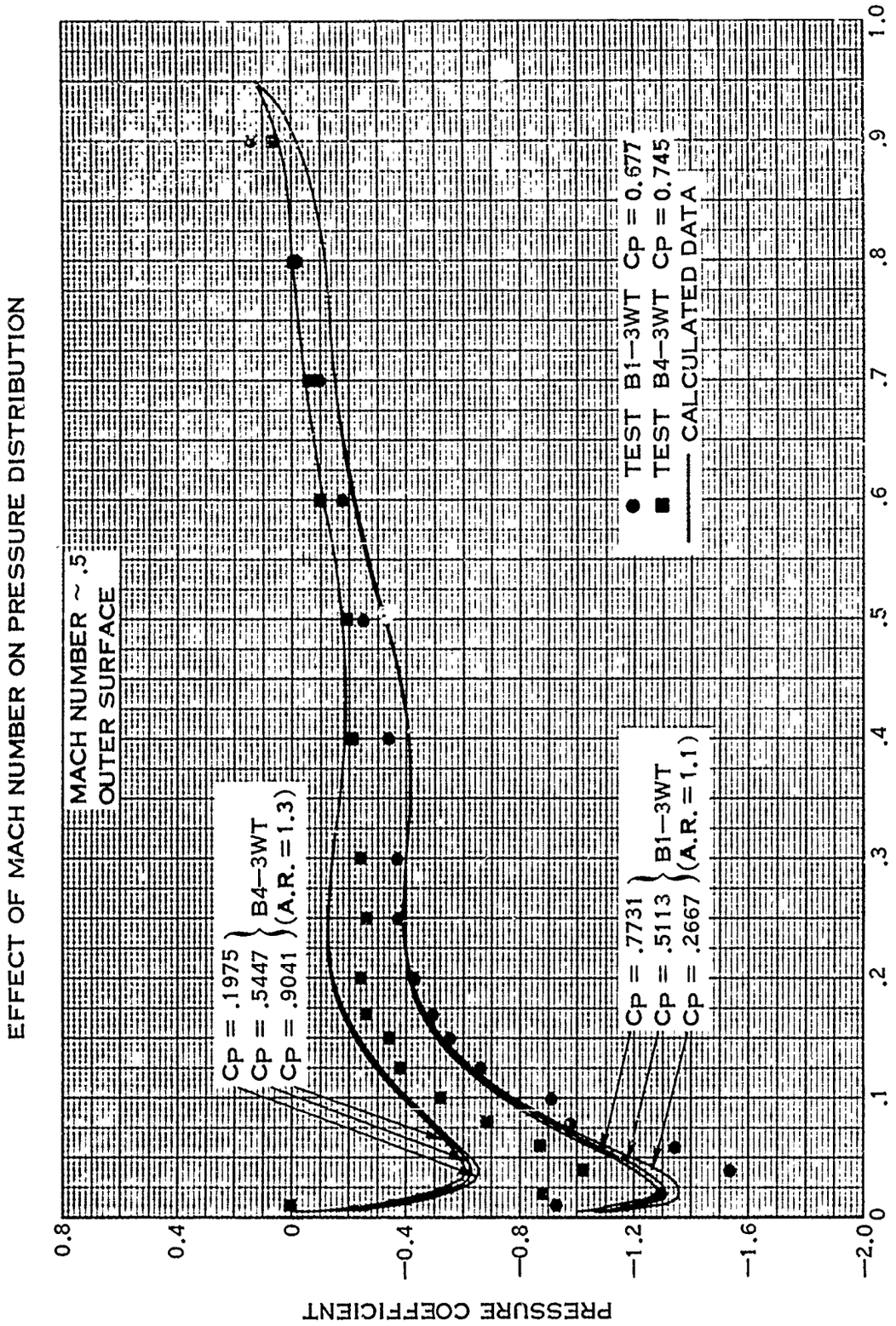
EFFECT OF MACH NUMBER ON PRESSURE DISTRIBUTION
MACH NUMBER ~ .5
OUTER SURFACE
Cp = .1975
Cp = .5447
Cp = .9041
B4—3WT (A.R. = 1.3)
Cp = .7731
Cp = .5113
Cp = .2667
B1—3WT (A.R. = 1.1)
● TEST B1—3WT Cp = 0.677
■ TEST B4—3WT Cp = 0.745
—— CALCULATED DATA
PRESSURE COEFFICIENT
0.8
0.4
0
—0.4
—0.8
—1.2
—1.6
—2.0
0
.1
.2
.3
.4
.5
.6
.7
.8
.9
1.0
PERCENTAGE OF CHORD, X/C

FIGURE 7.

6.2.4 (Continued)

b) An initial estimate is made for the induced velocity in the propeller plane due to shroud vorticity (the thickness and centerbody induced velocities are known in terms of the shroud and centerbody thickness forms, as discussed in paragraph 6.1).

c) The Goldstein strip theory is then used to obtain the propeller circulation and propeller induced velocities at each station. An iterative process is involved in this computation, as described in paragraph 6.6.2.

d) Having an estimated propeller circulation, the shroud vorticity distribution is determined and the shroud induced velocity at the propeller plane computed.

e) This computed velocity is compared with the initial estimate. If the two agree within a specified tolerance, the solution is complete. If not, a new estimate is made and the process repeated until convergence of the velocity field results.

Experience with this method indicates convergence requires 4 to 5 iterations. The computer program has been written to include the iterative process and is described more fully in paragraph 6.6.

6.2.5 Discussion of Linearization Assumptions

6.2.5a Introduction

The greatest restrictions imposed on the T.A.R. model result from the linearizations necessary to make the theory mathematically tractable. These linearizations require that the induced velocities due to the various singularities in the flow field be small relative to the free stream velocity, which in turn requires that the camber and thickness be small.

Due to these restrictions, extension of the theory to low free stream velocities, or for a high free stream velocity, to large cambers and thicknesses, is questionable. Since both of these areas are of interest, various investigations were made during the course of this contract to remove some of the linearization assumptions inherent in the model. These investigations will be discussed in the following paragraphs and are divided into three categories:

1. Representation of Shroud and Centerbody Geometry

2. Representation of Propeller and Wake

3. Satisfaction of Shroud Boundary Conditions

6.2.5b Representation of Shroud and Centerbody Geometry

The centerbody is represented by a distribution of sources and sinks along the shroud centerline. The shroud geometry is represented by a distribution of source-sink rings and vortex rings along the shroud reference cylinder, the source-sink rings representing the thickness and the vortex rings representing the camber. Consideration was given to redistributing the shroud singularities along the mean camber line instead of the shroud reference cylinder. This, however, would entail major changes in the equations defining the shroud induced velocities. In addition, changing the shroud reference cylinder radius from that defined by the T.A.R. theory (i.e., the intersection of the camber line with the propelier plane) to the shroud trailing edge had a secondary effect on the shroud pressure distribution and propeller performance, indicating that the added mathematical complexity required by the modification would result in only secondary changes and is, therefore, not warranted.

In computing the shroud pressure distributions, the velocity at the shroud surface is approximated by its value along the shroud reference cylinder. The error inherent in this assumption was investigated by computing the velocity distribution in the plane of the propeller from the shroud reference cylinder inward towards the centerline. The true shroud surface velocity at the propeller plane was then compared with the velocity at the shroud reference cylinder. This velocity was converted to a pressure coefficient, and the ratio of the difference in pressure coefficient divided by the pressure coefficient at the shroud reference cylinder is plotted in Fig. 8 as a function of propeller power coefficient for the 1.1 (B1) and 1.3 (B4) area ratio shrouds. The change in pressure coefficient is of the order of 4-12% depending on the propeller power coefficient. However, the effect of using the shroud surface is to increase the pressure coefficient at the propeller location, which would cause poorer agreement between test and theory. The effects of compressibility tend to compensate for this increase in pressure coefficient and account in part for the good agreement exhibited between test and theory. The fact that differences on the order of 4-12% can occur indicates that consideration should be given to the calculation of velocities on the shroud surface. This entails a change in the velocity equations, a corresponding change in the computer program, and a slight increase in computer time. It is recommended that this modification be further investigated and incorporated during future studies.

6.2.5c Riegels Factor

The distribution of shroud vorticity along the reference cylinder results in a singularity in velocity at the shroud leading edge. This singularity causes the pressure coefficient to approach minus infinity at the leading edge, rendering the leading edge results invalid. Such a singularity is inherent in all thin airfoil theory and is observed in the classical solution for the flow about a flat plate (See, for example, Ref. 6). Removal of this singularity has been incorporated in the program by application of a correction due to Riegels (Ref. 7). This correction eliminates the singularity at the

EFFECT OF FIELD POINT LOCATION ON SHROUD PRESSURE COEFFICIENT

POINT ON INNER SURFACE OF SHROUD, AT PROPELLER PLANE

$$\Delta C_{PRESS} = C_{PRESS} - C_{PRESS/S}$$

C_{PRESS} = PRESSURE COEFFICIENT AT SHROUD REFERENCE CYLINDER
$C_{PRESS/S}$ = PRESSURE COEFFICIENT AT SHROUD SURFACE

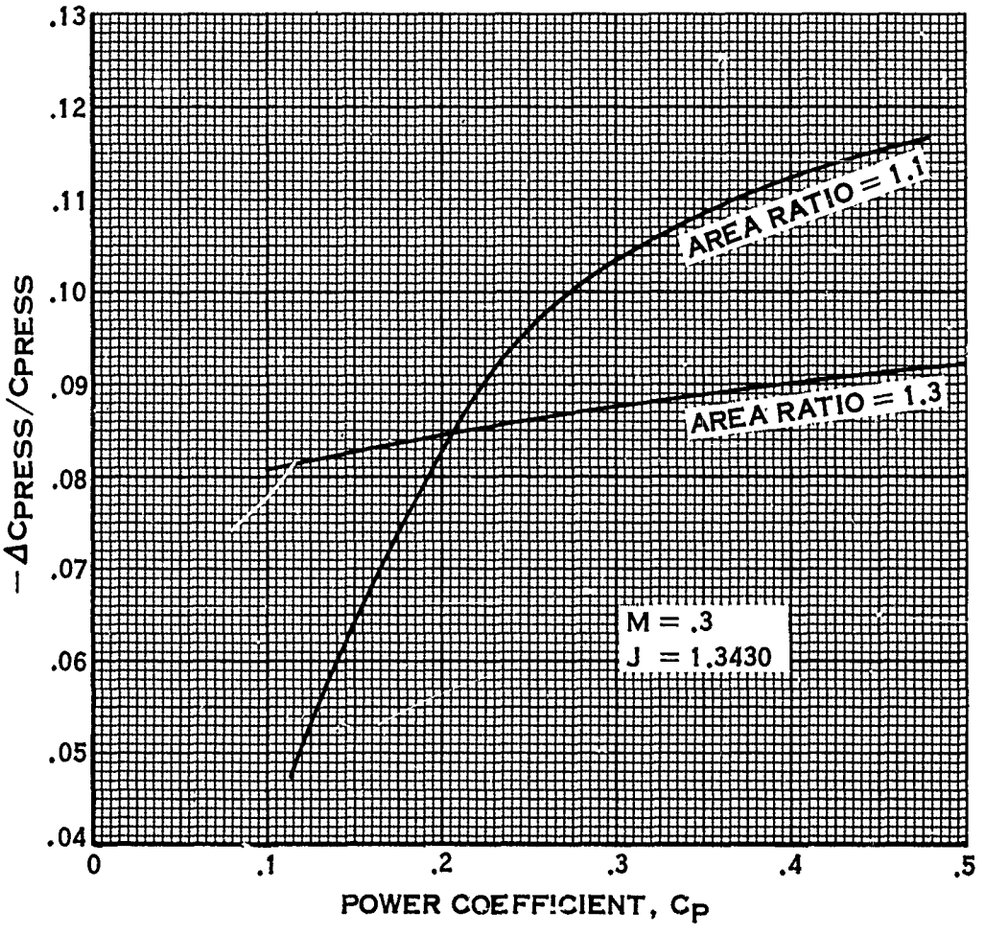

FIGURE 8.

6.2.5c (Continued)

leading edge by treating the flow as though the leading edge were elliptical instead of the sharp edge representative of the reference cylinder vorticity distribution. The correction is given in terms of the slope of the thickness form and is applied to the velocity calculated by the linearized theory, i.e.,

$$V_{corrected} = \frac{V_{linearized}}{\sqrt{1 + \left(\frac{d\bar{y}}{d\bar{x}}\right)^2}} \qquad (15)$$

where $V_{linearized}$ is the total velocity at some chordwise position based on the linearized theory and $d\bar{y}/d\bar{x}$ is the slope of the thickness form. This correction is significant only in the leading edge region, where the rate of change of thickness with chord is large and approaches infinity at the leading edge. In the program, this correction is applied from the leading edge to the point of zero slope of the shroud thickness form.

The velocity, $V_{linearized}$, is composed of contributions from the shroud source-sink distribution, propeller wake, and centerbody as well as the shroud vorticity. Of these, the shroud vorticity and source-sink contributions are unbounded as the leading edge is approached, and warrant further investigation. Note that the shroud source-sink contribution is unbounded because, within the linearized assumptions, the source-sink distribution is proportional to $d\bar{y}/d\bar{x}$, which is infinite at the leading edge. It is necessary then to investigate the limit of Eq. (15) as $\bar{x} \rightarrow -\lambda$, (i.e., as the shroud leading edge is approached). To do this, it is necessary to investigate only the singular terms of the velocity contributions, since the non-singular terms approach zero with application of the correction. For the shroud source-sink distribution, this term is of the form,

$$V_{thick} = A \ln \left| \frac{\frac{\bar{x}}{\lambda} - 1}{\frac{\bar{x}}{\lambda} + 1} \right| \qquad (16)$$

where A is a constant.

The shroud vorticity equation takes the form,

6.2.5c (Continued)

$$V_{vort} = \frac{b_{oo}}{2}\left[\frac{1-\frac{\bar{x}}{\lambda}}{\sqrt{1-\left(\frac{\bar{x}}{\lambda}\right)^2}}\right] \tag{17}$$

Before substituting Eq. (16) and (17) into (15), the thickness form must be expressed in terms of $\bar{x}$. In the T.A.R. theory, the thickness form, $\bar{y}$, is expanded into the following series.

$$\bar{y} = A_o\sqrt{\bar{x}+\lambda} \quad + \sum_n A_n (\bar{x}+\lambda)^n \tag{18}$$

Taking the derivative of Eq. (18), retaining only the singular term, and substituting into Eq. (15), the value of the corrected velocity becomes

$$\lim_{\bar{x}\to-\lambda} V_{corrected} = \lim_{\bar{x}\to-\lambda}\left[\frac{A\ln\left|\frac{\bar{x}/\lambda-1}{\bar{x}/\lambda+1}\right|}{\frac{A_o}{2}\left(\bar{x}+\lambda\right)^{-1/2}} + \frac{\frac{b_{oo}}{2}\left[\frac{1-\bar{x}/\lambda}{\left(1-\left(\bar{x}/\lambda\right)^2\right)^{1/2}}\right]}{\frac{A_o}{2}\left(\bar{x}+\lambda\right)^{-1/2}}\right] \tag{19}$$

The limit of the first term in Eq. (19), representing the thickness contribution, is zero, whereas the limit of the second term becomes

$$\lim_{\bar{x}\to-\lambda} V_{corrected} = \frac{2b_{oo}}{A_o}\sqrt{2\lambda}$$

where A_o is related to the shroud leading edge radius.

6.2.5c (Continued)

Application of the Riegels correction thus causes the singularity due to thickness to become zero and the singularity due to camber to approach a finite limit. The results of applying this factor to a typical case are shown in Fig. 9 and 10. The dotted line represents the uncorrected linearized theory, the solid line represents the corrected theory, and the symbols represent the test data. The agreement with test in the leading edge region greatly improved, not only for the case shown, but for all cases investigated (See for example Fig. 4 thru 7). This factor has been incorporated in the program, and all pressure distributions are corrected by its application.

In summary, the shortcomings of the shroud and centerbody representation discussed were:

a) The use of a shroud reference cylinder for the distribution of vorticity and sources and sinks.

b) The use of the reference cylinder instead of the shroud surface for computation of velocity.

c) The singularity in pressure coefficient at the leading edge inherent in thin airfoil theory.

The effect of incorporating item (a) appears to be small and is not warranted because of its added mathematical complexity. Item (b) was seen to be significant for thicker shrouds such as the 1.5% thick shroud of this test program, and it is recommended that any further activities include this modification. The singularity of item (c) represented a serious limitation on the usefulness of the pressure distributions, but, as was shown, the Riegels correction eliminated the singularity and greatly improved the agreement between test and theory.

6.2.5d Representation of Propeller and Wake

Having discussed the limitations of the shroud and centerbody representation, discussion of the propeller and its wake remains. In defining the flow field of the propeller, be it actuator disk or finite bladed, it is necessary to specify the pitch of the helical sheets which represent the propeller wake.

The geometric pitch of the propeller, defined as the axial distance a blade element travels in one revolution, is given as

$$P_g/R = 2\pi V_o/R_p\Omega$$

and is invariant with radius.

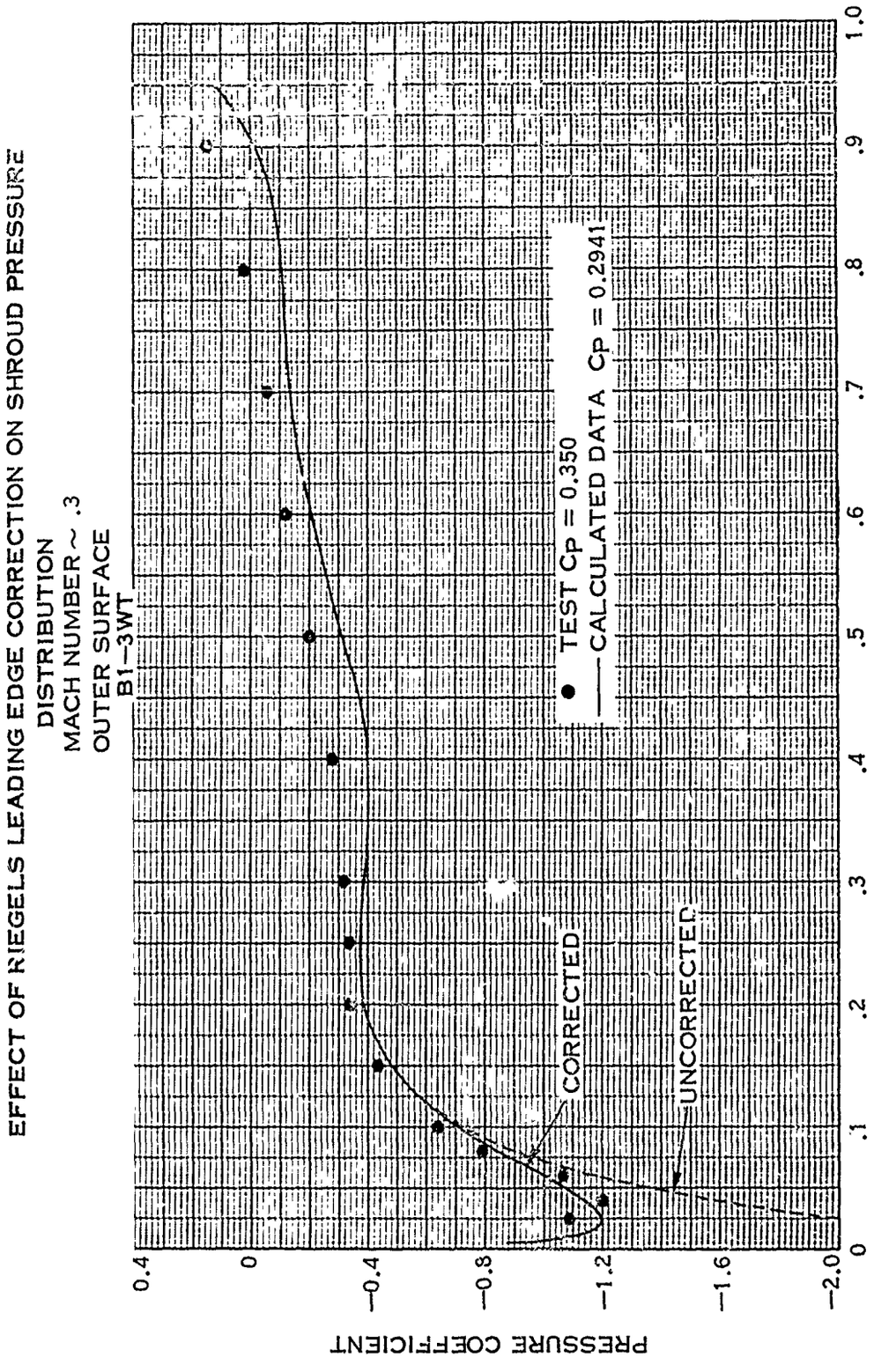
EFFECT OF RIEGELS LEADING EDGE CORRECTION ON SHROUD PRESSURE DISTRIBUTION
MACH NUMBER ~ .3
OUTER SURFACE
B1-3WT
TEST Cp = 0.350
CALCULATED DATA Cp = 0.2941
CORRECTED
UNCORRECTED
PRESSURE COEFFICIENT
0.4
0
-0.4
-0.8
-1.2
-1.6
-2.0
0
.1
.2
.3
.4
.5
.6
.7
.8
.9
1.0
PERCENTAGE OF CHORD, X/C

FIGURE 9.

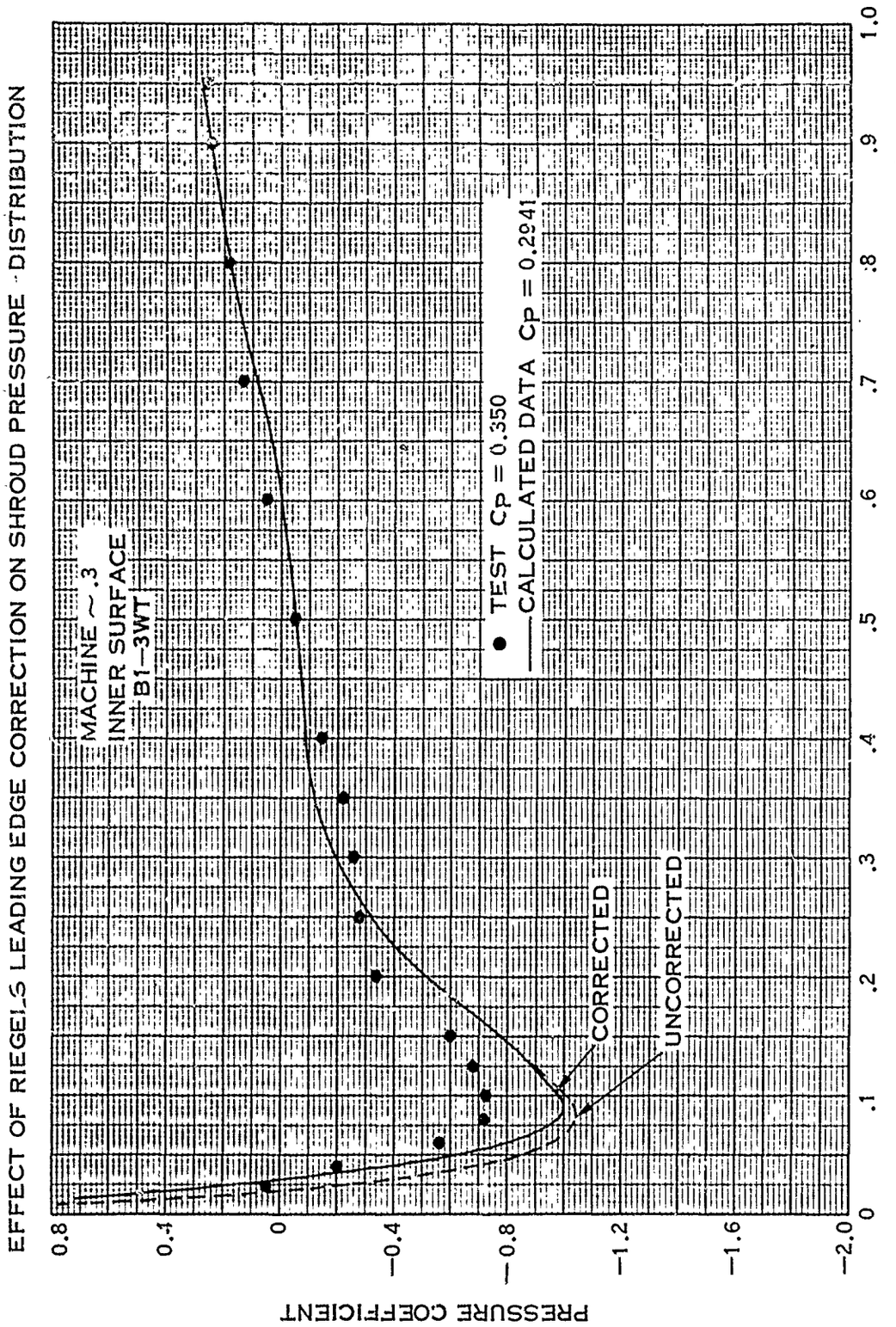
EFFECT OF RIEGELS LEADING EDGE CORRECTION ON SHROUD PRESSURE - DISTRIBUTION
MACHINE ~ .3
INNER SURFACE
B1—3WT
● TEST Cp = 0.350
——CALCULATED DATA Cp = 0.2941
CORRECTED
UNCORRECTED
PRESSURE COEFFICIENT
0.8
0.4
0
—0.4
—0.8
—1.2
—1.6
—2.0
0
.1
.2
.3
.4
.5
.6
.7
.8
.9
1.0
PERCENTAGE OF CHORD, X/C

FIGURE 10.

6.2.5d (Continued)

The actual pitch of a helical filament, which, in reality is convected downstream by the local velocity, is a function of radius and is given as

$$P_t/R_p = \frac{2\pi V_a}{\Omega R_p}$$

where the tangential induced velocity is neglected relative to $R_p\Omega$ and where V_a is the axial velocity at the blade, and includes the induced velocities. For the light loading case at high forward speed, $V_a \approx V_o$, and so

$$\frac{P_t}{R_p} \approx \frac{2\pi V_o}{R_p \Omega} \approx \frac{P_e}{R_p}$$

These are the conditions under which the assumptions that the wake pitch is constant and equal to the geometric pitch are valid.

For shrouds with large thickness ratios and/or camber lines, or for low forward speed, the shroud induced velocity can be large compared to V_o, and so the assumption that $V_a \approx V_o$ is invalid. It is necessary, therefore, to replace the geometric pitch by the actual pitch in describing the propeller wake. This is an integral part of the Hamilton Standard method for calculating the propeller wake induced velocity and so needs to be accounted for only in the expression for the radial velocity at the shroud reference cylinder due to the propeller wake. This velocity is given in Ref. 1 in terms of J_o', the geometric advance ratio, as

$$\frac{V_r}{V_o} = \frac{1}{2}\,\frac{B}{2\pi^2}\int_0^{\mu} \frac{\bar{\Gamma}'(\bar{r}_v)}{J_o'}\, Q_{1/2}(\tilde{\omega}_3)\,\bar{r}_v^{1/2}\, d\bar{r}_v \qquad (20)$$

where J_o', the geometric advance ratio is defined as the tangent of the geometric pitch angle and is given by

$$J_o' \quad \frac{V_o}{R_p \Omega}$$

6.2.5d (Continued)

In the spirit of the discussion above, the definition of advance ratio should be based on the local pitch, i.e.,

$$J'_2 = \frac{V_a}{\bar{r}_v \Omega} = J'_2 (\bar{r}_v)$$

To evaluate V_a, it is necessary to know the shroud and propeller induced velocities. Since Hamilton Standard has altered the T.A.R. method to accept propeller geometry by iteration on V_a, it is straighforward to include the evaluation of J'_2 at the end of each iteration. As noted, the effect of wake pitch is accounted for in the propeller induced velocities through the use of the Hamilton Standard propeller theory.

A preliminary investigation into the use of J'_2 as a function of radius in Eq. (20) (i.e., a distorted helical wake), indicated that a major change in the integration method was required. Instead, J'_2 was defined in terms of the average axial induced velocity over the disk and was thus not a function of radius. Use of J'_2 so defined, instead of J'_0, in Eq. (20) then becomes a matter of straight-forward substitution. In this manner, a better representation of the wake was obtained with little added cost in complexity and computer time. The good agreement between test and theory exhibited in paragraph 7.4 further justifies this approach.

The propeller thrust and power coefficients as functions of blade angle calculated by use of J'_0 and J'_2 are compared in Fig. 11 for the B1-3WT and the B4-3WT shrouds. A Mach number of about 0.3 has been used for the comparison. The effects on performance are seen to be negligible for both area ratios, although the use of J'_2 tends to give slightly higher values of C_P and $C_{T\ prop}$. The comparison of these calculations with experiment is shown in Fig. 12. Due to the small differences between the two methods, both have been plotted on a single line. The predicted variation of propeller thrust coefficient with power coefficient is seen to agree very well with the data. The blade angle agreement, on the other hand, is not as good. For a given power coefficient the predicted blade angles are higher than the experimental values. As is shown in the following section, this agreement is improved by use of a correction to the propeller wake representation which accounts for the proximity of the shroud.

The shroud pressure distributions resulting from the use of J'_0 and J'_2 are tabulated in Fig. 13 for the B1-3WT only, since the conclusions for the B4-3WT are the same. Again the effect of the advance ratio definition on pressure distribution is quite small. The test values are also shown in Fig. 13, and as can be seen the comparison between test and theory is very good, except for the leading edge region. The disagreement in the leading edge region is typical and has been discussed previously. At the lower Mach numbers, a more pronounced effect is noted and will be discussed in paragraph 7.4.2.

EFFECT ON THEORETICAL PERFORMANCE OF USING J'_0 OR J'_2 IN EQUATION (20)

B1–3WT
M = .3053
J = 1.5087

$\theta^{\circ}_{3/4}$	J'_0		J'_2	
	C_T PROP	C_P	C_T PROP	C_P
30	.0310	.0582	.0312	.0584
34	.0919	.1581	.0922	.1584
38	.1485	.2679	.1491	.2687
42	.2019	.3884	.2028	.3896

B4–3WT
M = .310
J = 1.511

$\theta^{\circ}_{3/4}$	J'_0		J'_2	
	C_T PROP	C_P	C_T PROP	C_P
38	.0724	.1521	.0726	.1526
42	.1363	.2936	.1369	.2948
46	.1956	.4452	.1968	.4472
50	.2483	.6059	.2498	.6083

FIGURE 11.

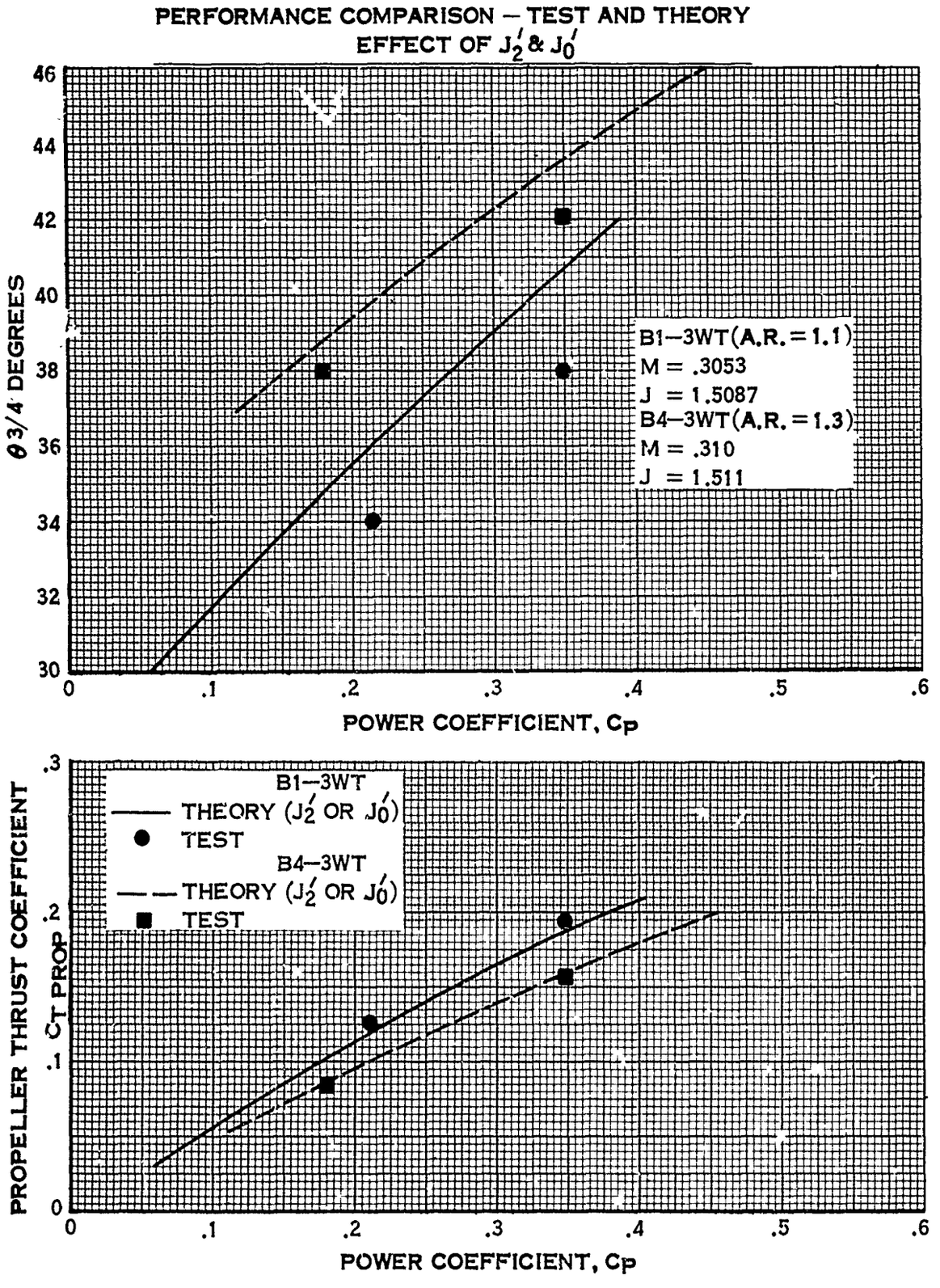
PERFORMANCE COMPARISON — TEST AND THEORY
EFFECT OF J_2' & J_0'
θ3/4 DEGREES
46
44
42
40
38
36
34
32
30
0
.1
.2
.3
.4
.5
.6
POWER COEFFICIENT, Cp
B1—3WT(A.R.=1.1)
M = .3053
J = 1.5087
B4—3WT(A.R.=1.3)
M = .310
J = 1.511
PROPELLER THRUST COEFFICIENT
CT PROP
.3
.2
.1
0
B1—3WT
THEORY (J_2' OR J_0')
TEST
B4—3WT
THEORY (J_2' OR J_0')
TEST
POWER COEFFICIENT, Cp

FIGURE 12.

EFFECT OF J_0' & J_2' ON SHROUD PRESSURE DISTRIBUTION

B1–3WT
M = .3053
J = 1.5087
$\theta_{3/4} = 38°$

	THEORY				TEST	
	J_0'		J_2'			
X/C	INNER	OUTER	INNER	OUTER	INNER	OUTER
.0125	.7137	−1.0985	.7330	−1.1409	.150	−1.1
.025	.1228	−1.1748	.1524	−1.2092	−.20	−1.2
.05	−.6535	−1.0585	−.6194	−1.0835	−.57	−1.08
.075	−.9587	−.8708	−.9263	−.8902	−.72	−0.8
.10	−.9985	−.6999	−.9690	−.7155	−.74	−0.76
.15	−.7827	−.4753	−.7597	−.4867	−.60	−0.42
.20	−.5170	−.3824	−.4991	−.3917	−.35	−0.35
.25	−.3189	−.3669	−.3048	−.3746	−.29	−0.37
.3	−.1953	−.3830	−.1842	−.3897	−.25	−0.31
.4	−.0906	−.3913	−.0840	−.3958	−.15	−0.28
.5	−.0541	−.3112	−.0515	−.3142	−.05	−0.20
.6	−.0067	−.2080	−.007	−.2097	.05	−0.12
.7	.0856	−.1396	.0836	−.1409	.12	−0.05
.8	.1839	−.1119	.1811	−.1134	.19	0.02
.9	.2460	−.0152	.2432	−.0169	.25	0.15
.95	.2809	.1254	.2781	.1237	.28	0.12

FIGURE 13.

6.2.5d (Continued)

In calculating the propeller wake induced portion of the velocity diagram, the Goldstein representation of the wake is used. This representation assumes that the wake is isolated and therefore does not account for the presence of the shroud. Ref. 8 by Goodman presents a correction to the flow field of the propeller wake in the presence of a wall. The flow about the edge of the true helical wake is approximated by an array of semi-infinite flat plates whose spacing is equal to the pitch of the helix, while the wall, which extends from plus infinity to minus infinity, is placed a distance d away, as shown in Fig. 14. The derivation of the correction and its application to the Goldstein representation of the propeller wake are discussed in detail in Appendix 11.2.

The correction is derived for the case of a wall extending to infinity. In the shrouded propeller case, the wall, which represents the inside surface of the shroud, does not extend to infinity and is adjacent to the wake for only a finite distance downstream. However, in computing the velocity field of the propeller wake, the elements of wake vorticity in the immediate vicinity of the propeller have the largest contribution. It is this portion of the wake then that should be represented as accurately as possible, prompting the use of the Goodman correction. The error introduced by assuming the shroud extends to infinity should be small except for those cases in which the propeller is located near the shroud trailing edge. For the geometries involved in this program, this was not the case and the correction should be valid.

The effect of this correction on the analytically predicted performance and shroud pressure distribution for B1-3WT and B4-3WT are shown in Fig. 15 through 17 for the .3 Mach number case. The tabulation of Fig. 15 shows that for a given blade angle the power and thrust coefficients are increased by application of the correction. The predicted and experimental results are compared in Fig. 16. The propeller C_T versus C_P plot shows excellent agreement between test and theory and a negligible effect of the Goodman correction on the theoretical predictions. A significant change results in the blade angle versus C_P plot. The application of the Goodman tip correction greatly improves the correlation between test and theory. Fig. 17 indicates that the tip correction has a small effect on the shroud pressure distribution and that agreement between test and theory is fair.

The improved agreement brought about by application of the Goodman tip correction can be understood by inspecting Fig. A-5 of Appendix 11.2. The factor F is directly proportional to the blade loading or circulation, whereas f is proportional to $(1-\frac{r_v}{R_p})$. As $r_v \rightarrow R_p$, $f \rightarrow 0$, so at the tip, $\Gamma = 0$ and the circulation is zero. The

MODEL FOR TIP CORRECTION

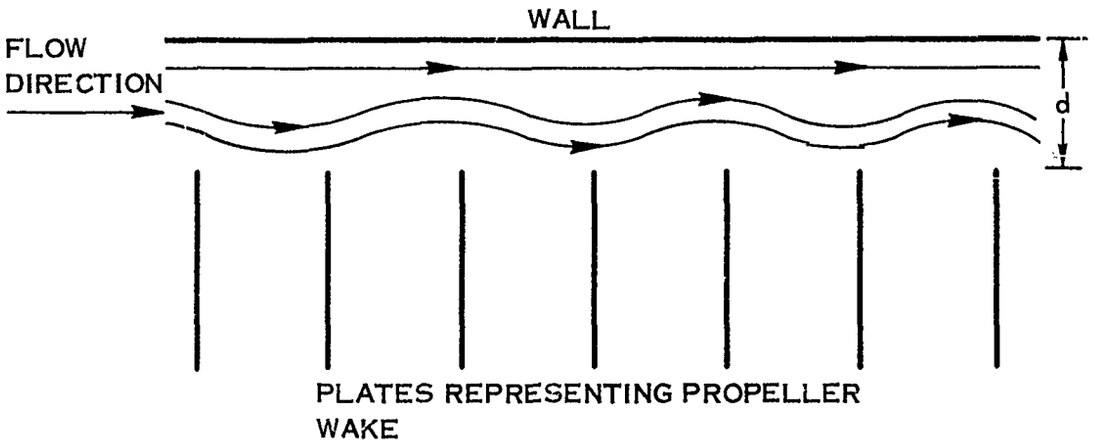

FIGURE 14.

EFFECT OF GOODMAN TIP CORRECTION ON THEORETICAL PERFORMANCE

(J_2' USED IN EQUATION 20).

B1–3WT
M = .3053
J = 1.5087

$\theta^\circ_{3/4}$	NO GOODMAN		WITH GOODMAN	
	C_T PROP	C_P	C_T PROP	C_P
30	.0312	.0584	.0330	.0608
34	.0922	.1584	.1012	.1718
38	.1491	.2687	.1654	.2940
42	.2028	.3896	.2250	.4291

B4–3WT
M = .31
J = 1.511

$\vartheta^\circ_{3/4}$	NO GOODMAN		WITH GOODMAN	
	C_T PROP	C_P	C_T PROP	C_P
38	.0726	.1526	.0809	.1674
42	.1369	.2948	.1542	.3270
46	.1968	.4472	.2229	.4999
50	.2498	.6083	.2814	.6824

FIGURE 15.

EFFECT OF GOODMAN TIP CORRECTION —
PERFORMANCE COMPARISON OF TEST & THEORY
J_2' USED IN EQUATION (20)

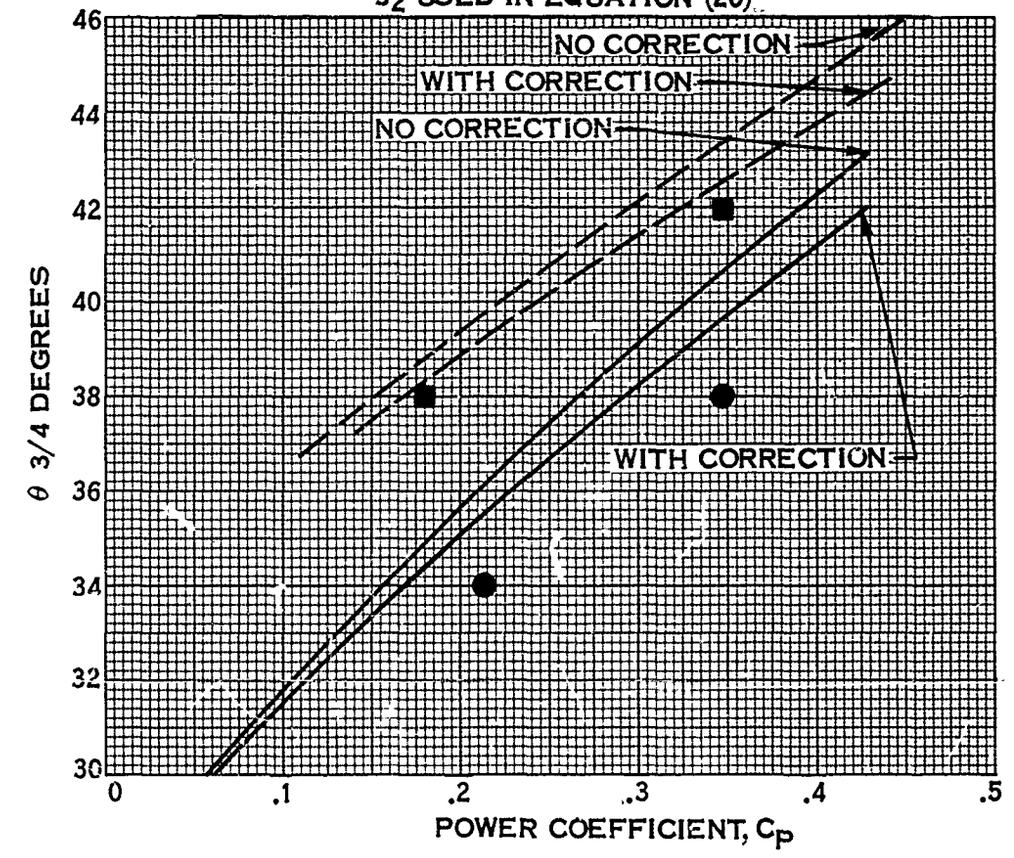

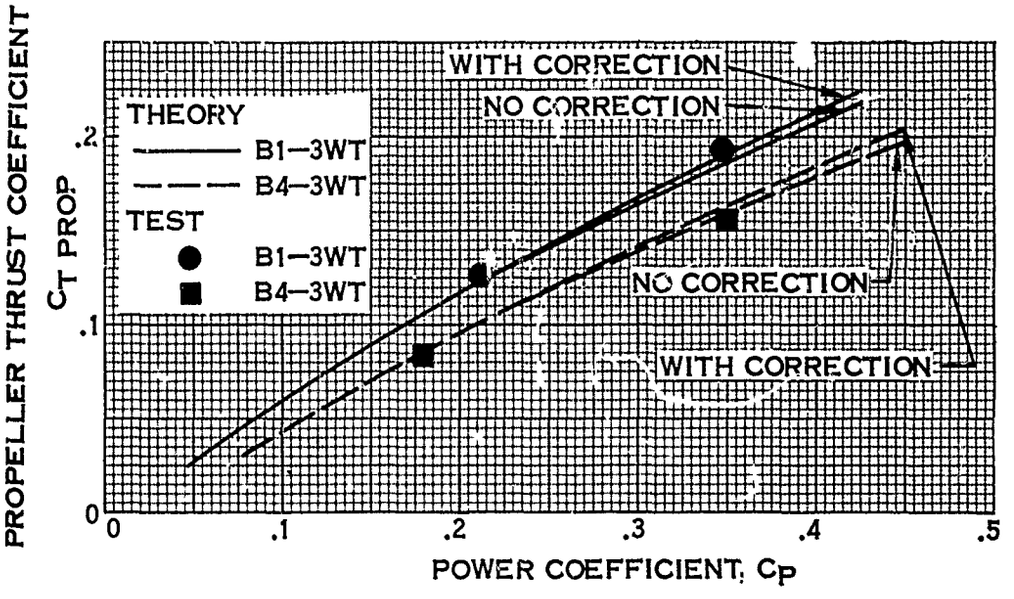

FIGURE 16.

EFFECT OF GOODMAN TIP CORRECTION ON SHROUD PRESSURE DISTRIBUTION

B1—3WT
M = .3053
J = 1.5087
$\theta 3/4 = 38°$
($J_{\frac{1}{2}}$ USED IN EQUATION 20).

	THEORY				TEST	
	NO TIP CORRECTION		WITH TIP CORRECTION			
X/C	INNER	OUTER	INNER	OUTER	INNER	OUTER
.0125	.7330	−1.1409	.7107	−1.0962	.150	−1.1
025	.1524	−1.2092	.1176	−1.1739	−.20	−1.2
.05	−.6194	−1.0835	−.6605	−1.0589	−.57	−1.08
.075	−.9263	−.8902	−.9664	−.8717	−.72	−.80
.1	−.9690	−.7155	−1.0064	−.7012	−.74	−.76
.15	−.7597	−.4867	−.7905	−.4769	−.6	−.42
.2	−.4991	−.3917	−.5244	−.3844	−.35	−.35
.25	−.3048	−.3746	−.3260	−.3694	−.29	−.37
.3	−.1842	−.3897	−.2018	−.3859	−.25	−.31
.4	−.0840	−.3958	−.0930	−.3920	−.15	−.28
.5	−.0515	−.3142	−.0507	−.3076	−.05	−.20
.6	−.007	−.2097	−.0028	−.2051	.05	−.12
.7	.0836	−.1409	.0888	−.1373	.12	−.05
.8	.1811	−.1134	.1860	−.1098	.19	.02
.9	.2432	−.0169	.2476	−.0133	.25	.15
.95	.2781	.1237	.2825	.1269	.28	.12

FIGURE 17.

6.2.5d (Continued)

parameter g on the curve is proportional to the spacing between the tip of the propeller and the shroud. As the spacing decreases from infinity towards some finite value, the load the propeller carries at any given station increases as indicated by the larger value of F. This increase in loading results in an increase in both power absorption and propeller thrust for a given blade angle. The increase in thrust and power is such that the excellent agreement of the C_T versus C_P comparisons is maintained. The poor agreement between blade angle and C_P is however improved. The Goodman tip correction therefore manifests itself as an increase in loading near the propeller tip due to the presence of the shroud. Its validity is substantiated by the improved comparison of test and theory.

In this section, two modifications to the representation of the propeller and its wake have been discussed. The first was the inclusion of J'_2 instead of J'_0 in Eq. (20). Comparisons with test data indicated small changes in performance and shroud pressure distribution for the 0.3 Mach number case and good agreement between test and theory. The second modification accounted for the presence of the shroud in the flow field of the propeller wake through the use of the Goodman tip correction. This correction did not alter the $C_{T\ prop}$ versus C_P and shroud pressure distribution agreement with test data, which was good, but did bring the blade angle-C_P relationship into much better agreement.

6.2.5e Discussion of Shroud Boundary Conditions

The satisfaction of the no-flow boundary condition on the shroud, due to the linearization procedures, reduces to the independent satisfaction of two boundary conditions; one for the shroud camber line and one for the shroud thickness. The former led to the equation for the shroud vorticity distribution (Eq. 4) discussed in paragraph 6.1.2. This equation was derived from Eq. (1), the linearized boundary condition on the shroud camber line. In the following, a more exact version of Eq. (1) will be derived, based on the exact boundary condition equations and the assumption that the singularities be distributed along the shroud camber line.

The no-flow boundary condition is shown schematically in Fig. 18, and results in the following equations:

$$\tan \epsilon_u(X) = \frac{V_{ru}}{V_o + U_u} \tag{21a}$$

$$\tan \epsilon_L(X) = \frac{V_{rL}}{V_o + U_L} \tag{21b}$$

SCHEMATIC REPRESENTATION OF SHROUD BOUNDARY CONDITION

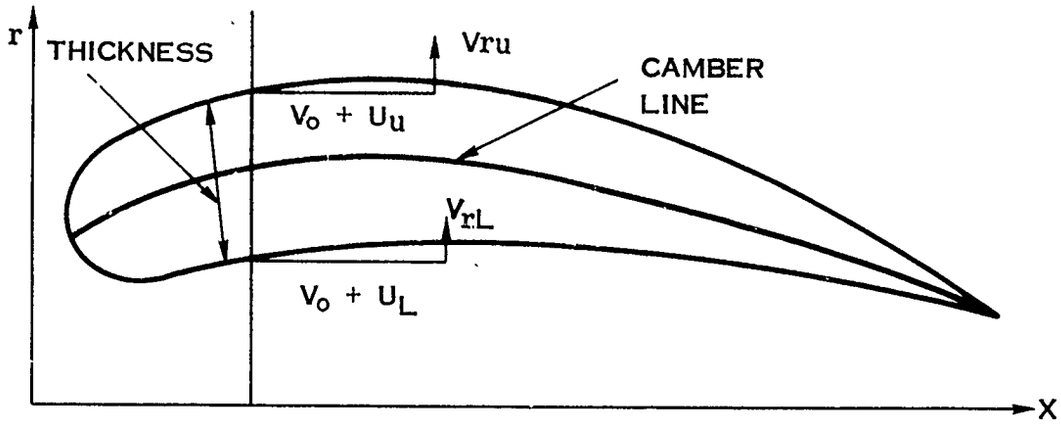

ϵ = SLOPE OF THE CAMBER LINE

$$\tan \epsilon_u = \frac{V_{ru}}{V_o + U_u}$$

$$\tan \epsilon_L = \frac{V_{rL}}{V_o + U_L}$$

FIGURE 18.

6.2.5e (Continued)

These equations can be simplified by approximating the values of the perturbation velocities at the upper and lower surfaces by calculation on the shroud camber line. The radial and axial velocity above and below the shroud can then be divided into a continuous and discontinuous part. The continuous part is due to singularities in the flow field remote from the field point in question whereas the discontinuous is due to singularities at the field point. For the particular case of a field point on the shroud camber line, the discontinuous part is due to the shroud vorticity and source-sink distributions. These discontinuous velocities are shown schematically in Fig. 19. The velocity discontinuities are proportional to the local source sink and vorticity strengths and manifest themselves as equal but opposite contributions above and below the camber line. Utilizing the notation of Fig. 19, the boundary conditions (Eq. [21a]and [21b]) become, in terms of the axial and radial components of the continuous and discontinuous velocities

$$\tan \epsilon_u = \frac{V_{rc} + V_{rD}}{V_o + U_c - U_D} \tag{22a}$$

$$\tan \epsilon_L = \frac{V_{rc} - V_{rD}}{V_o + U_c - U_D} \tag{22b}$$

Before proceeding, it is necessary to define the left hand side of these equations in terms of the camber distribution and thickness form. The assumption that the shroud is thin and slightly cambered implies that ϵ_u and ϵ_L are small, so that $\tan \epsilon_u \cong \epsilon_u$, $\tan \epsilon_L \simeq \epsilon_L$. This approximation is valid for values of ϵ approaching .5. For example at $\epsilon = .5$, $\tan \epsilon = .55$ so the error in the assumption is of the order of 10%. Replacing $\tan \epsilon_u$ by ϵ_u and $\tan \epsilon_L$ by ϵ_L, the slopes of the upper and lower surfaces are defined by the slope of the mean camber line and the slope of the thickness form. If ϵ is the slope of the mean camber line and t' the slope of the thickness form, then for thin slightly cambered sections,

$$\epsilon_u = \epsilon + t'$$

$$\epsilon_L = \epsilon - t'$$

and Eq. (22a) and (22b) become

DISCONTINUOUS VELOCITIES ALONG SHROUD CAMBER LINE

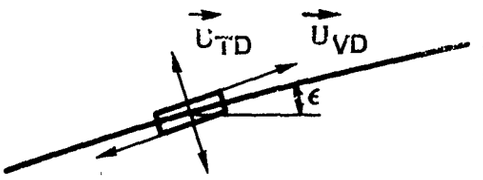

$\vec{U}_{TD}$ = DISCONTINUOUS VELOCITY DUE TO SOURCE–SINK DISTRIBUTION

$\vec{U}_{VD}$ = DISCONTINUOUS VELOCITY DUE TO VORTICITY DISTRIBUTION

DISCONTINUOUS VELOCITIES

$$\vec{U}_D = \vec{U}_{TD} + \vec{U}_{VD}$$

$$\vec{U}_D = U_D \vec{t} + V_{rD} \vec{1}_r$$

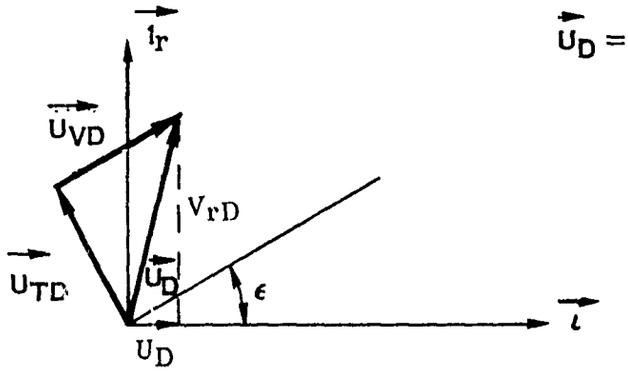

RESOLUTION OF DISCONTINUOUS VELOCITY INTO AXIAL & RADIAL COMPONENTS – (UPPER SURFACE)

FIGURE 19.

6.2.5e (Continued)

$$\epsilon + t' = \frac{V_{rc} + V_{rD}}{V_o + U_c + U_D} \tag{23a}$$

$$\epsilon - t' = \frac{V_{rc} - V_{rD}}{V_o + U_c - U_D} \tag{23b}$$

The small camber and thickness assumption indicates that the shroud camber line never deviates significantly from the shroud reference cylinder. This affords a further simplification in that the velocity components can be evaluated on the shroud reference cylinder instead of the shroud camber line and the singularities distributed on the shroud reference cylinder.

Dividing top and bottom of Eq. (23) by V_o and adding, there results

$$2\epsilon = \frac{V_{rc}}{V_o}\left[\frac{1}{1+\frac{U_c}{V_o}+\frac{U_D}{V_o}} + \frac{1}{1+\frac{U_c}{V_o}-\frac{U_D}{V_o}}\right] + \frac{V_{rD}}{V_o}\left[\frac{1}{1+\frac{U_c}{V_o}+\frac{U_D}{V_o}} - \frac{1}{1+\frac{U_c}{V_o}-\frac{U_D}{V_o}}\right]$$

Defining barred quantities to be non-dimensional velocities, this equation becomes, after algebraic manipulation,

$$2\epsilon = \frac{2\,\bar{V}_{rc}\,(1+\bar{U}_c) - 2\,\bar{U}_D\,\bar{V}_{rD}}{(1+\bar{U}_c)^2 - \bar{U}_D^2}$$

Now the last term in the numerator is of second order compared to the first order term $\bar{V}_{rc}\,(1+\bar{U}_c)$ and is neglected. The $\bar{U}_D^2$ term in the denominator is also second order compared to the $(1+\bar{U}_c)^2$ term, and it also can be neglected. Note that the term $\bar{U}_c$ was not neglected when compared to 1, so the equation becomes

$$\epsilon = \frac{\bar{V}_{rc}}{1+\bar{U}_c} \tag{24}$$

Eq. (24) is in much simpler form than Eq. (22) and depends only on the continuous part of the velocity, $\bar{U}_c$. As will be discussed, this form permits a more rigorous satisfaction of the boundary condition within the existing framework of the analysis.

6.2.5e (Continued)

To reduce Eq. (24) to the boundary condition of Eq. (1), it is further necessary to assume that $\bar{U}_c << 1$. Thus the boundary condition Eq. (24) requires less restrictive assumptions for its derivation.

To indicate the order of magnitude of the velocity $\bar{U}_c$, the continuous part of the axial velocity, which is used in the calculation of the shroud pressure distribution, was plotted as a function of shroud chordwise position in Fig. 20 for the B1 - 3 WT shroud at a Mach number .3. The assumption that $\bar{U}_c$ is much less than unity is seen to be violated, indicating the need for the more accurate boundary condition of Eq. (24). This assumption is violated further as the free stream velocity approaches zero. To improve the accuracy of the theory in the forward flight regime and to extend its validity to lower forward flight velocities, the use of Eq. (24) in place of Eq. (1) was investigated.

Solution for the shroud vorticity distribution must now be based on Eq. (24) instead of Eq. (1). The appearance of the term $\bar{U}_c$ in Eq. (24) greatly complicates its solution. However, by an additional iteration procedure, it is possible to satisfy Eq. (24) and still to use the method of solution described in paragraph 6.1.2 for Eq. (1). Thus incorporation of Eq. (24) requires only small changes in the computer program. For the first iteration, U_c is assumed zero. The solution then proceeds in the normal fashion and results in a first estimate of the axial velocity $\bar{U}_c^{(1)}$. The next step is to define a new shroud camber by multiplying the true camber distribution by $(1 + \bar{U}_c^{(1)})$. The camber distribution for the second iteration is thus $\epsilon_{(2)} = \epsilon(1 + U_c^{(1)})$, and Eq. (24) takes the form

$$\epsilon_{(2)} = \bar{V}_{rc} = \epsilon (1 + \bar{U}_c^{(1)}) \qquad (25)$$

Eq. (25) has the same form as Eq. (1), and is solved by the existing method in terms of $\epsilon_{(2)}$ instead of the geometric camber ϵ . This process is repeated until $\left|\bar{U}_c^{(n)} - \bar{U}_c^{(n+1)}\right| \leq \delta$, where δ is some desired tolerance. Note, in general, that $\epsilon_n = \epsilon(1 + \bar{U}_c^{(n-1)})$, that is, the geometric camber is corrected by the latest value of U_c to obtain the effective camber for the subsequent iteration.

Application of this correction to the .3 and .6 Mach number cases was investigated. The low Mach number case will be discussed in paragraph 7.1.2 although qualitatively the conclusions are similar to the .3 case discussed in the following.

Utilizing Fig. 20, the effective camber $\epsilon_{(2)}$ for the second iteration was computed. Plots of $\epsilon_{(2)}$ and ϵ the geometric camber are shown in Fig. 21. The value of $\epsilon_{(2)}$ at X/C = 0 was obtained by extrapolation from the 0.025 station because the continuous contribution from the shroud source-sink distribution exhibits a singularity at the leading edge which would lead to an unrealistic correction.

AVERAGE AXIAL INDUCED VELOCITY AT SHROUD REFERENCE CYLINDER
VS CHORDWISE LOCATION

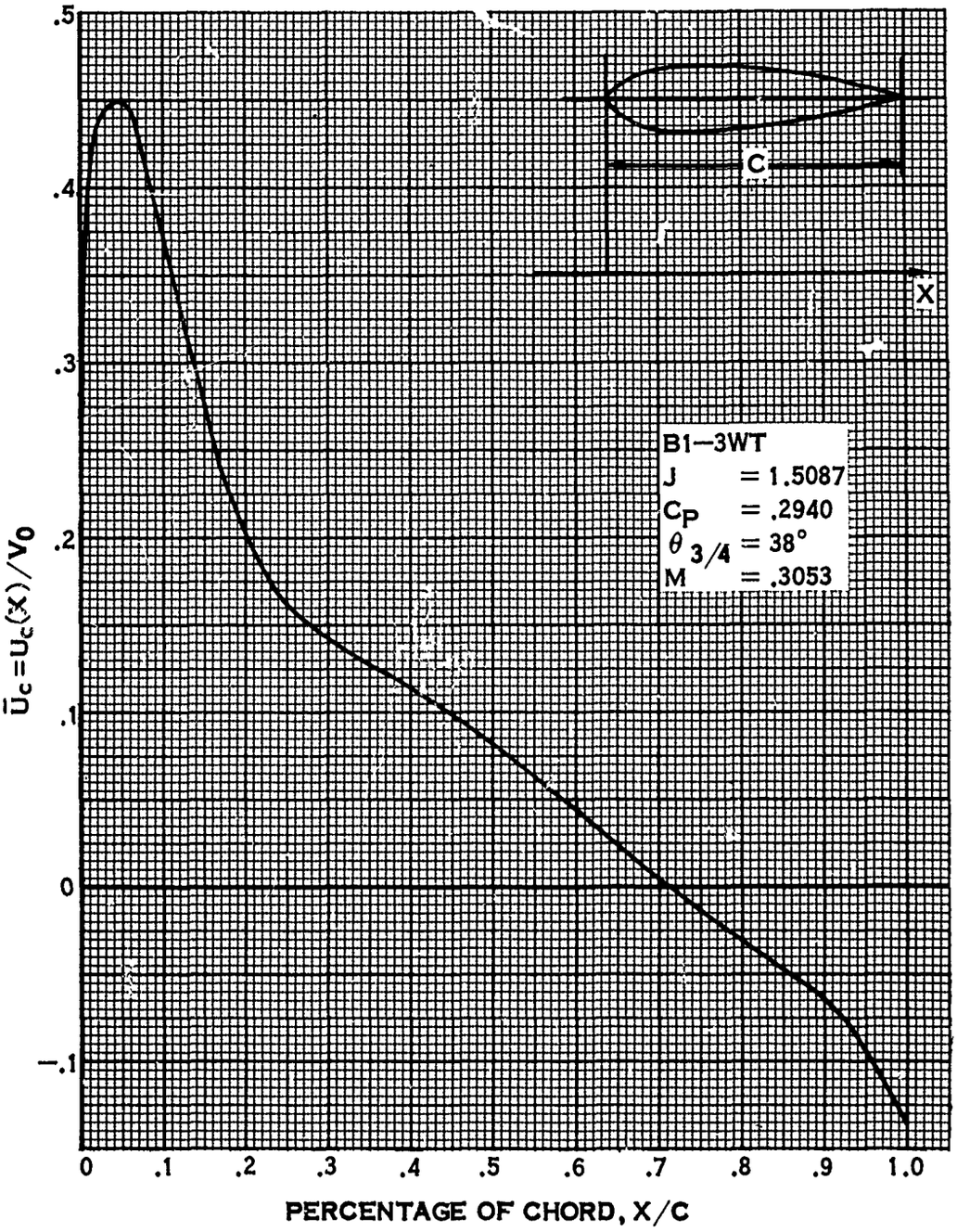

FIGURE 20.

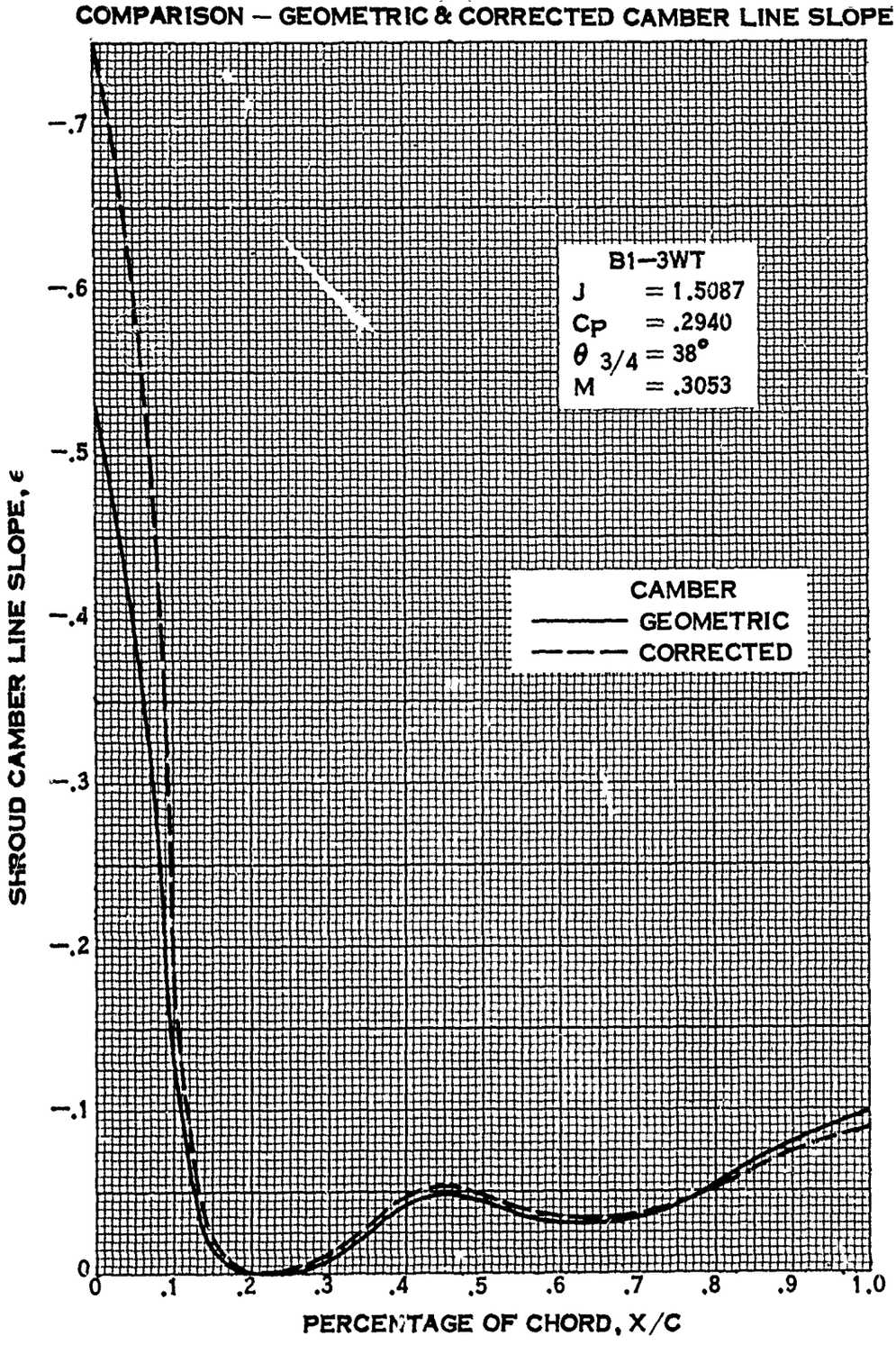
COMPARISON — GEOMETRIC & CORRECTED CAMBER LINE SLOPE
B1—3WT
J = 1.5087
Cp = .2940
θ 3/4 = 38°
M = .3053
CAMBER
GEOMETRIC
CORRECTED
SHROUD CAMBER LINE SLOPE, ε
−.7
−.6
−.5
−.4
−.3
−.2
−.1
0
0
.1
.2
.3
.4
.5
.6
.7
.8
.9
1.0
PERCENTAGE OF CHORD, X/C

FIGURE 21.

6.2.5e (Continued)

The effect on performance of utilizing $\epsilon_{(2)}$ instead of ϵ was found to be small. The effect on pressure distribution was also small and in a direction that hurt the agreement between test and theory. In addition, the changes in the continuous axial velocity, $\bar{U}_c(X)$ were small enough to warrant only two iterations. The pressure distributions for the first and second iterations are plotted in Fig. 22. The performance changes for the 38° blade angle are shown in the following table:

$\theta = 38$ M = .3 J = 1.5087

Iteration No.	C_P	$C_{T\ Prop}$
1	.2940	.1654
2	.2915	.1634

Similar results were noted for the .5 Mach number case. The effect of this correction on the low Mach number results was also investigated, and while the correction ($1 + \bar{U}_c$) was much larger, it had a small effect on performance and shroud pressure distribution, and is discussed further in paragraph 7.4.2. Since the effect of the correction on performance was small for the Mach number range, .05 to .5, while the computer time for its calculation nearly doubles because of the added iteration, it has not been incorporated into the program. If, in use of the program, a case arises where this correction is desired, it can be implemented by calculating the correction ($1 + \bar{U}_c$) from the printed output, applying it to the known geometric camber and inputing the resulting corrected camber for execution of the second iteration.

6.2.5f Summary of Linearization Assumptions

Removal of some of the restrictive assumptions imposed by the T.A.R. method were investigated. These investigations were divided into three items dealing with:

1. Shroud and centerbody geometry
2. Propeller geometry and its wake
3. Shroud boundary conditions

Under Item 1, the effect of changing the location of the shroud reference cylinder was found to be negligible. The effect of computing the shroud surface velocities at the shroud surface instead of the shroud reference cylinder was found to result in changes in pressure coefficient on the order of 12% but due to the major program changes required, could not be incorporated into the present method. It was recommended that future attempts at improving the theory include this effect. The leading edge singularity in pressure inherent in the linearized model was corrected by the use of the Riegels factor, and resulted in much better agreement between test and theory.

PRESSURE COEFFICIENT WITH AND WITHOUT BOUNDARY CONDITION CORRECTION

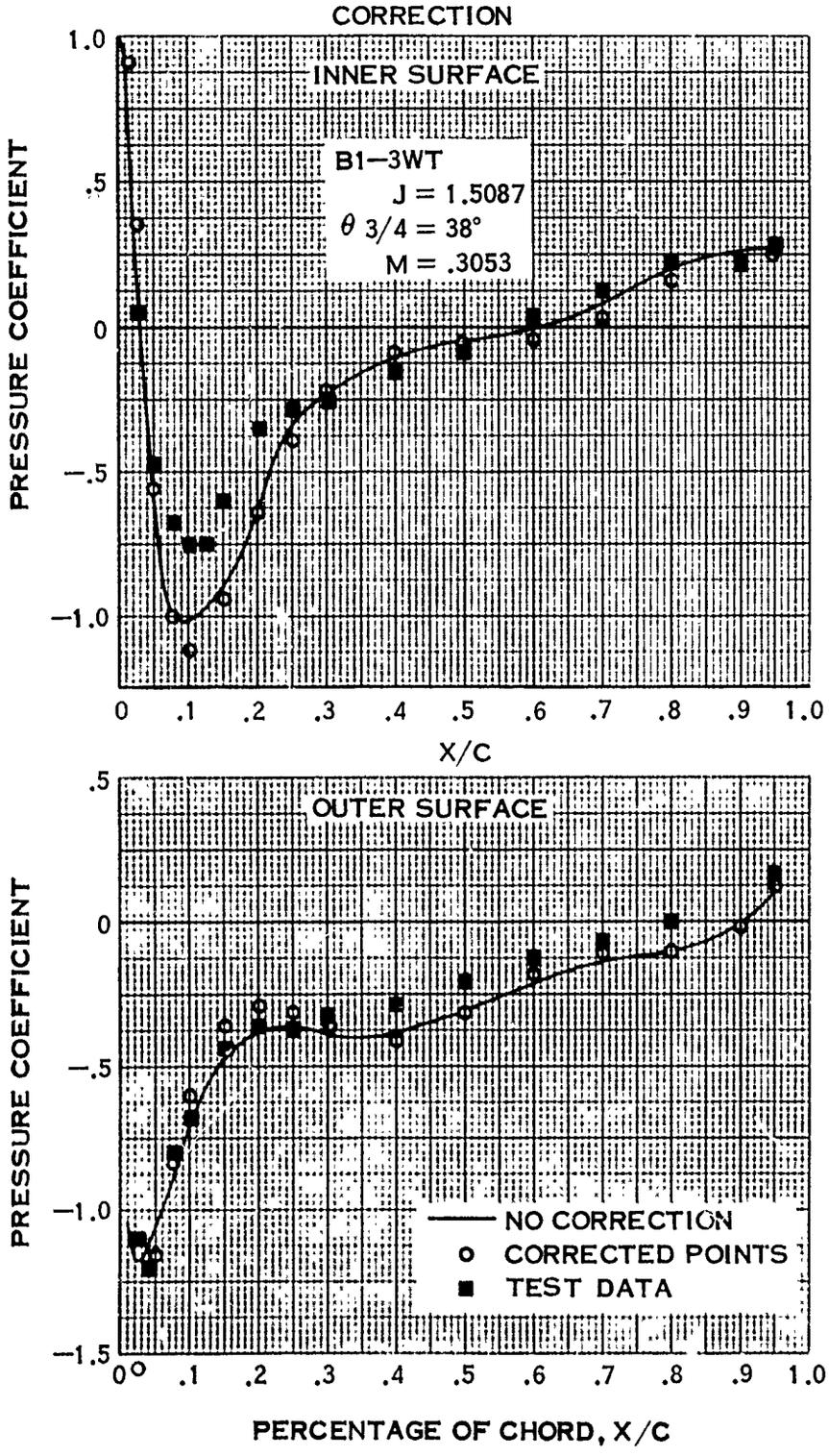

FIGURE 22.

6.2.5f (Continued)

This factor has been incorporated as an integral part of the program.

Under Item 2, two corrections were investigated and incorporated, the first being the use of J'_2 instead of J'_0, the second being the application of the Goodman tip correction to account for the effects of the shroud on the flow field of the propeller wake.

Finally, under item 3, a more accurate boundary condition was derived to permit extension of the theory to lower forward flight velocities and/or to thicker shrouds at the higher velocities. Application of this significant correction, by use of an iteration procedure, resulted in small changes in overall performance and shroud pressure distribution. Due to the increased computer time required, it was not included as an integral part of the program, although it can be utilized with the existing program by the intermediate use of a simple hand calculation.

6.2.6 Summary of Limiting Assumptions

Limitations of the T.A.R. method have been discussed, and the method presented herein utilizes the T.A.R. model and solution with the addition of the following refinements.

1. The Hamilton Standard propeller method, based on Goldstein, for the calculation of the propeller induced velocity field.

2. The iteration process which permits propeller geometry to be specified.

3. The use of an average J'_2 instead of J'_0 in Eq. (20).

4. The use of the Goodman tip correction.

5. The use of the Riegels factor for correction of the shroud pressure distribution in the leading edge region.

6. The option, requiring an intermediate hand calculation, for the inclusion of the more accurate boundary condition given by Eq. (24).

7. The effects of an arbitrary propeller centerbody.

6.3 SHROUD THRUST CALCULATION - INVISCID

6.3.1 Introduction

The preceding discussions were concerned with increasing the accuracy of the predicted velocity field of the shrouded propeller. The subject of shroud thrust has been deferred, since its prediction depends in part on an accurate knowledge of the velocity

6.3.1 (Continued)

field. Methods for computing shroud thrust will be discussed next. Two approaches leading to three methods for the calculation of shroud thrust have been investigated. The first approach, suggested by T.A.R., obtains the shroud thrust by integrating the forces on the shroud vorticity and source-sink distribution. The first method requires knowledge of the velocity field as well as the source-sink and vorticity distribution and is the method utilized in Ref. 9 for the calculation of shroud thrust. The second approach applies the momentum theorem to a control volume surrounding the shroud, and results in an expression for total thrust. Different estimates of the jet velocity in this expression result in the second and third methods for calculating total thrust. Corrections for viscous drag are discussed in paragraph 6.4.

6.3.2 Shroud Thrust - Detailed Integration Method (Method 1)

Consider Fig. 23, which shows the shroud source-sink and vorticity distributions. The thrust force on an element of vorticity is given by the classical equation for the force on a vortex element in terms of the radial velocity at the shroud reference cylinder. This radial velocity is due only to those singularities external to the shroud vorticity distribution and is, therefore, composed of contributions from the centerbody and propeller wake. The elemental axial force due to the shroud vorticity is shown in Eq. (26).

$$dF_V = \rho(V_{\bar{\Gamma}}' + V_{CB})\ 2\pi R\gamma dX_s \tag{26}$$

where the sign convention is defined in Fig. 23. $V_{\bar{\Gamma}}'$ is the radial velocity due to the propeller wake and V_{CB} that due to the centerbody. The radial velocities $V_{\bar{\Gamma}}'$ and V_{CB} have been evaluated previously for use in Eq. (4) and their sum is given in Eq. (27) in terms of the known $b_{o\nu}^{2\text{-}D}$'s discussed in paragraph 6.1.2.

$$\frac{V_{\bar{\Gamma}}'}{V_o} + \frac{V_{CB}}{V_o} = -\frac{1}{2}\left[\frac{b_{oo}^{2\text{-}D(CB)}}{2} + \frac{b_{oo}^{2\text{-}D(\bar{\Gamma}')}}{2} - \frac{1}{2}\sum_{\nu=1}\left(b_{o\nu}^{2\text{-}D(CB)} + b_{o\nu}^{2\text{-}D(\bar{\Gamma}')}\right)\cos\nu\phi_s\right] \tag{27}$$

where ϕ_s is the Glauert variable defined by

$$\frac{X_s}{R} = -\lambda\cos\phi_s$$

FORCES ON SHROUD VORTICITY AND SOURCE – SINK DISTRIBUTIONS

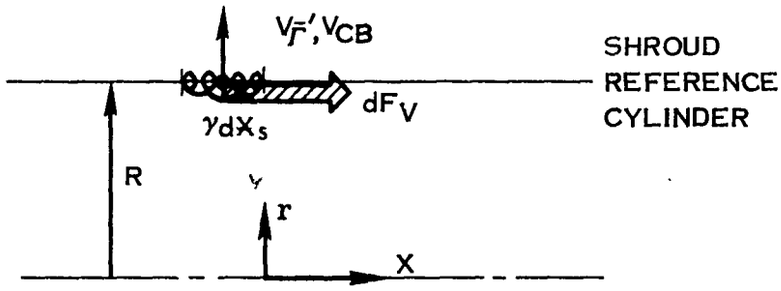

FORCE ON VORTICITY DISTRIBUTION

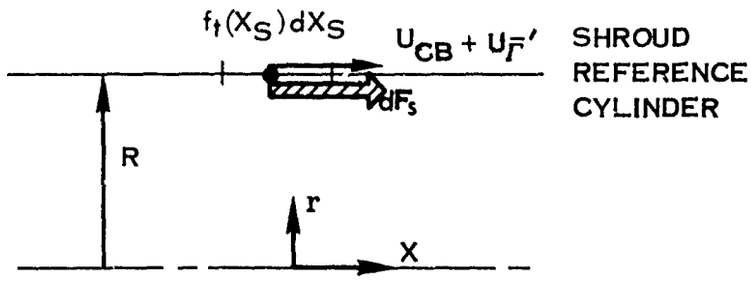

FORCE ON SOURCE–SINK DISTRIBUTION

FIGURE 23.

6.3.2 (Continued)

and the superscript in brackets indicates the contribution to $b_{o\nu}^{2\text{-D}}$ as indicated, i.e. $b_{o\nu}^{2\text{-D}}(\bar{\Gamma}')$ is the contribution to $b_{o\nu}^{2\text{-D}}$ due to the propeller wake, etc.
In addition, the shroud vorticity distribution is known from the solution of Eq. (4) and is given in terms of the known $b_{o\nu}$'s as

$$\frac{\gamma(\phi_s)}{V_o} = \frac{b_{oo}}{2}\cot\phi_s + \sum_{\nu}\frac{b_{o\nu}}{2}\sin\nu\phi_s \tag{28}$$

Substituting Eq. (27) and (28) into (26), integrating over ϕ_s and defining:

$$\beta_{o\nu} = b_{o\nu}^{2\text{-D (CB)}} + b_{o\nu}^{2\text{-D}(\bar{\Gamma}')}, \quad \nu = 0, 1, 2,$$

$$C_{T_V} = F_v/2\pi\rho R_p^2 V_o^2$$

$$\mu = R_p/R$$

there results

$$\mu^2 C_{T_V} = -\frac{\lambda}{8}\int_0^{\pi}\left[\beta_{oo} - \sum_{\gamma}\beta o\nu\cos\nu\phi_s\right]\left[b_{oo}\cot\phi_s + \sum_{\nu} b_{o\nu}\sin\nu\phi_s\right]\sin\phi_s\, d\phi_s \tag{29}$$

Performing the indicated integration and rearranging terms,

$$C_{T_V} = -\frac{\lambda\pi}{\mu^2 8}\left[\beta_{oo}b_{oo} + \frac{\beta_{oo}b_{o1}}{2} - \frac{b_{oo}\beta_{o1}}{2} + \frac{b_{o1}\beta_{o2}}{4} - \frac{1}{4}\sum_{\nu=2} b_{o\nu}(\beta_{o\nu-1} - \beta_{o\nu+1})\right] \tag{30}$$

Eq. (30) represents the shroud thrust due to shroud vorticity.

The shroud axial force due to thickness is considered next. An equation for the elemental force similar to Eq. (26) is derived starting with Eq. (6), page 471 of Ref. 10. This equation gives the force on a body in the presence of external singularities in terms of the strengths of the singularities and the velocity at the singularities due to the body. Appendix 11.3, starting with this equation derives an equivalent equation for the force on the source-sink distribution representing the body in terms of the velocities at the body due to the external singularities. This equation, illustrated in Fig. 23, has the form

$$dF_s = 2\pi\rho R^2 U(\bar{X}_s) f_t(\bar{X}_s)\, d\bar{X}_s \tag{31}$$

where $U(\bar{X}_s)$ is the axial velocity at the source element $f_t(\bar{X}_s)\, d\bar{X}_s$ due to all the singularities external to the body, i.e. the axial velocities due to the centerbody and propeller wake. $f_t(\bar{X}_s)$ is the strength of the source-sink distribution, and is related to the derivative of the thickness form. The axial velocity $U(\bar{X}_s)$ is represented by an

6.3.2 (Continued)

Nth order polynomial through the axial velocities along the shroud reference cylinder, which are available from the shroud pressure distribution calculation. The source-sink distribution is represented by the existing polynomial used in the T.A.R. method. (See Ref. 3.) Thus

$$\left(\frac{U(\bar{X}_s)}{V_o}\right)_{\substack{CB \\ \pm \Gamma'}} = \sum_{n=o}^{N} \alpha_n \bar{X}_s^{\,n} \tag{32}$$

$$F_t(\bar{X}_s) \qquad \frac{f_t(\bar{X}_s)}{V_o} = \frac{a_o}{\sqrt{\lambda + \bar{X}_s}} + \sum_{n=1} a_n \bar{X}_s^{\,n-1} \tag{33}$$

where the a_n's are known in terms of the shroud thickness form. Substituting Eq. (32) and (33) into Eq. (31) and defining:

$$C_{T_S} - F_s / 2\pi\rho R_p^{\,2} V_o^{\,2}$$

the thrust coefficient due to thickness becomes,

$$\mu^2 C_{T_S} = \int_{\lambda-}^{\lambda} \left(\frac{a_o}{\sqrt{\lambda + \bar{X}_s}} + \sum a_n \bar{X}_s^{\,n-1}\right)\left(\sum_{i=o}^{N} \alpha_i \bar{X}_s^{\,i}\right) d\bar{X}_s \tag{34}$$

Integrating Eq. (34) and rearranging terms, the expression for thrust due to thickness becomes,

$$\mu^2 C_{T_S} \qquad \sum_{n=o}^{N} \alpha_n a_o \lambda^{\,n+1/2} Z_n + \sum_{n=o}^{N} \sum_{1=1} \frac{\alpha_n a_1 \lambda^{\,n+1}}{n+1} \left(1-(-1)^{\,n+1}\right) \tag{35}$$

where

$$Z_n = \sum_{i=o}^{n} \frac{{}_nC_i\,(-1)^{\,i}\,2^{\,n-i+1/2}}{(n-i+1/2)}$$

and ${}_nC_i$ are the binomial coefficients. The total shroud thrust coefficient is given by the sum of Eq. (30) and (35).

The thrust computed in this manner depends on the product of the distribution strength and a perturbation velocity. Both of these quantities, because of the linearized theory,

6.3.2 (Continued)

are considered accurate only to first order. Multiplying these two first order quantities results in a small second order quantity. The accuracy of the thrust coefficients, which is based on such second order quantities, is, therefore questionable, unless the propeller loading is light, and shroud camber and thickness are small. This is verified in a later section where comparisons with test data are made. Due to this accuracy question an alternate approach to the shroud thrust problem based on momentum concepts was pursued.

6.3.3 Shroud Thrust Based on Momentum Theorem Using Propeller Circulation (Method 2).

Ref. 11, chapter I presents an expression for the forces on a control volume enclosing an arbitrary body. For the steady, axisymmetric case, this expression reduces to the integration of velocity and pressure over the surfaces of the volume. By choosing a volume as shown in Fig. 24, with all its surfaces far removed from the shroud, the surface integration requires a knowledge of the flow field at great distances from the shroud. In Fig. 24, the control surface is located at distances far enough away from the shroud to insure that the velocity everywhere but in the wake approaches V_o and the pressure everywhere on the surface including the wake approaches p_∞ . The radius of the wake and the velocity profile in the wake at the control surface are unknown. Since the theory is linearized and all perturbation velocities are assumed small compared to V_o, it follows that the propeller wake distortion from the shroud to downstream infinity should also be small. Consistent with this observation is the assumption that the circulation distribution in the far wake be a scaled version of the propeller circulation distribution. The scaling is included to allow for the small amount of wake contraction or expansion caused by the shroud. Having specified the circulation distribution in the wake, the wake velocity field can be obtained, and application of continuity between the propeller disk and far wake then permits the wake radius to be defined. In this manner, the complete velocity and pressure field over the surface of the control volume has been specified, and the system thrust (shroud plus propeller) can be obtained by application of the momentum theorem to the control surface. The details of the derivation are contained in Appendix 11.4, but the final equation allowing for the presence of a centerbody, is given below,

$$C'_{T_{tot}} = \frac{T_{tot}}{\frac{1}{2}\rho V_o^2 \pi R_p^2} = 4\left[1 - \left(\frac{R_{cb}}{R_p}\right)^2\right] \frac{\bar{V}_a}{V_o} \frac{\bar{U}_{jp}}{V_o} + 16\left(\frac{r_j}{R}\right) \int_o^2 \left(\frac{\delta_p}{V_o}\right) \frac{r}{r_j} \, d\left(\frac{r}{r_j}\right) \quad (36)$$

where

$$\frac{\bar{U}_{jp}}{V_o} = \int_o^1 \frac{r}{r_j} \frac{U_{jp_\infty}}{V_o} \, d\left(\frac{r}{r_j}\right) = \frac{1}{2} \frac{\bar{U}_{jp_\infty}}{V_o} = \frac{1}{2} \quad \text{Average Velocity In Wake}$$

CONTROL VOLUME AROUND SHROUD

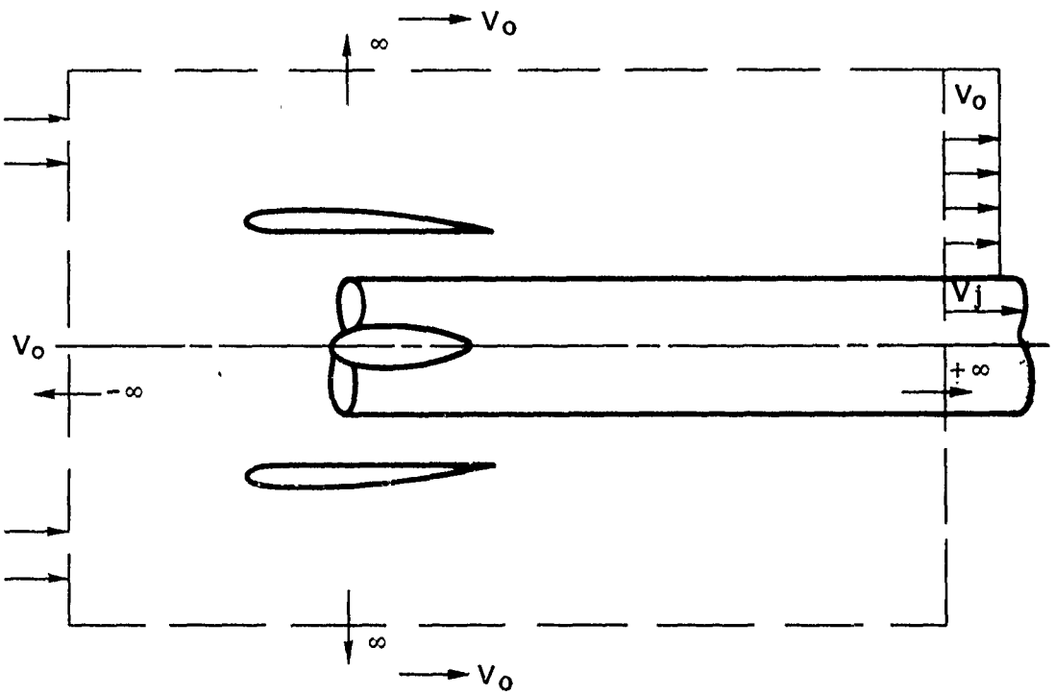

FIGURE 24.

6.2.3 (Continued)

$$\frac{\bar{V}_a}{V_o} = 1 + \frac{2}{1-\left(\frac{R_{cb}}{R_p}\right)^2} \int_{\frac{R_{cb}}{R_p}}^{1} \left(\frac{U_s}{V_o} + \frac{U_{jp}}{V_o} + \frac{U_{cb}}{V_o}\right) \frac{r}{R_p}\, d\left(\frac{r}{R_p}\right)$$ = Average Vel. in Propeller plane

and

U_s = axial velocity at propeller plane due to shroud

U_{jp} = axial velocity at propeller plane due to propeller wake

U_{cb} = axial velocity at propeller plane due to centerbody

U_{jp_∞} = axial velocity in wake due to propeller wake = $2U_{jp}$

$$\frac{\delta_p}{V_o} = \frac{U_{jp_\infty}}{V_o} - \frac{\overline{U_{jp_\infty}}}{V_o}$$ = deviation from average velocity

The first term represents the contribution to the thrust due to the average velocity, whereas the second represents a correction due to deviations from the average. The velocity U_{jp_∞} due to the propeller wake is related to the propeller circulation by the following: (See Appendix 11.4, Eq. (15),

$$\frac{U_{jp_\infty}}{V_o} = \frac{B\Gamma(r)\Omega}{2\pi V_o^2}$$

and r_j/R_p the ratio of wake radius to propeller radius is obtained from continuity as

$$\frac{r_j}{R_p} = \sqrt{\left(1-\left(\frac{R_{cb}}{R_p}\right)^2\right)\left(\frac{\bar{V}_a/V_o}{1+2\frac{\overline{U_{jp}}}{V_o}}\right)}$$

The propeller circulation distribution, shroud and centerbody induced velocities are known from the T.A.R. solution so the right side of Eq. (36) can be evaluated for the total thrust coefficient. This equation has been incorporated into the program, but due to the assumption that the wake circulation distribution can be scaled from the propeller circulation, which depends on the condition that $U << V_o$, this equation is expected to be valid only in the forward flight regime. This technique for computing shroud inviscid thrust is called Method 2.

6.3.4 Shroud Thrust Based on Momentum Theorem Using Propeller Thrust Coefficient (Method 3)

If only average velocities are considered, it is possible to obtain an expression for shroud thrust that is valid in the forward as well as static regime. The only limitation then is the accuracy with which the average velocities can be computed. This approach is utilized in Ref. 12 and is analogous to the momentum result discussed above. In fact, Eq. (36) reduces to the equation in Ref. 12 if $\delta_p = o$, i.e. if only average velocities are considered. Thus, for this special case

$$C'_{T_{tot}} = 4\left[1-\left(\frac{R_{cb}}{R_p}\right)^2\right]\frac{\bar{V}_a}{V_o}\frac{\bar{U}_{jp}}{V_o} \tag{37}$$

where $\bar{V}_a/V_o$ represents the average velocity in the plane of the propeller and $\bar{U}_{jp}/V_o$ is 1/2 the average velocity in the far wake. Two approaches are available for the calculation of $\bar{U}_{jp}/V_o$. The first utilizes the propeller circulation distribution to define the average velocity. It is equivalent to Method 2 with $\delta_p = o$ and is not considered further. An alternate approach is to relate $\bar{U}_{jp}/V_o$ to the propeller thrust coefficient in the manner outlined in Ref. 12. Consider a control volume surrounding the propeller disk. Assuming average values for velocity and pressure, application of the momentum theorem to this control volume leads to the following expression for propeller thrust.

$$T_{PROP} = (p_2 - p_1) A_p \tag{38}$$

where

p_2 = the pressure just downstream of the disk,

p_1 = the pressure upstream,

A_p = the propeller area = $\pi(R_p^2 - R_{cb}^2)$

R_{cb} = centerbody radius

Applying Bernoulli's equation from the downstream side of the disk to the wake at infinity, assuming that the static pressure in the ultimate wake is p_∞, and denoting the slipstream or wake velocity by $\bar{V}_j$, there results

$$p_2 + \frac{1}{2}\rho\bar{V}_a^2 = p_\infty + \frac{1}{2}\rho\bar{V}_j^2 \tag{39}$$

where $\bar{V}_a$ is the average axial velocity at the propeller disk.

Application from the upstream side of the disk to upstream infinity yields

6.3.4 (Continued)

$$p_1 + \frac{1}{2}\rho \bar{V}_a^2 = p_\infty + \frac{1}{2}\rho V_o^2 \tag{40}$$

Subtracting Eq. (40) from Eq. (39),

$$p_2 - p_1 = \frac{1}{2}\rho \left(\bar{V}_j^2 - V_o^2\right) \tag{40a}$$

Substituting into Eq. (38) and rearranging terms, the propeller thrust coefficient becomes

$$C'_{T_{prop}} = \frac{T_{prop}}{\frac{1}{2}\rho V_o^2 \pi R_p^2} = \left[\left(\frac{\bar{V}_j}{V_o}\right)^2 - 1\right]\left[1 - \frac{R_{cb}^2}{R_p^2}\right]$$

solving for $\bar{V}_j/V_o$ in terms of $C'_{T_{prop}}$

$$\frac{\bar{V}_j}{V_o} = \sqrt{1 + \frac{C'_{T_{prop}}}{\left(1 - \frac{R_{cb}^2}{R_p^2}\right)}} \tag{41}$$

Finally substituting Eq. (41) into Eq. (37) and noting that

$$\frac{\bar{V}_j}{V_o} = \frac{\bar{U}_{jp\infty}}{V_o} + 1 = 2\frac{\bar{U}_{jp}}{V_o} + 1$$

the total thrust coefficient becomes

$$C'_{T_{tot}} = 2\left[1 - \left(\frac{R_{cb}}{R_p}\right)^2\right]\frac{\bar{V}_a}{V_o}\left[\sqrt{1 + \frac{C'_{T_{prop}}}{\left(1 - \frac{R_{cb}^2}{R_p^2}\right)}} - 1\right] \tag{42}$$

where $\bar{V}_a/V_o$ and $C'_{T_{prop}}$ are known from the T.A.R. solution. Computing the thrust in this fashion is referred to as Method 3.

6.3.5 Evaluation of the Three Methods for Computing Shroud Thrust

Three methods for computing inviscid thrust have been described. The first, based on detailed integration of the forces acting on the shroud singularities, results in the integration of second order expressions of questionable accuracy for the shroud thickness, camber and propeller loadings typical of this report. The second and third are based on momentum concepts, which require specification of the velocity field in the plane of the propeller and in the wake at infinity. The second accounts for the details of the velocity distribution, which is expressed in terms of the propeller circulation distribution, requiring the assumption of negligible wake distortion; this limits its applicability to the higher forward speeds. The last based on average velocities expresses the jet velocity in terms of the propeller thrust coefficient by an additional application of the momentum theorem to the propeller disk, and is valid for all flight regimes. Its only limitation rests on the accuracy with which C_T propeller and $\overline{V_a/V_o}$ are computed by the T.A.R. theory.

Due to the questionable accuracy of Method 1, the detailed integration method, comparison of the thrust coefficients computed by the three methods for a representative Mach number of 0.3 and the 1.1 area ratio shroud was made. The results, including the effects of drag, are shown in Fig. 25. Estimates of shroud drag are based on Eq. (53), which is discussed in the following section. The Method 1 net thrust coefficients are seen to be much lower than test data and the predictions of Methods 2 and 3. This trend is observed for the full range of Mach numbers and substantiates the theoretical misgivings discussed above. In light of these findings, Method 1 is dismissed from further consideration. Discussion of the two remaining methods is reserved for paragraph 7.4.4.

6.4 SHROUD DRAG PREDICTION

6.4.1 Introduction

Two methods of estimating shroud drag have been derived. The first treats the outer and inner surfaces as flat plates whose free stream velocities are V_o and the propeller plane velocity respectively. The second again treats the surfaces as flat plates, but accounts for the pressure gradients along these surfaces.

6.4.2 Shroud Drag - No Pressure Gradient

It is assumed that flat plate friction can be used to obtain a reasonable estimate of viscous drag on the shroud. The friction force is a product of the dynamic pressure, wetted area, and friction coefficient. On the external surface this is

$$F_{De} = q_o \, 2\pi RC \, C_{fe} \qquad (43)$$

On the internal surface, the velocity is not the free stream, but is increased due to the propeller. The velocity just in front of the propeller can be taken as representative, so that the internal drag is:

6.3.5 Evaluation of the Three Methods for Computing Shroud Thrust

Three methods for computing inviscid thrust have been described. The first, based on detailed integration of the forces acting on the shroud singularities, results in the integration of second order expressions of questionable accuracy for the shroud thickness, camber and propeller loadings typical of this report. The second and third are based on momentum concepts, which require specification of the velocity field in the plane of the propeller and in the wake at infinity. The second accounts for the details of the velocity distribution, which is expressed in terms of the propeller circulation distribution, requiring the assumption of negligible wake distortion; this limits its applicability to the higher forward speeds. The last based on average velocities expresses the jet velocity in terms of the propeller thrust coefficient by an additional application of the momentum theorem to the propeller disk, and is valid for all flight regimes. Its only limitation rests on the accuracy with which C_T propeller and $\overline{V_a}/V_o$ are computed by the T.A.R. theory.

Due to the questionable accuracy of Method 1, the detailed integration method, comparison of the thrust coefficients computed by the three methods for a representative Mach number of 0.3 and the 1.1 area ratio shroud was made. The results, including the effects of drag, are shown in Fig. 25. Estimates of shroud drag are based on Eq. (53), which is discussed in the following section. The Method 1 net thrust coefficients are seen to be much lower than test data and the predictions of Methods 2 and 3. This trend is observed for the full range of Mach numbers and substantiates the theoretical misgivings discussed above. In light of these findings, Method 1 is dismissed from further consideration. Discussion of the two remaining methods is reserved for paragraph 7.4.4.

6.4 SHROUD DRAG PREDICTION

6.4.1 Introduction

Two methods of estimating shroud drag have been derived. The first treats the outer and inner surfaces as flat plates whose free stream velocities are V_o and the propeller plane velocity respectively. The second again treats the surfaces as flat plates, but accounts for the pressure gradients along these surfaces.

6.4.2 Shroud Drag - No Pressure Gradient

It is assumed that flat plate friction can be used to obtain a reasonable estimate of viscous drag on the shroud. The friction force is a product of the dynamic pressure, wetted area, and friction coefficient. On the external surface this is

$$F_{De} = q_o \, 2\pi RC \, C_{fe} \tag{43}$$

On the internal surface, the velocity is not the free stream, but is increased due to the propeller. The velocity just in front of the propeller can be taken as representative, so that the internal drag is:

COMPARISON OF NET THRUST CALCULATION METHODS

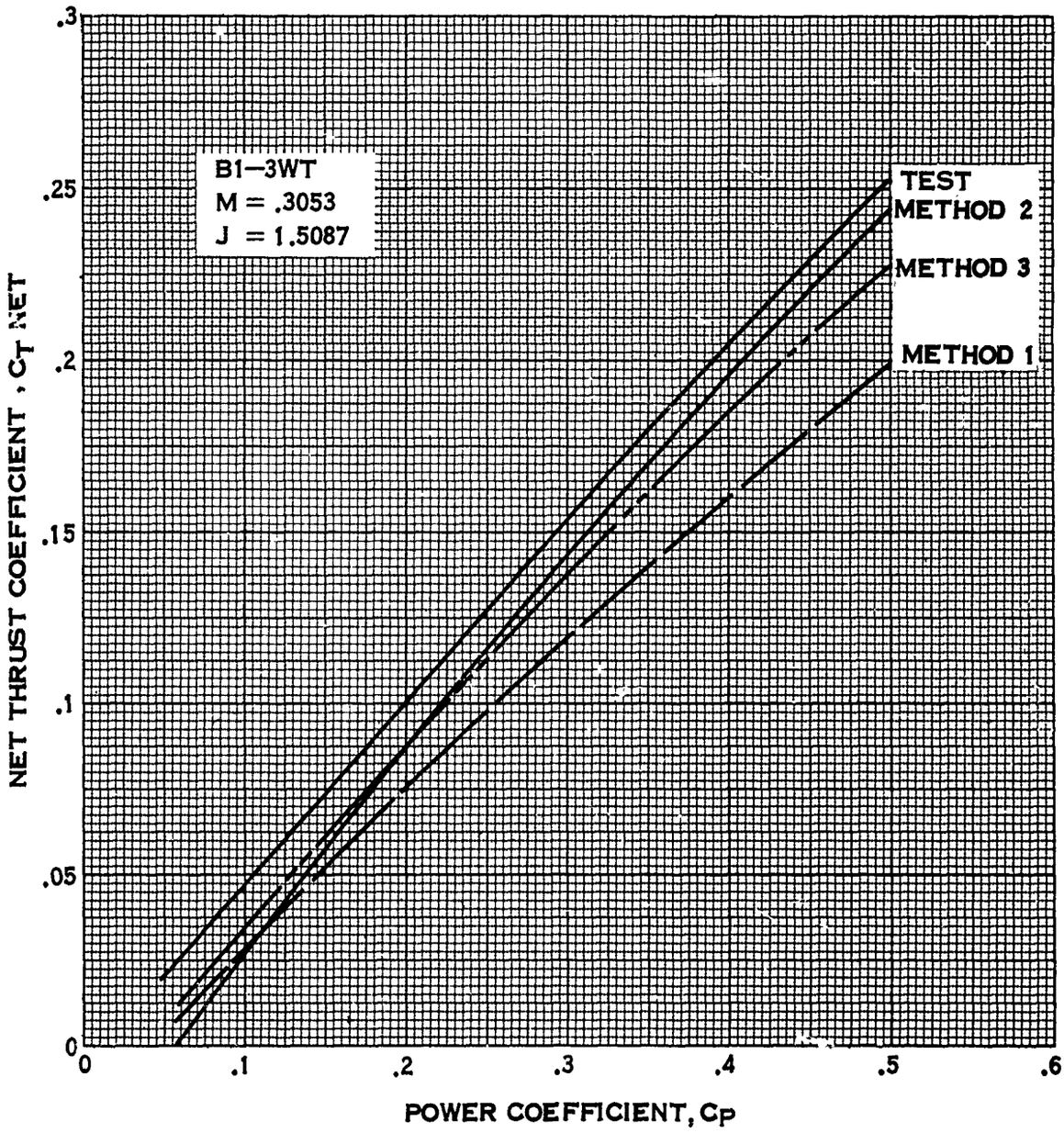

FIGURE 25.

6.4.2 (Continued)

$$F_{Di} = q_a \, C2 \, \pi \, R \, C_{fi} \tag{44}$$

where

$$q_a = 1/2 \, \rho \, \bar{V}_a^{\,2}$$

If it is assumed that the boundary layer flow is turbulent inside and out (or that the transition length is small), the value of skin friction for a smooth flat plate can be used, i.e.

$$C_f = .074/R_e^{\,2} \tag{45}$$

where

$$R_e = \frac{VC}{\nu} \tag{46}$$

Defining

$$R_{eo} = \frac{V_o C}{\nu} \text{ and } Re2 = \frac{\bar{V}_a C}{\nu} \, ,$$

Adding Eq. (43) and (44) and substituting in Eq. (45) and (46), the friction drag force becomes

$$F_D = 1/2 \, \pi \, DC \, \rho \left[\frac{V_o^{\,2}}{R_{co}^{\,2}} + \frac{\bar{V}_a^{\,2}}{R_{e2}^{\,2}} \right] .074 \tag{47}$$

An equation relating the velocity in front of the propeller $\bar{V}_a$ and the free stream velocity V_o is needed. Eq. (40a) relates the pressure jump across the disk $p_2 - p_1$ to the dynamic pressure in the far wake q_j, i.e.

$$p_2 - p_1 = q_j - q_o \tag{48}$$

Using Eq. (38) to eliminate the pressure jump $p_2 - p_1$, there results

$$q_j - q_o = T_{prop}/A_p \tag{49}$$

Rearranging Eq. (49)

$$\bar{V}_j^{\,2} / V_o^{\,2} = 1 + \frac{2 \, T_{prop}}{\rho V_o^{\,2} A_p} \tag{50}$$

By continuity:

$$\frac{\bar{V}_a}{\bar{V}_j} = \frac{A_j}{A_p} \tag{51}$$

6.4.2 (Continued)

So that:

$$\left(\frac{\bar{V}_a}{V_o}\right)^2 = \left(\frac{A_j}{A_p}\right)^2 \left[1 + \frac{2\,T_{prop}}{\rho A_p V_o^2}\right] \tag{52}$$

The friction drag coefficient becomes, noting that $C'_{T_{prop}} = \frac{2T_{prop}}{\rho A_p V_o^2}$

$$C_{DF} = \frac{F_D}{1/2\ \rho V_o^2 A_p} = \frac{(.074)(4)\lambda}{\mu^2 R_{eo}^{.2}} \left[1 + \left(\frac{A_j}{A_p}\right)^{1.8} \left(1 + C'_{T_{prop}}\right)^{.9}\right] \tag{53}$$

Eq. (53) relates the total drag coefficient of the shroud to the shroud geometry, Reynolds number, area ratio and propeller thrust coefficient subject to the assumption of flat plate drag for the inner and outer surfaces.

6.4.3 Shroud Drag - With Pressure Gradient

The second approach for obtaining shroud drag accounts for the shroud pressure distribution. The drag force on a duct is a function of the boundary layer, which depends strongly on the pressure gradient along the wall. This drag can be estimated by assuming that the duct is a thin cylinder with unseparated turbulent boundary layers on the inner and outer surfaces.

Neglecting the laminar portion of the boundary layer, and assuming large Reynolds numbers, Ref. 13 gives the momentum thickness of the boundary layer as

$$\frac{\theta_t}{C} = \frac{C_f}{2} \left(\frac{u}{V_o}\right)^{-3} \left\{\int_o^x \left(\frac{u}{V_o}\right)^{10/3} dx\right\}^{6/7} \tag{54}$$

where C is the shroud chord, u is the local velocity at the edge of the boundary layer, V_o is the free stream velocity, x is the nondimensional axial distance, θ_t is the momentum thickness, and C_f is the flat plate drag coefficient when $u = V_o$.

As in Ref. 14, the velocity distribution is taken to be linear, with a value of $u = u_o$ at $x = o$ and $u = V_o$ at $x = 1$, where u_o = maximum velocity on shroud surface; thus

$$\frac{u}{V_o} = \frac{u_o}{V_o} - x\left(\frac{u_o}{V_o} - 1\right) \tag{55}$$

6.4.3 (Continued)

Ref. 13 relates the drag coefficient to the momentum thickness at the trailing edge,

$$C_D' = \frac{F_D}{q_o \pi D C} = \frac{2\theta_t}{C} \tag{56}$$

where D is the diameter of the duct reference cylinder, q_o is the free stream dynamic pressure, $\frac{\rho V_o^2}{2}$, F_D is the drag force, and θ_t is the momentum thickness at the trailing edge of the duct.

Putting Eq. (55) into Eq. (54), and the resulting equation into Eq. (56) the drag coefficient in terms of the velocity u_o and the flat plate drag coefficient becomes

$$C_D' = C_f \left\{ \frac{3\left[\left(\frac{u_o}{V_o}\right)^{13/3} - 1\right]}{13\left[\frac{u_o}{V_o} - 1\right]} \right\}^{6/7} \tag{57}$$

The pressure coefficient is defined as follows: $C_p = \frac{p - p_\infty}{1/2\,\rho V_o^2}$, so

$$C_{p_o} = 1 - \frac{u_o^2}{V_o^2} \tag{58}$$

where p_∞ is the free stream pressure and p the local pressure. Putting Eq. (58) into (57) the drag coefficient becomes in terms of the shroud pressure coefficient:

$$C_D' = C_f \left\{ \frac{3\left[(1-C_{p_o})^{13/6} - 1\right]}{13\left(\sqrt{1-C_{p_o}} - 1\right)} \right\}^{6/7} \tag{59}$$

The flat plate drag coefficient, using the 1/7 power profile approximation for the turbulent boundary layer velocity profile, is

$$C_f = .074/R_{co}^{.2} \tag{60}$$

Putting Eq. (60) into (59) the drag coefficient becomes

6.4.3 (Continued)

$$C_D' = \frac{.074}{R_{eo}^{.2}} \left\{ \frac{3\left[(1-C_{p_o})^{13/6} - 1\right]}{13\left(\sqrt{1-C_{p_o}} - 1\right)} \right\}^{6/7} \tag{61}$$

Converting C_D' as defined in Eq. (59) to a drag coefficient based on propeller area instead, leads to

$$C_{D_F} = \frac{F_D}{1/2\rho V_o^2 A_p} = \frac{4\lambda}{\mu^2} C_D' \tag{62}$$

Applying the conversion Eq. (62) to (61), there results

$$C_{DF} = \frac{4\lambda}{\mu^2} \frac{(0.074)}{R_{eo}^{.2}} \left[\frac{3\left|(1-C_{po})^{13/6} - 1\right|}{13\left(\sqrt{1-C_{po}} - 1\right)} \right] \tag{63}$$

The total shroud drag coefficient is obtained by applying Eq. (63) to the upper and lower surfaces of the shroud and adding the results.

In the limit, as $C_{p_o} \rightarrow o$, Eq. (63) should reduce to the drag coefficient for one side of a flat plate, i.e. the first term on the right hand side of Eq. (53). This is verified by taking the limit of Eq. (63), i.e.,

$$\lim_{C_{p_o} \rightarrow o} C_{DF} = \frac{(.074)(4)\lambda}{\mu^2 R_{eo}^{.2}}$$

6.4.4 Shroud Drag Evaluation

The two methods of estimating shroud drag were evaluated in conjunction with Methods 2 and 3 for computing the shroud inviscid thrust. Comparisons of the resulting net thrusts with those from the test program showed that neither drag method gave consistently superior agreement. The first method, based on the flat plate friction drag estimate, was therefore chosen for the program because of its simpler form. The other method, accounting for the effects of pressure gradient, is included for completeness and for consideration in future efforts on the subject of shroud drag.

6.5 THRUST COEFFICIENT NOMENCLATURE

In paragraphs 6.3 and 6.4 the thrust and drag coefficients have been normalized by use of the free stream velocity. In practical propeller applications, these coefficients are defined in terms of tip speed, i.e.

$$C_T = \frac{\text{THRUST}}{\rho n^2 D^4}, \quad J = \frac{V_o}{nD}$$

where

n = propeller rotation speed - rps

D = propeller diameter - ft.

ρ = density - pounds sec^2/ft^4

V_o = velocity in feet per second

The conversions are given in Eq. (64) where the prime signifies the nomenclature of paragraphs 6.3 and 6.4.

$$C_T = C_T' \frac{\pi J^2}{8}, \quad J = \pi J_o' \tag{64}$$

In the following discussion, unless otherwise noted, the propeller definition of thrust coefficient C_T and advance ratio J will be used.

6.6 COMPUTER PROGRAM

6.6.1 Introduction

Basically, the computer program permits the calculation of shroud performance and shroud surface pressure coefficient distribution. The calculations can be made for the cases of (1) defined shroud and propeller geometry, (2) defined shroud geometry and propeller circulation, or (3) shroud alone.

The procedure has been programmed in FORTRAN IV for the Univac 1108 in three separate computer decks. Hamilton Standard Deck H193 permits the computations requiring as some of its input certain shroud thickness and camber data generated by Deck H194 and centerbody data generated by Deck H060. The detailed instructions for input, as well as sample cases of input and the corresponding output are presented in Volume II. Volume II also includes the FORTRAN IV listings of the three computer programs and brief flow charts showing how the various subroutines are used.

Hamilton Standard Deck H193 is discussed in some detail below.

6.6.2 Hamilton Standard Computer Deck H193

6.6.2a General Description

The computational procedure as previously defined in paragraph 6.1 through 6.5 has been programmed in FORTRAN IV. For a given shroud and propeller geometry or circulation, the calculations consist of defining the propeller circulation by obtaining the following velocity diagram at the propeller plane.

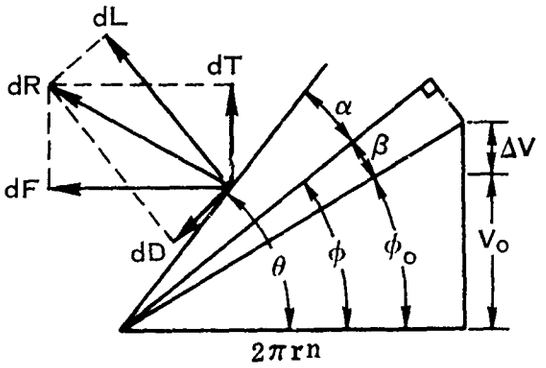

A velocity increment ΔV due to the shroud and centerbody is assumed. The iterative process described in paragraph 6.2.4 is then used in conjunction with the Goldstein propeller theory, two-dimensional airfoil data, and the corresponding iterative process in establishing the final sectional induced angles (β), profile angles of attack (α), and ΔV. The iterative process on ΔV is considered converged when subsequent values of ΔV are within .2% of each other. The iterative process with respect to the Goldstein propeller theory is assumed converged when α and β are so defined that the operating $C_L = f(\alpha)$ from the two-dimensional airfoil data and the operating $C_L = f(\beta)$ from the Goldstein relationship agree within a tolerance of 0.004. In the case of the shroud alone, the calculations do not require the iterative processes.

Two integration techniques are used in the program. The Gauss 10 point integration method is used with respect to the integration of propeller thrust and power derivatives. Hamilton Standard has found this technique gives very good accuracy and since it uses only ten points, minimizes computer running time. Simpson's integration rule is used for integrations along the shroud and centerbody. Eighty-one intervals were selected since adding more intervals changes the integrated values by less than 0.05%.

As was discussed in paragraph 6.1.2, the number of elements in the matrix $\{b_{0\nu}^{2\text{-}D}\}$ and the power of the [P] matrix used in defining ($b_{0\nu}$) must be defined so that convergence is obtained. For the range of computations that were made for comparisons of calculations and tests, it was noted that the first three terms are the most significant and it was found that seven terms in total would be within required tolerance.

Because of the complexity of the T.A.R. theory, considerable effort was undertaken to be certain that the theory had been correctly programmed. Therefore, before changes were made to the basic T.A.R. theory, comparisons were made with the

6.6.2a (Continued)

Hamilton Standard computer program and sample cases in Ref. 1, 2, 3 and 9. These included comparisons of net average pressure distributions, the various components of ($b_{0\nu}^{2-D}$), ($b_{0\nu}$) and net thrust. The comparisons were made for shroud alone and for shroud plus a propeller circulation. The good agreement with these T.A.R. sample cases gave further assurance that the theory had been correctly programmed.

Furthermore, the computer program has been coded in such a manner that changes can be readily incorporated. Therefore, for example, if it is desirable to incorporate some airfoil data other than the family included at present, a subroutine for the required airfoil family can be substituted. Similarly, as improvements are made to any portion of the computational procedure, for example, the computation of net thrust coefficient, it can be readily incorporated.

The computations are limited to $0.25 \leq \lambda \leq 0.998$, $0.75 \leq \mu \leq 0.998$, and $J > 0$.

6.6.2b Inputs for Computer Program

The input requirements as defined on Fig. 26 are categorized with respect to (1) operating condition, (2) shroud data, (3) propeller data and (4) centerbody data.

Each operating condition is defined by a given advance ratio (J), free stream Mach number (M), and propeller blade angle ($\theta_{3/4}$).

The shroud is defined by the overall parameters of shroud diameter, λ, $\bar{X}p$, and μ as well as shroud thickness coefficients and 2-D shroud camber Glauert coefficients. Area ratio and shroud location beyond which the Riegels correction does not apply are also included. Furthermore, locations along the shroud for which shroud surface pressure coefficients will be computed must be included as part of the input.

The propeller is defined by number of blades, diameter, propeller hub to diameter ratio, and blade sectional properties of thickness, width, pitch, and camber for the 10 Gauss stations.

The centerbody is included as input in the form of axial velocities induced by the centerbody in the propeller plane and on the shroud reference cylinder. The radial velocities induced along the shroud reference cylinder in terms of Glauert coefficients are also included. These data are obtained from Hamilton Standard Deck H060.

6.6.2c Outputs from Computer Program

Performance results are presented in terms of the nondimensional power coefficient C_P, and thrust coefficient, C_T. The $C_{T\,net}$ (shroud + propeller) and the breakdown

INPUT REQUIREMENTS

I. OPERATING CONDITION

J, $\theta_{3/4}$, M.

II. SHROUD DATA

A) λ, $\overline{X_P}$, μ, SHROUD DIAMETER
B) SHROUD h/b COEFFICIENTS AND 2-D SHROUD CAMBER GLAUERT COEFFICIENTS (HS DECK H194)
C) AREA RATIO
D) RIEGELS FACTOR LIMIT
E) LOCATIONS ALONG SHROUD FOR WHICH SHROUD SURFACE PRESSURE COEFFICIENTS WILL BE COMPUTED.

III. PROPELLER DATA

A) NUMBER OF BLADES
B) PROPELLER DIAMETER
C) HUB DIAMETER TO PROPELLER DIAMETER RATIO
D) BLADE SECTIONAL CHARACTERISTICS X, t/b, b/D, DES C_L, $\Delta\theta$ OR PROPELLER CIRCULATION.

IV. CENTERBODY DATA (HAMILTON STANDARD DECK H060)

A) RADIAL VELOCITIES ALONG SHROUD SURFACE EXPRESSED AS GLAUERT COEFFICIENTS
B) AXIAL VELOCITIES INDUCED BY CENTERBODY IN THE PLANE OF PROPELLER
C) AXIAL VELOCITIES INDUCED BY THE CENTERBODY ON THE SHROUD SURFACE

FIGURE 26.

6.6.2c (Continued)

to C_T propeller, C_T shroud and shroud C_D (drag coefficient) are computed. For computations based on shroud alone, only the shroud drag is calculated.

The shroud surface velocity ratio (ratio of velocity at shroud surface to free stream velocity) and pressure coefficients are computed for specified points along the shroud. The following components which define the velocity distributions are listed to permit a better understanding of how each component contributes to the velocity. These components do not include the effect of the Riegels correction, although the final inner and outer surface velocities are corrected. The velocity components are induced by the following.

1. Shroud vorticity distribution (discontinuous part) due to the local shroud vortex strength

2. Shroud vorticity distribution (continuous) plus shroud thickness (3-dimensional effect) due to shroud vortex distribution, or equivalently, the effective camber and shroud thickness.

3. Shroud thickness (2-dimensional effect) due to the local source sink distribution.

4. The propeller wake contribution due to propeller circulation.

5. The velocity induced by the centerbody.

Furthermore, to better understand what is happening, additional data is computed in the form of slipstream contraction (ratio of slipstream diameter to propeller diameter), ratio of average slipstream velocity to free stream velocity, and ratio of the average duct velocity at the propeller plane to free stream velocity. The duct velocity includes the summation of the velocities induced by shroud, propeller and centerbody.

Various components of the velocity content along the propeller plane are calculated. The nondimensional velocity induced by the shroud vorticity and source-sink distribution, propeller wake, and centerbody are listed for ten points in the specified propeller plane. Total and assumed velocity ratios are included to show the convergence of the velocity iterative process. Also included are the propeller induced velocity increments based on Goldstein and momentum propeller theories. The former is used in propeller performance computations and the latter in the calculation of net thrust. Furthermore, for the given shroud and propeller configuration, the sectional swirl angles are computed. Swirl angle is defined as the angle formed by the leaving absolute velocity and the axially induced velocity.

To permit a thorough examination of the computational procedure, the following print options are available. Blade elemental printouts permit the examination of the sectional

6.6.2c (Continued)

aerodynamic components required to compute the thrust and power derivatives. Another option permits the display of the various matrices and characteristic functions used in the analytical procedure. The final option permits the examination of the contents of the 2-dimensional Glauert coefficient $b_{0\nu}^{2\text{-D}}$, i.e., the contributions due to the centerbody, shroud thickness, propeller wake and shroud camber. Fig. 27 summarizes the printout option. It should be noted that the use of these options is predicated on a complete understanding of the mathematics of the theory.

Sample printouts are included in Fig. 28a for the shroud and propeller defined, Fig. 28b for the shroud and propeller circulation, and Fig. 28c for the shroud alone.

6.6.2d Computer Running Time

On the Univac 1108, twenty-five operating points are computed per minute with Hamilton Standard Deck H193. The pertinent information from Decks H194 and H060 are obtained in nominal running times and need to be generated only once for each shroud configuration. With such fast running time, this computer program can be readily used to investigate many variations of the shroud, propeller and centerbody variables.

As noted in the introduction, detailed instructions are included in Volume II, as well as the pertinent FORTRAN IV information.

OPTIONAL PRINTOUTS

I. BLADE ELEMENTAL PRINTOUT

θ, α, β, ϕ, ϕ_0, C_L, C_D/C_L, DC_P/DX, DC_T/DX, M/M_{CRIT}

II. MATRICES AND CHARACTERISTICS FUNCTION

P (K,L) — CURVATURE COEFFICIENTS (REF. 2, P 24 — 27)

M (K,L) — MATRIX USED IN DEFINING SHROUD THICKNESS EFFECT ON 2—DIMENSIONAL GLAUERT COEFFICIENTS (REF. 3, P 39—42)

S (K,L) — MATRIX USED IN DEFINING SHROUD VORTICITY — DISTRIBUTION (CONTINUOUS PART) CONTRIBUTION TO SHROUD PRESSURE DISTRIBUTION (REF. 3, P 63 — 66)

T (K,L) — TRANSPOSED MATRIX USED IN DEFINING SHROUD THICKNESS (3—DIMENSIONAL PART) CONTRIBUTION TO SHROUD SURFACE PRESSURE (REF. 3, P 57 — 60)

CHI (J,NU) — INTEGRAL OF THE CHARACTERISTICS FUNCTIONS USED IN DEFINING THE PROPELLER EFFECT ON THE 2—DIMENSIONAL GLAUERT COEFFICIENTS (VOLUME I APPENDIX 11. 7)

VELC — CHARACTERISTICS FUNCTIONS USED IN DEFINING VELOCITIES INDUCED BY THE SHROUD VORTICITY AT THE PROPELLER PLANE (VOLUME I, APPENDIX 11. 6)

VELH — CHARACTERISTICS FUNCTIONS USED IN DEFINING VELOCITIES INDUCED BY SHROUD THICKNESS AT THE PROPELLER PLANE (VOLUME I, APPENDIX 11. 6)

III. 2—DIMENSIONAL GLAUERT COEFFICIENTS CONTENT

SHROUD CAMBER AND THICKNESS

PROPELLER CIRCULATION

CENTERBODY

FIGURE 27.

Hamilton Standard — DIVISION OF UNITED AIRCRAFT CORPORATION — UA®

SAMPLE CASE FOR DEFINED SHROUD AND PR

HS COMPUTER DECK H193
HS SHROUDED PROPELLER PERFORMANCE P
HAMILTON STANDARD
WINDSOR LOCKS, CONN.
1967

1 ROSE WOROBEL 10/13/67
2 SAMPLE INPUT FOR HS DECK H193

**** PROPELLER CHARACTERISTICS ****

3 B1-3WT

NO.OF BLADES= 3. AF= 168.0
DIAMETER FT.= 2.4940 CLI= .4000
HUB X = .2500

X=	.9903	.9493	.8797	.7875	.6807	.5693	.4626	.3
T/B=	.0320	.0420	.0570	.0770	.1040	.1380	.1770	.2
B/D=	.1192	.1165	.1125	.1065	.1000	.0928	.0862	.0
DES CL=	.1760	.3390	.4360	.4910	.4980	.4700	.4170	.3
DELTA θ=	-5.20	-4.70	-3.50	-1.25	3.30	9.40	16.30	23

**** SHROUD CHARACTERISTICS ****

SHROUD NO. = 1. LAMBDA= .6070
XP-BAR=-.1023 MU = .9110
SHROUD INNER SURFACE DIAMETER FT.= 2.5000
SHROUD REFERENCE DIAMETER FT.= 2.7377
RIEGELS FACTOR LIMIT = .1875
AREA RATIO = 1.1000

T/C CONTRIBUTION TO VORTICITY (THICKNESS COEFF.)= .5270 .2506 -7
SLOPE OF MEAN CAMBER LINE (GLAUERT COEFF.)= -.5100 .4742

**** CENTERBODY CHARACTERISTICS ****

CONTRIBUTION TO VORTICITY (GLAUERT COEFF.)= -.0930 -.0338 .0

**** CALCULATIONS ARE BASED ON BOTH PROPELLER AND SHROUD CHARACTERISTIC

**** IN THE SUBSEQUENT MATRICES THE SUBSCRIPT L REFERS TO THE ROW AND T

P(K,L) DATA LAMBDA= .6070

.09336	.00000	.04670	.00000	-.00002	.00000
.18672	.11179	.00000	-.01857	.00000	.00013
.03608	.00000	.02459	.00000	-.00618	.00000
-.00009	-.00619	.00000	.00911	.00000	-.00297

A-1

ED SHROUD AND PROPELLER GEOMETRY

COMPUTER DECK H193
ROPELLER PERFORMANCE PROGRAM
AMILTON STANDARD
NDSOR LOCKS,CONN.
1967

	.5693	.4626	.3700	.3005	.2600
	.1380	.1770	.2140	.2450	.2650
	.0928	.0862	.0800	.0760	.0735
	.4700	.4170	.3510	.2940	.2570
	9.40	16.30	23.10	28.70	32.30

.5270	.2506	-7.4200	30.5670	-64.6900	73.8190	-43.2900	10.2380
-.5100	.4742	.5894	.3748	.2473	.0951	-.0456	

-.0930	-.0338	.0142	-.0007	-.0009	.0000	.0000	-.0000

SHROUD CHARACTERISTICS ****

FERS TO THE ROW AND THE SUBSCRIPT K REFERS TO THE COLUMN ****

002	.00000	.00000
000	.00013	.00000
018	.00000	.00003
000	-.00297	.00000

FIGURE 28A.
(SHEET 1 OF 5)

B.

Hamilton Standard
DIVISION OF UNITED AIRCRAFT CORPORATION
U A®

SAMPLE CASE FOR DEFINED SHROUD AND F

```
   -.00025     .00000    -.00309     .00000     .00472     .0000
   -.00000     .00003     .00000    -.00178     .00000     .0029
    .00000     .00000     .00001     .00000    -.00116     .0000
 M(K,L) MATRIX LAMBDA=  .6070
    .77577     .42779    -.00000     .05230    -.00000     .00910    -.
   -.24243    -.00000     .08170    -.00000     .01588    -.00000
    .02740     .06795    -.00000    -.00439    -.00000    -.00125    -.
   -.00531    -.00000    -.01624    -.00000    -.00079    -.00000
    .00278     .00628    -.00000     .00430    -.00000     .00042    -.
   -.00142    -.00000    -.00220    -.00000    -.00119    -.00000    -.
    .00076     .00181    -.00000     .00080    -.00000     .00029    -.
   -.00051    -.00000    -.00075    -.00000    -.00028    -.00000    -.

 S(K,L) DATA LAMBDA=  .6070
    1.34181     .67251    -.00000    -.00157    -.00000    -.0000
   -.63085    -.00000    -.31730    -.00000     .00193    -.0000
    .00633     .15863    -.00000    -.15604    -.00000     .0005
    .00374    -.00000     .10401    -.00000    -.10232    -.0000
    .00008    -.00051    -.00000     .07676    -.00000    -.0763
   -.00006    -.00000    -.00019    -.00000     .06103    -.0000
   -.00001    -.00000    -.00000    -.00012    -.00000     .0507

 TT(K,L) DATA LAMBDA=  .6070
    .02255     .00000    -.00781     .00000    -.00185     .0000
    .07153     .04805     .00000     .00417     .00000     .0009
    .01847     .00000    -.00641     .00000    -.00114     .0000
   -.00088    -.00320     .00000     .00040     .00000    -.0000
   -.00002     .00000    -.00002     .00000     .00001     .0000
   -.00009    -.00012     .00000    -.00012     .00000     .0000
    .00000     .00000     .00001     .00000     .00003     .0005

 **** IN THE SUBSEQUENT MATRIX THE SUBSCRIPT J REFERS TO THE RO

 CHI(J,NU) INTEGRAL DATA   LAMBDA=  .607 MU=  .911 XPB= -.10230
                .368797    -.098303     .043780    -.024433
               -.070586     .024980    -.011631     .006482
                .162295    -.071615     .037169    -.022480
                .043807    -.025107     .014595    -.009236
               -.042131     .024995    -.016077     .010445
               -.023317     .016541    -.011489     .007988
                .011405    -.009108     .005867    -.004348

 RAD.STA.          VELC(NU) AS NU GOES FROM 0 TO 7
   .9903  8.55389  5.62314  1.28969 -2.85074 -1.63158  1.48951
   .9493  8.00916  5.09583  1.08626 -2.29601 -1.21526  1.06647
   .8797  7.07703  4.29719   .80696 -1.59809  -.73598   .61247
   .7875  5.87233  3.40182   .53993  -.99936  -.37977   .30118
   .6807  4.58011  2.55458   .33623  -.58796  -.17831   .13677
   .5693  3.39057  1.84241   .20297  -.34065  -.08217   .06184
   .4626  2.41270  1.28978   .12265  -.20034  -.03940   .02936
   .3700  1.68862   .89415   .07656  -.12301  -.02059   .01527
   .3005  1.21798   .64189   .05152  -.08208  -.01262   .00930
   .2600   .97338   .51153   .03952  -.06279  -.00916   .00684


 RAD.STA.          VELH(NU) AS NU GOES FROM 0 TO 7
   .9903  1.60236  -.31274  -.83864   .06054  -.13508   .01172
   .9493  1.40222  -.29308  -.72793   .04479  -.12216   .00960
   .8797  1.10414  -.25748  -.57043   .02503  -.10112   .00637
   .7875   .78950  -.20963  -.41068   .00916  -.07669   .00319
   .6807   .52496  -.15820  -.27832   .00023  -.05414   .00101
```

A.

D SHROUD AND PROPELLER GEOMETRY

```
  .00472      .00000     -.00176
  .00000      .00292      .00000
 -.00116      .00000      .00199

0000     .00910    -.00000    -.00100
1588    -.00000     .00058    -.00000
0000    -.00125    -.00000     .00089
0079    -.00000     .00003    -.00000
0000     .00042    -.00000    -.00012
0119    -.00000    -.00003    -.00000
0000     .00029    -.00000    -.00014
0028    -.00000    -.00001    -.00000


 -.00000     -.00001     -.00000
  .00193     -.00000     -.00000
 -.00000      .00051     -.00000
 -.10232     -.00000      .00019
 -.00000     -.07637     -.00000
  .06103     -.00000     -.06095
 -.00000      .05079     -.00000


 -.00185      .00000     -.00041
  .00000      .00093      .00000
 -.00114      .00000      .00011
  .00000     -.00004      .00000
  .00001      .00000      .00001
  .00000      .00004      .00000
  .00003      .00000     -.00002
```

J REFERS TO THE ROW AND THE SUBSCRIPT NU REFERS TO THE COLUMN ****

```
 .911 XPB= -.10230
780    -.024433     .015646    -.010819     .007970
531     .006482    -.004140     .002873    -.002080
169    -.022480     .014742    -.010497     .007697
595    -.009236     .006222    -.004451     .003320
977     .010445    -.007399     .005321    -.004095
589     .007988    -.005775     .004285    -.003307
967    -.004348     .003083    -.002396     .001816

70 7
-1.63158  1.48951  1.56171  -.61415
-1.21526  1.06647  1.03086  -.39701
 -.73598   .61247   .51115  -.19412
 -.37977   .30118   .20465  -.07843
 -.17831   .13677   .07286  -.02874
 -.08217   .06184   .02566  -.01048
 -.03940   .02936   .00969  -.00408
 -.02059   .01527   .00423  -.00184
 -.01262   .00930   .00210  -.00100
 -.00916   .00684   .00175  -.00075


70 7
 -.13508   .01172  -.03064   .00276
 -.12216   .00960  -.02816   .00235
 -.10112   .00637  -.02385   .00166
 -.07669   .00319  -.01852   .00091
 -.05414   .00101  -.01333   .00035
```

FIGURE 28A.
(SHEET 2 OF 5)

B.

Hamilton Standard
DIVISION OF UNITED AIRCRAFT CORPORATION
U A®

SAMPLE CASE FOR DEFINED SHROUD AI

.5693	.33604	-.11248	-.18255	-.00312	-.0365
.4626	.21298	-.07698	-.11832	-.00357	-.0241
.3700	.13749	-.05222	-.07763	-.00299	-.0160
.3005	.09433	-.03698	-.05390	-.00236	-.0111
.2600	.07369	-.02932	-.04232	-.00196	-.0086

A.

FINED SHROUD AND PROPELLER GEOMETRY

55	-.00312	-.03654	-.00005	-.00913	.00006
82	-.00357	-.02413	-.00039	-.00608	-.00006
53	-.00299	-.01601	-.00042	-.00406	-.00008
90	-.00236	-.01119	-.00036	-.00285	-.00007
52	-.00196	-.00881	-.00031	-.00225	-.00007

FIGURE 28A.
(SHEET 3 OF 5)

B.

Hamilton Standard
DIVISION OF UNITED AIRCRAFT CORPORATION

SAMPLE CASE FOR DEFINED SHROUD AN

*** PERFORMANCE ***

CONDITION J= 1.5087 THETA 3/4=42.000 MN= .3053 CP=

NET THRUST COEFF.(SHROUD + PROPELLER) = .2102
SHROUD THRUST COEFFICIENT = -.0148
SHROUD FRICTION DRAG COEFFICIENT = .0216
PROPELLER THRUST COEFFICIENT = .2250

SLIPSTREAM CONTRACTION= .95

RATIO OF AVERAGE DUCT VEL./FREE STREAM VEL.= 1.0957

RATIO OF AVERAGE SLIPSTREAM VEL./FREE STREAM VEL.= 1.1317

**** INDUCED VELOCITY CONTENT ****

PROP. X =	.9903	.9493	.8797	.7875	.6807
CENTERBODY DV/V0=	-.0084	-.0086	-.0089	-.0092	-.0092
SHROUD T/C DV/V0=	.1316	.1255	.1152	.1023	.0891
VORTICITY DV/V0=	-.0712	-.0680	-.0646	-.0621	-.0605
TOTAL V/V0=	1.0520	1.0489	1.0417	1.0310	1.0194
ASSUMED V/V0=	1.0514	1.0484	1.0414	1.0308	1.0196
PROP.IND.G. VP/V=	.1940	.1662	.1363	.1074	.0873
PROP.IND.M. VP/V=	.0740	.0880	.0888	.0813	.0738
SWIRL ANGLE =	3.6107	4.2513	4.3162	4.0163	3.7084

**** GLAUERT COEFFICIENTS CONTENT ****

NU	SHROUD CAMBER	SHROUD T/C	PROP. CIRC.	CENTER -BODY	TOTAL 2-D	3-D
-0	-.5100	-.0770	.0814	-.0930	-.3676	-.3719
1	.4742	-.0245	-.0176	-.0338	.4719	.4449
2	.5894	.0001	.0467	.0142	.6501	.6509
3	.3748	-.0009	.0152	-.0007	.3911	.3917
4	.2473	-.0081	-.0156	-.0009	.2470	.2463
5	.0951	-.0054	-.0103	.0000	.0956	.0952
6	-.0456	-.0055	.0054	.0000	-.0293	-.0296

**** SHROUD SURFACE VELOCITIES AND PRESSURE COEFFICIENTS *

	VELOCITY COMPONENTS			
SHROUD X	VORT.DIS.	2-D THICK.	3-D THICK.+ VORT.CONT.	PROP WAKE
.0				
.00010	9.27679	.19128	-.03645	.01551
.00500	1.16724	.37954	-.03476	.01560
.01250	.60794	.43680	-.03238	.01573
.02500	.29398	.47207	-.02889	.01596
.05000	.05831	.47070	-.02350	.01641

A.

ED SHROUD AND PROPELLER GEOMETRY

MN= .3053 CP= .4292

.2102
-.0148
.0216
.2250

.= 1.0957

AM VEL.= 1.1317

.7875	.6807	.5693	.4626	.3700	.3005	.2600
-.0092	-.0092	-.0084	-.0067	-.0039	-.0005	.0021
.1023	.0891	.0780	.0698	.0644	.0613	.0599
-.0621	-.0605	-.0592	-.0581	-.0573	-.0568	-.0566
1.0310	1.0194	1.0104	1.0050	1.0032	1.0040	1.0055
1.0308	1.0196	1.0107	1.0054	1.0036	1.0044	1.0059
.1074	.0873	.0685	.0497	.0340	.0231	.0174
.0813	.0738	.0628	.0495	.0365	.0269	.0216
4.0163	3.7084	3.2153	2.5809	1.9296	1.4356	1.1585

AL

	3-D
676	-.3719
719	.4449
501	.6509
911	.3917
470	.2463
956	.0952
293	-.0296

E COEFFICIENTS ****

TS ---------

K.+			OUTER SURFACE		INNER SURFACE	
NT.	PROP WAKE	CB EFF.	V/VINF	CPRESS	V/VINF	CPRESS
					-.8568	.2659
3645	.01551	-.00530	.9492	.0990	-.7374	.4563
3476	.01560	-.00530	1.3318	-.7737	.0992	.9902
3238	.01573	-.00530	1.4280	-1.0393	.5697	.6755
2889	.01596	-.00530	1.4596	-1.1303	.9686	.0619
2350	.01641	-.00520	1.4248	-1.0300	1.3152	-.7299

FIGURE 28A.
(SHEET 4 OF 5)

B.

Hamilton Standard
DIVISION OF UNITED AIRCRAFT CORPORATION
UA®

.07500	-.03427	.43353	-.01987	.01686	-.
.10000	-.07184	.38498	-.01761	.01731	-.
.15000	-.07519	.28996	-.01601	.01814	-.
.20000	-.04174	.21918	-.01672	.01876	-.
.25000	-.00226	.17644	-.01840	.01885	-.
.30000	.03024	.15560	-.02027	.01771	-.
.40000	.06032	.14512	-.02316	.00406	-.
.50000	.05587	.13347	-.02466	-.01566	-.
.60000	.04725	.10324	-.02552	-.01891	-.
.70000	.05566	.06518	-.02618	-.01785	-.
.80000	.07476	.03178	-.02604	-.01607	-.
.90000	.06859	-.01239	-.02383	-.01433	-.
.95000	.04324	-.06159	-.02171	-.01352	-.

**** BLADE ELEMENTAL PRINTOUT ****

J= 1.5087 THETA 3/4= 42.00 FREE STREAM M.N.= .3053

X=	.9903	.9493	.8797	.7875	.6807	.5693
THETA=	36.80	37.30	38.50	40.75	45.30	51.40
ALPHA=	4.07	4.28	4.40	4.66	5.86	7.45
PHI=	32.73	33.02	34.10	36.09	39.44	43.95
BETA=	5.72	5.08	4.48	3.93	3.71	3.50
PHI 0=	27.02	27.94	29.62	32.15	35.73	40.45
CL3=	.5699	.7147	.7875	.8193	.8684	.8844
CD/CL=	.0446	.0296	.0182	.0162	.0172	.0189
DCP/DX=	1.1067	1.1997	1.0619	.8285	.6241	.4288
DCT/DX=	.5027	.5806	.5459	.4442	.3427	.2394
SECT.EFF.=	.6853	.7301	.7756	.8088	.8283	.8424
SECT.MN=	.7032	.6804	.6413	.5899	.5319	.4747
M/MCRIT=	.7738	.7989	.7889	.7587	.7193	.7086

A.

NED SHROUD AND PROPELLER GEOMETRY

.01686	-.00520	1.3605	-.8510	1.4275	-1.0379
.01731	-.00530	1.2981	-.6852	1.4408	-1.0759
.01814	-.00540	1.2111	-.4667	1.3614	-.8535
.01876	-.00570	1.1738	-.3777	1.2573	-.5807
.01885	-.00610	1.1685	-.3655	1.1731	-.3760
.01771	-.00660	1.1767	-.3845	1.1162	-.2459
.00406	-.00780	1.1785	-.3890	1.0579	-.1192
-.01566	-.00910	1.1399	-.2994	1.0282	-.0572
-.01891	-.01050	1.0956	-.2002	1.0011	-.0021
-.01785	-.01170	1.0651	-.1345	.9538	.0903
-.01607	-.01250	1.0519	-.1065	.9024	.1857
-.01433	-.01280	1.0052	-.0105	.8681	.2465
-.01352	-.01270	.9337	.1282	.8472	.2822

.3053

.6807	.5693	.4626	.3700	.3005	.2600
45.30	51.40	58.30	65.10	70.70	74.30
5.86	7.45	8.93	9.92	10.36	10.62
39.44	43.95	49.37	55.18	60.34	63.68
3.71	3.50	3.14	2.69	2.26	1.97
35.73	40.45	46.23	52.49	58.08	61.71
.8684	.8844	.8351	.7282	.6048	.5215
.0172	.0189	.0277	.0400	.0577	.0747
.6241	.4288	.2682	.1558	.0930	.0647
.3427	.2394	.1497	.0855	.0488	.0321
.8283	.8424	.8421	.8278	.7920	.7480
.5319	.4747	.4245	.3859	.3610	.3485
.7193	.7086	.7196	.7050	.6082	.6085

FIGURE 28A.
(SHEET 5 OF 5)

B.

Hamilton Standard — DIVISION OF UNITED AIRCRAFT CORPORATION — UA®

SAMPLE CASE FOR DEFINED SHROUD AND P

HS COMPUTER DECK H193
HS SHROUDED PROPELLER PERFORMANC
HAMILTON STANDARD
WINDSOR LOCKS, CONN.
1967

1 ROSE WOROBEL 10/13/67
2 GIVEN PROPELLER CIRCULATION

**** PROPELLER CHARACTERISTICS ****

3 B1-3WT

NO.OF BLADES= 3. AF= 168.0
DIAMETER FT.= 2.4900 CLI= .4000
HUB X = .2500

X=	.9903	.9493	.8797	.7875	.6807	.5693	.4626
CIRCULATION=	.1489	.1769	.1788	.1632	.1484	.1262	.0995

**** SHROUD CHARACTERISTICS ****

SHROUD NO. = 1. LAMBDA= .6070
XP-BAR=-.1023 MU = .9110
SHROUD INNER SURFACE DIAMETER FT.= 2.5000
SHROUD REFERENCE DIAMETER FT.= 2.7377
RIEGELS FACTOR LIMIT = .1875
AREA RATIO = 1.1000

T/C CONTRIBUTION TO VORTICITY (THICKNESS COEFF.)= .5270 .2506
SLOPE OF MEAN CAMBER LINE (GLAUERT COEFF.)= -.5100 .4742

**** CENTERBODY CHARACTERISTICS ****

CONTRIBUTION TO VORTICITY (GLAUERT COEFF.)= -.0930 -.0338

**** CALCULATIONS ARE BASED ON SHROUD CHARACTERISTICS AND GIVEN PRO

A.

ED SHROUD AND PROPELLER CIRCULATION

COMPUTER DECK H193
ROPELLER PERFORMANCE PROGRAM
AMILTON STANDARD
NDSOR LOCKS, CONN.
1967

7	.5693	.4626	.3700	.3005	.2600
4	.1262	.0995	.0734	.0540	.0435

.5270	.2506	-7.4200	30.5670	-64.6900	73.8190	-43.2900	10.2380
-.5100	.4742	.5894	.3748	.2473	.0951	-.0456	

-.0930	-.0338	.0142	-.0007	-.0009	.0000	.0000	-.0000

TICS AND GIVEN PROPELLER CIRCULATION ****

FIGURE 28B.
(SHEET 1 OF 3)

B.

Hamilton Standard — DIVISION OF UNITED AIRCRAFT CORPORATION — UA®

SAMPLE CASE FOR DEFINED SHROUD AN

*** PERFORMANCE ***

CONDITION J= 1.5087 MN= .3053

NET THRUST COEFF.(SHROUD + PROPELLER) = .2102
SHROUD THRUST COEFFICIENT = -.0148
SHROUD FRICTION DRAG COEFFICIENT = .0216
PROPELLER THRUST COEFFICIENT = .2250

SLIPSTREAM CONTRACTION= .95

RATIO OF AVERAGE DUCT VEL./FREE STREAM VEL.= 1.0957

RATIO OF AVERAGE SLIPSTREAM VEL./FREE STREAM VEL.= 1.1317

**** INDUCED VELOCITY CONTENT ****

PROP. X =	.9903	.9493	.8797	.7875	.6807	
CENTERBODY DV/V0=	-.0084	-.0086	-.0089	-.0092	-.0092	-
SHROUD T/C DV/V0=	.1316	.1255	.1152	.1023	.0891	
VORTICITY DV/V0=	-.0712	-.0680	-.0646	-.0621	-.0605	-
TOTAL V/V0=	1.0520	1.0489	1.0417	1.0309	1.0194	1

**** GLAUERT COEFFICIENTS CONTENT ****

NU	SHROUD CAMBER	SHROUD T/C	PROP. CIRC.	CENTER -BODY	TOTAL 2-D	3-D
-0	-.5100	-.0770	.0814	-.0930	-.3676	-.3719
1	.4742	-.0245	-.0176	-.0338	.4719	.4449
2	.5894	.0001	.0466	.0142	.6501	.6509
3	.3748	-.0009	.0152	-.0007	.3911	.3917
4	.2473	-.0081	-.0156	-.0009	.2470	.2463
5	.0951	-.0054	-.0103	.0000	.0956	.0952
6	-.0456	-.0055	.0054	.0000	-.0293	-.0296

**** SHROUD SURFACE VELOCITIES AND PRESSURE COEFFICIENTS ***

	VELOCITY COMPONENTS			
SHROUD X	VORT.DIS.	2-D THICK.	3-D THICK.+ VORT.CONT.	PROP WAKE
.0				
.00010	9.27720	.19128	-.03645	.01550
.00500	1.16730	.37954	-.03477	.01559
.01250	.60797	.43680	-.03238	.01572
.02500	.29401	.47207	-.02889	.01595
.05000	.05833	.47070	-.02350	.01640
.07500	-.03426	.43353	-.01987	.01685
.10000	-.07182	.38498	-.01762	.01730
.15000	-.07518	.28996	-.01602	.01813
.20000	-.04173	.21918	-.01672	.01875

A.

NED SHROUD AND PROPELLER CIRCULATION

.2102
-.0148
.0216
.2250

.= 1.0957

AM VEL.= 1.1317

.7875	.6807	.5693	.4626	.3700	.3005	.2600
-.0092	-.0092	-.0084	-.0067	-.0039	-.0005	.0021
.1023	.0891	.0780	.0698	.0644	.0613	.0599
-.0621	-.0605	-.0592	-.0582	-.0573	-.0568	-.0566
1.0309	1.0194	1.0104	1.0050	1.0032	1.0040	1.0055

AL

	3-D
676	-.3719
719	.4449
501	.6509
911	.3917
470	.2463
956	.0952
293	-.0296

E COEFFICIENTS ****

TS ---------

NT.	PROP WAKE	CB EFF.	OUTER SURFACE V/VINF	OUTER SURFACE CPRESS	INNER SURFACE V/VINF	INNER SURFACE CPRESS
					-.8568	.2659
3645	.01550	-.00530	.9492	.0990	-.7374	.4562
3477	.01559	-.00530	1.3318	-.7738	.0991	.9902
3238	.01572	-.00530	1.4281	-1.0394	.5696	.6755
2889	.01595	-.00530	1.4596	-1.1304	.9685	.0619
2350	.01640	-.00520	1.4248	-1.0301	1.3152	-.7298
1987	.01685	-.00520	1.3605	-.8510	1.4275	-1.0378
1762	.01730	-.00530	1.2982	-.6852	1.4408	-1.0758
1602	.01813	-.00540	1.2111	-.4667	1.3614	-.8534
1672	.01875	-.00570	1.1738	-.3777	1.2572	-.5807

FIGURE 28B.
(SHEET 2 OF 3)

B.

Hamilton Standard
DIVISION OF UNITED AIRCRAFT CORPORATION

.25000	-.00225	.17644	-.01841	.01884	-.
.30000	.03024	.15560	-.02028	.01770	-.
.40000	.06032	.14512	-.02317	.00406	-.
.50000	.05587	.13347	-.02466	-.01566	-.
.60000	.04725	.10324	-.02552	-.01890	-.
.70000	.05566	.06518	-.02618	-.01784	-.
.80000	.07476	.03178	-.02604	-.01607	-.
.90000	.06859	-.01239	-.02383	-.01432	-.
.95000	.04324	-.06159	-.02171	-.01351	-.

A.

INED SHROUD AND PROPELLER CIRCULATION

.01884	-.00610	1.1685	-.3655	1.1730	-.3760
.01770	-.00660	1.1767	-.3845	1.1162	-.2459
.00406	-.00780	1.1785	-.3890	1.0579	-.1191
-.01566	-.00910	1.1399	-.2994	1.0282	-.0572
-.01890	-.01050	1.0956	-.2003	1.0011	-.0021
-.01784	-.01170	1.0651	-.1345	.9538	.0903
-.01607	-.01250	1.0519	-.1066	.9024	.1856
-.01432	-.01280	1.0053	-.0105	.8681	.2465
-.01351	-.01270	.9337	.1281	.8472	.2822

FIGURE 28B.
(SHEET 3 OF 3)

B,

Hamilton Standard
DIVISION OF UNITED AIRCRAFT CORPORATION

SAMPLE CASE FOR SHROU

HS COMPUTER DECK
HS SHROUDED PROPELLER PERFO
HAMILTON STANDA
WINDSOR LOCKS,CO
1967

1 ROSE WOROBEL 10/13/67
2 SHROUD ALONE
3 B1

**** SHROUD CHARACTERISTICS ****

SHROUD NO. = 1. LAMBDA= .6070
XP-BAR=-.1023 MU = .9132
SHROUD INNER SURFACE DIAMETER FT.= 2.5000
SHROUD REFERENCE DIAMETER FT.= 2.7377
RIEGELS FACTOR LIMIT = .1875
AREA RATIO = 1.1000
CENTERBODY X IN SPECIFIED PLANE = .2500

T/C CONTRIBUTION TO VORTICITY (THICKNESS COEFF.)= .5270 .2
SLOPE OF MEAN CAMBER LINE (GLAUERT COEFF.)= -.5100 .4

**** CENTERBODY CHARACTERISTICS ****

CONTRIBUTION TO VORTICITY (GLAUERT COEFF.)= -.0930 -.033

**** CALCULATIONS ARE BASED ON THE SHROUD ALONE ****

A.

ASE FOR SHROUD ALONE

HS COMPUTER DECK H193
ED PROPELLER PERFORMANCE PROGRAM
HAMILTON STANDARD
WINDSOR LOCKS, CONN.
1967

.)= .5270 .2506 -7.4200 30.5670 -64.6900 73.8190 -43.2900 10.2380
.)= -.5100 .4742 .5894 .3748 .2473 .0951 -.0456

= -.0930 -.0338 .0142 -.0007 -.0009 .0000 .0000 -.0000

E ****

FIGURE 28C.
(SHEET 1 OF 3)

B.

Hamilton Standard
DIVISION OF UNITED AIRCRAFT CORPORATION

SAMPLE CASE FOR SHROU

*** PERFORMANCE ***

CONDITION MN= .3053

SHROUD FRICTION DRAG COEFFICIENT = .0079

SLIPSTREAM CONTRACTION= .96

RATIO OF AVERAGE DUCT VEL./FREE STREAM VEL.= .9825

**** INDUCED VELOCITY CONTENT ****

PROP. X	=	.9903	.9493	.8797	.7875	.6807	.5693
CENTERBODY	DV/V0=	-.0084	-.0086	-.0089	-.0092	-.0092	-.0084
SHROUD T/C	DV/V0=	.1319	.1258	.1155	.1025	.0893	.0781
VORTICITY	DV/V0=	-.1181	-.1145	-.1102	-.1065	-.1032	-.1004
TOTAL	V/V0=	1.0054	1.0027	.9964	.9869	.9769	.9693

**** GLAUERT COEFFICIENTS CONTENT ****

NU	SHROUD CAMBER	SHROUD T/C	PROP. CIRC.	CENTER -BODY	TOTAL 2-D	3-D
-0	-.5100	-.0770	.0000	-.0930	-.4490	-.4644
1	.4742	-.0245	.0000	-.0338	.4895	.4456
2	.5894	.0001	.0000	.0142	.6034	.5994
3	.3748	-.0009	.0000	-.0007	.3759	.3763
4	.2473	-.0081	.0000	-.0009	.2626	.2622
5	.0951	-.0054	.0000	.0000	.1059	.1055
6	-.0456	-.0055	.0000	.0000	-.0347	-.0350

**** SHROUD SURFACE VELOCITIES AND PRESSURE COEFFICIENTS ****

	-------- VELOCITY COMPONENTS --------				
SHROUD X	VORT.DIS.	2-D THICK.	3-D THICK.+ VORT.CONT.	PROP WAKE	CB EFF
.0					
.00010	11.58799	.19128	-.06053	.00000	-.00
.00500	1.49560	.37954	-.05881	.00000	-.00
.01250	.81715	.43680	-.05636	.00000	-.00
.02500	.44391	.47207	-.05276	.00000	-.00
.05000	.16751	.47070	-.04719	.00000	-.00
.07500	.05778	.43353	-.04337	.00000	-.00
.10000	.01049	.38498	-.04091	.00000	-.00
.15000	-.00410	.28996	-.03879	.00000	-.00
.20000	.02185	.21918	-.03879	.00000	-.00
.25000	.05443	.17644	-.03958	.00000	-.00
.30000	.07956	.15560	-.04037	.00000	-.00
.40000	.09309	.14512	-.04072	.00000	-.00
.50000	.07239	.13347	-.03955	.00000	-.00
.60000	.05223	.10324	-.03802	.00000	-.01

A.

ASE FOR SHROUD ALONE

825

.6807	.5693	.4626	.3700	.3005	.2600
-.0292	-.0084	-.0067	-.0039	-.0005	.0021
.0993	.0781	.0699	.0645	.0613	.0599
-.1032	-.1004	-.0980	-.0963	-.0951	-.0946
.9769	.9693	.9652	.9643	.9657	.9675

-D
4644
4456
3994
3763
2622
1055
0350

ICIENTS ****

		OUTER SURFACE		INNER SURFACE	
ROP WAKE	CB EFF.	V/VINF	CPRESS	V/VINF	CPRESS
				-1.0697	-.1443
.00000	-.00530	1.1557	-.3356	-.9511	.0954
.00000	-.00530	1.4843	-1.2030	-.0951	.9910
.00000	-.00530	1.5477	-1.3954	.3939	.8448
.00000	-.00530	1.5515	-1.4071	.8101	.3437
.00000	-.00520	1.4897	-1.2192	1.1750	-.3806
.00000	-.00520	1.4111	-.9911	1.2980	-.6849
.00000	-.00530	1.3396	-.7945	1.3187	-.7391
.00000	-.00540	1.2413	-.5407	1.2494	-.5611
.00000	-.00570	1.1965	-.4317	1.1528	-.3290
.00000	-.00610	1.1852	-.4047	1.0763	-.1585
.00000	-.00660	1.1882	-.4118	1.0291	-.0590
.00000	-.00780	1.1897	-.4154	1.0035	-.0070
.00000	-.00910	1.1572	-.3391	1.0124	-.0250
.00000	-.01050	1.1070	-.2253	1.0025	-.0050

FIGURE 28C.
(SHEET 2 OF 3)

B.

Hamilton Standard
DIVISION OF UNITED AIRCRAFT CORPORATION
UA®

SAMPLE CASE FOR SHROUD

.70000	.05633	.06518	-.03679	.00000	-.0117
.80000	.07651	.03178	-.03523	.00000	-.0125
.90000	.07068	-.01239	-.03188	.00000	-.0126
.95000	.04343	-.06159	-.02921	.00000	-.0127

A.

CASE FOR SHROUD ALONE

.00000	-.01170	1.0730	-.1514	.9604	.0777
.00000	-.01250	1.0606	-.1248	.9075	.1764
.00000	-.01280	1.0136	-.0274	.8723	.2392
.00000	-.01270	.9399	.1165	.8531	.2723

FIGURE 28C,
(SHEET 3 OF 3)

B.

7.0 COMPARISONS OF CALCULATIONS AND TESTS

7.1 INTRODUCTION

The T.A.R. theory, modified as discussed in the previous sections is now evaluated by comparing its predicted performance and pressure distributions with the test results of Phase I (Ref. 15). The discussion includes pertinent information on the test program and some comparisons of calculations and test for the isolated and shrouded propeller configurations. The shrouded propeller comparisons are made for a Mach number range of .05 to .5 for a variety of shroud and propeller geometries. Comparisons of propeller thrust, net thrust, shroud surface pressure distribution, propeller thrust derivatives, and axial velocities in the propeller plane are made. The net thrust evaluations are based on Methods 2 and 3 (paragraphs 6.3.3 and 6.3.4) for calculating inviscid thrust and the drag method using zero pressure gradient (paragraph 6.4.2). A discussion is also included with respect to the centerbody effect on performance.

7.2 DISCUSSION OF TEST DATA

A comprehensive wind tunnel test was conducted in the United Aircraft Research Laboratory's 18 foot low speed and 8 foot high speed tunnel facilities. A parametric series of 2.5 foot diameter shrouded propeller models were tested from near static velocities to a Mach number of 0.5 over a range of propeller power loadings and tip speeds. These models incorporated interchangeable shroud lips, exit sections and propellers so that the effect of a shape change in either shroud, propeller, or shroud-propeller combination could be examined.

The shroud shape variables investigated consisted of lip shape, area ratio, chord length, exterior shape, vanes, and propeller position within the shroud. The propeller shape variables included blade planform, number of blades, and tip clearance. One propeller was selected to investigate all the shroud variables and similarly, one shroud was selected to investigate all the propeller variables.

The shroud and propeller configurations are defined in Fig. 29 through 32. Fig. 29 shows the shroud shapes tested as well as the parameter variations. The parameters are defined as follows.

$$\text{Area Ratio } (A_4/A_2) = \frac{\text{Open Area at Shroud Exit}}{\text{Open Area at Propeller Plane}}$$

$$\text{Shroud Lip Shape} = \frac{\text{(Shroud Leading Edge Diameter)}}{\text{Propeller Diameter}} - 1$$

$$\text{Shroud Length } (\lambda) = \frac{\text{Shroud Reference Cylinder Length}}{\text{Shroud Reference Diameter}}$$

7.2 (Continued)

$$\text{Propeller Position } (\bar{X}p) = \frac{\text{Distance of Propeller } \text{℄} \text{ from Shroud Mid-chord}}{\text{Shroud Reference Cylinder Length}}$$

Fig. 30a defines the shroud thickness ratio distribution and Fig. 30b the shroud camber line slope distribution. As can be seen from Fig. 30a and 30b, the changes in area ratio resulted in simultaneous variations of the camber line and thickness forms. Fig. 31 shows the propeller blades tested and Fig. 32a and 32b the model blade sectional characteristics.

The wind tunnel test was undertaken as Phase I of contract NOw-64-0707-d. The results are reported in Ref. 15. Performance changes due to the various parameters are presented. Since some of the parameter presentation nomenclature of Phase I was changed in Phase III, the nomenclature for Phases I and III are included in Fig. 33 for correlation between this report and Ref. 15. The parameters for shroud length, propeller position and tip clearance have been changed to be compatible with the computational procedure. Since some of the Phase III parameters have been previously defined, the list will be completed with the following definitions:

$$\text{Propeller Tip Clearance } (\mu) = \frac{\text{Propeller Diameter}}{\text{Shroud Reference Diameter}}$$

$$\text{Propeller Planform} = \frac{\text{Blade Tip Chord}}{\text{Propeller Diameter}}$$

The Phase I definitions can be obtained from Ref. 15 if required.

7.3 PERFORMANCE COMPARISONS - ISOLATED PROPELLER

As part of the Phase I test program, a limited amount of test data was obtained for the isolated propeller for Mach numbers of .05, .1 and .2. Fig. 34 shows the comparison of calculations and tests for propeller thrust coefficients for the Mach number range. The computations were made for the corresponding test power coefficients also shown in Fig. 34. The excellent agreement is another example of the favorable comparisons of calculations and test obtained by using a computational procedure based on the Goldstein propeller theory.

7.4 PERFORMANCE COMPARISONS SHROUDED PROPELLER

7.4.1 Introduction

Comparison of calculations and Phase I test results have been made to establish the validity of the computational procedure. Pertinent shroud and propeller parameters required for the computations are listed in Fig. 35. The discussion is divided into two categories. The first accounts for variations in performance due to what are

HAMILTON STANDARD SHROUDED PROPELLER TEST
SHROUD SHAPES

NOTATION	PARAMETER VARIATIONS				
EXTERIOR SHAPE	AREA RATIO	SHROUD LIP SHAPE	SHROUD LENGTH λ	PROPELLER POSITION $\overline{X}_P$	EXTERNAL SHAPE
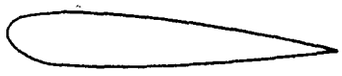 B1	1.1	0.133	0.607	−0.1023	X
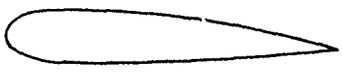 B2		0.172			
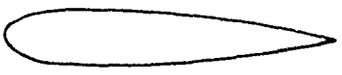 B3	1.2				
B4	1.3				
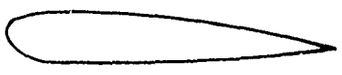 B5				−0.2528	
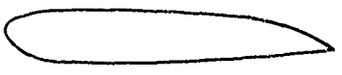 B6					X
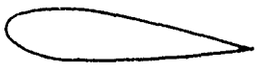 B7			0.456		

FIGURE 29.

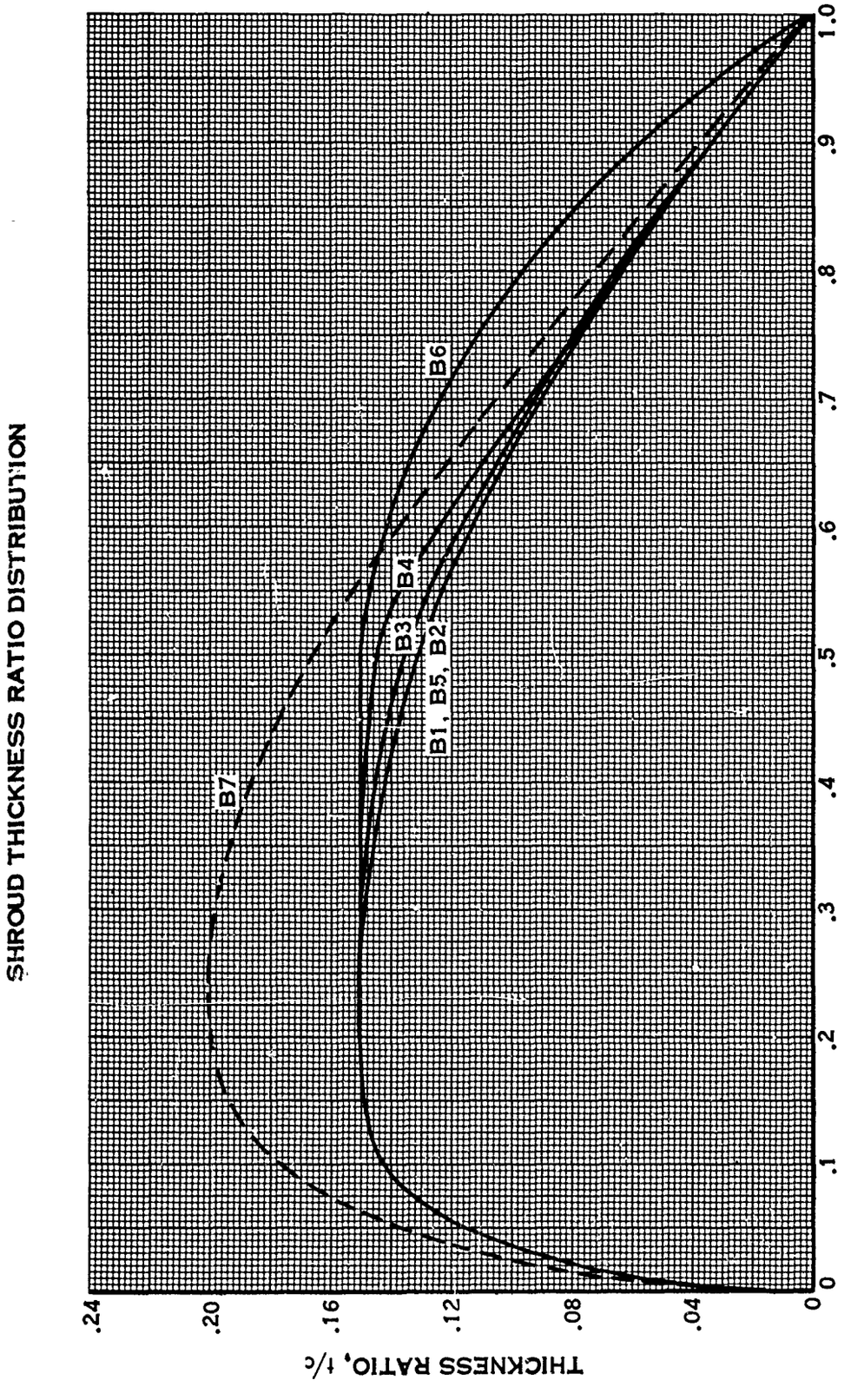
SHROUD THICKNESS RATIO DISTRIBUTION
B7
B6
B4
B3
B1, B5, B2
.24
.20
.16
.12
.08
.04
0
THICKNESS RATIO, t/c
0
.1
.2
.3
.4
.5
.6
.7
.8
.9
1.0
PERCENT OF CHORD, X/C

FIGURE 30A.

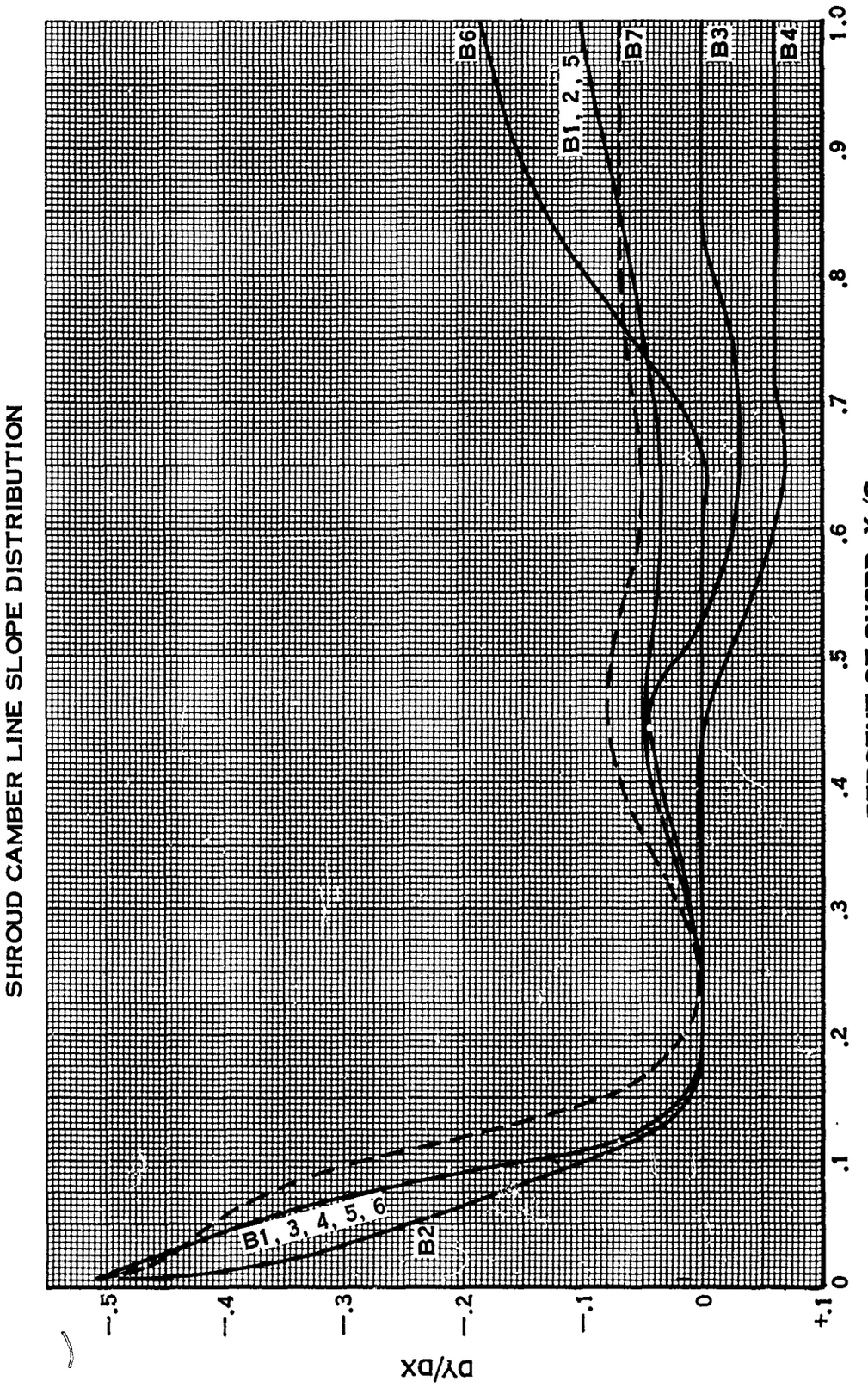
SHROUD CAMBER LINE SLOPE DISTRIBUTION
B6
B1, 2, 5
B7
B3
B4
B1, 3, 4, 5, 6
B2
1.0
.9
.8
.7
.6
.5
.4
.3
.2
.1
0
+.1
−.1
−.2
−.3
−.4
−.5
dY/dX
PERCENT OF CHORD, X/C

FIGURE 30B.

PROPELLER TEST BLADES

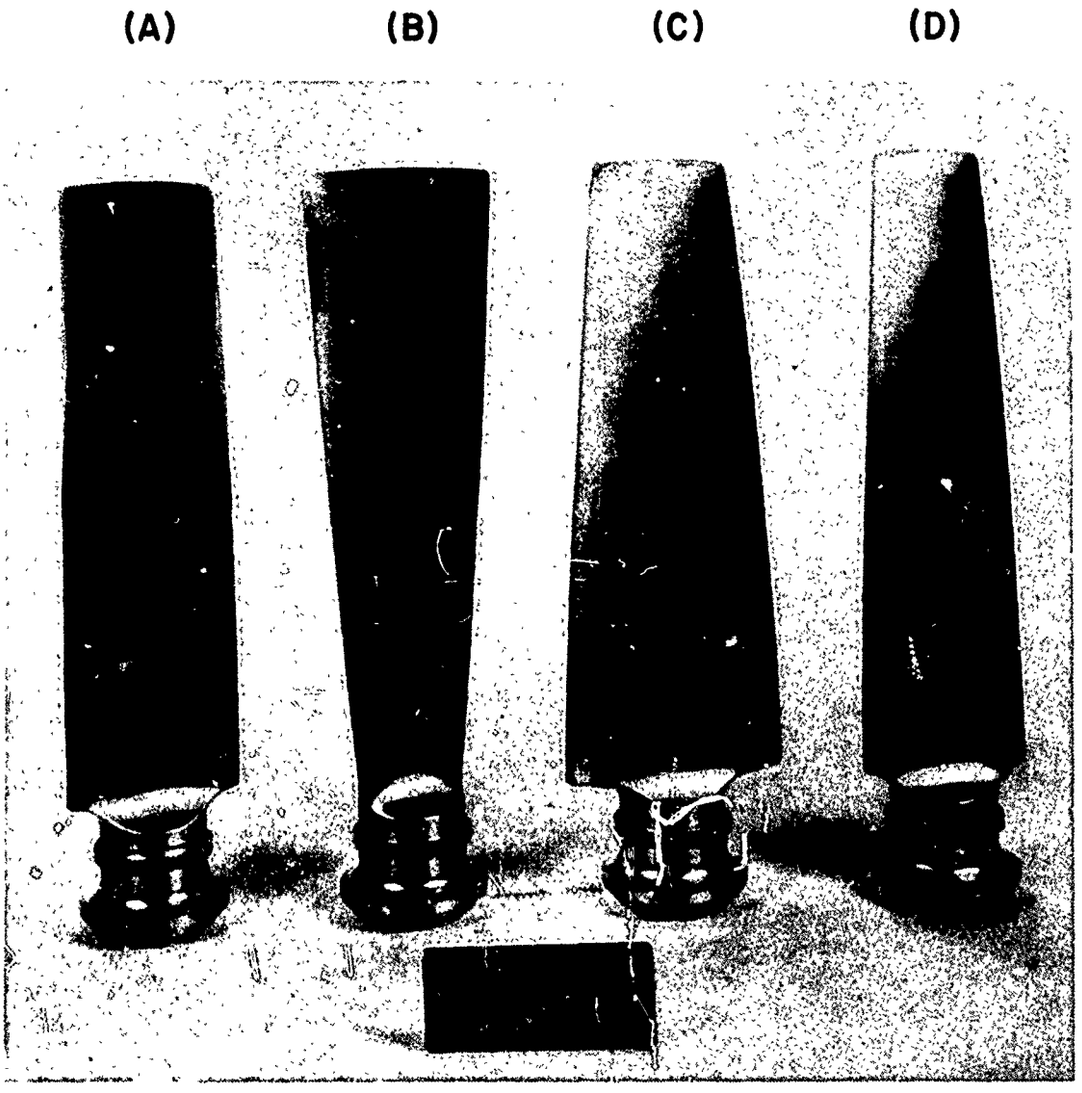

FIGURE 31.

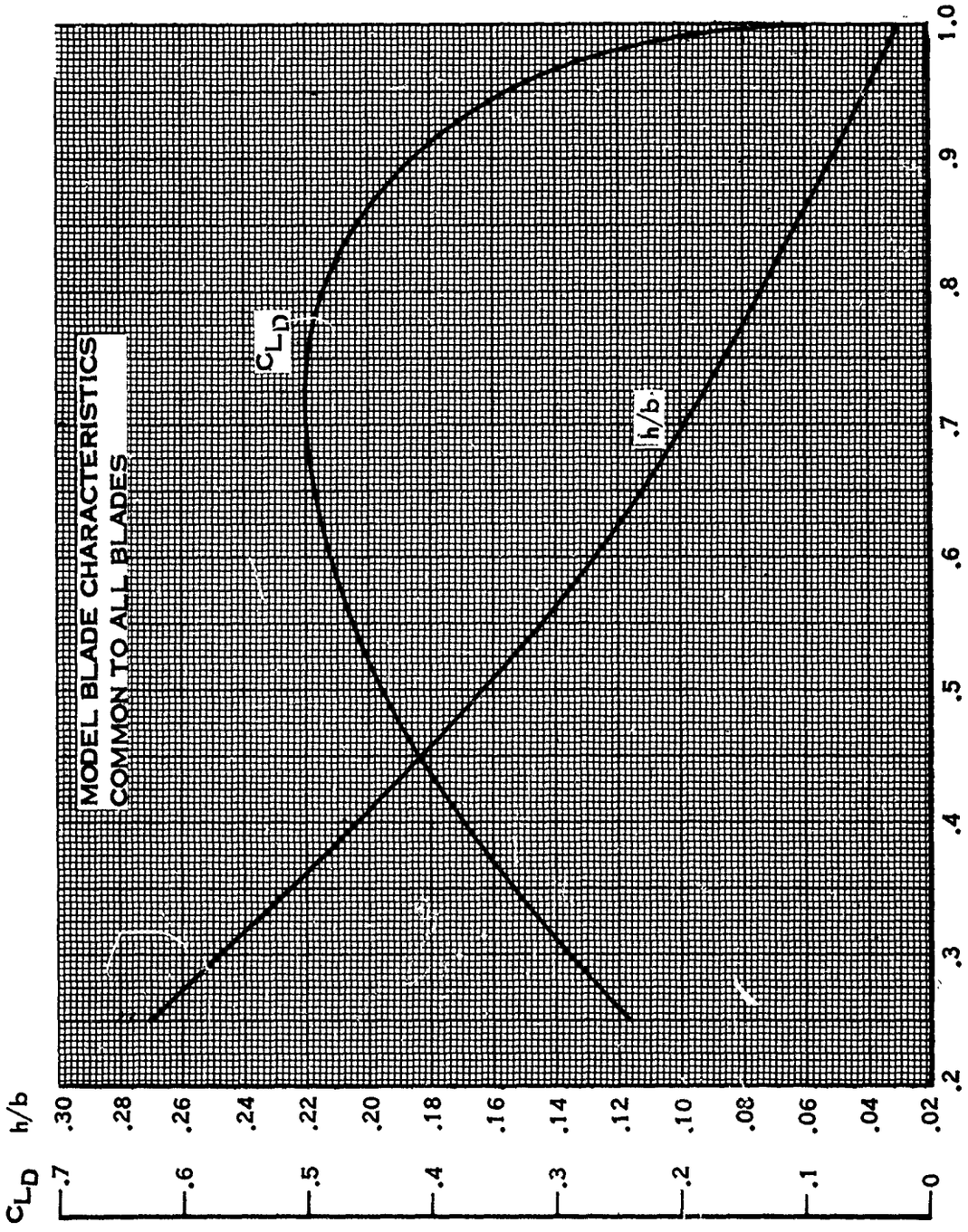
MODEL BLADE CHARACTERISTICS
COMMON TO ALL BLADES
C_{L_D}
h/b
C_{L_D} .7 .6 .5 .4 .3 .2 .1 0
h/b .30 .28 .26 .24 .22 .20 .18 .16 .14 .12 .10 .08 .06 .04 .02
.2 .3 .4 .5 .6 .7 .8 .9 1.0
X PROPELLER

FIGURE 32A.

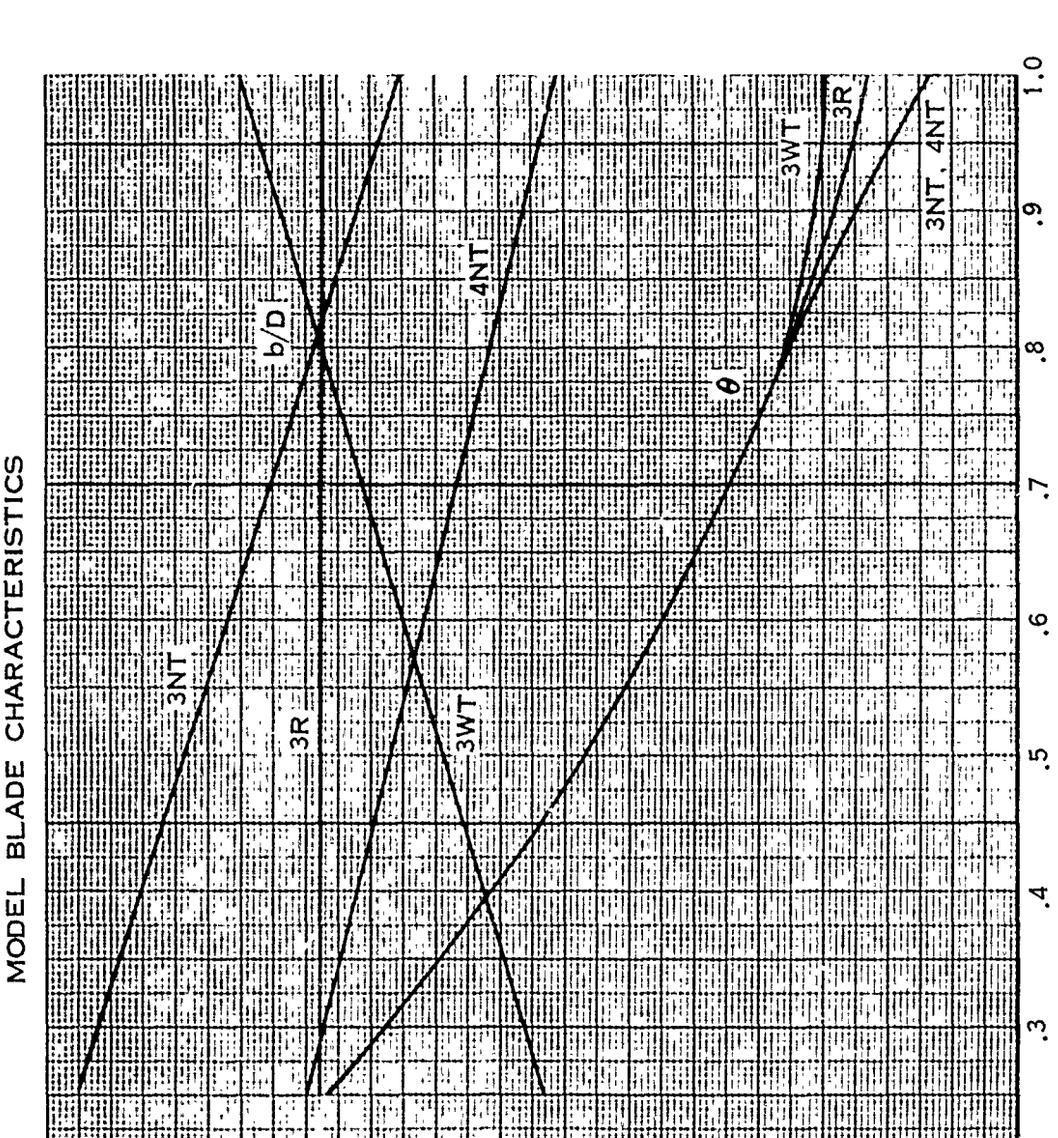
MODEL BLADE CHARACTERISTICS
b/D
θ
.14
.12
.10
.08
.06
.04
.02
0
50
40
30
20
10
0
−10
−20
.2
.3
.4
.5
.6
.7
.8
.9
1.0
3NT
3R
3WT
4NT
b/D
θ
3WT
3R
3NT, 4NT
X PROPELLER

FIGURE 32B.

NOMENCLATURE COORDINATION

PARAMETER	PHASE I NOTATION	PHASE III NOTATION
AREA RATIO	AREA RATIO A_4/A_2 B1 — 3WT 1.1 B3 — 3WT 1.2 B4 — 3WT 1.3	SAME AS PHASE I
SHROUD LIP SHAPE	$\left(\frac{\text{SHROUD LEADING EDGE DIAMETER}}{\text{PROPELLER DIAMETER}}\right)-1$ B1—3WT .133 B2—3WT .172	SAME AS PHASE I
SHROUD LENGTH	SHROUD LENGTH B1 — 3NT .667 B7 — 3NT .500	λ B1 — 3NT .607 B7 — 3NT .456
PROPELLER POSITION	PROPELLER POSITION B1 — 3WT .40 B5 — 3WT .25	$\overline{X}_P$ B1 — 3WT —.1023 B5 — 3WT —.2528
PROPELLER TIP CLEARANCE	TIP CLEARANCE B1 — 3R .00119 B1 — 3R1/2M .00259 B1 — 3RM .00559	μ B1 — 3R .911 B1 — 3R1/2M .909 B1 — 3RM .903
PROPELLER PLANFORM	$\left(\frac{\text{BLADE TIP CHORD}}{\text{PROPELLER DIAMETER}}\right)$ B1 — 3NT .0949 B1 — 3R .1077 B1 — 3WT .1198	SAME AS PHASE I
NUMBER OF BLADES	NUMBER OF BLADES B1 — 3NT 3 B1 — 4NT 4	SAME AS PHASE I

FIGURE 33.

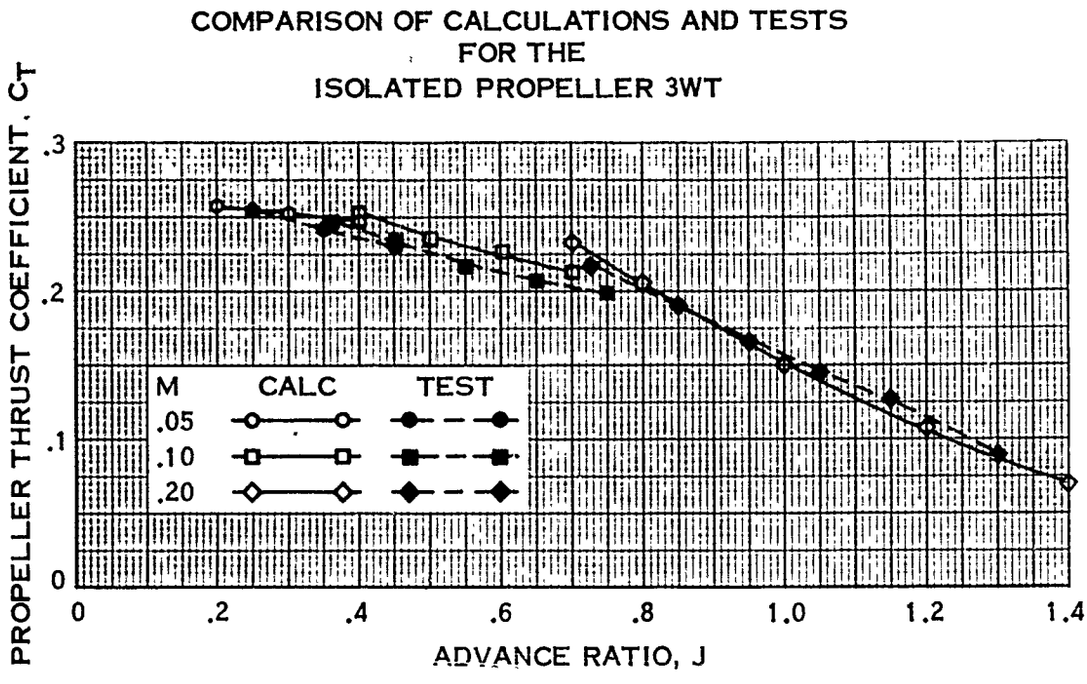
COMPARISON OF CALCULATIONS AND TESTS
FOR THE
ISOLATED PROPELLER 3WT
PROPELLER THRUST COEFFICIENT, C_T
.3
.2
.1
0
M
CALC
TEST
.05
.10
.20
0
.2
.4
.6
.8
1.0
1.2
1.4
ADVANCE RATIO, J

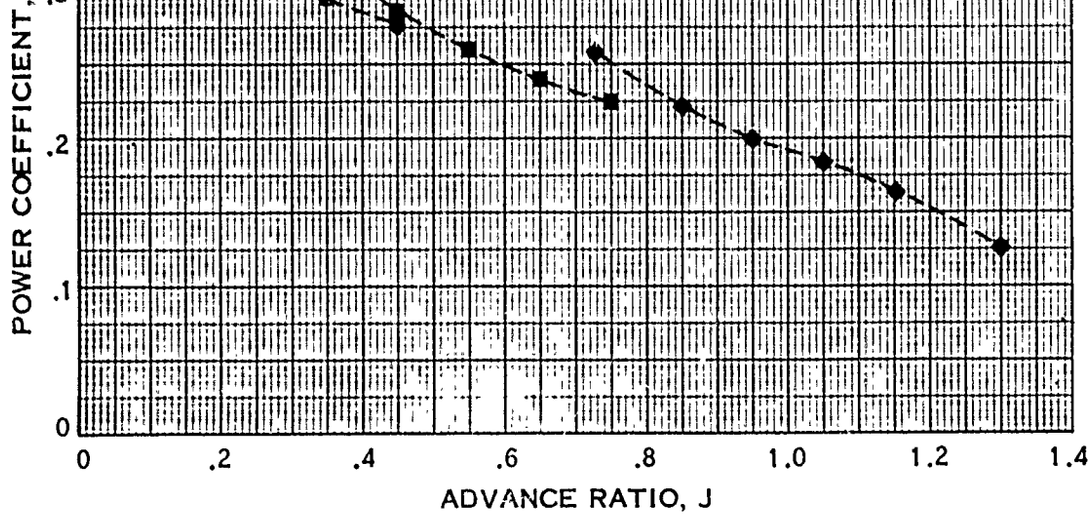
POWER COEFFICIENT, C_P
.4
.3
.2
.1
0
0
.2
.4
.6
.8
1.0
1.2
1.4
ADVANCE RATIO, J

FIGURE 34.

SIGNIFICANT SHROUD AND PROPELLER PARAMETERS

CONFIGURATION	SHROUD * DIAMETER FEET	SHROUD ** REFERENCE DIAMETER FEET	λ	$\overline{X_P}$	μ	A_4/A_2	PROPELLER DIAMETER FEET	NUMBER OF BLADES	AF/BLADE	INTE-GRATED DESIGN C_L
B1—3WT	2.5	2.737	.607	—.1023	.911	1.1	2.494	3	168	.400
B1—3NT	2.5	2.737	.607	—.1023	.911	1.1	2.494	3	168	.400
B1—3R	2.5	2.737	.607	—.1023	.911	1.1	2.494	3	168	.400
B1—4NT	2.5	2.737	.607	—.1023	.911	1.1	2.494	4	126	.400
B1—3R1/2M	2.5	2.737	.607	—.1023	.909	1.1	2.487	3	168	.400
B1—3RM	2.5	2.737	.607	—.1023	.903	1.1	2.472	3	168	.400
B2—3WT	2.5	2.737	.6075	—.1028	.911	1.1	2.494	3	168	.400
B3—3WT	2.5	2.739	.606	—.1023	.910	1.2	2.494	3	168	.400
B4—3WT	2.5	2.747	.605	—.1023	.968	1.3	2.494	3	168	.400
B5—3WT	2.5	2.750	.604	—.2528	.907	1.1	2.494	3	168	.400
B6—3WT	2.5	2.750	.604	—.1023	.907	1.1	2.494	3	168	.400
B7—3WT	2.5	2.729	.456	—.1040	.913	1.1	2.494	3	168	.400

*INNER SURFACE SHROUD DIAMETER
**MEAN CAMBER LINE SHROUD DIAMETER

FIGURE 35.

7.4.1 (Continued)

defined as primary parameters. The second accounts for variations due to secondary parameters. It is interesting to note these catagories generally are associated with aerodynamic and geometric variables respectively. The primary parameters are:

1. Power coefficient, Cp
2. Advance ratio, J = f (Mach no. and tip speed)
3. Area ratio

The secondary parameters are:

1. External shroud shape
2. Lip shape
3. Shroud length
4. Propeller position in shroud
5. Propeller planform
6. Number of blades
7. Tip clearance

7.4.2 Shroud Pressure Distribution Comparisons

In this section, the effects of the primary parameters on shroud pressure distribution will be evaluated. The changes due to changes of the secondary parameters are negligible. The primary parameters considered in the performance evaluation are power coefficient, area ratio and Mach number, for a propeller rotative speed of 6000 RPM (tip speed of 785 ft/sec). The pressure distribution comparisons will be made at 5500 RPM (tip speed of 720 ft/sec) since most of the pressure measurements were taken at this speed. Comparisons of pressure distributions will account for Mach number variation, power coefficient variation and area ratio variation, all for the 5500 RPM case. In addition, the effect of a rotative speed change for a given Mach number, area ratio and power coefficient will be investigated. The area ratio 1.1 shroud will be used to evaluate the effects of changes in power coefficient, rotative speed and Mach number. The variations due to area ratio will be based on the 1.1 and 1.3 area ratio shrouds. All the pressure distributions discussed in this section have been corrected by application of the Riegels factor.

7.4.2a Power Coefficient

The variation of pressure distribution due to changes in power coefficient for the 1.1 area ratio shroud is shown in Fig. 36a and 36b for a Mach number of .3. The M = .5 case is similar and will not be discussed.

Two interesting features are exhibited by both the theoretical curves and the test data.

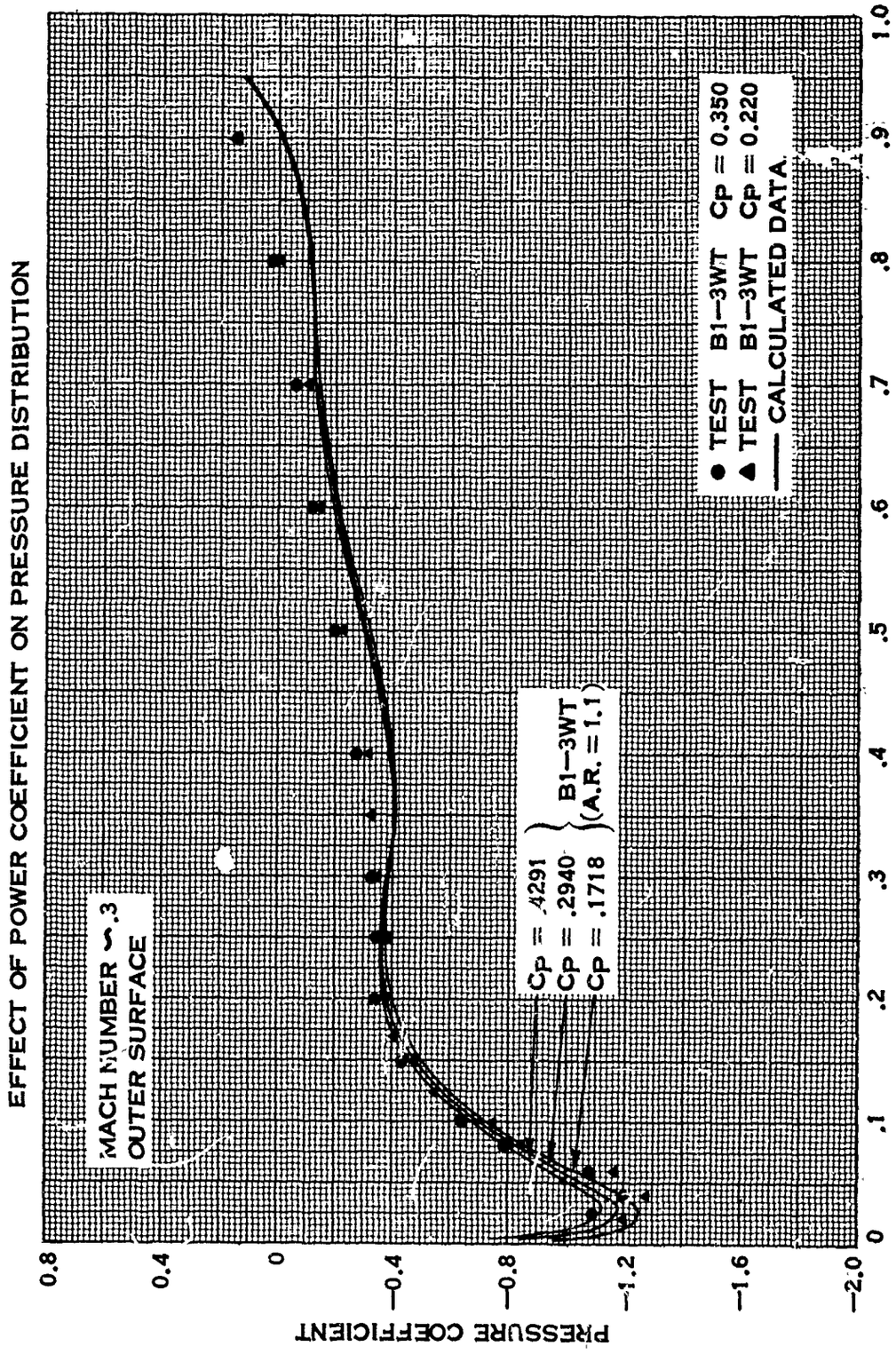
EFFECT OF POWER COEFFICIENT ON PRESSURE DISTRIBUTION
MACH NUMBER = .3
OUTER SURFACE
Cp = .4291
Cp = .2940
Cp = .1718
B1—3WT
(A.R. = 1.1)
● TEST B1—3WT Cp = 0.350
▲ TEST B1—3WT Cp = 0.220
—— CALCULATED DATA
PRESSURE COEFFICIENT
0.8
0.4
0
−0.4
−0.8
−1.2
−1.6
−2.0
0
.1
.2
.3
.4
.5
.6
.7
.8
.9
1.0
PERCENTAGE OF CHORD, X/C

FIGURE 36A.

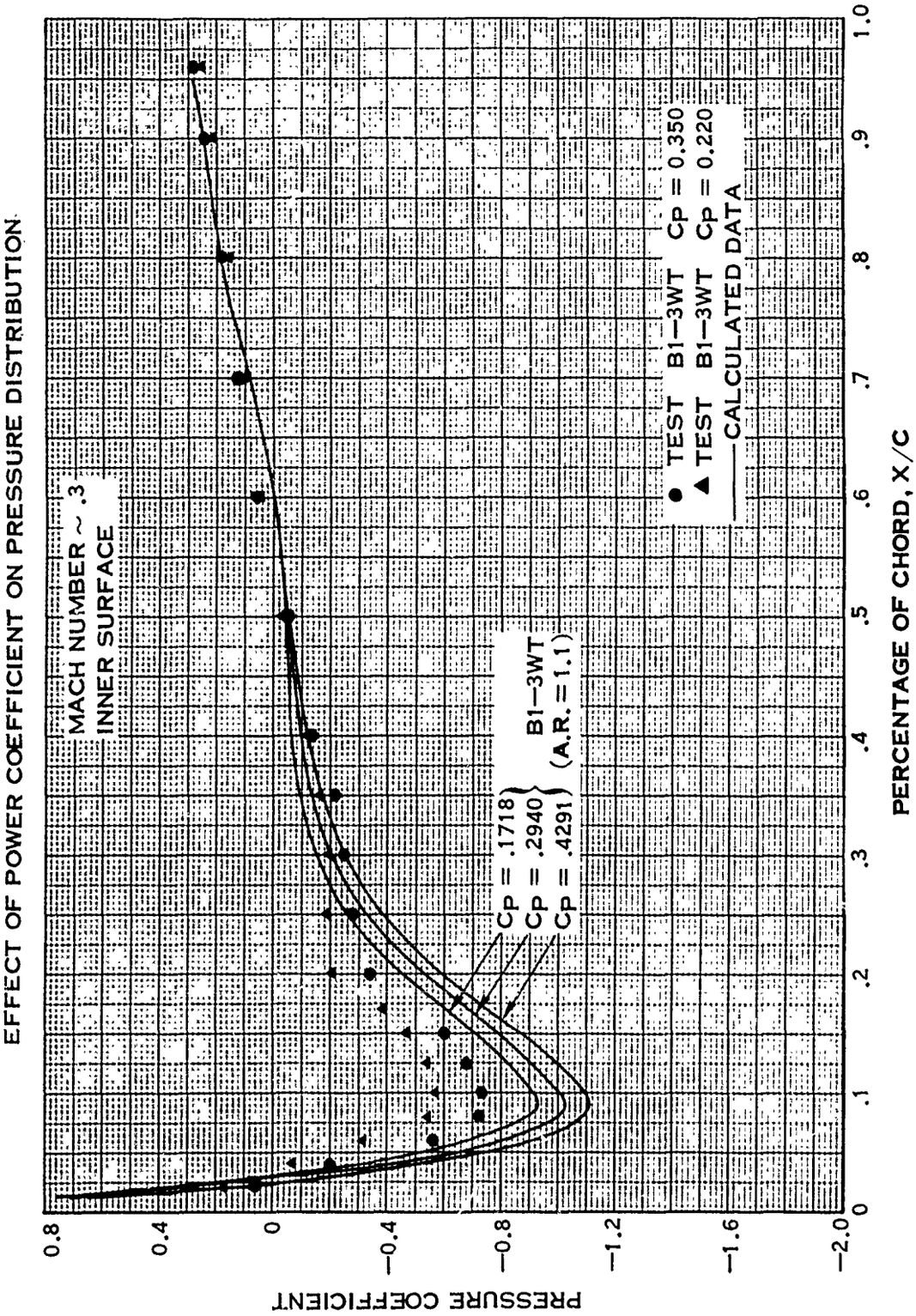
EFFECT OF POWER COEFFICIENT ON PRESSURE DISTRIBUTION
MACH NUMBER ~ .3
INNER SURFACE
B1—3WT (A.R. = 1.1)
Cp = .1718
Cp = .2940
Cp = .4291
● TEST B1—3WT Cp = 0.350
▲ TEST B1—3WT Cp = 0.220
——— CALCULATED DATA
PRESSURE COEFFICIENT
0.8
0.4
0
−0.4
−0.8
−1.2
−1.6
−2.0
0
.1
.2
.3
.4
.5
.6
.7
.8
.9
1.0
PERCENTAGE OF CHORD, X/C

FIGURE 36B.

7.4.2a (Continued)

1. The effect of power coefficient is most pronounced near the leading edge, with the higher power coefficient resulting in the more negative pressure coefficient.

2. From the mid-chord station to the trailing edge there is no significant effect of power coefficient, indicating the propeller influence on pressure in this region is negligible.

From these features it can be concluded that the theory predicts the effect of the propeller in a qualitative sense. The discrepancy between test and theory in the forward half of the shroud is probably due to the errors in the calculated velocity distribution along the shroud reference cylinder for both the shroud and propeller. However, for the downstream half of the shroud, where the propeller effect is negligible, discrepancies between test and theory must be due to the shroud velocity field only. In addition, the assumptions of the theory near the leading edge are violated, forcing the use of the Riegels correction. Since this correction is based on an elliptic nose shape, some of the deviations can be attributed to the nonelliptic nose shape of the shroud. In the downstream region of the shroud where the theory is expected to be applicable, the agreement is quite good.

7.4.2b Area Ratio

The area ratio variation is shown for the 1.1 (B1) and 1.3 area ratio (B4) shrouds in Fig. 4 and 5 for M = .3 and tip speed = 720 ft/sec. The test power coefficient is .35 for the 1.1 area ratio and .352 for the 1.3. The theoretical curves are for the range of Cp's indicated. The Cp effect discussed above is again observed. The area ratio effect is qualitatively predicted by the theory with very good agreement for the downstream portion of the shroud where the effect of propeller power coefficient is small. The effect in the leading edge region is qualitatively predicted, the discrepancies being of the form discussed in the section above.

7.4.2c Rotative Speed

In order to investigate the effect of rotative speed on performance, the test data for the 1.1 area ratio shroud at M = .3 was cross plotted to yield the inner surface pressure coefficient variation at two values of rotative speed for a constant power coefficient. The rotative speeds correspond to J's of 1.845 and 1.455, both for a power coefficient of .235. Corresponding theoretical cases are compared to the test results in Fig. 37. As was the case for the C_p variation, the effect of J on the pressure coefficient is negligible from the mid-chord of the shroud to the trailing edge. The agreement between test and theory is very good in this region. In the vicinity of the leading edge the theoretical method predicts a more negative pressure coefficient, but the trend with J is correct. The discrepancy can be due to the inaccuracies inherent in the theoretically predicted shroud velocity distribution near the leading edge and/or inaccuracies in the propeller induced velocities.

EFFECT OF TIP SPEED ON PRESSURE COEFFICIENT

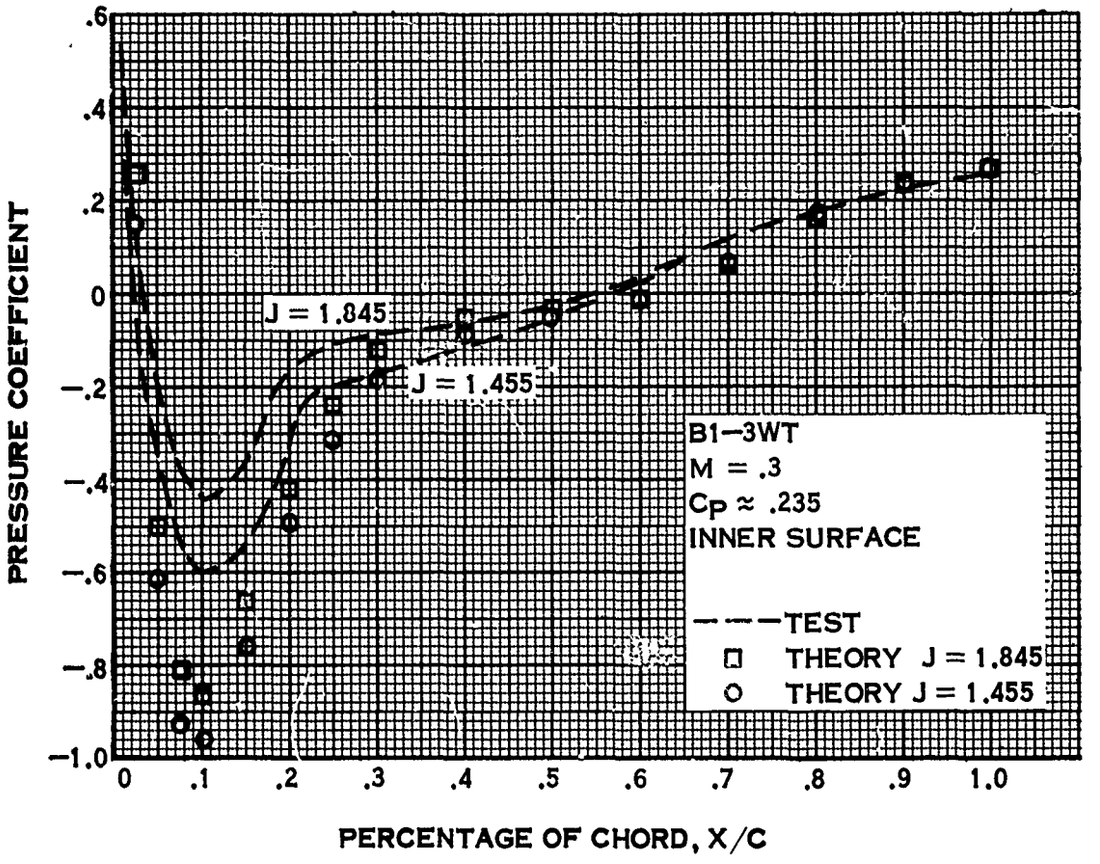

FIGURE 37.

7.4.2d Effect of Mach Number

In this paragraph the effect of Mach number on pressure distribution is investigated for B1-3WT and B4-3WT with tip speed = 720 ft/sec. Varying the Mach number at a constant rotative speed varies the effects of compressibility as well as the forward flight speed, thereby varying the ratio of the perturbation velocity to free stream velocity, U/V_o. At Mach numbers of .3 or higher, the perturbation to free stream velocity ratio is small, and the effect of Mach number change is primarily compressibility. This aspect has been discussed in paragraph 6.2.3 where it was shown that the pressure distributions are well predicted for both M = .3 and M = .5, i.e., see Fig. 4 through 7. Lowering the Mach number below about .3, on the other hand, has the effect of increasing U/V_o, whereas the compressibility changes become negligible. It is this latter effect which is discussed in the following.

Fig. 38 and 39 show comparisons of theoretical and experimental inner surface pressure distributions for the 1.1 and 1.3 area ratio shrouds at M = .05. In paragraph 6.2.5 three improvements to the theory were discussed; the use of J_2' instead of J_o', the use of the Goodman tip correction to the flow field of the propeller wake and the first order correction to the shroud camber line boundary condition. The effect of these corrections is considered in the following for M = .05.

Both the B1-3WT and the B4-3WT comparisons show that the experimental pressure coefficients are much more negative than the theoretically predicted ones. In addition, the various corrections did not improve the comparison. The Goodman tip correction had a negligible effect and is not shown.

The first order correction to the shroud camber line boundary condition had a very small effect on the pressure distribution. This was caused by the shapes of the shroud camber line correction and the shroud camber line slope. The first order correction for the B1-3WT is shown in Fig. 40. The corrected and uncorrected shroud camber lines are shown in Fig. 41. The correction is largest in magnitude over the leading half of the shroud. The camber line slope, however, is such that it is largest in the region $0. \leq \frac{X}{C} \leq .2$. Thus, the significant changes in camber line slope occur near the leading edge of the shroud ($0 \leq \frac{X}{C} \leq .1$). This correction then manifests itself as a significant alteration to the shroud vorticity distribution in the leading edge region (as shown in Fig. 42 for B1-3WT) where its effect on the pressure coefficient is greatly diminished by application of the Riegels factor. The effect is similar for the B4-3WT.

It is hard to ascertain whether the small effect noted above of the first order correction to shroud camber is uniquely related to the particular camber line slopes used in this program. Should a camber line be used which exhibits large slopes in the mid-chord region, the above conclusions could be changed. It is therefore recommended that this correction be investigated whenever the program is used for camber lines which deviate significantly from those used in this report (shown in Fig. 30b). This is easily accomplished since the continuous axial velocity at the shroud

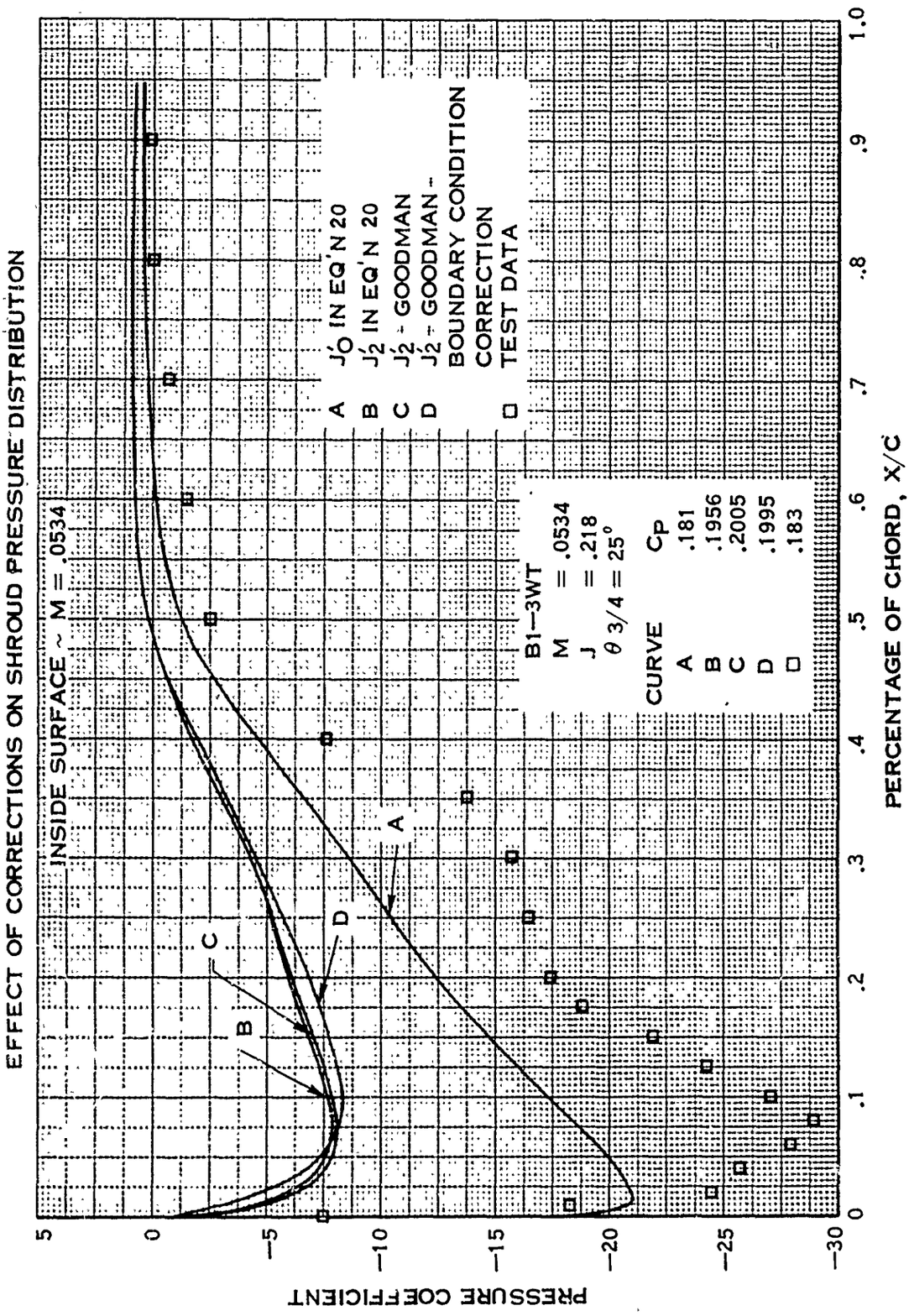
EFFECT OF CORRECTIONS ON SHROUD PRESSURE DISTRIBUTION
INSIDE SURFACE ~ M = .0534
A J'0 IN EQ'N 20
B J'2 IN EQ'N 20
C J'2 - GOODMAN
D J'2 - GOODMAN - BOUNDARY CONDITION CORRECTION
□ TEST DATA
B1—3WT
M = .0534
J = .218
θ 3/4 = 25°
CURVE Cp
A .181
B .1956
C .2005
D .1995
□ .183
PRESSURE COEFFICIENT
5
0
—5
—10
—15
—20
—25
—30
0
.1
.2
.3
.4
.5
.6
.7
.8
.9
1.0
PERCENTAGE OF CHORD, X/C

FIGURE 38.

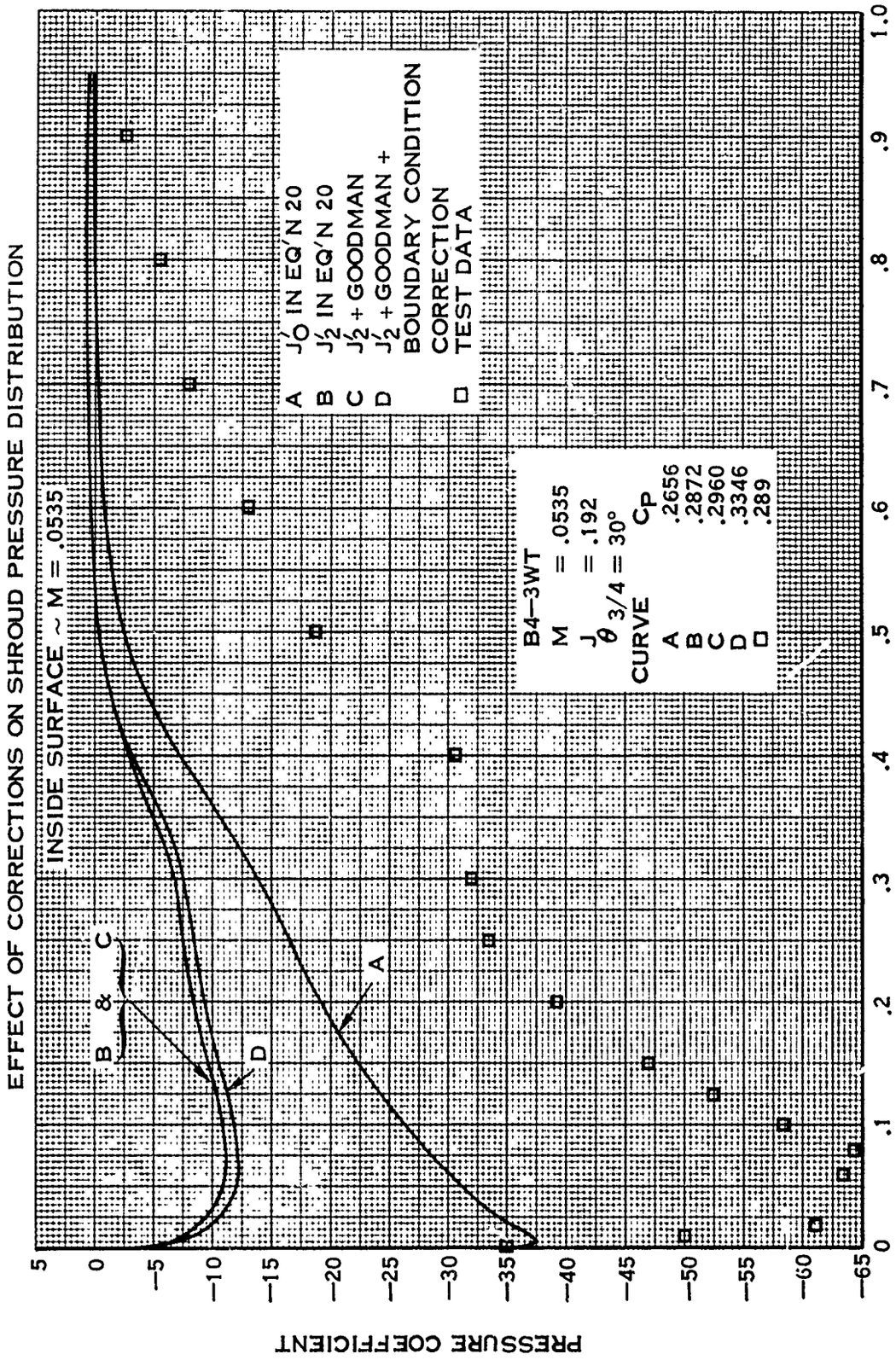
EFFECT OF CORRECTIONS ON SHROUD PRESSURE DISTRIBUTION
INSIDE SURFACE ~ M = .0535
B4—3WT
M = .0535
J = .192
θ 3/4 = 30°
CURVE Cp
A .2656
B .2872
C .2960
D .3346
□ .289
A J'O IN EQ'N 20
B J'½ IN EQ'N 20
C J'½ + GOODMAN
D J'½ + GOODMAN + BOUNDARY CONDITION CORRECTION
□ TEST DATA
PRESSURE COEFFICIENT
5 0 −5 −10 −15 −20 −25 −30 −35 −40 −45 −50 −55 −60 −65
0 .1 .2 .3 .4 .5 .6 .7 .8 .9 1.0
PERCENTAGE OF CHORD, X/C

FIGURE 39.

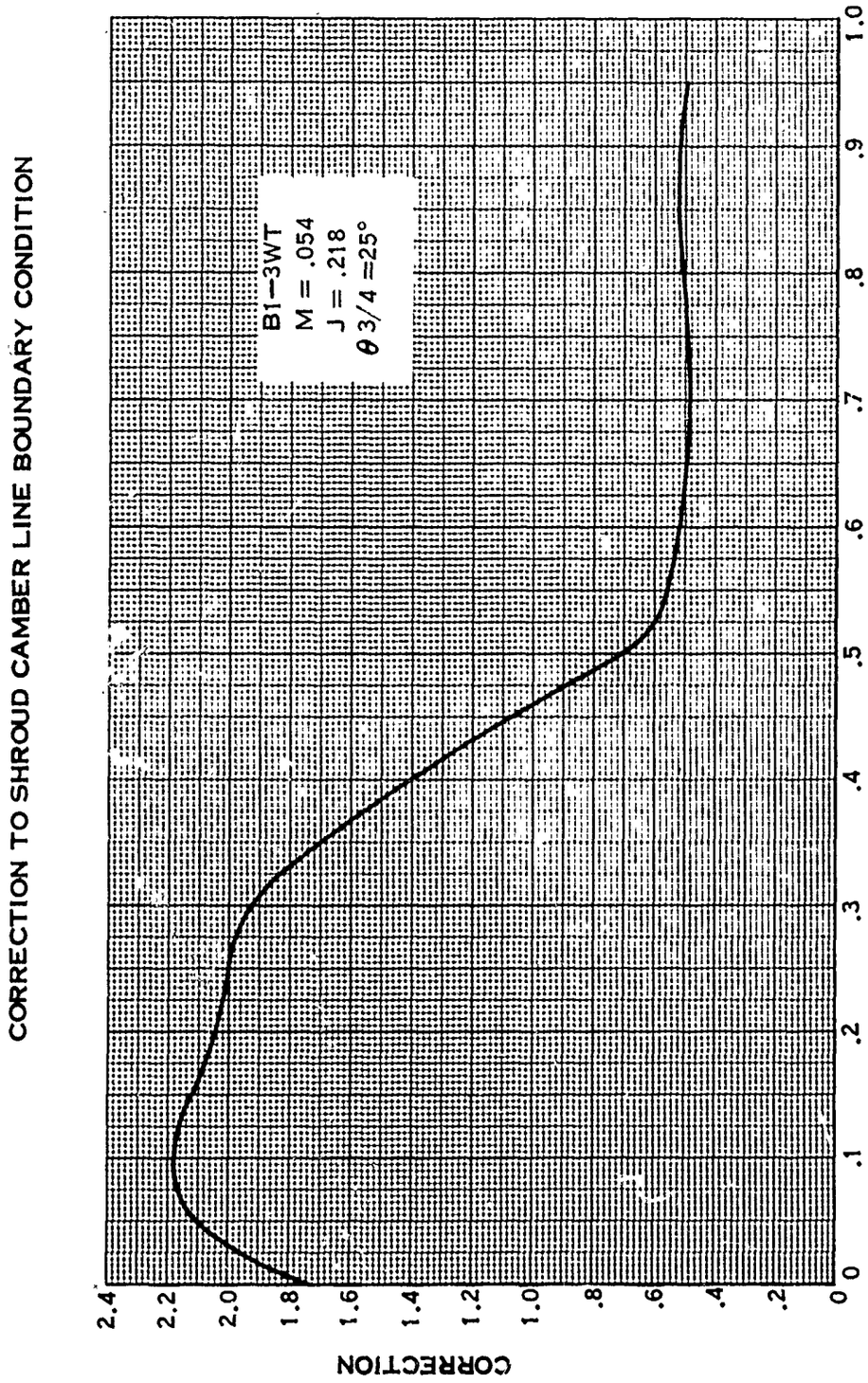
CORRECTION TO SHROUD CAMBER LINE BOUNDARY CONDITION
B1—3WT
M = .054
J = .218
θ 3/4 =25°
CORRECTION
2.4
2.2
2.0
1.8
1.6
1.4
1.2
1.0
.8
.6
.4
.2
0
.1
.2
.3
.4
.5
.6
.7
.8
.9
1.0
PERCENTAGE OF CHORD, X/C

FIGURE 40.

COMPARISON OF GEOMETRIC & CORRECTED CAMBER LINE SLOPE

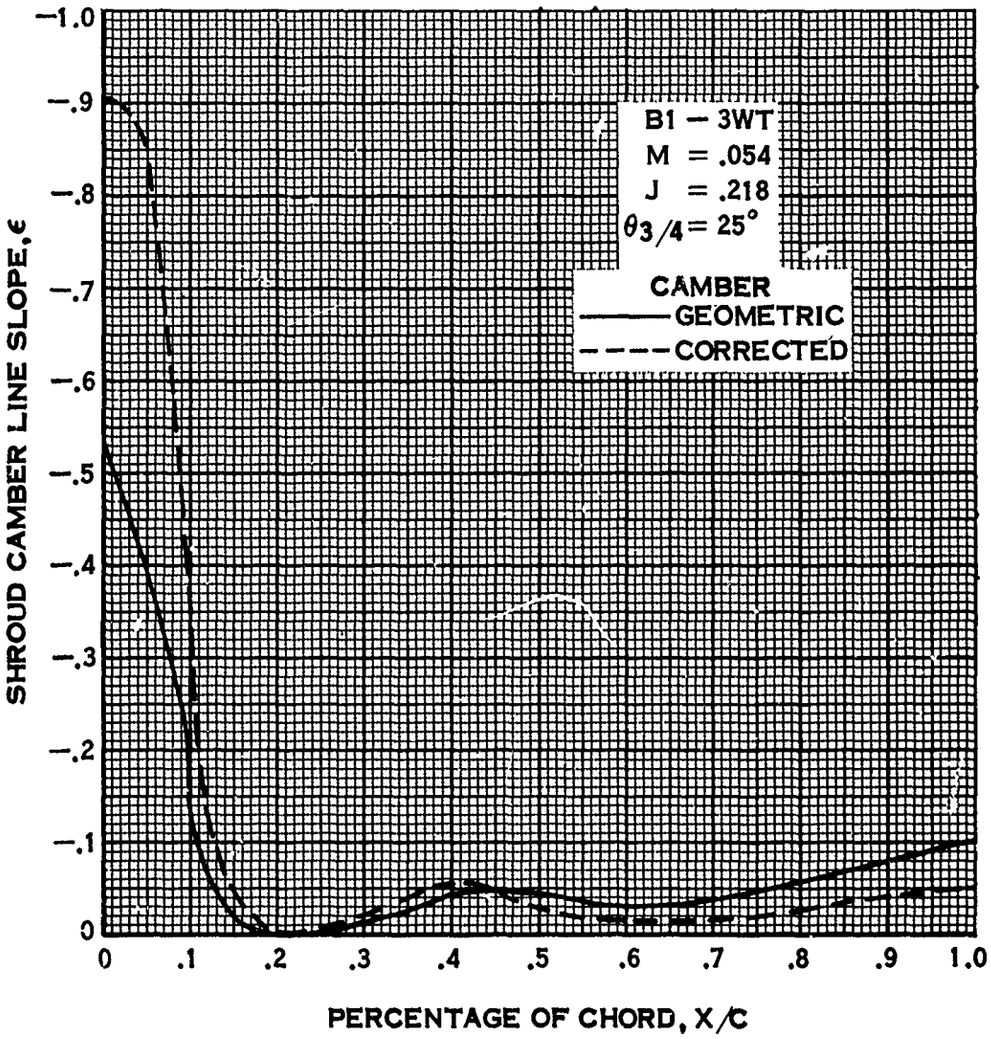

FIGURE 41.

SHROUD VORTICITY DISTRIBUTION COMPARISON

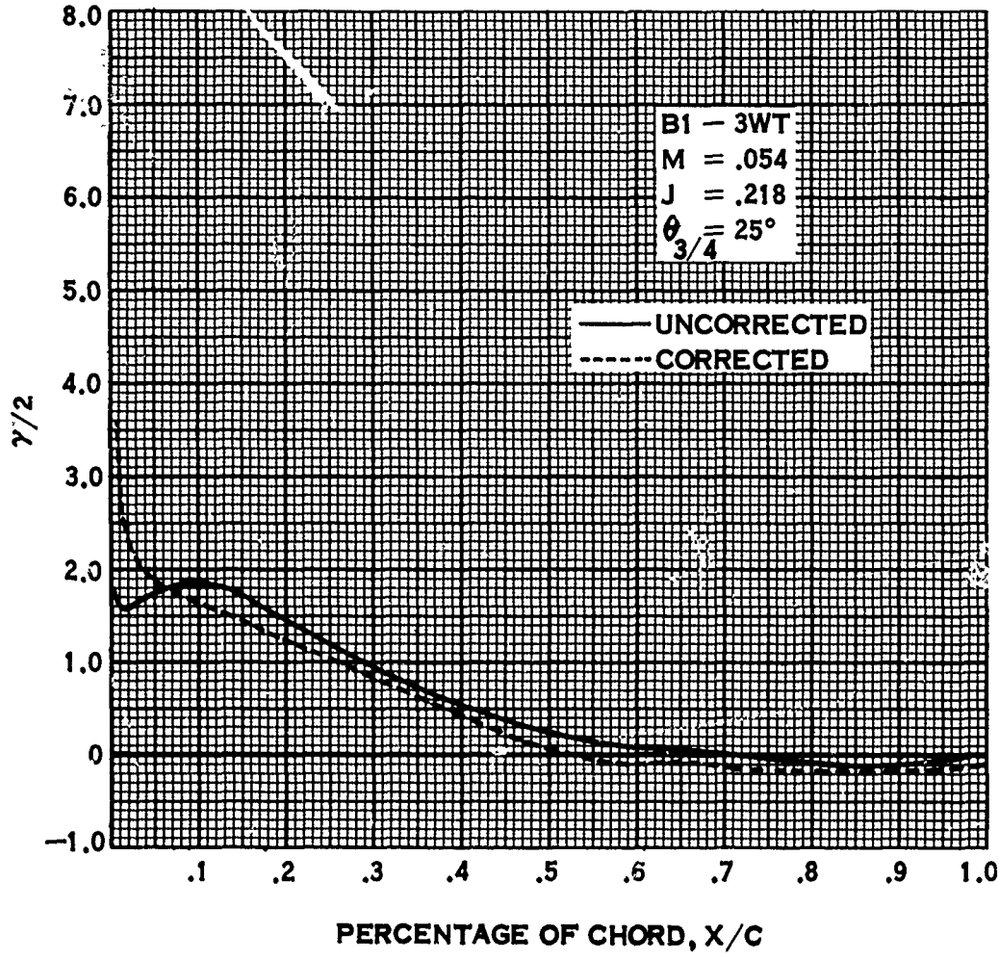

FIGURE 42.

7.4.2d (Continued)

reference cylinder is available from the program print out. The procedure for deriving the correction is given in paragraph 6.2.5e.

Future efforts in improving the shrouded propeller prediction method should include an evaluation of this correction for a range of camber lines which are likely to be met in practice.

The largest changes were caused by the use of J'_2 instead of J'_0 in Eq. (20). Unfortunately, use of the theoretically more accurate J'_2 caused the pressure coefficient to become less negative, thereby worsening the agreement between test and theory. At first glance this would indicate that the propeller contribution to shroud pressure distribution is being predicted incorrectly. However, at these low Mach numbers, other portions of the theory are also questionable, for example, the method in which the shroud thickness form is represented. To further investigate this effect, an estimate of the actual shroud thickness form consistent with the specified source-sink distribution was made for the M = 0.05 case. It will be recalled that the source-sink distribution was obtained from the specified shroud thickness form, subject to the assumption that $U \angle\angle V_0$. At M = 0.05, this is not the case. Invalidation of this assumption but use of the source-sink distribution derived subject to this assumption manifests itself in the use of a shroud thickness which deviates significantly from the specified thickness. An estimate of this "utilized" shape or thickness form can be made by subtracting Eq. (23b) from (23a) and following an analysis which parallels the derivation of the correction to the shroud camber line boundary condition contained in paragraph 6.2.5e. This analysis leads to a similar first order correction to the boundary condition on thickness which is shown below:

$$t' = \frac{\bar{V}_{rD}}{1 + \bar{U}_c} \tag{65}$$

where $\bar{V}_{rD}$ = the discontinuous portion of the radial velocity divided by V_0

$\bar{U}_c$ = continuous portion of the axial velocity divided by V_0

t' slope of the thickness form

In the forward flight regime, $\bar{U}_c \angle\angle 1$, Eq. (65) reduces to the form used in the method, i.e.,

$$t' = \bar{V}_{rD} \tag{66}$$

where $\bar{V}_{rD}$, being the discontinuous portion of the radial velocity, can be related directly to the source-sink distribution representing shroud thickness. Returning

7.4.2d (Continued)

to Eq. (65), the discontinuous part of the radial velocity, even at the lower Mach numbers, is known in terms of the shroud source-sink distribution, which is proportional to t'_{act} the actual or inputted shroud thickness form. The t' on the left side of Eq. (65) represents the shape actually utilized in the method, so

$$t'_{utilized} = t'_{act}(1 + \bar{U}_c)^{-1} \qquad (67)$$

The utilized thickness form can be obtained from the actual form through the use of Eq. (67) and the term $(1 + \bar{U}_c)$, the shroud camber line boundary condition correction, which is shown in Fig. 40 for the B1-3WT at M = 0.05.

The resulting utilized thickness form is shown in Fig. 43 along with the actual. Large differences exist, which in part account for the differences in pressure distribution observed. Qualitatively, the utilized form has a smaller leading edge radius and thickness in the leading edge region, which leads to smaller velocities and more positive pressure coefficients than actually exist. This is the effect exhibited by the comparisons of test and theory. Thus, the way in which shroud thickness is accounted for is invalid at the lower Mach numbers, and should be based on Eq. (65) instead of (66).

The use of Eq. (65) instead of Eq. (66) greatly complicates the mathematical solution of the problem. With Eq. (66), the discontinuous radial velocity $\bar{V}_{r\,D}$ is directly related to the source-sink distribution and therefore leads immediately to the specification of the source-sink strength as being proportional to the known thickness form. Use of Eq. (65) to obtain the source-sink distribution on the other hand is much more difficult. The source-sink distribution must now give rise to a distribution of $\bar{V}_{r\,D}$ along the shroud reference cylinder which when divided by $(1 + \bar{U}_c)$, results in the defined thickness form. In this case, there is no simple correlation between the source-sink distribution and the thickness form. In fact, the appearance of $(1 + \bar{U}_c)$ causes the source-sink distribution to depend not only on the thickness form, but also on the shroud vorticity distribution and propeller load through the dependance of $\bar{U}_c$ on these variables.

Due to the complete change in the nature by which the shroud source-sink distribution is calculated when Eq. (65) is considered, it was not possible to incorporate it into the program during this contract. It is recommended for consideration in future efforts aimed at extension of the method to the static and low flight speed regime, where the effect is most pronounced.

The variations in performance due to the three corrections for the low Mach number case used in the above pressure distribution evaluation are summarized below for the B1-3WT and the B4-3WT:

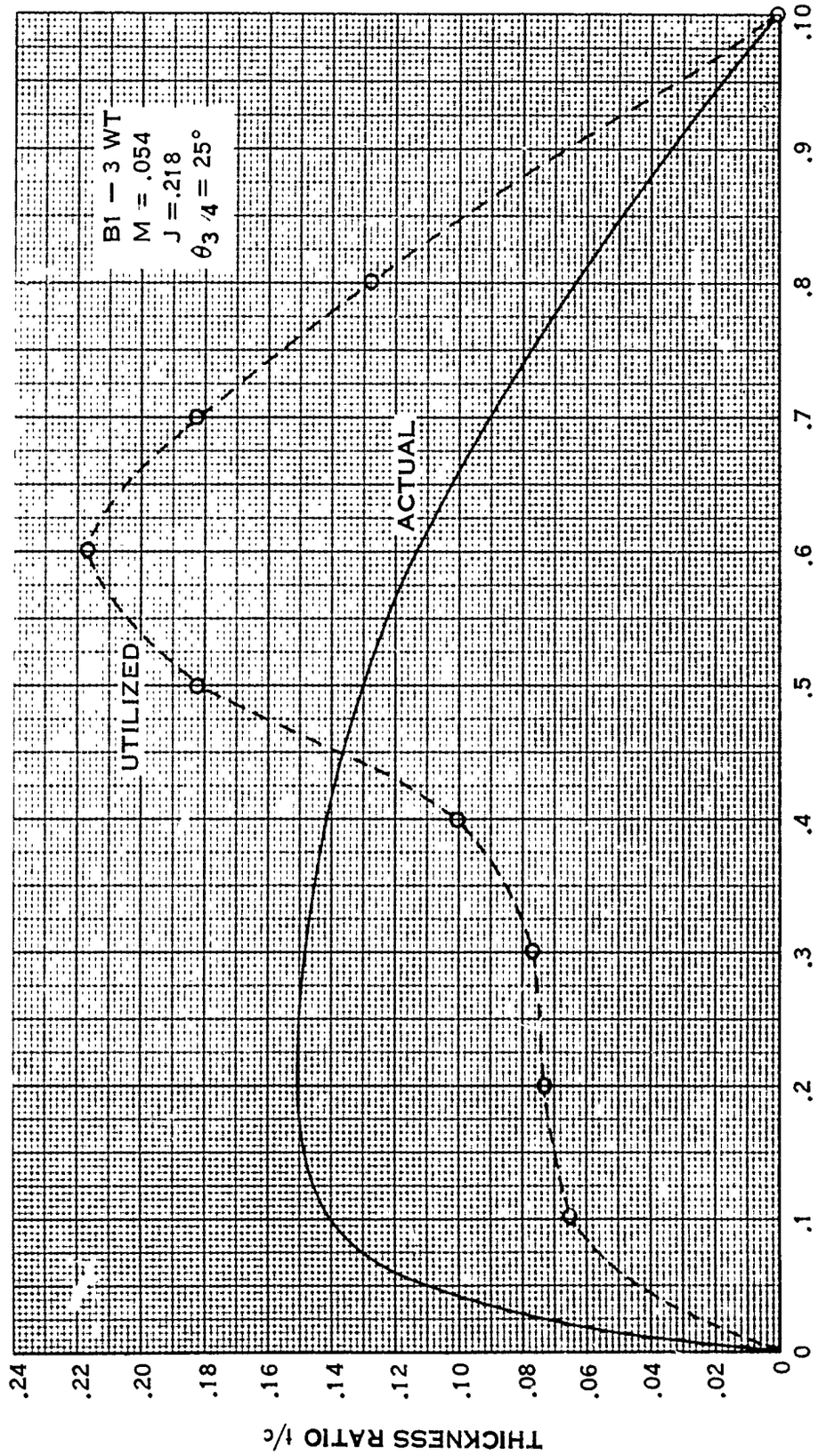

COMPARISON OF UTILIZED AND ACTUAL SHROUD THICKNESS FORMS

FIGURE 43

7.4.2d (Continued)

	B1-3WT		B4-3WT	
Operating Condition	J = 0.218 M = 0.0534 $\theta_{3/4}$ = 25°		J = 0.192 M = 0.0535 $\theta_{3/4}$ = 30°	
Correction	C_P	$C_{T_{prop}}$	C_P	$C_{T_{prop}}$
J'_0	0.181	0.2087	0.2656	0.2378
J'_2	0.1956	0.2254	0.2872	0.2492
J'_2 + Goodman Tip Correction	0.2005	0.2309	0.2960	0.2563
J'_2 + Goodman Tip Correction + First Order Correction to Boundary Condition	0.1995	0.2299	0.2972	0.2566
Test	0.183	0.196	0.289	0.231

The effects of the various corrections are small. The use of J'_2 instead of J'_c and the Goodman tip correction result in the largest changes. The first order correction to the boundary condition has a negligible effect, as it did for the pressure distribution. The good agreement exhibited between test and theory is fortuitous. Choice of a different operating point would have resulted in poorer agreement, as will be shown by the comparisons in paragraph 7.4.3 and Fig. 47.

7.4.2e Summary - Pressure Distribution Comparison

These discussions indicate that for the higher Mach numbers, the pressure distribution along the shroud is well predicted by the theory except for the region near the leading edge. The changes in pressure distribution due to changes in power coefficient, area ratio and rotative speed are predicted by the theory. At a Mach number of 0.05 the theory does not predict the pressure distributions, as might be expected, because the perturbation velocity is of the order of the free stream velocity, thereby violating the assumptions of the theory.

7.4.3 Propeller Performance Comparisons

Comparisons of calculations and test results for propeller performance will be discussed in this section. Also included are propeller thrust derivation comparisons as well as axial velocities in the propeller plane.

7.4.3a Primary Parameters

Fig. 44, 45 and 46 show the comparison of propeller thrust coefficient, $C_{T\ prop}$, versus power coefficient, C_P, for constant Mach numbers from 0.02 to 0.5 for area ratios of 1.1, 1.2, and 1.3. Good agreements are shown for Mach numbers greater than or equal to 0.20 with deviations becoming greater with further reductions in Mach number. This effect can be seen more clearly on Fig. 47 where the data has been plotted as a function of Mach number for constant C_P for each area ratio.

To better understand what is happening, curves of computed J_2 versus C_P were plotted for the range of Mach numbers for area ratio of 1.1 and 1.3 (Fig. 48). J_2 is defined as the average advance ratio at the propeller plane including the propeller induced effects. With J (free stream advance ratio) also being included on the curve, it can be seen that the lower the Mach number the larger percentage change from J_2 to J. The T.A.R. theory is predicated on small changes between J and J_2. Consequently, the accuracy diminishes as the Mach number is reduced.

In addition, as the Mach number varies from 0.05 to 0.0, the velocity in the propeller plane will decrease and possibly give rise to a significant amount of wake distortion. Consequently, the Goldstein theory will not properly define the propeller contribution. The same situation has occurred with the free air propeller and considerable effort is being expended by various concerns to properly define this region. The applicability of the theory to the lower Mach numbers is further discussed in Section 8.0.

The predictions of area ratio effect is better shown in Fig. 49 where C_T is plotted versus C_P for the three area ratios at 0.3 Mach number and 785 ft/sec tip speed. It can be seen that the area ratio effect is being well predicted with the area ratio of 1.3 being off a bit more than the other two. This would be expected since Fig. 48 showed that the J_2 for 1.3 area ratio deviated from J more than the 1.1 area ratio J_2. The area ratio variation with Mach number for a constant C_P is shown in Fig. 50. Again, good agreements are shown for $M \geq 0.2$. The trends are predicted at $M = 0.1$ although the magnitudes are off. For 0.05 Mach number, neither trends nor magnitude are predicted.

The tip speed comparison was made at 0.3 Mach number for the range of test tip speeds. The results are plotted in Fig. 51 and show that the tip speed variation is being well predicted.

PROPELLER PERFORMANCE COMPARISONS OF CALCULATION AND TEST – EFFECT OF MACH NUMBER

TIP SPEED = 785 FPS
B1–3WT AR = 1.1

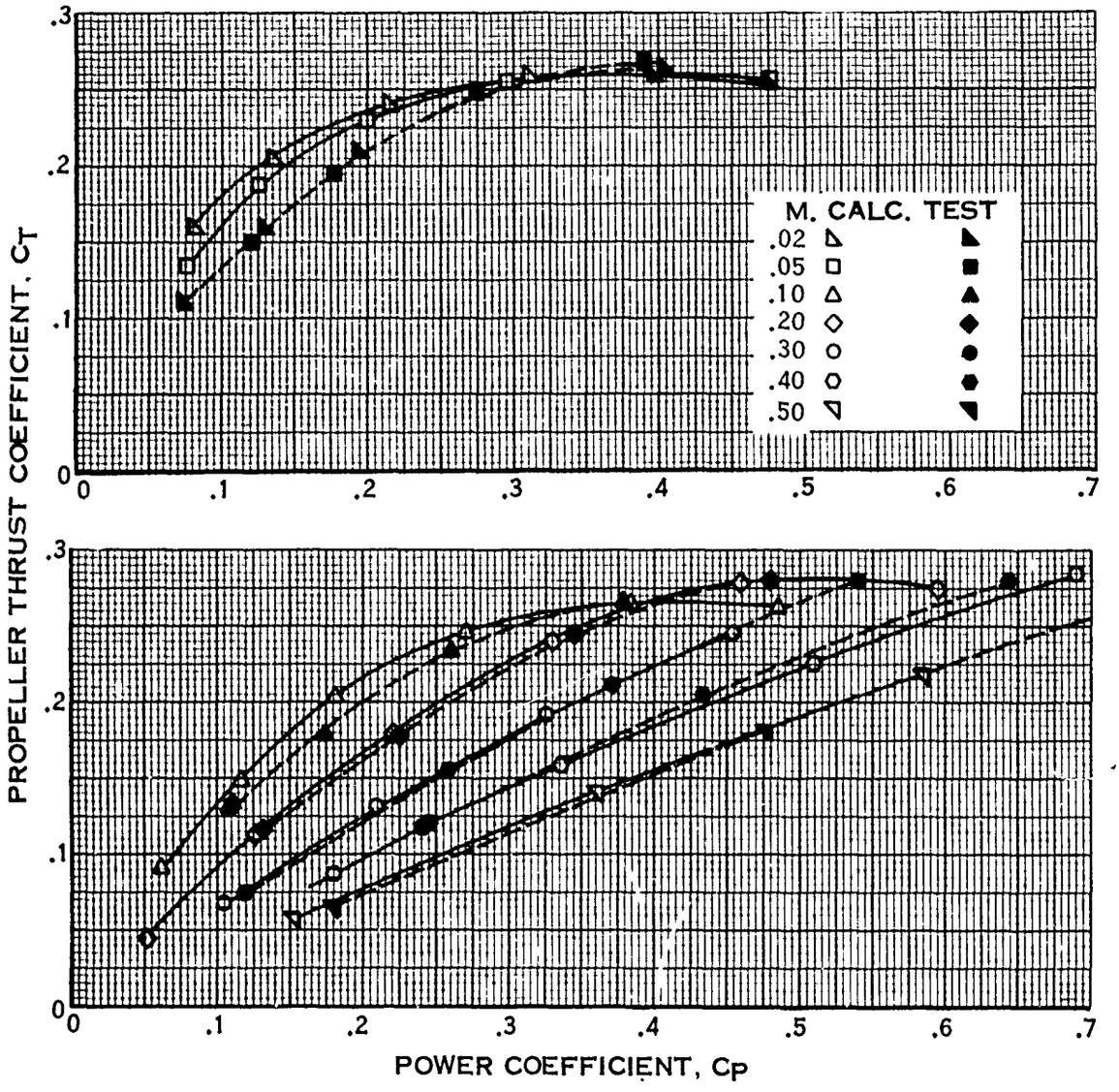

FIGURE 44.

PROPELLER PERFORMANCE COMPARISONS OF CALCULATION AND TEST – EFFECT OF MACH NUMBER

TIP SPEED = 785 FPS
B3–3WT AR = 1.2

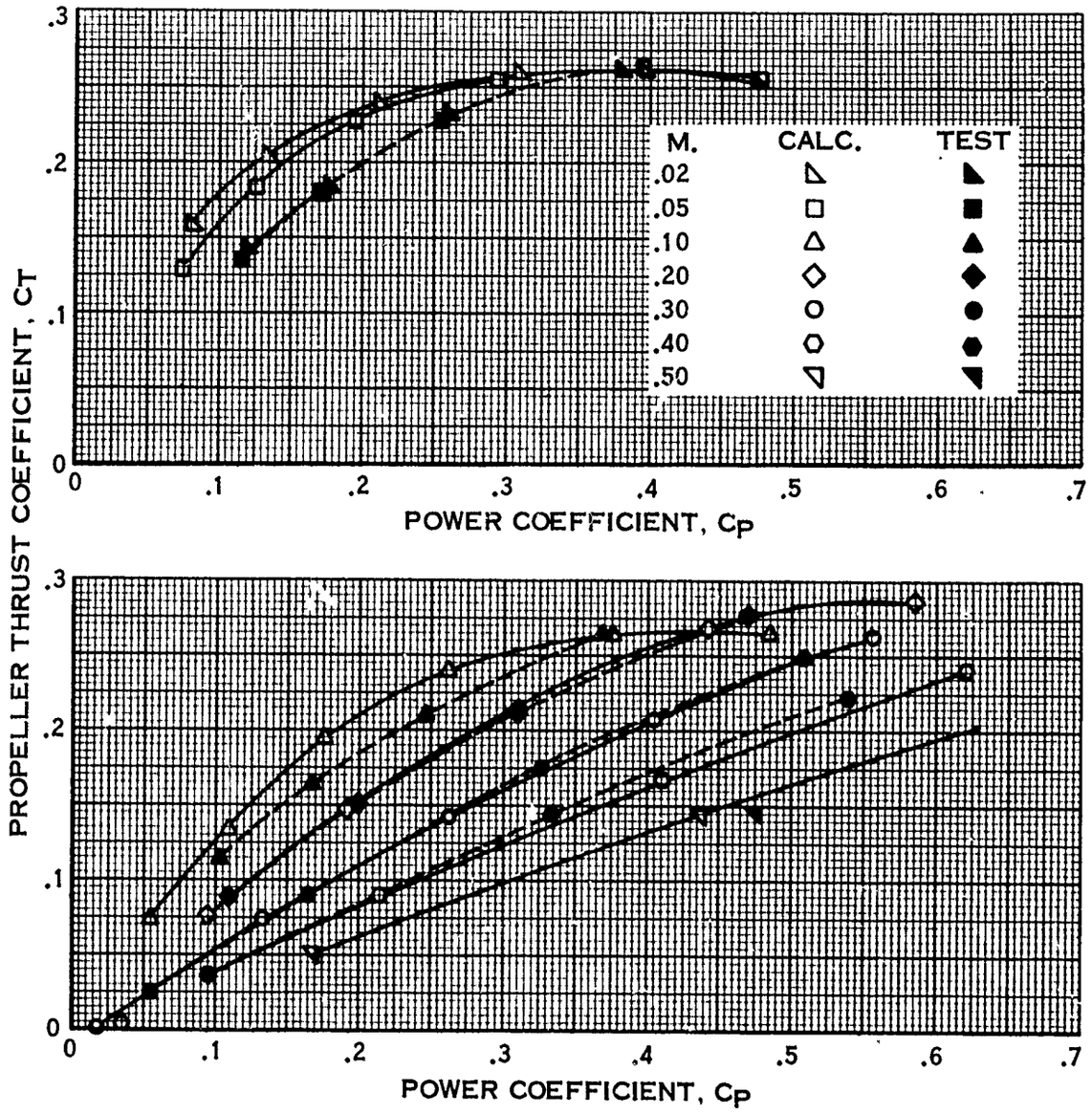

FIGURE 45.

PROPELLER PERFORMANCE COMPARISONS OF CALCULATION AND TEST – EFFECT OF MACH NUMBER

TIP SPEED = 785 FPS
B4–3WT AR = 1.3

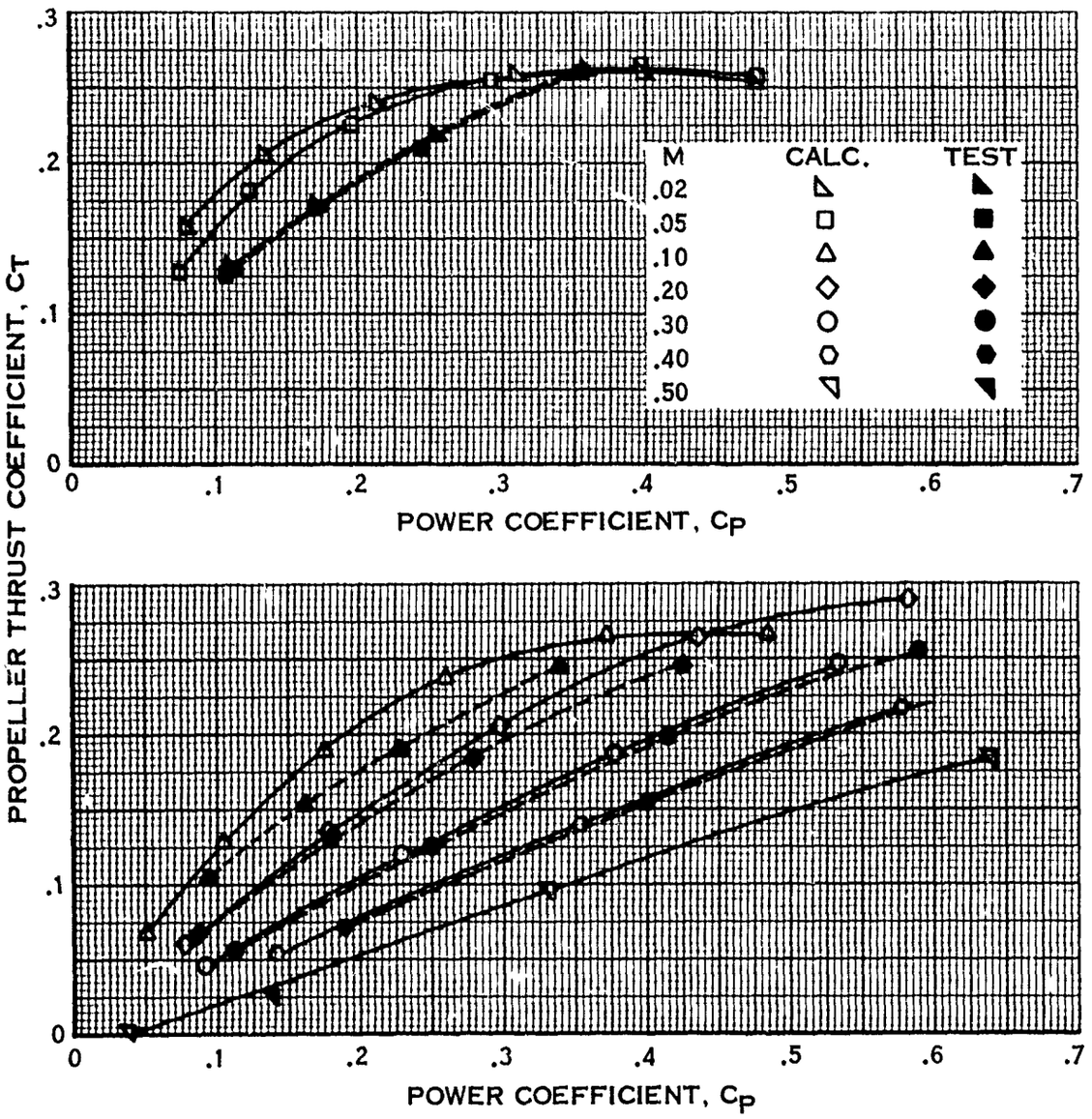

FIGURE 46.

PROPELLER PERFORMANCE COMPARISONS OF CALCULATION AND TEST – EFFECT OF MACH NUMBER

TIP SPEED = 785 FPS

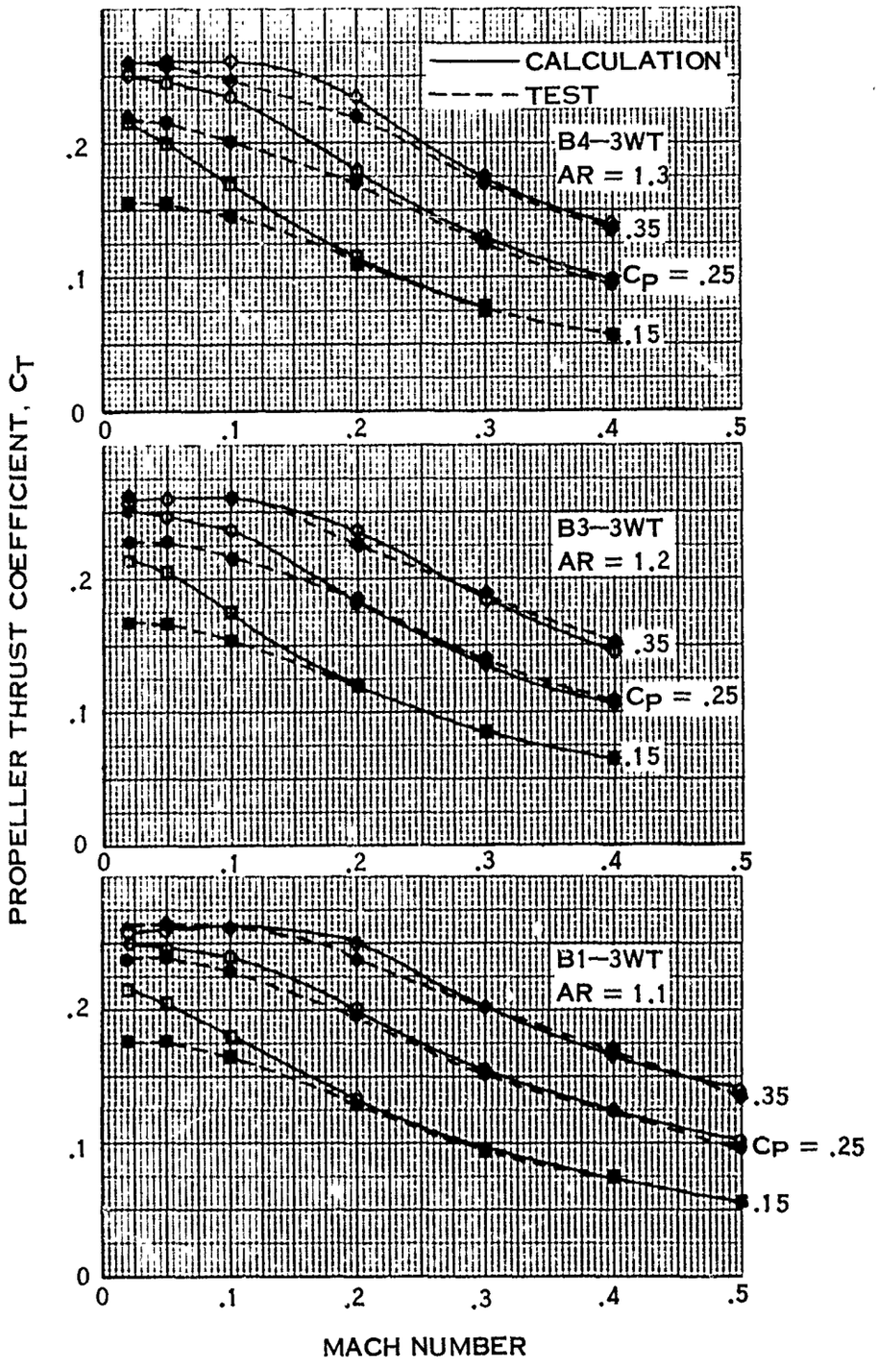

FIGURE 47.

EFFECT OF AREA RATIO ON THE COMPUTED ADVANCE RATIO AT THE PROPELLER PLANE

TIP SPEED = 785 FPS

——— B1–3WT A.R. = 1.1

– – – – – – B4–3WT A.R. = 1.3

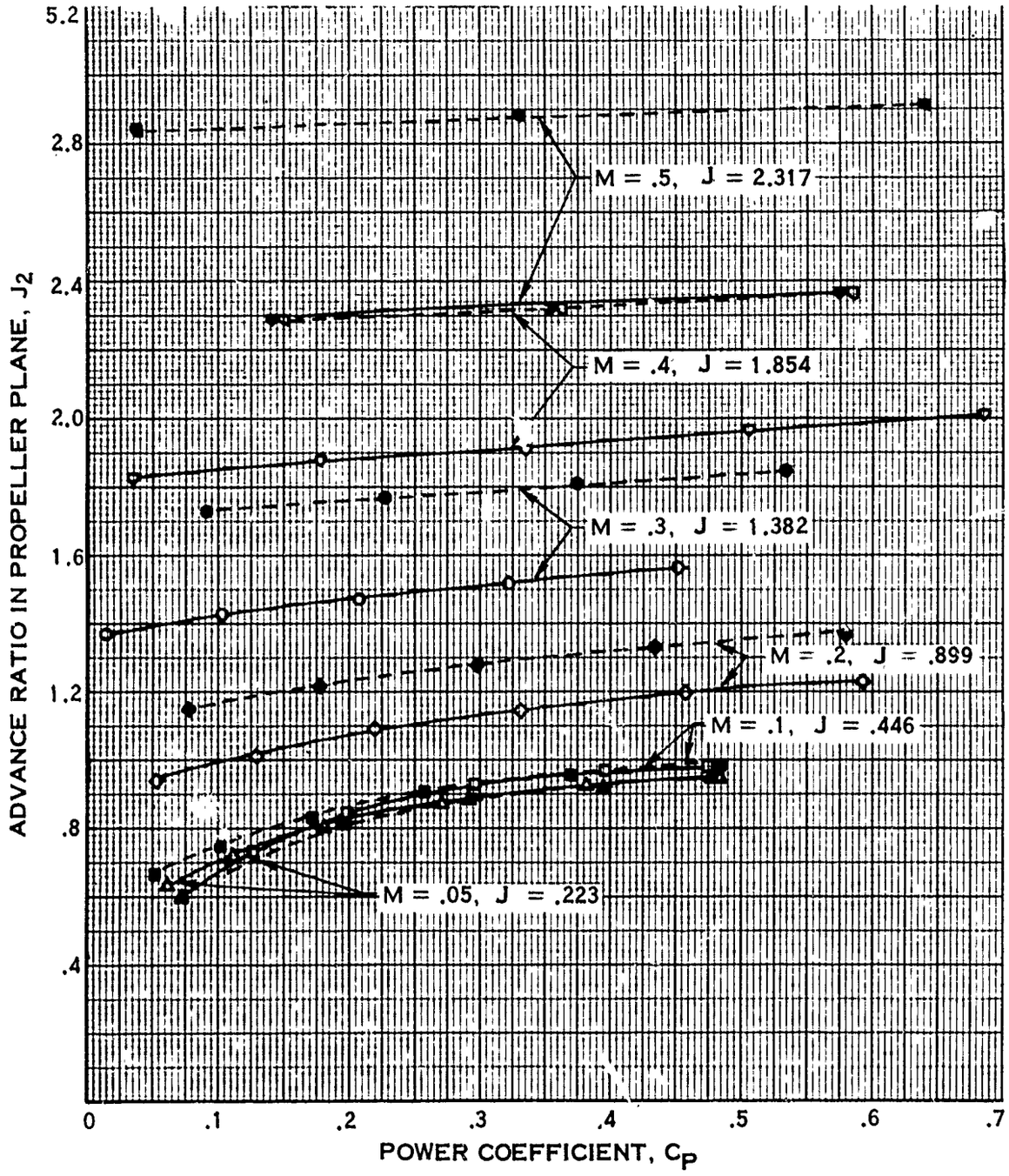

FIGURE 48.

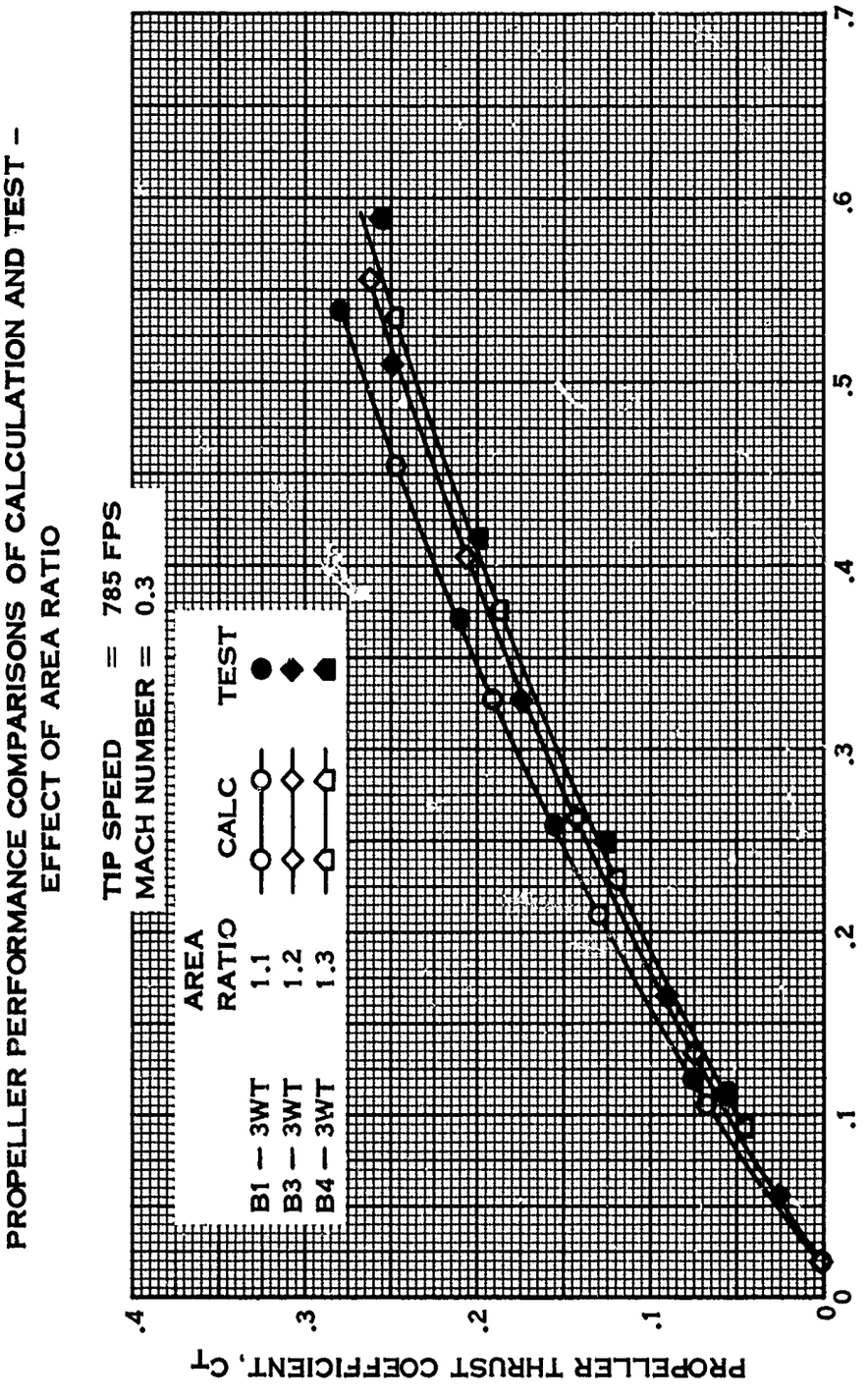
PROPELLER PERFORMANCE COMPARISONS OF CALCULATION AND TEST –
EFFECT OF AREA RATIO
TIP SPEED = 785 FPS
MACH NUMBER = 0.3
AREA RATIO
CALC
TEST
B1 — 3WT 1.1
B3 — 3WT 1.2
B4 — 3WT 1.3
PROPELLER THRUST COEFFICIENT, C_T
POWER COEFFICIENT, C_P
0
.1
.2
.3
.4
.5
.6
.7

FIGURE 49.

PROPELLER PERFORMANCE COMPARISONS OF CALCULATION AND TEST—
EFFECT OF AREA RATIO
TIP SPEED = 785 FPS
C_P = 0.20

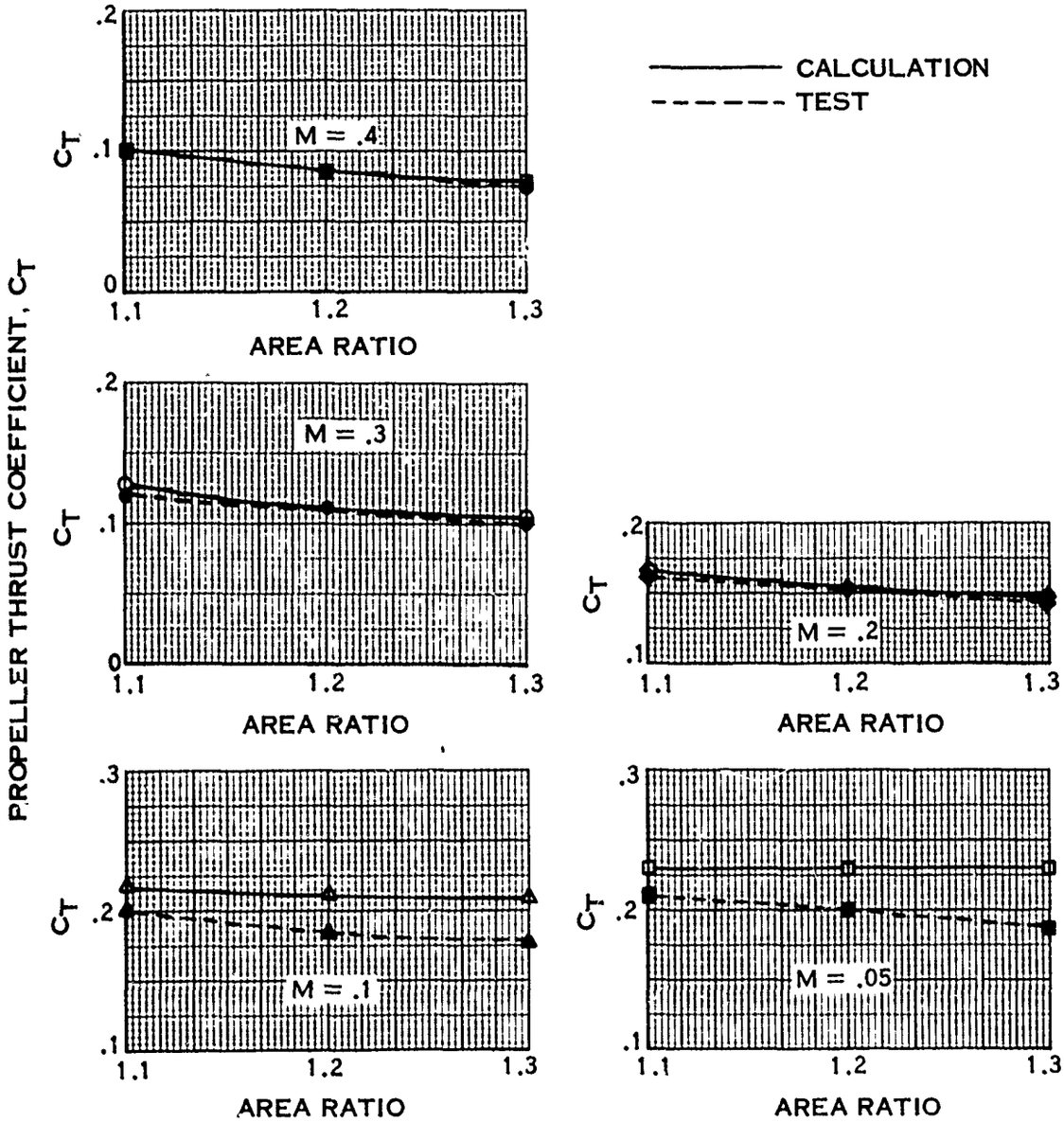

FIGURE 50.

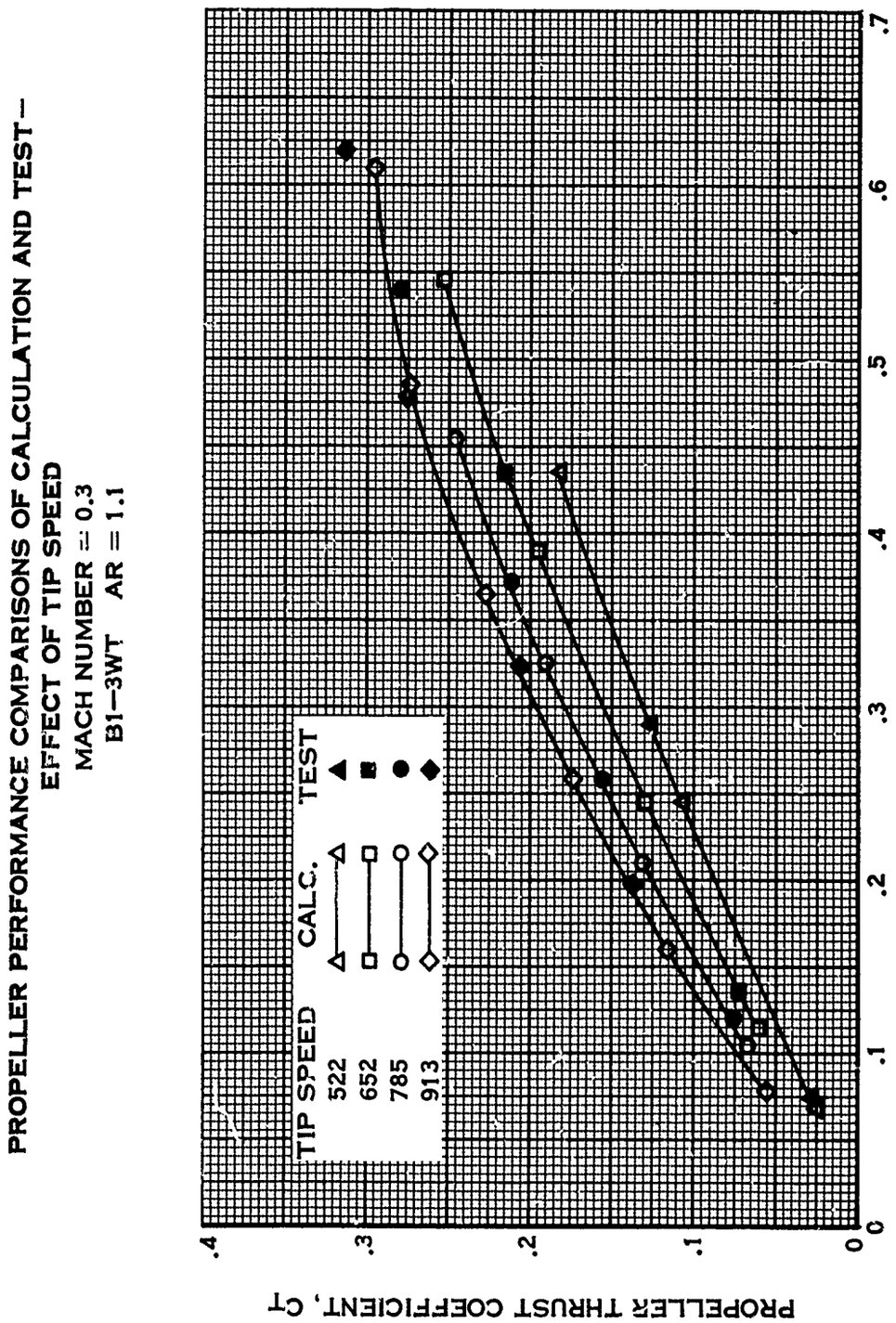
PROPELLER PERFORMANCE COMPARISONS OF CALCULATION AND TEST—
EFFECT OF TIP SPEED
MACH NUMBER = 0.3
B1—3WT AR = 1.1
TIP SPEED
CALC.
TEST
522
652
785
913
PROPELLER THRUST COEFFICIENT, CT
POWER COEFFICIENT, CP
0
.1
.2
.3
.4
.5
.6
.7

FIGURE 51.

7.4.3a (Continued)

In summary, the prime factors are well predicted for Mach number $\gtrsim 0.20$. The deviations in the lower Mach number range are due to deficiencies in the basic theory. Since the propeller theory is also doubtful in the static region, it is recommended that when a successful propeller static thrust theory is developed that it be included in the computer program.

7.4.3b Secondary Parameters

The evaluation of the computational validity of the secondary effects are included in Fig. 52 through 58. Propeller thrust coefficients, $C_{T\ prop}$ are plotted versus power coefficients, C_P for 0.3 Mach Number and 785 ft/sec tip speeds for calculations and test.

Fig. 52 shows that test data predicts a slight difference in propeller performance for the shroud external shape. Calculations, however, show the B6 shroud to have better propeller performance than the B1 shroud. The basic shroud (B1) has a gradual fairing of the outside surface starting from the 25% chordal position. The exterior of the B6 shroud, on the other hand, was built with the camber side of a NACA Series 16 airfoil from the 50% chord position to the shroud trailing edge.

The effect of shroud lip shape is shown in Fig. 53. Tests show an average of a 2% improvement in performance for B1 shroud over B2 shroud where B1 has the larger leading edge thickness. Calculations predict a negligible change in performance for the two shroud lip shapes.

Calculations and tests both predict at the lower C_P range that the long shroud is better than the short shroud. However, calculations do not predict the crossover as indicated at the higher C_P range. The data is summarized in Fig. 54.

The good agreement between calculations and test for the effect of propeller position is shown in Fig. 55. Both show that the propeller performance is essentially the same for propeller centerlines located at 40% ($X_p = -0.1023$) and 25% ($X_p = -0.2528$) of the shroud chord length back from the shroud leading edge.

The negligible effect of planform on propeller performance as predicted by test is also shown to be so by calculations. The comparison is plotted in Fig. 56. These propellers were wide tip trapezoidal (3WT), narrow tip trapezoidal (3NT), and rectangular (3R) in planform.

The computed number of blades effect well matches test results in the lower C_P range and slightly overestimates in the higher range as shown in Fig. 57.

PROPELLER PERFORMANCE COMPARISONS OF CALCULATION AND TEST — EFFECT OF SHROUD EXTERNAL SHAPE

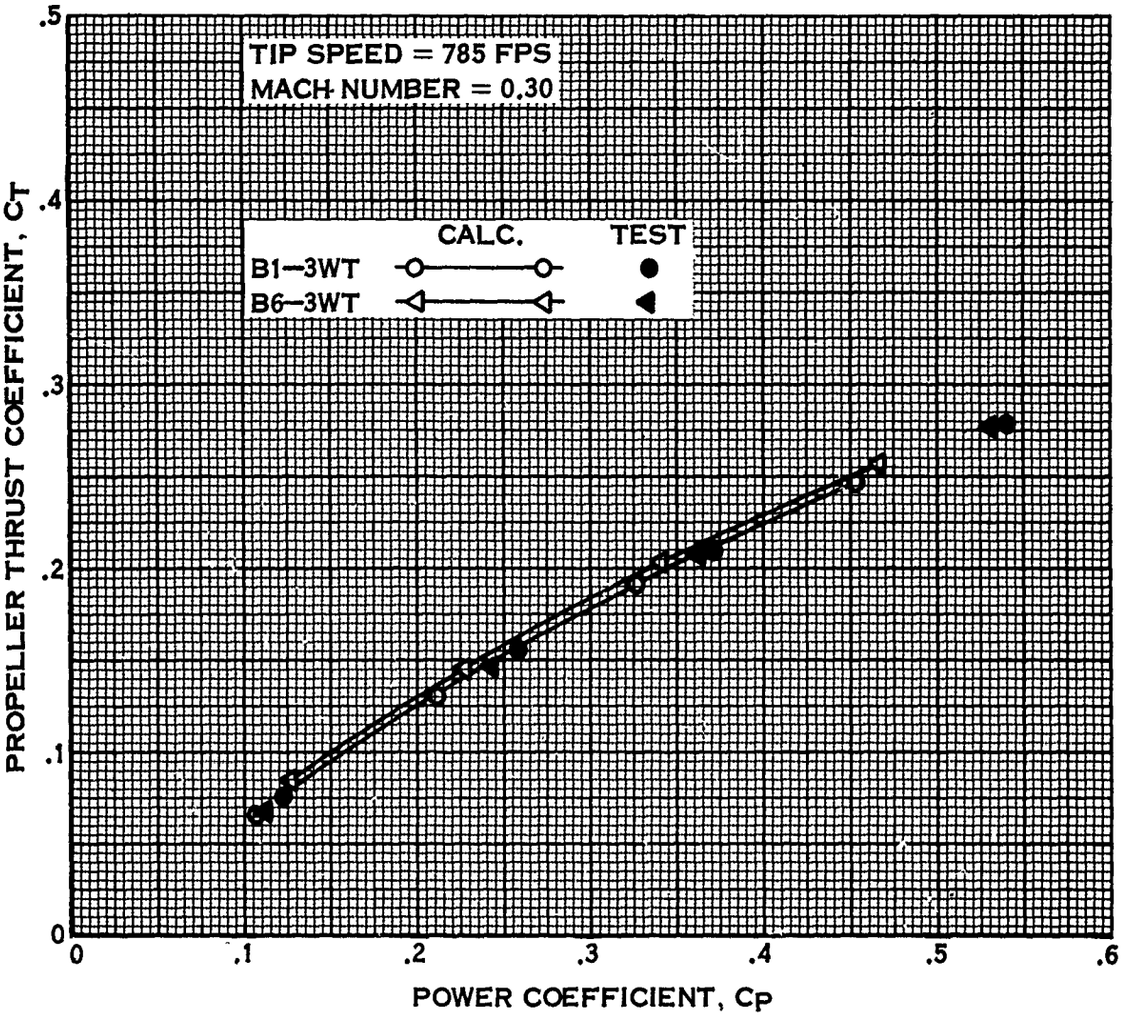

FIGURE 52.

PROPELLER PERFORMANCE COMPARISONS OF CALCULATION AND TEST — EFFECT OF SHROUD LIP SHAPE

TIP SPEED = 785 FPS
MACH NUMBER = 0.3

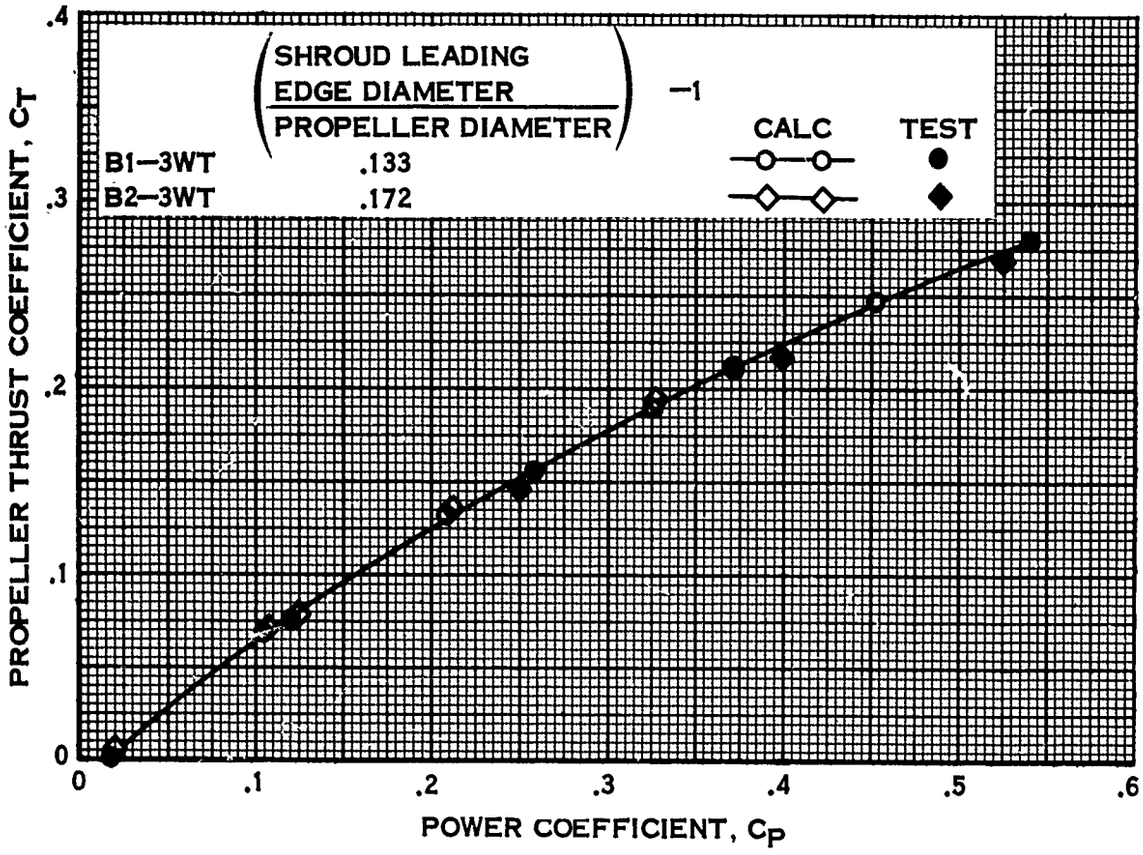

FIGURE 53.

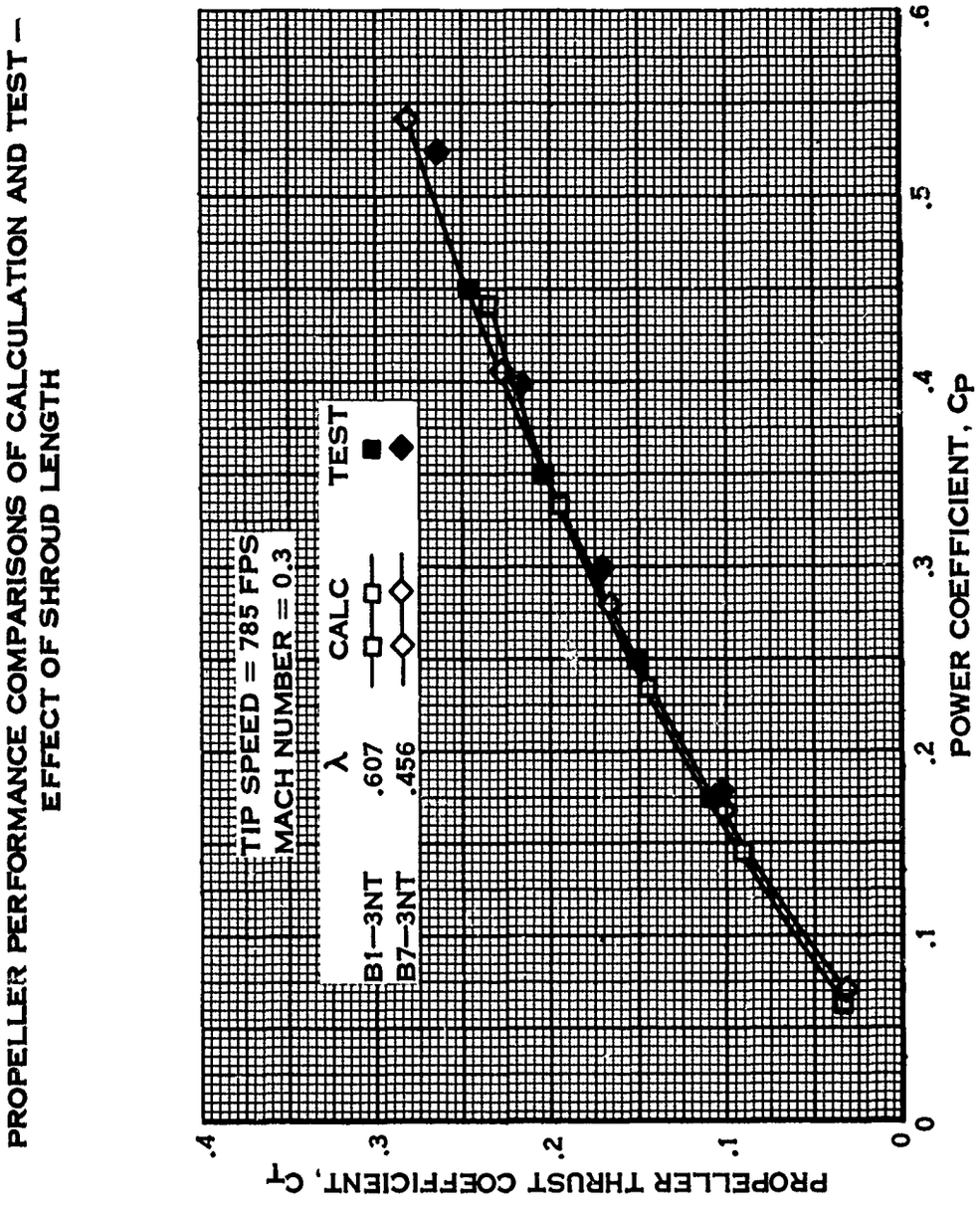
PROPELLER PERFORMANCE COMPARISONS OF CALCULATION AND TEST —
EFFECT OF SHROUD LENGTH
TIP SPEED = 785 FPS
MACH NUMBER = 0.3
λ CALC TEST
B1—3NT .607
B7—3NT .456
PROPELLER THRUST COEFFICIENT, C_T
POWER COEFFICIENT, C_P
0
.1
.2
.3
.4
.5
.6

FIGURE 54.

PROPELLER PERFORMANCE COMPARISONS OF CALCULATION AND TEST — EFFECT OF PROPELLER POSITION

TIP SPEED = 785 FPS
MACH NUMBER = 0.30

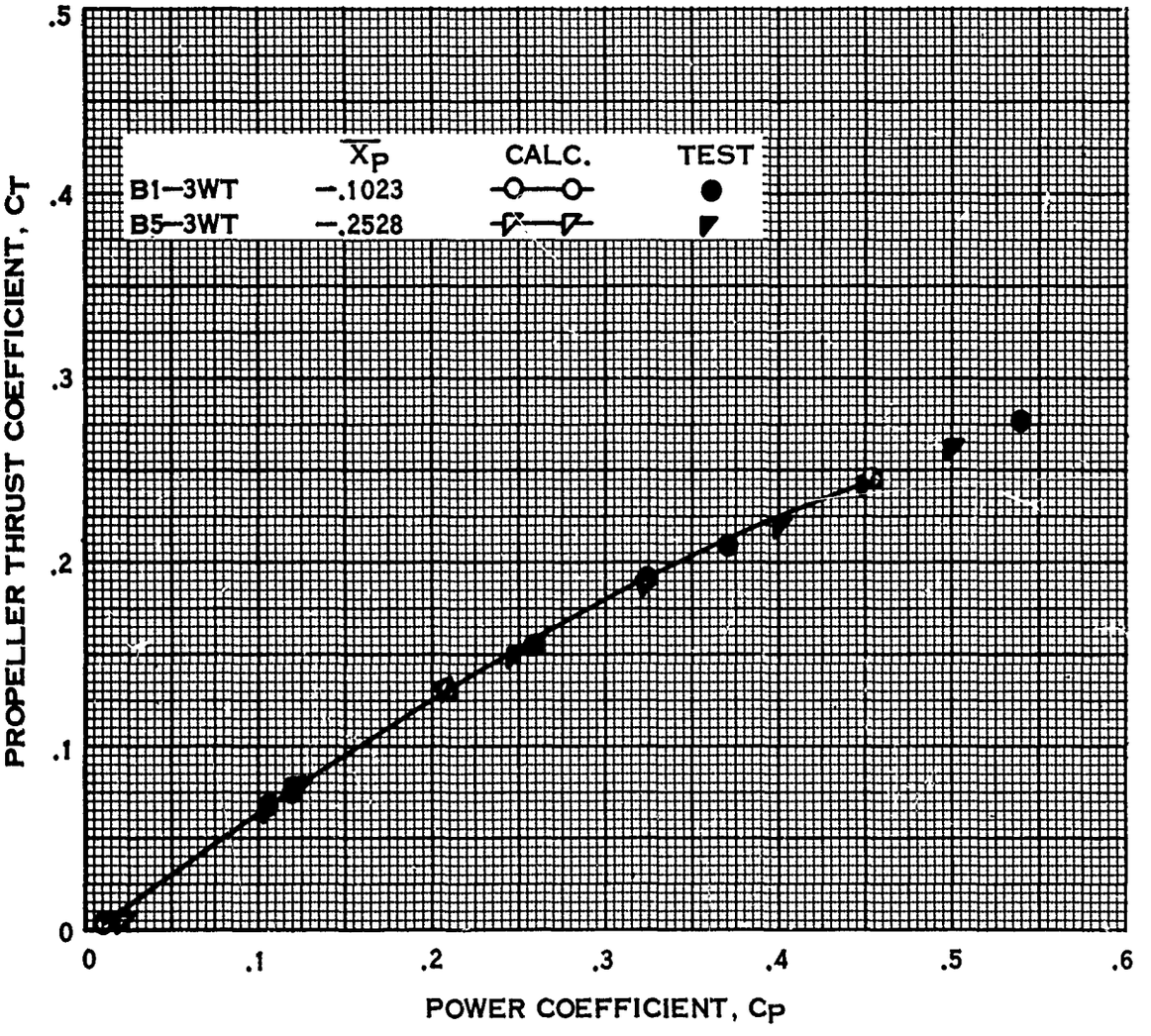

FIGURE 55.

PROPELLER PERFORMANCE COMPARISONS OF CALCULATION AND TEST —
EFFECT OF PROPELLER PLANFORM
TIP SPEED = 785 FPS
MACH NUMBER = 0.3

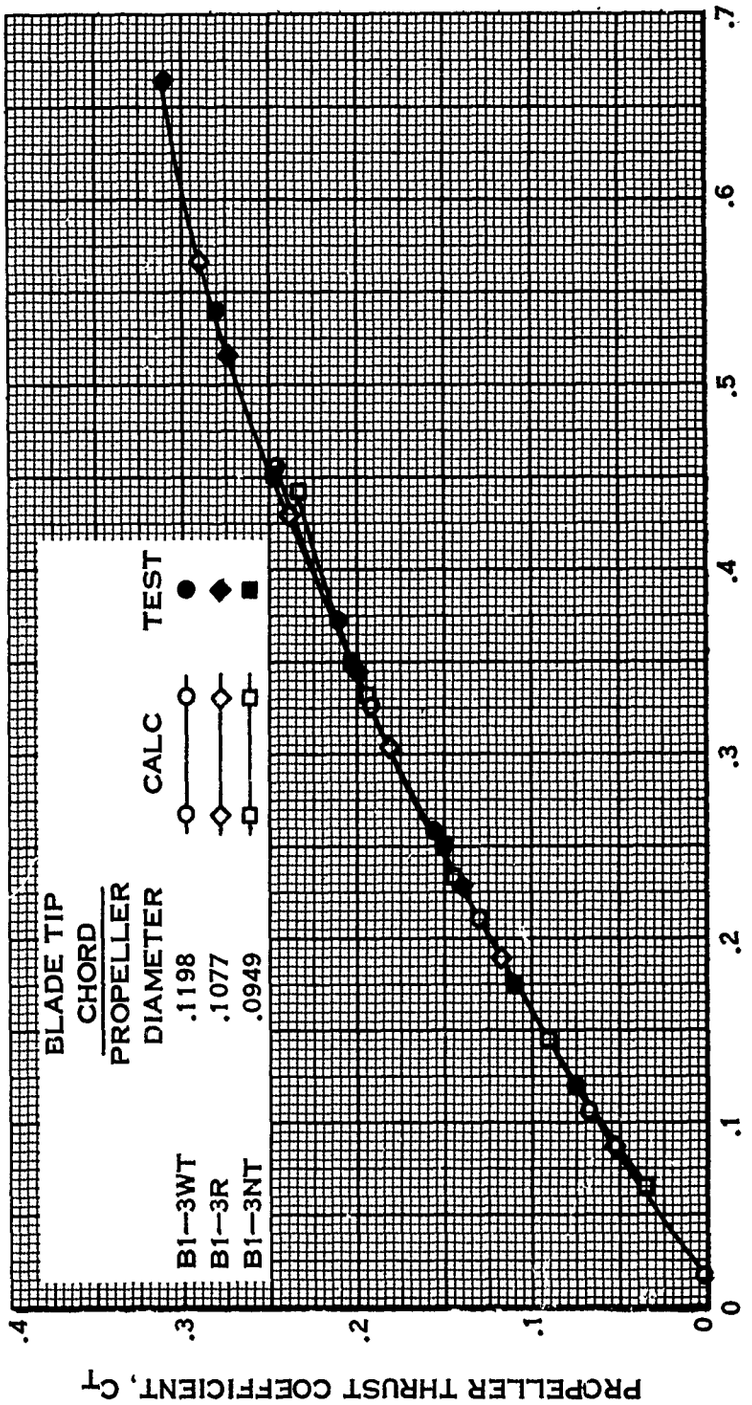

FIGURE 56.

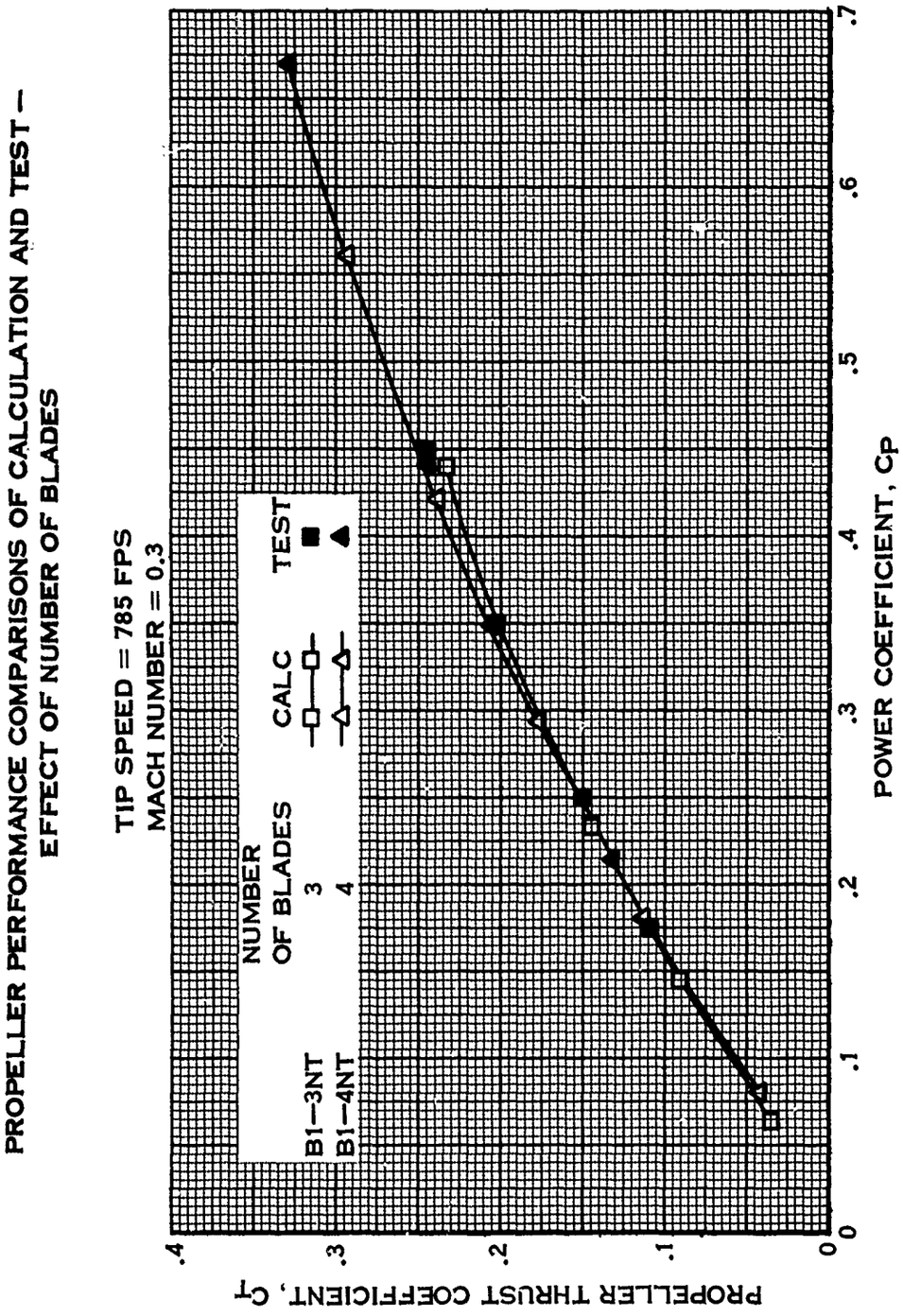
PROPELLER PERFORMANCE COMPARISONS OF CALCULATION AND TEST – EFFECT OF NUMBER OF BLADES
TIP SPEED = 785 FPS
MACH NUMBER = 0.3
NUMBER OF BLADES
CALC
TEST
B1–3NT
B1–4NT
3
4
PROPELLER THRUST COEFFICIENT, C_T
POWER COEFFICIENT, C_P
0
.1
.2
.3
.4
.5
.6
.7

FIGURE 57.

7.4.3b (Continued)

The effect of blade tip clearance is shown in Fig. 58. Tests show that for the nominal radial tip clearance of 0.038" (3R), 0.078" (3R 1/2M), and 0.168" (3RM) corresponding to $\mu = 0.911$, 0.909, and 0.903 on the $C_{T\ prop}$, C_P basis, the propeller performance is within 1% of each other. Calculations show that the performance is essentially the same. It should be noted that to get the true tip clearance effect for a given operating condition, performance should be compared at different C_P's for each tip clearance since the propeller diameters differ. However, since the calculations match test so well, the tip clearance effect will also be well predicted for specific operating conditions.

In summary, test data show that all of the secondary factors have small or no effects. Calculations also essentially show small or no effects.

7.4.3c Comparison of Axial Velocity Distributions

During the Phase I testing, axial velocity distributions were measured at a point located 0.24 chord lengths upstream of the propeller centerline. The computer program permits only the computations of the velocity in the propeller plane. Therefore, the comparisons in Fig. 59 through 63 can be examined only for general trends and not necessarily for magnitudes. Fig. 59 shows that area ratio difference is predicted over a Mach number range. Tests and calculations both show that planform changes have a small effect on axial velocity (Fig. 60). Number of blades also produce small effects as shown in Fig. 61. The axial velocity differential due to shroud length is well predicted as shown in Fig. 62. A variation with propeller speed is also indicated by calculations as is shown in Fig. 63. Therefore, it can be concluded that axial velocity differentials due to the various shroud and propeller singularities are being predicted.

7.4.3d Comparison of Propeller Thrust Derivatives

As was noted in the Phase I report (Ref. 16, Volume I, Page XII-14), propeller thrust and power distributions were obtained from shroud exit traverse probe measurements. The integration of the thrust derivatives obtained in this manner gave thrust coefficients which agreed well with the force measurement values. A similar correlation of the power data was found to be poor due to the direct dependence of dC_P/dx on measured swirl angles which have sizeable errors. Therefore, only comparisons of the thrust derivatives were made with calculated values. Fig. 64 through 68 show such comparisons for the basic configuration for a Mach number range of 0.05 to 0.5. The good comparisons are further substantiation that the velocities are being properly predicted in the plane of the propeller. The somewhat greater deviation between test and calculations in the tip region with increase in Mach Number is probably due to the measurements being made at the shroud exit where they inadvertantly include boundary lager build up and erroneously reflect its effect back to the propeller plane.

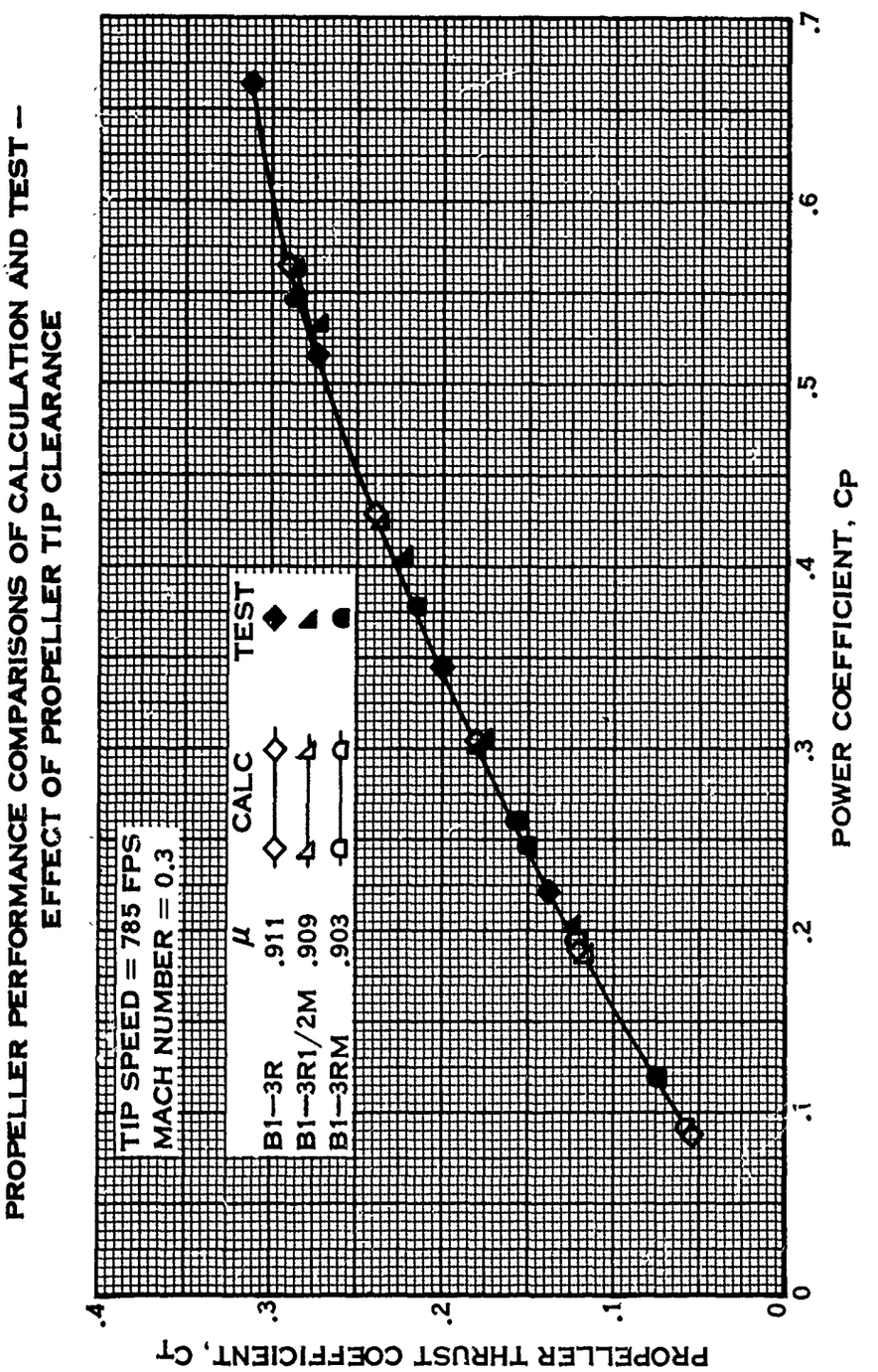
PROPELLER PERFORMANCE COMPARISONS OF CALCULATION AND TEST –
EFFECT OF PROPELLER TIP CLEARANCE
TIP SPEED = 785 FPS
MACH NUMBER = 0.3
μ CALC TEST
B1—3R .911
B1—3R1/2M .909
B1—3RM .903
PROPELLER THRUST COEFFICIENT, CT
POWER COEFFICIENT, CP
0
.1
.2
.3
.4
.5
.6
.7

FIGURE 58.

COMPARISON OF CALCULATION AND TEST OF RADIAL DISTRIBUTION OF PROPELLER PLANE AXIAL VELOCITIES - EFFECT OF AREA RATIO
TIP SPEED = 720 FPS

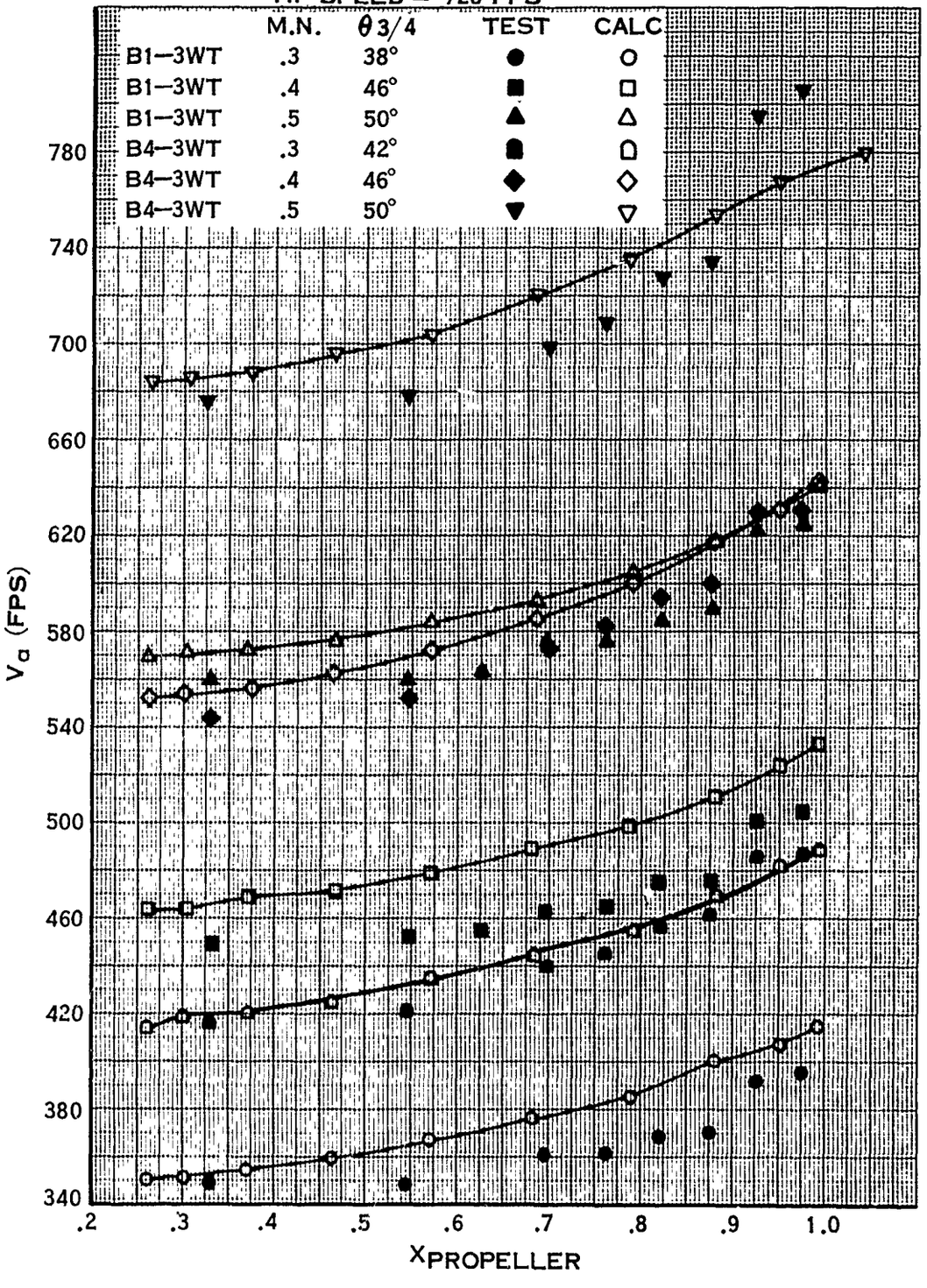

FIGURE 59.

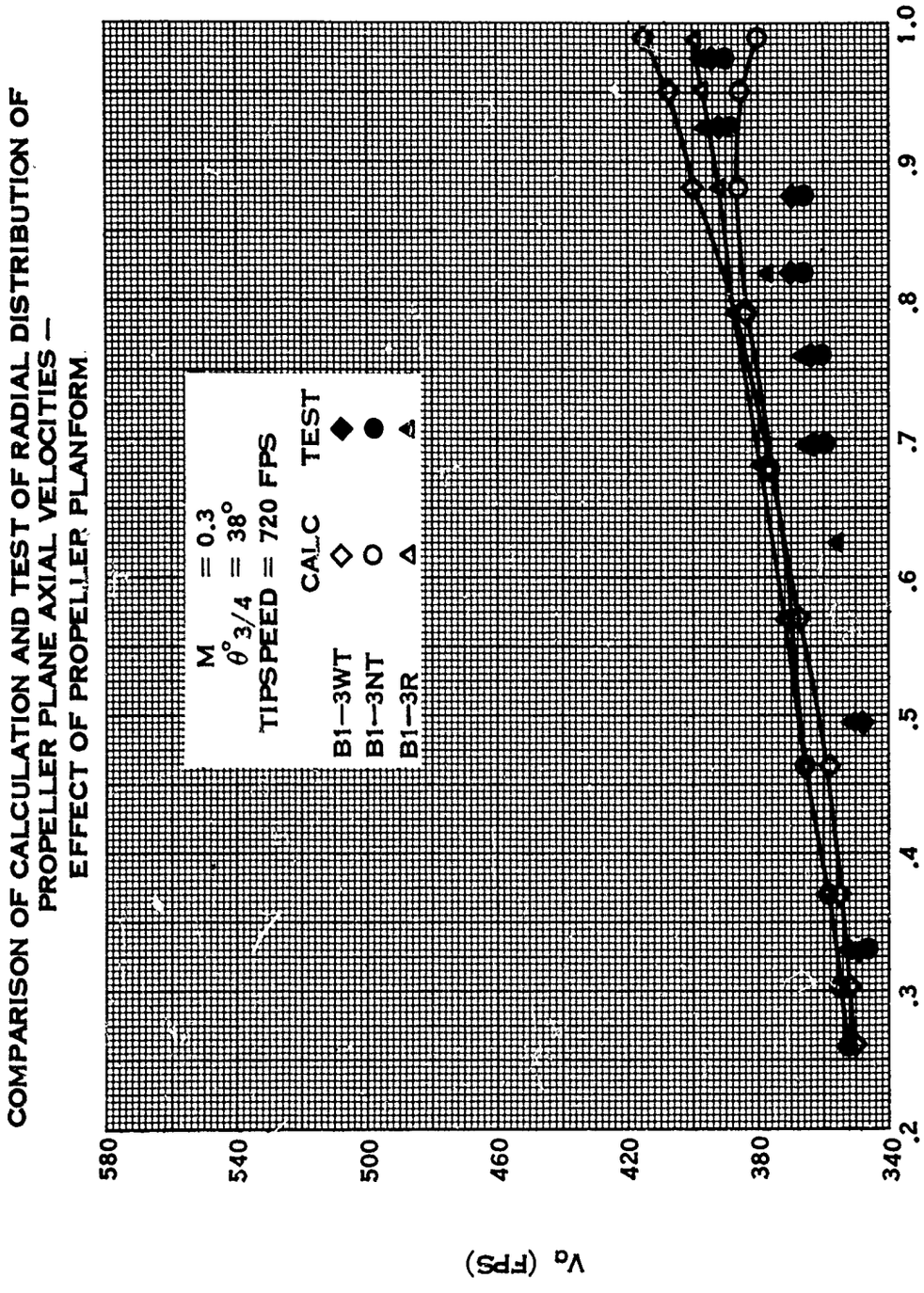
COMPARISON OF CALCULATION AND TEST OF RADIAL DISTRIBUTION OF PROPELLER PLANE AXIAL VELOCITIES — EFFECT OF PROPELLER PLANFORM
M = 0.3
θ°3/4 = 38°
TIPSPEED = 720 FPS
CALC TEST
B1—3WT
B1—3NT
B1—3R
Vα (FPS)
580
540
500
460
420
380
340
.2
.3
.4
.5
.6
.7
.8
.9
1.0
XPROPELLER

FIGURE 60.

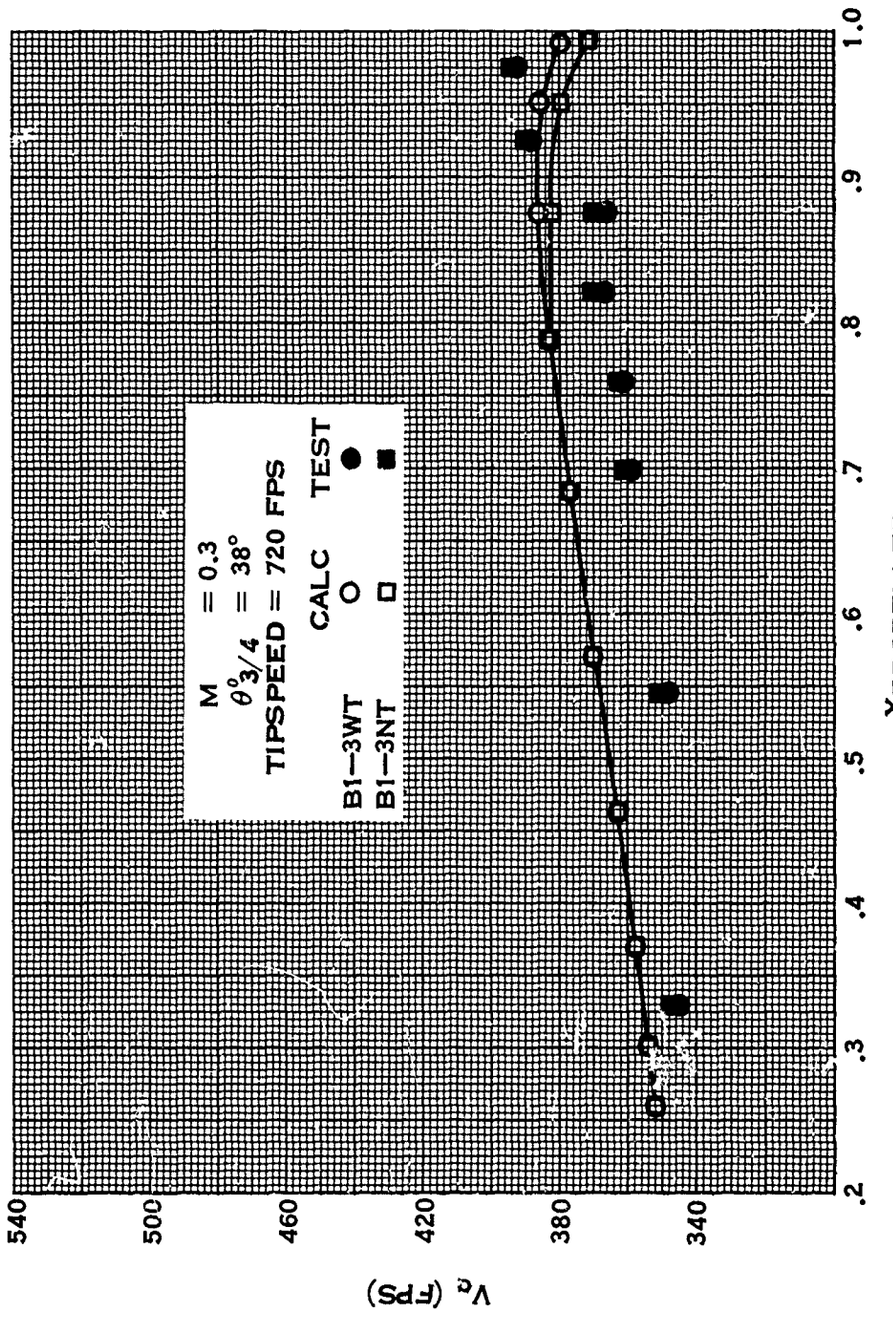
COMPARISON OF CALCULATION AND TEST OF RADIAL DISTRIBUTION OF PROPELLER PLANE AXIAL VELOCITIES — EFFECT OF NUMBER OF BLADES
M = 0.3
θ°3/4 = 38°
TIPSPEED = 720 FPS
CALC TEST
B1—3WT ○ ●
B1—3NT □ ■
Vc (FPS)
540
500
460
420
380
340
.2
.3
.4
.5
.6
.7
.8
.9
1.0
XPROPELLER

FIGURE 61.

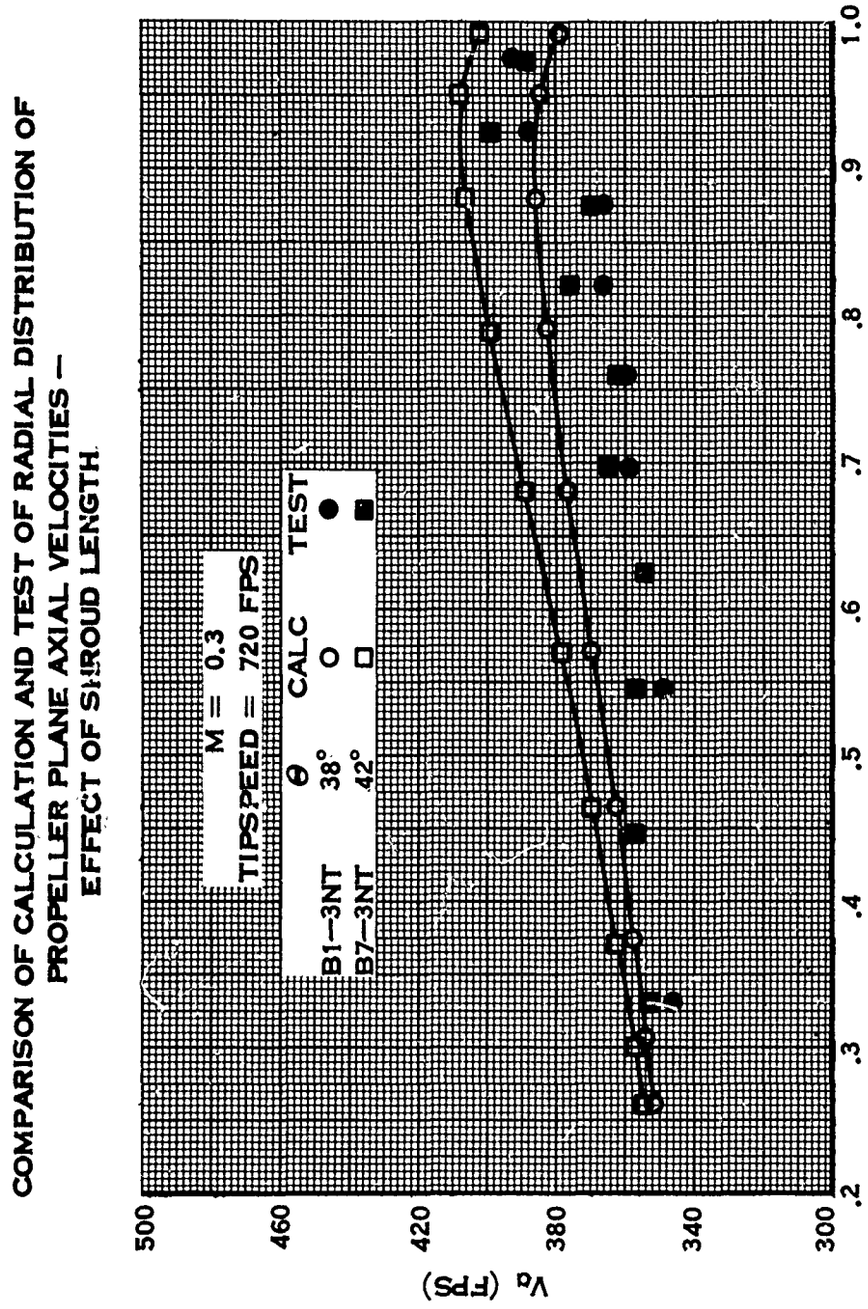
COMPARISON OF CALCULATION AND TEST OF RADIAL DISTRIBUTION OF PROPELLER PLANE AXIAL VELOCITIES — EFFECT OF SHROUD LENGTH
M = 0.3
TIPSPEED = 720 FPS
θ CALC TEST
B1—3NT 38° O ●
B7—3NT 42° □ ■
V_a (FPS)
500
460
420
380
340
300
.2
.3
.4
.5
.6
.7
.8
.9
1.0
$X_{PROPELLER}$

FIGURE 62.

COMPARISON OF CALCULATION AND TEST OF RADIAL DISTRIBUTION OF PROPELLER PLANE AXIAL VELOCITIES — EFFECT OF RPM

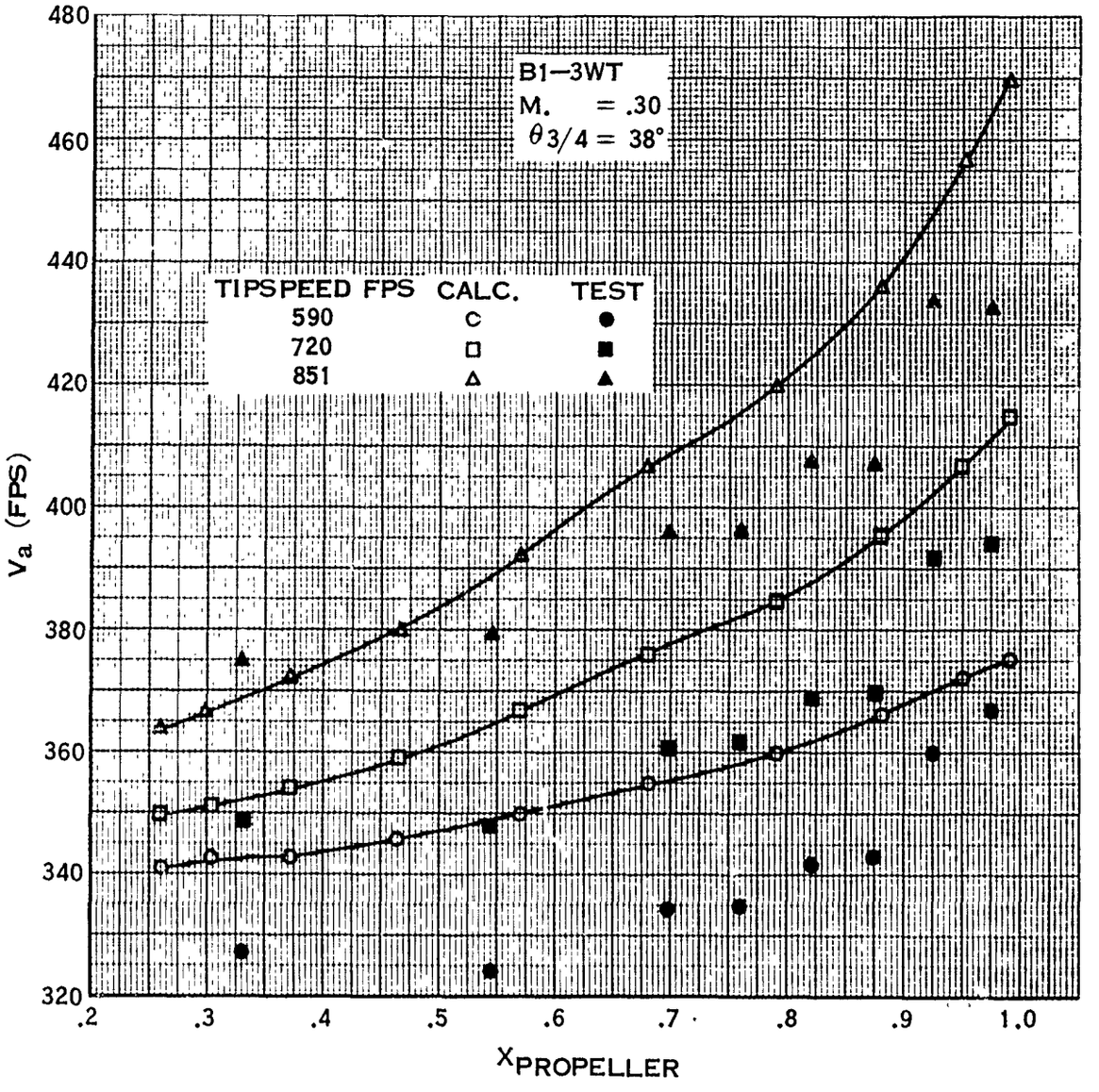

FIGURE 63.

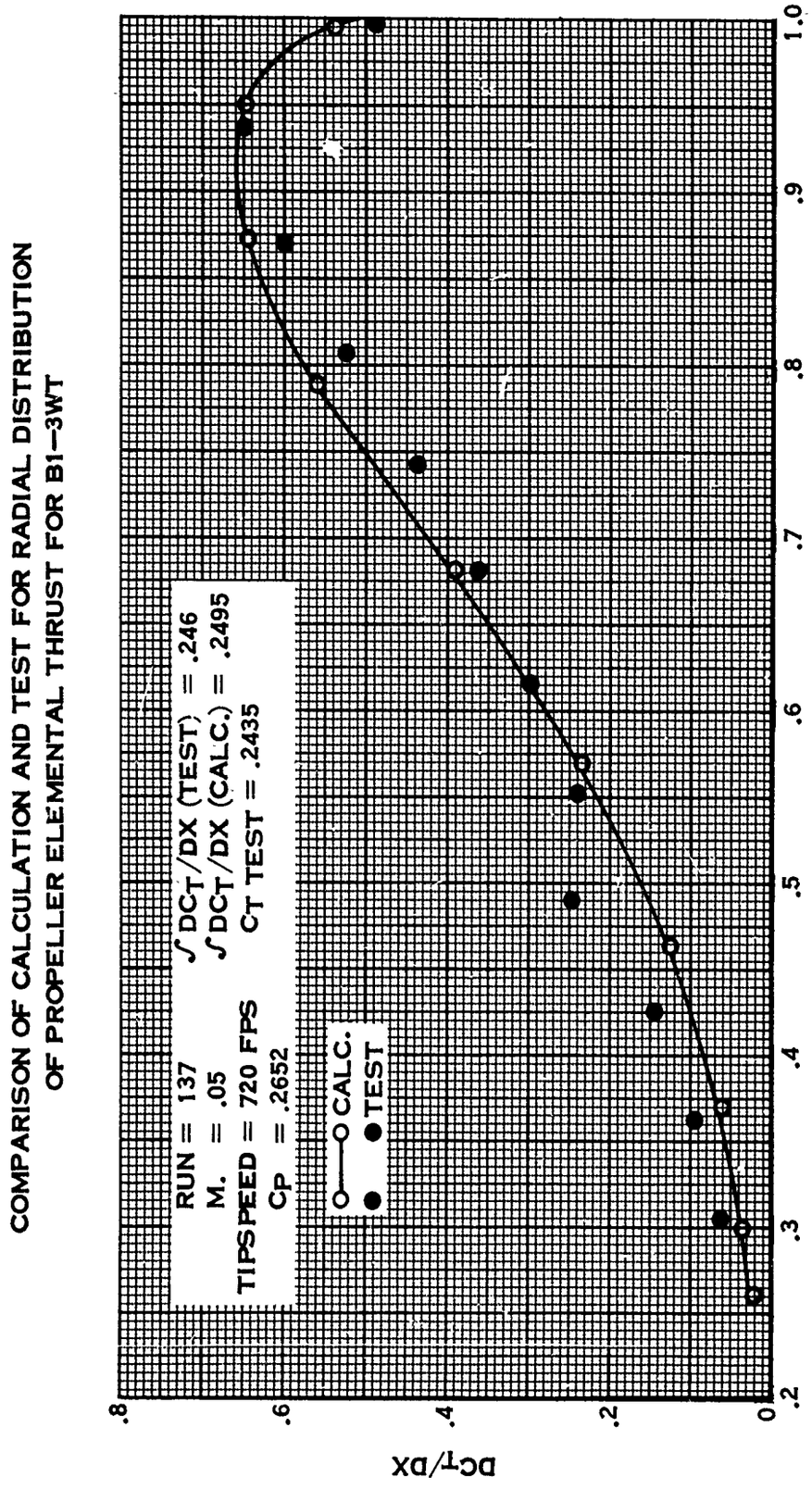
COMPARISON OF CALCULATION AND TEST FOR RADIAL DISTRIBUTION
OF PROPELLER ELEMENTAL THRUST FOR B1—3WT
RUN = 137
M. = .05
TIPSPEED = 720 FPS
CP = .2652
∫ DCT/DX (TEST) = .246
∫ DCT/DX (CALC.) = .2495
CT TEST = .2435
CALC.
TEST
DCT/DX
XPROPELLER
.8
.6
.4
.2
0
.2
.3
.4
.5
.6
.7
.8
.9
1.0

FIGURE 64.

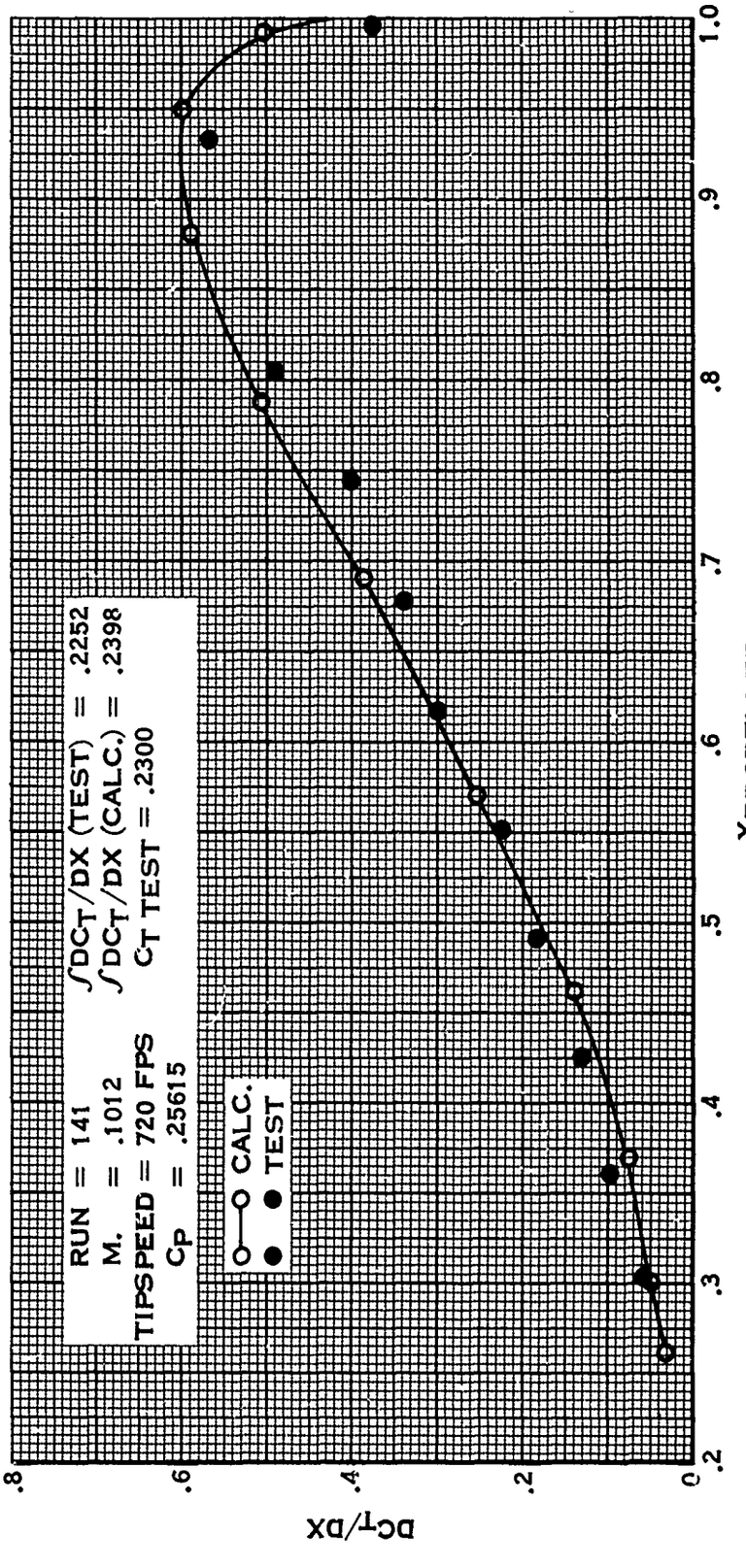
COMPARISON OF CALCULATION AND TEST FOR RADIAL DISTRIBUTION
OF PROPELLER ELEMENTAL THRUST FOR B1-3WT
RUN = 141
M. = .1012
TIPSPEED = 720 FPS
CP = .25615
∫DCT/DX (TEST) = .2252
∫DCT/DX (CALC.) = .2398
CT TEST = .2300
CALC.
TEST
DCT/DX
XPROPELLER
0
.2
.4
.6
.8
.2
.3
.4
.5
.6
.7
.8
.9
1.0

FIGURE 65.

COMPARISON OF CALCULATION AND TEST FOR RADIAL DISTRIBUTION OF PROPELLER ELEMENTAL THRUST FOR B1-3WT

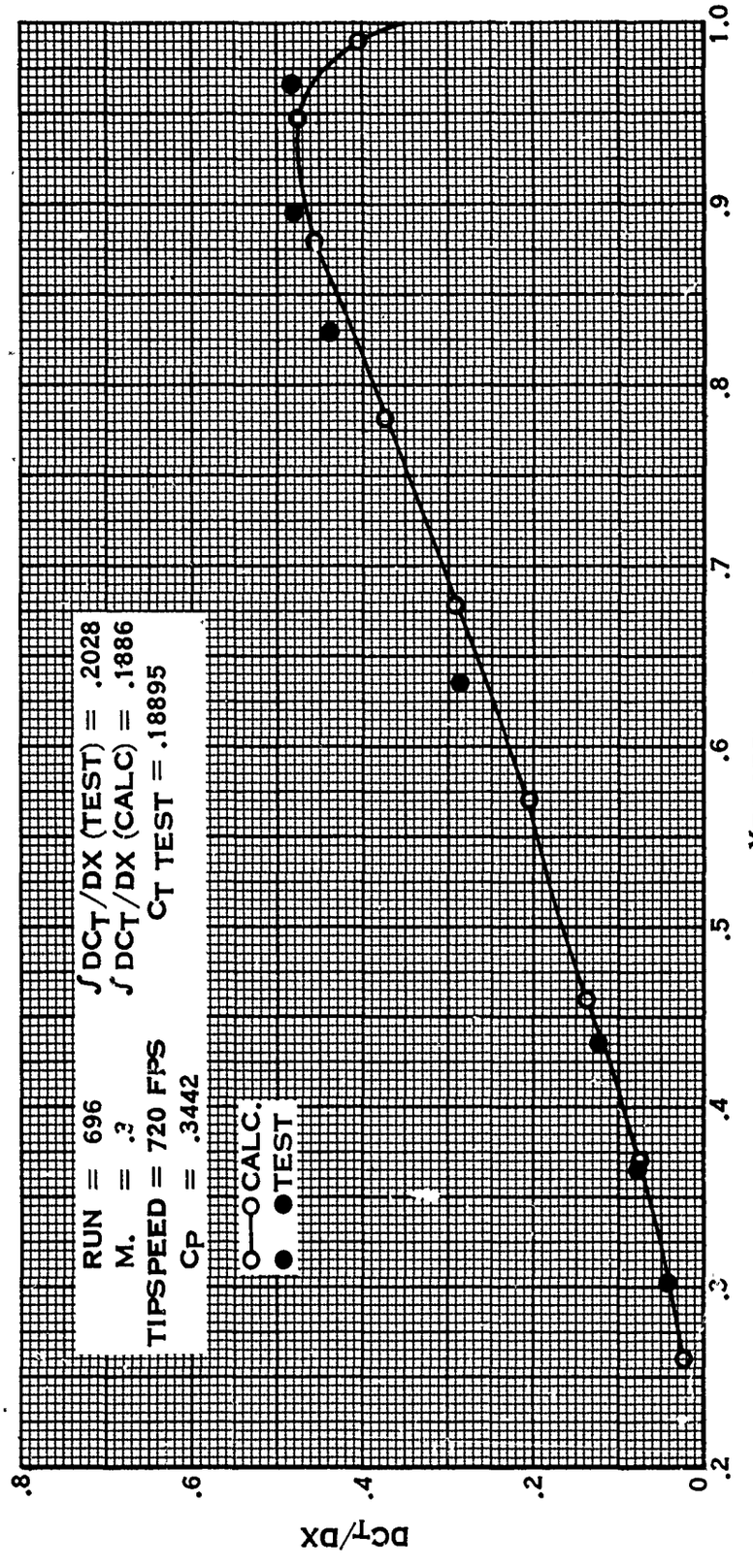

FIGURE 66.

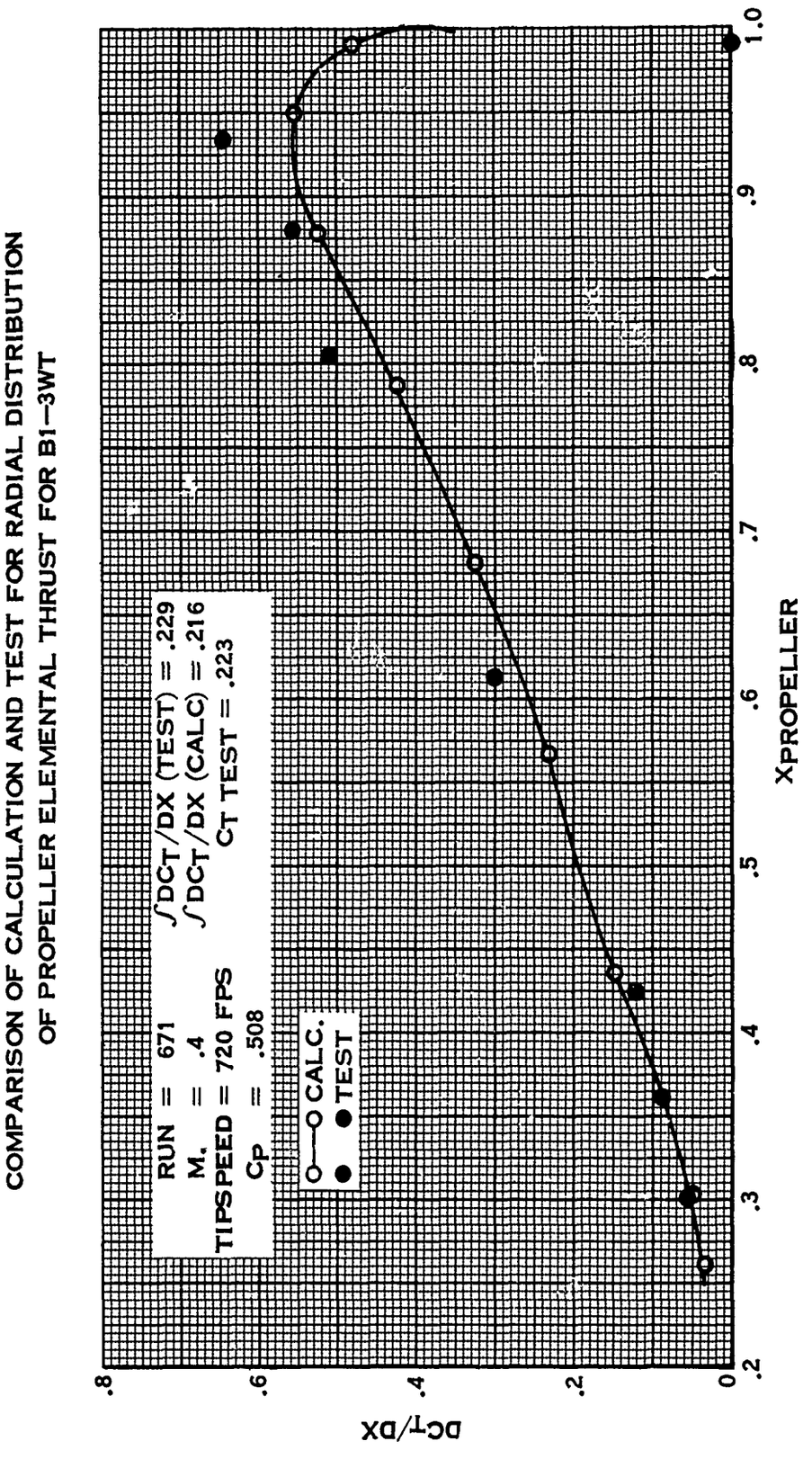
COMPARISON OF CALCULATION AND TEST FOR RADIAL DISTRIBUTION
OF PROPELLER ELEMENTAL THRUST FOR B1-3WT
RUN = 671
M. = .4
TIPSPEED = 720 FPS
CP = .508
∫DCT/DX (TEST) = .229
∫DCT/DX (CALC) = .216
CT TEST = .223
CALC.
TEST
DCT/DX
.8
.6
.4
.2
0
.2
.3
.4
.5
.6
.7
.8
.9
1.0
XPROPELLER

FIGURE 67.

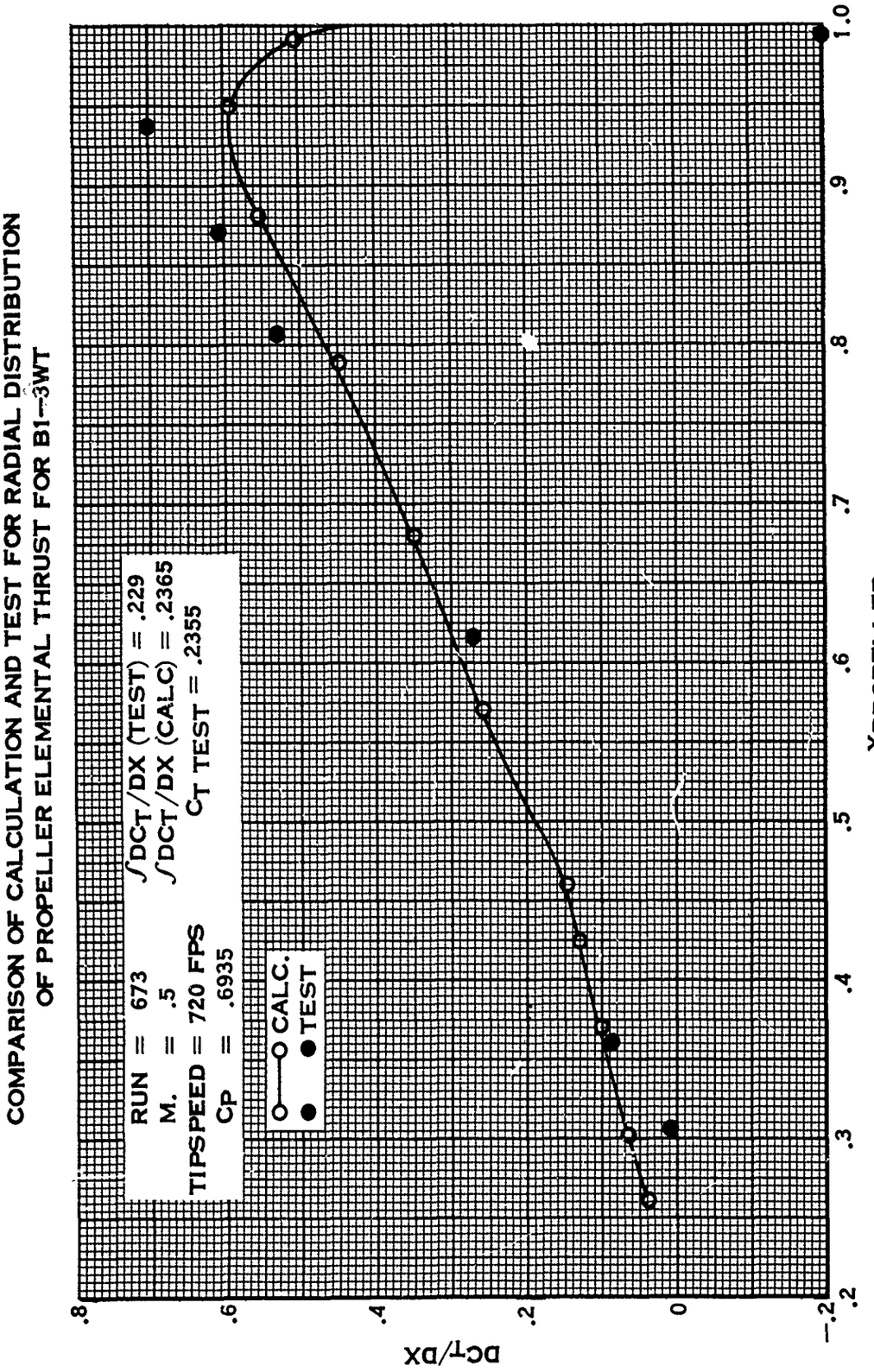
COMPARISON OF CALCULATION AND TEST FOR RADIAL DISTRIBUTION
OF PROPELLER ELEMENTAL THRUST FOR B1-3WT
RUN = 673
M. = .5
TIPSPEED = 720 FPS
Cp = .6935
∫DCT/DX (TEST) = .229
∫DCT/DX (CALC) = .2365
CT TEST = .2355
CALC.
TEST
DCT/DX
.8
.6
.4
.2
0
-.2
.2
.3
.4
.5
.6
.7
.8
.9
1.0
XPROPELLER

FIGURE 68.

7.4.3d (Continued)

In summary, the good performance comparisons of calculations and tests for Mach numbers $\gtrsim 0.20$, thrust derivative comparisons and axial velocity comparisons all confirm that the velocity flow field in the propeller plane is being well predicted.

7.4.4 Shroud Net Thrust Comparisons

The two methods chosen in paragraph 6.3 for the calculation of the shroud inviscid thrust are considered. The shroud drag is computed by the flat plate method described in paragraph 6.4.2 and Eq. (53). The net thrust coefficient $C_{T\ net}$ is defined as the difference of the inviscid thrust and shroud drag. The two methods for the inviscid drag calculation are listed below, for convenience:

Method 2 - Based on Momentum Theorem, jet velocity computed by scaling propeller circulation distribution

Method 3 - Based on Momentum Theorem, jet velocity computed in terms of propeller thrust coefficient.

As discussed in paragraph 7.4.1, the $C_{T\ net}$ comparison is divided into the two following categories.

A. Effects of primary parameters, i.e.,
   1. Power coefficient
   2. Area ratio
   3. Mach number
   4. RPM

B. Effects of secondary parameters, i.e.,
   1. Tip clearance
   2. Blade planform
   3. Propeller location
   4. Shroud chord/diameter ratio
   5. Shroud lip shape
   6. Number of blades

7.4.4a Primary Parameters

The primary parameters represent those variables which have a first order effect on performance and are the more important.

The variation of net thrust coefficient with the primary parameters for the 1.1, 1.2 and 1.3 area ratio shrouds is shown in Fig. 69, 70, and 71. Presented are plots of $C_{T\ net}$ versus propeller power coefficient for the range of Mach numbers 0.05 through 0.5 All curves are for a constant propeller rotative speed so the Mach number variation

7.4.4a (Continued)

is also equivalent to a J variation. Each figure contains 3 curves for each Mach number. The solid line represents the experimental results, the short dashed lines represent the momentum based on propeller thrust coefficient (Method 3) and the long dashed lines, the momentum based on propeller circulation distribution (Method 2). These curves lead to three primary conclusions:

1. The agreement between test and theory for either method is fair for the higher Mach numbers.

2. At the lower Mach numbers, Method 3 is superior.

3. Both methods qualitatively predict the variation of $C_{T\ net}$ with Mach number, area ratio and power coefficient in their regimes of applicability.

The $C_{T\ net}$ variation with Mach number and power coefficient is shown in each of Fig. 69, 70 and 71. The area ratio variation shown from figure to figure, is cross-plotted as $C_{T\ net}$ versus area ratio in Fig. 72a and 72b for the range of C_P's and Mach numbers. These figures show clearly the way in which each method predicts the area ratio effect. Overall, both methods are good at 0.3 Mach number as may be expected since here, compressibility effects are small while the forward flight velocity is high enough to satisfy the assumptions of the theory. At M = 0.2, the trend is better predicted by Method 3, as is also expected since its validity extends to the lower Mach numbers. At 0.4 Mach number, neither method excels, but this may be due to compressibility effects. In general, the trends are properly predicted by both methods; Method 2 tending to overestimate the effect of area ratio and Method 3 to underestimate it.

To further illustrate these points, an alternate presentation is considered in which the differences between test and theory are considered on a percent error basis.

To simplify the presentation of the large amount of data contained in Fig. 69 through 71, an error measure has been defined for each configuration and Mach number. This definition leads to the elimination of power coefficient as a variable, by replacing it by the root mean square error in $C_{T\ net}$ over the power coefficient range. This is better explained by the following development.

$C_{T\ net}$ is, in general, a function of C_P, M, and area ratio, i.e.,

$$C_{T_{net}} = f(C_P, M, A_4/A_2)$$

Choose a set of C_P's, $(C_{P_n}, n = 1, 2, \ldots\ldots)$.

For a constant Mach number and area ratio, the error in $C_{T\ net}$ for each C_P can be computed from Fig. 69, 70, or 71; i.e.,

SHROUD PERFORMANCE COMPARISONS OF CALCULATIONS AND TEST – EFFECT OF MACH NUMBER

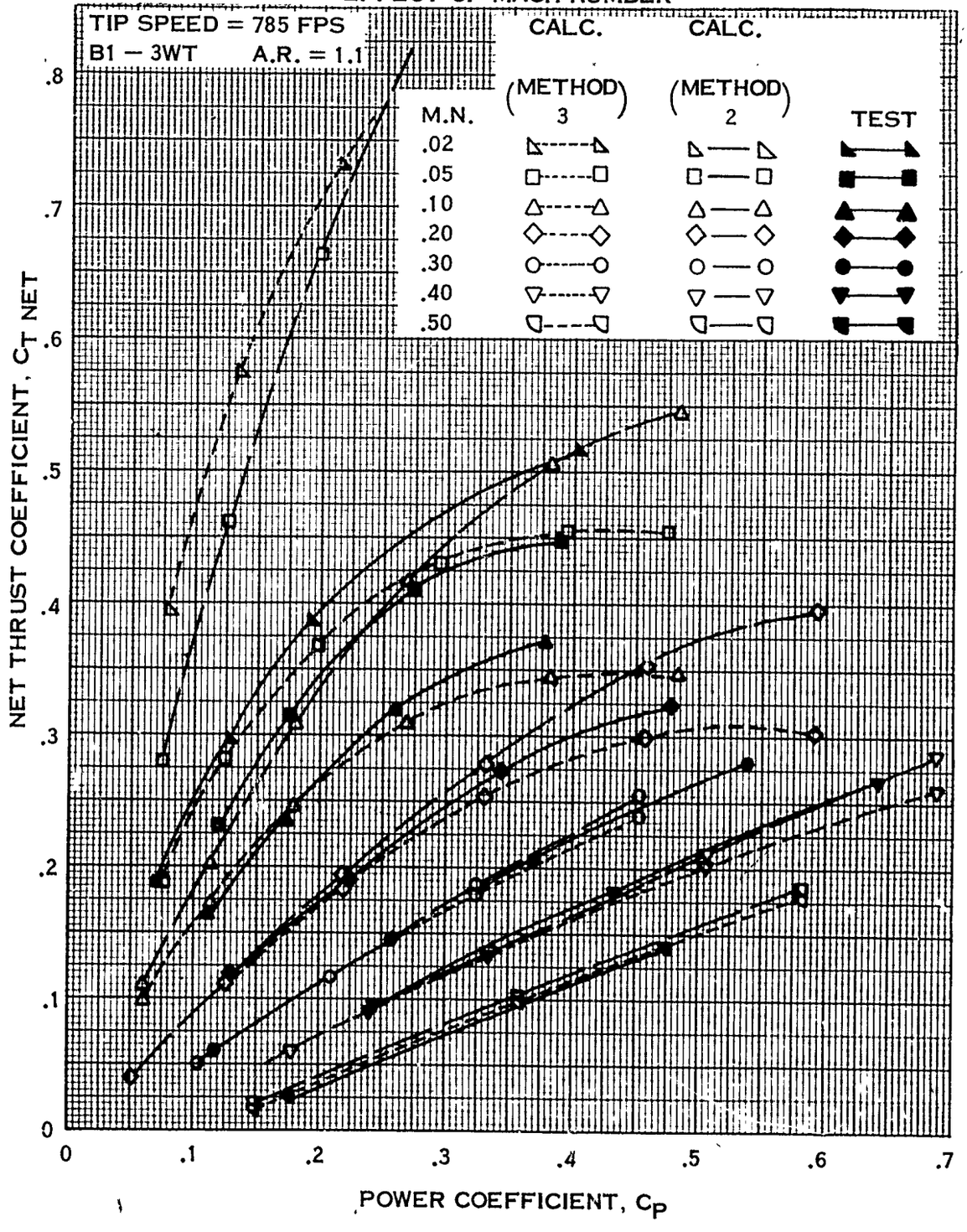

FIGURE 69.

SHROUD PERFORMANCE COMPARISONS OF CALCULATIONS AND TEST—
EFFECT OF MACH NUMBER

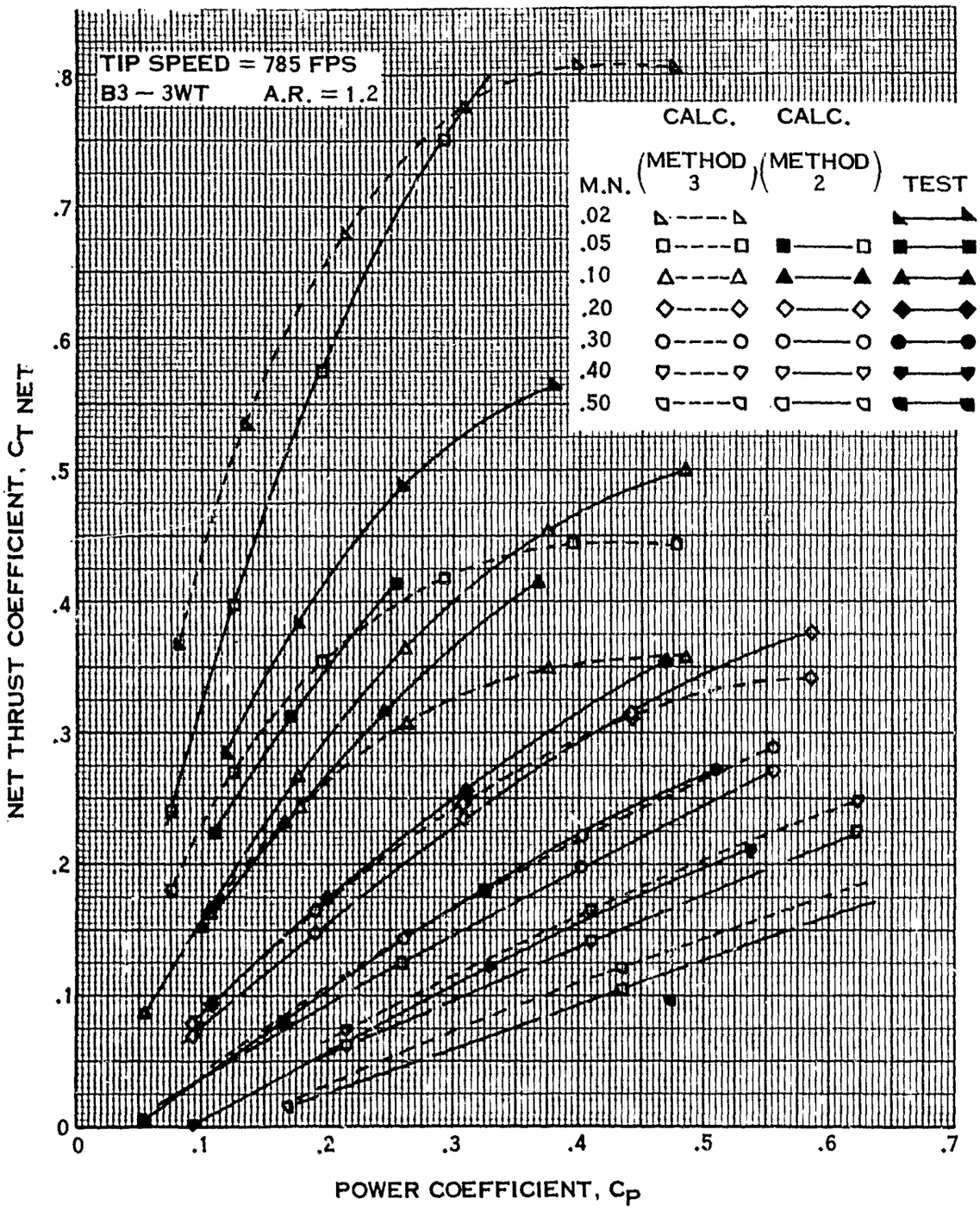

FIGURE 70.

SHROUD PERFORMANCE COMPARISONS OF CALCULATIONS AND TEST — EFFECT OF MACH NUMBER

TIP SPEED = 785 FPS
B4 — 3WT A.R. = 1.3

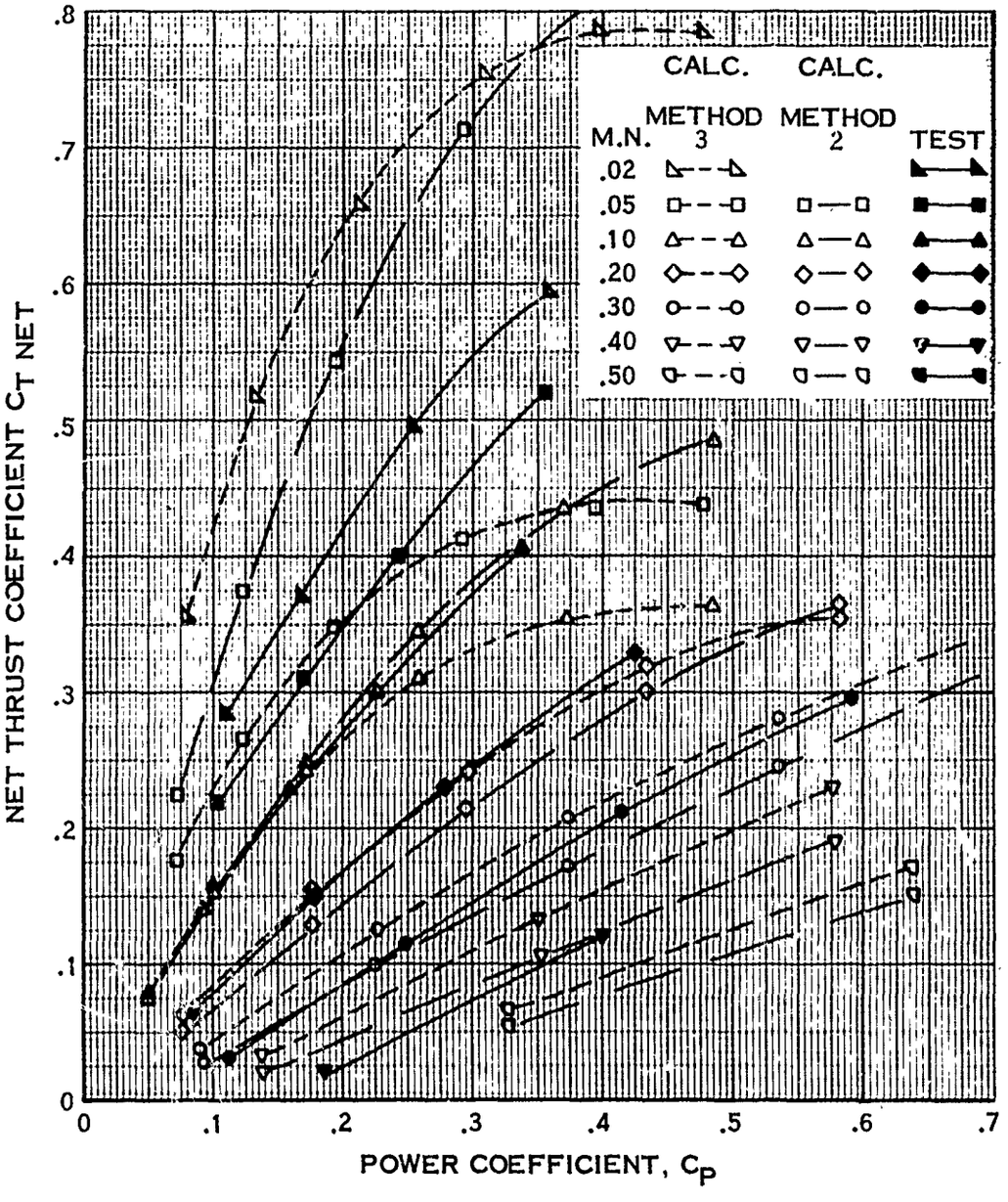

FIGURE 71.

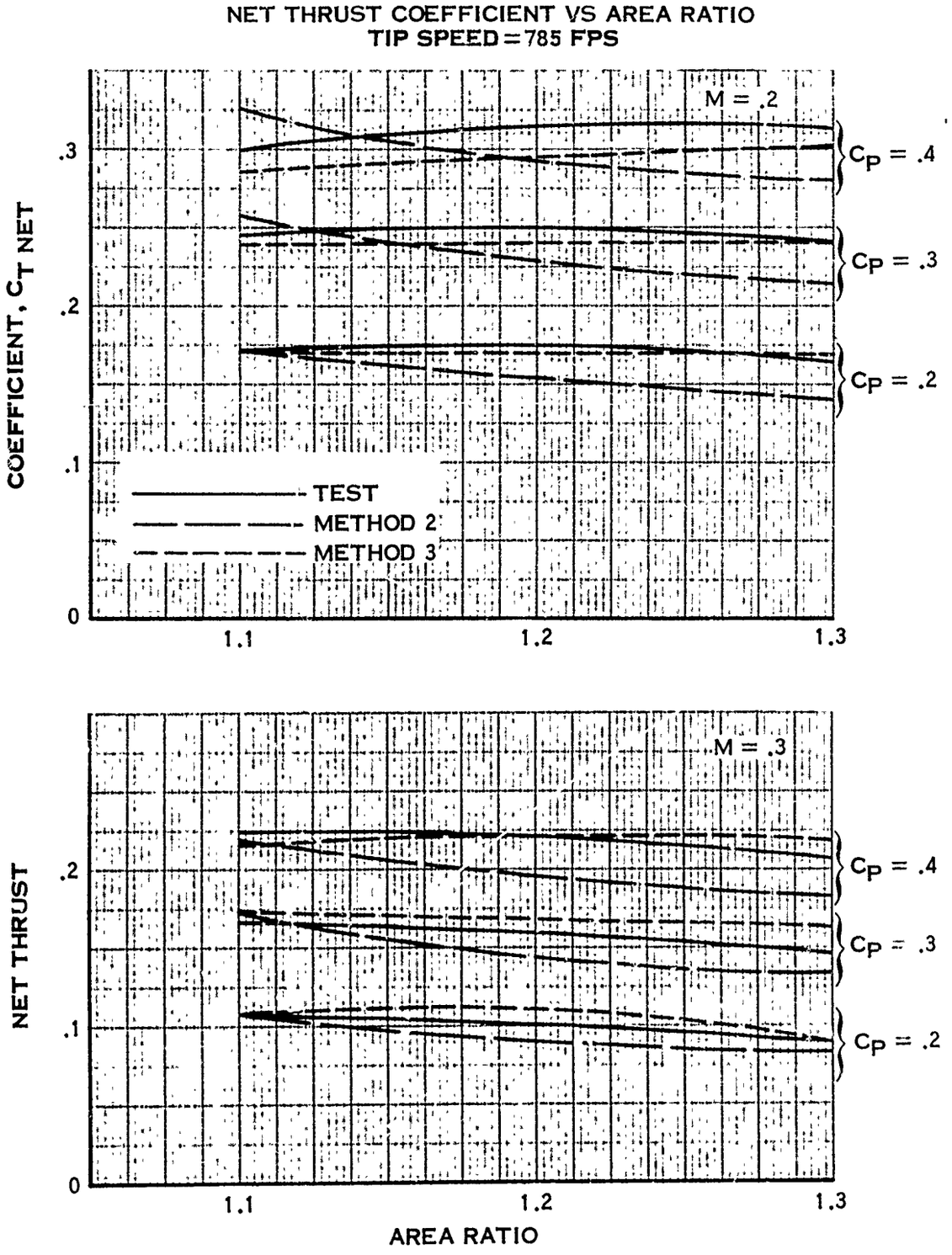
NET THRUST COEFFICIENT VS AREA RATIO
TIP SPEED = 785 FPS
M = .2
C_P = .4
C_P = .3
C_P = .2
COEFFICIENT, $C_{T\ NET}$
.3
.2
.1
0
TEST
METHOD 2
METHOD 3
1.1
1.2
1.3
M = .3
C_P = .4
C_P = .3
C_P = .2
NET THRUST
.2
.1
0
1.1
1.2
1.3
AREA RATIO

FIGURE 72A.

NET THRUST COEFFICIENT VS AREA RATIO

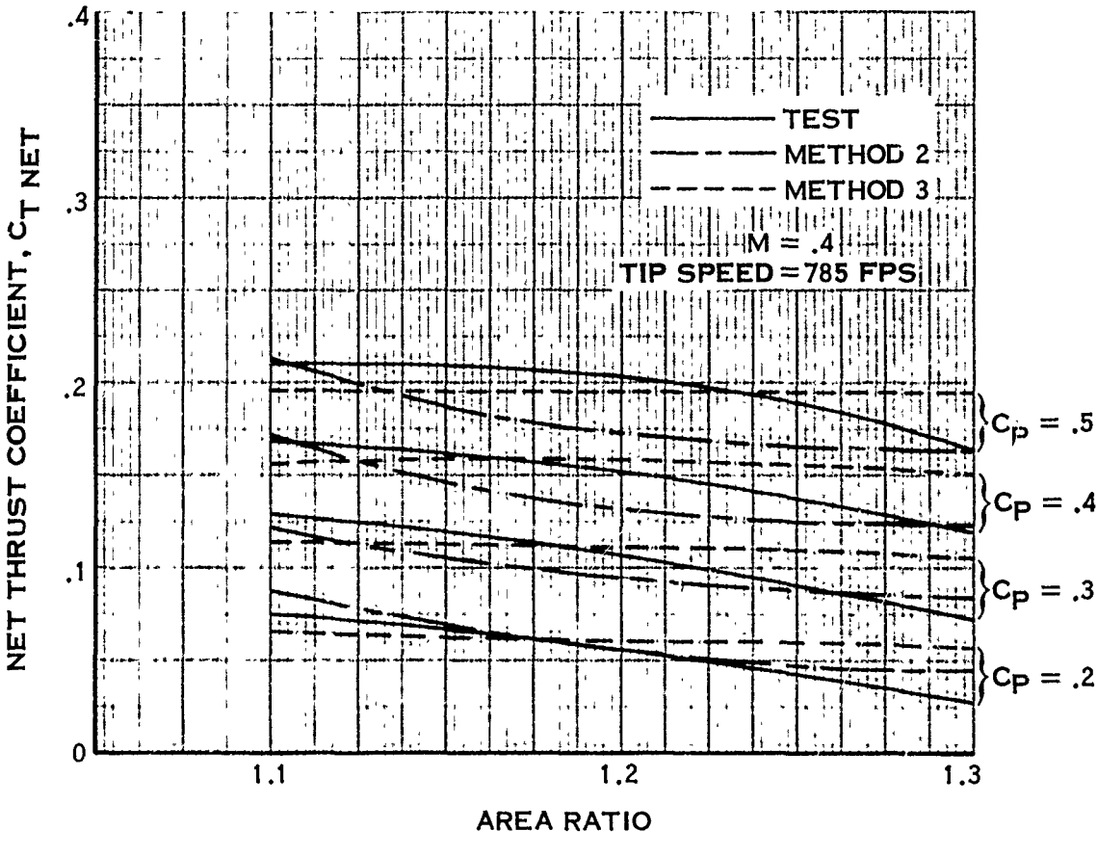

FIGURE 72B.

7.4.4a (Continued)

$$E_n = \left| \frac{C_{T\ net}^{calc} - C_{T\ net}^{theory}}{C_{T\ net}^{calc}} \right|_{\substack{C_P = C_{P_n} \\ M \\ A_4/A_2}} \qquad (68)$$

where the subscripts on the right designate that the indicated parameters be held fixed. Now an overall measure of the error incurred by the C_P variation can be obtained by taking the square root of the sum of the squares of E_n divided by N, the total number of C_{P_n}'s used, i.e.,

$$E = \sqrt{\frac{\sum_{n=1}^{N} E_n}{N}} = E(M, A_4/A_2) \qquad (69)$$

Eq. (69) is no longer a function of power coefficient and is a measure of the error incurred for the particular Mach number and area ratio considered. E as defined above, is plotted in Fig. 73 for the two calculation methods and each area ratio, as a function of Mach number. This curve again illustrates for the higher Mach numbers that the errors in the $C_{T\ net}$ calculation methods can be significant and that neither method is consistently superior. For example, Method 2 appears superior for the 1.1 area ratio shroud whereas Method 3 is superior for the 1.2 area ratio shroud. Results for the 1.3 area ratio shroud show that Method 2 is better for Mach numbers beyond 0.3 and worse below 0.3. Thus, it is difficult to choose one method at the expense of another. Theoretical considerations do not shed much light on the choice of methods since both share many of the same limiting assumptions although Method 2, because it accounts for detail in the far wake, should have a slight edge. The assumption of Method 2, however, which states that the circulation in the far wake is a scaled version of the propeller circulation, may be unrealistic, in view of the wake distortion that takes place as the wake passes through the shroud and over the centerbody. This may, in part, explain the lack of superiority of one method over the other. Another unknown which enters is the shroud drag. This has been obtained theoretically and could be partially responsible for the discrepancies observed between test and theory in Fig. 69 through 73.

The picture at the lower Mach numbers is clearer as far as choice of method is concerned. Theoretical considerations and comparison with test data both indicate the superiority of Method 3, which obtains the jet velocity in the far wake in terms of propeller thrust coefficient and, as discussed in paragraph 6.3.4, has no inherent limitations on its range of applicability. Limitations do enter, however, in that the propeller thrust and average disk velocity, the two variables that determine $C_{T\ net}$, are computed by the T.A.R. method which, as indicated, loses validity as the lower Mach numbers are approached.

RMS ERROR VERSUS MACH NUMBER

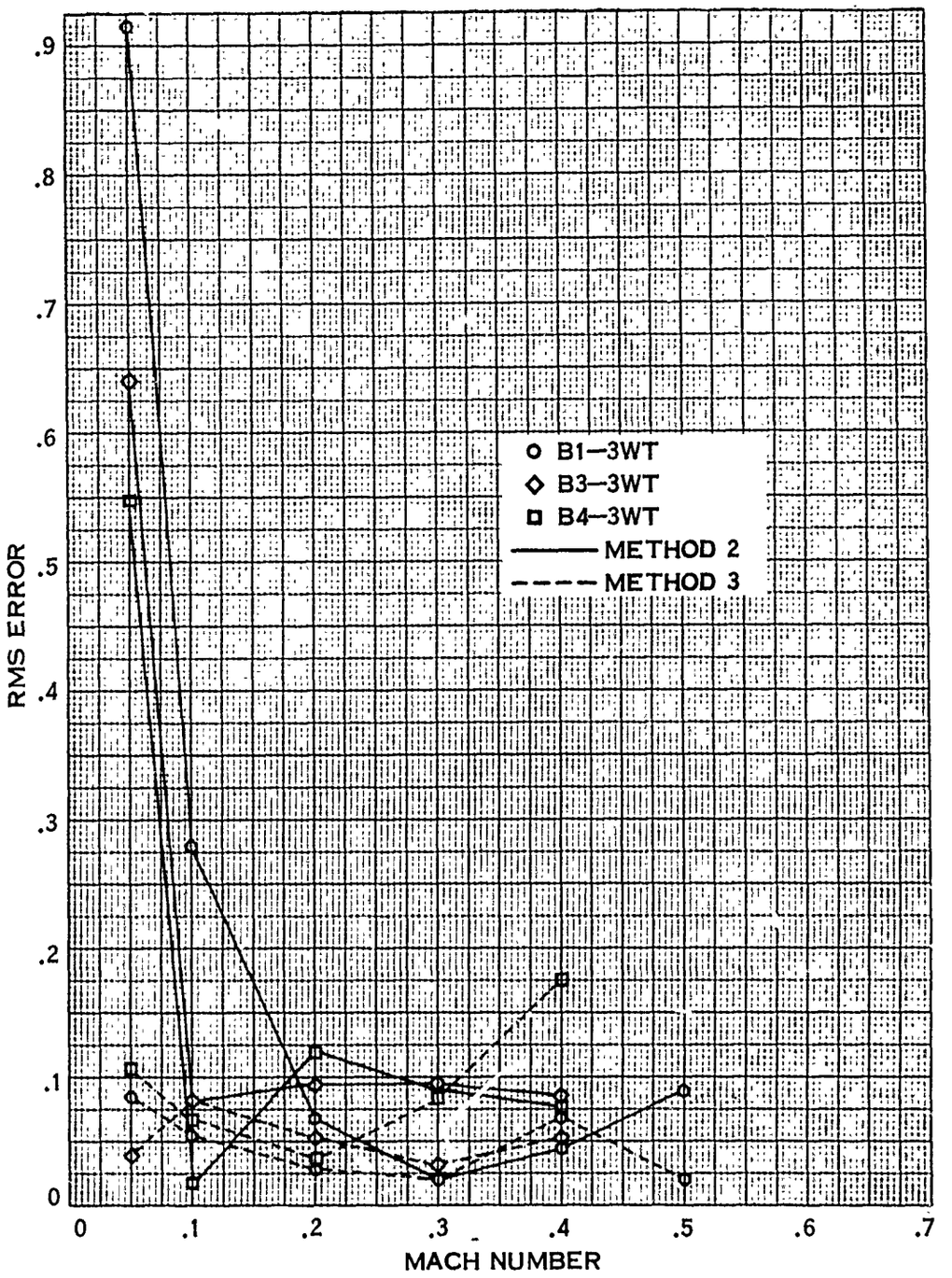

FIGURE 73.

7.4.4a (Continued)

The above discussion indicates that for the higher Mach number range, neither method gives consistently good results, although the general trends with area ratio, Mach number and power coefficient are predicted correctly, as shown in Fig. 69, 70 and 71. A maximum error on the order of 17% is exhibited in Fig. 73, with most errors being less than 10%. At the lower Mach numbers, Method 3 is far superior, as was anticipated, and here again the variations due to Mach number, area ratio and power coefficient are predicted, although the differences between test and theory are greater than is desirable. The next section will discuss the effects of the secondary parameters on theoretically predicted performance and their comparison with experimental results.

7.4.4b Secondary Parameters

Evaluation of the performance variations due to changes in the secondary parameters has been limited to the 0.3 Mach number case. The linearization assumptions are valid and the effects of compressibility are small at this Mach number, so it serves as a good basis for the evaluation. The variations due to changes in tip clearance, blade planform, propeller position and number of blades are shown in Fig. 74 through 77. Fig. 78, 79, and 80 show the variations due to changes in shroud lip shape, shroud length and shroud external shape.

The effect of tip clearance, as shown in Fig. 74 for tip clearance ratios, of 0.911, 0.909, and 0.903 is small. The theoretical predictions also show a small effect. The levels are better predicted by Method 2 but here again the differences are quite small.

Variations in blade planform were also investigated to see the effect of propeller circulation on shroud performance. The three planforms are described in paragraph 7.2, and the effect of this variation on performance ($C_{T\ net}$) is exhibited in Fig. 75. Again the effect is secondary with the B1-3R giving the higher thrust. This trend is predicted well by the theory, with Method 2 yielding slightly better agreement with test.

The effect of propeller position $\overline{Xp}$ is considered next, (Fig. 76). The propeller is located at $\overline{Xp}$ = -0.1023 and - 0.2528. The data and the calculations both show the effect of changing $\overline{Xp}$ to be negligible.

The number of blades variation, as shown in Fig. 77, causes a slight decrease in performance with the smaller number of blades. This was predicted by both methods, the results of Method 2 slightly higher than test while the results of Method 3 were slightly lower.

The effects of shroud lip shape, length and external shape on net thrust were found to be small also, again as predicted by both theoretical methods.

SHROUD PERFORMANCE COMPARISON OF CALCULATION AND TEST—
EFFECT OF PROPELLER TIP CLEARANCE

TIP SPEED = 785 FPS
MACH NUMBER = 0.3

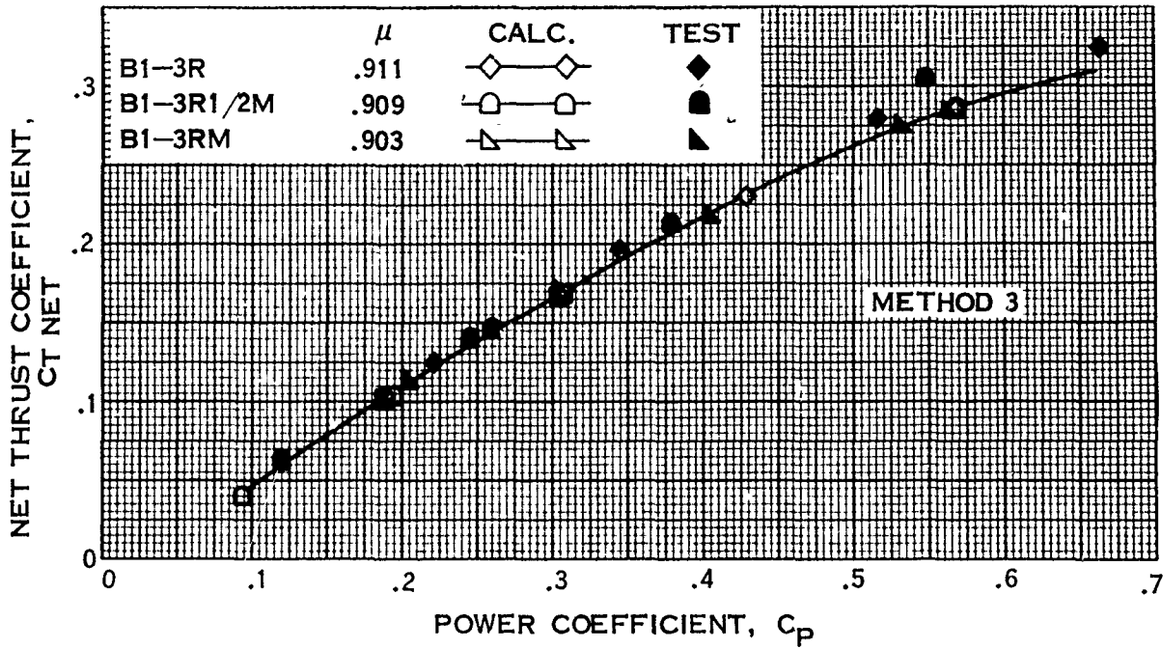

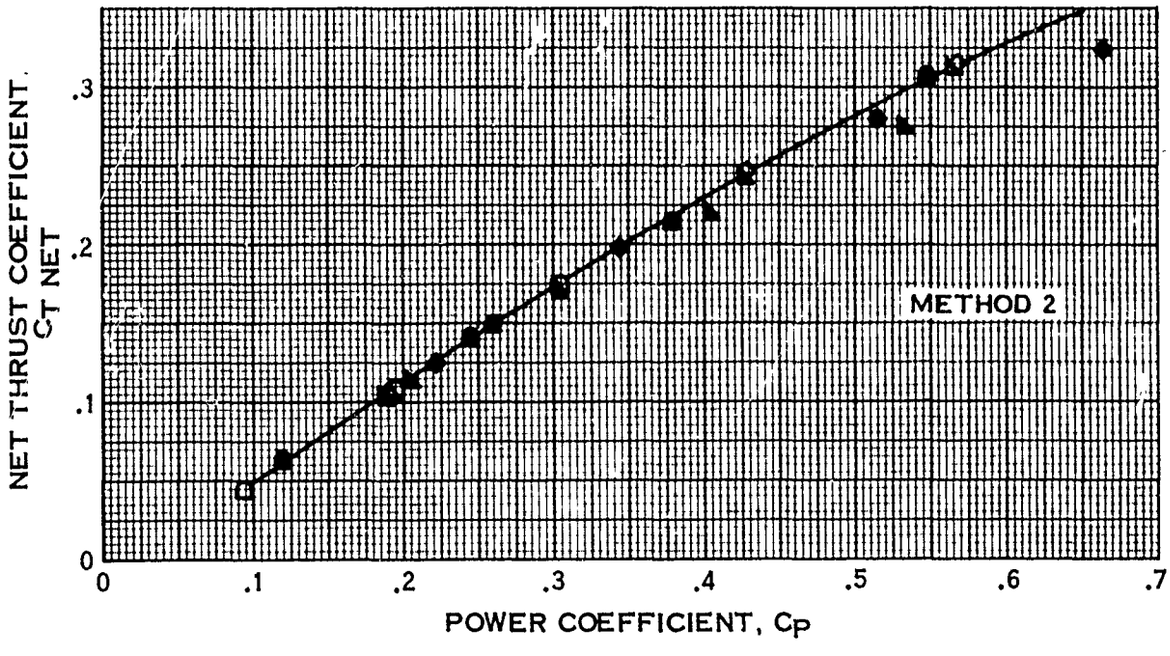

FIGURE 74.

SHROUD PERFORMANCE COMPARISON OF CALCULATION AND TEST—
EFFECT OF PROPELLER PLANFORM

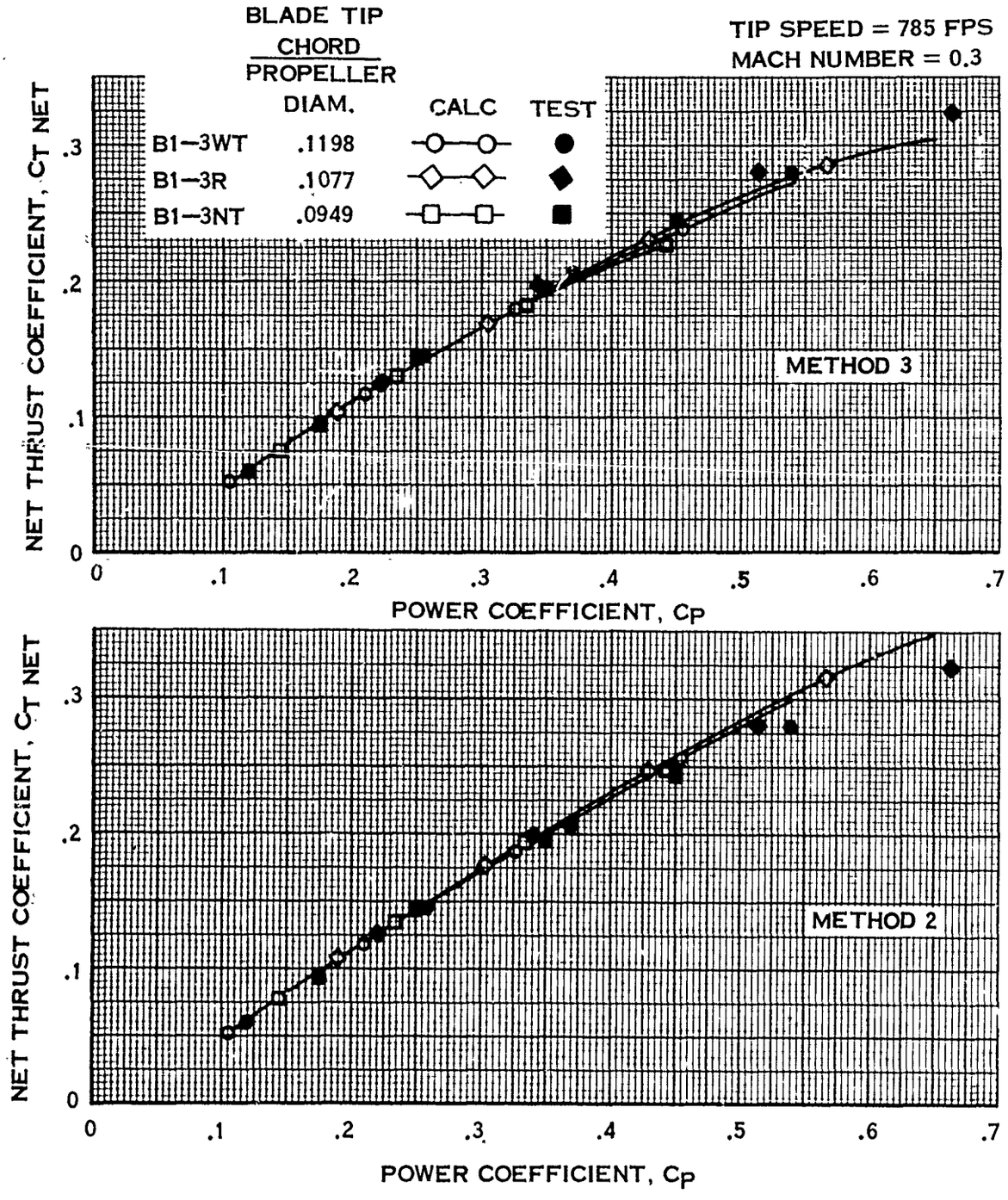

FIGURE 75.

SHROUD PERFORMANCE COMPARISON OF CALCULATION AND TEST—
EFFECT OF PROPELLER POSITION
TIP SPEED = 785 FPS
MACH NUMBER = 0.3

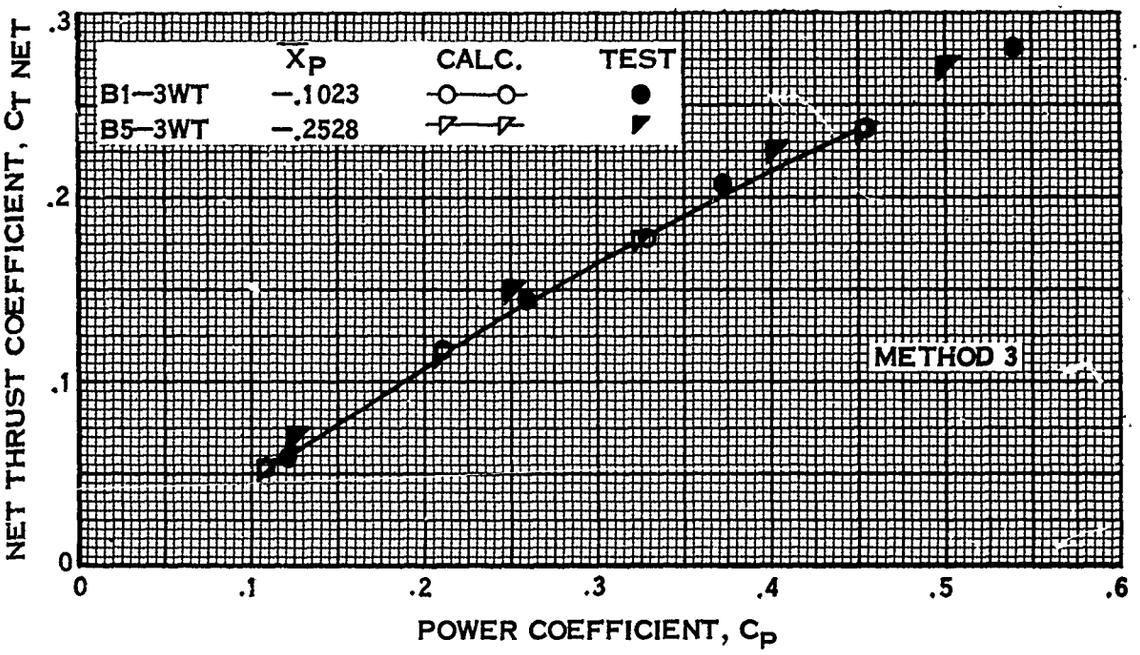

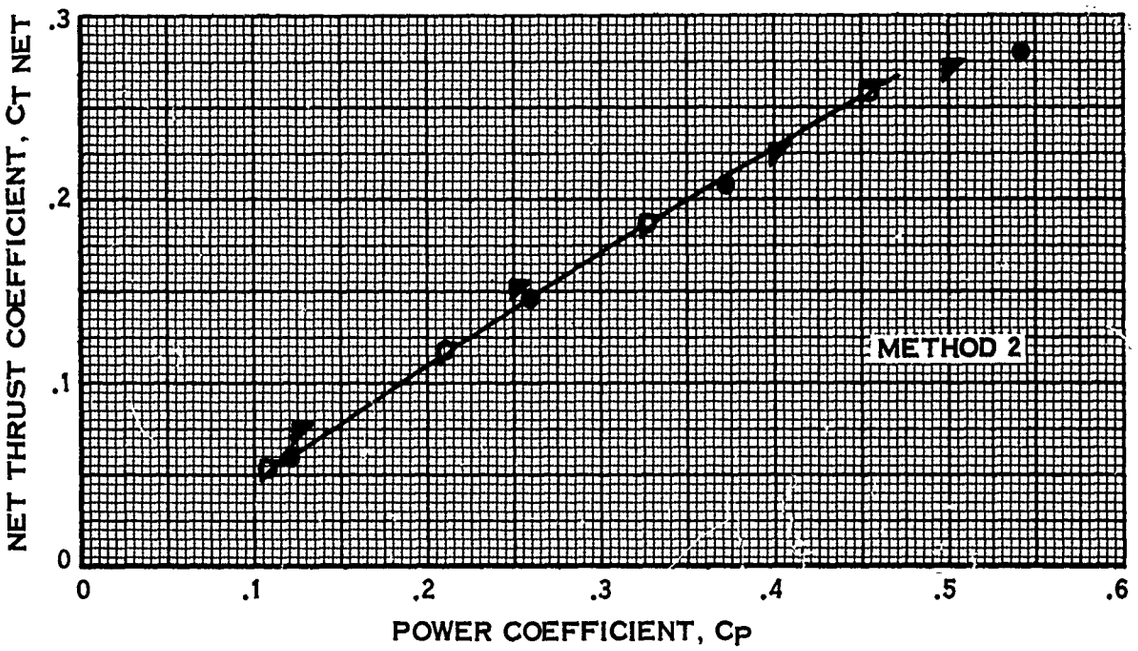

FIGURE 76.

SHROUD PERFORMANCE COMPARISON OF CALCULATION AND TEST—
EFFECT OF NUMBER OF BLADES

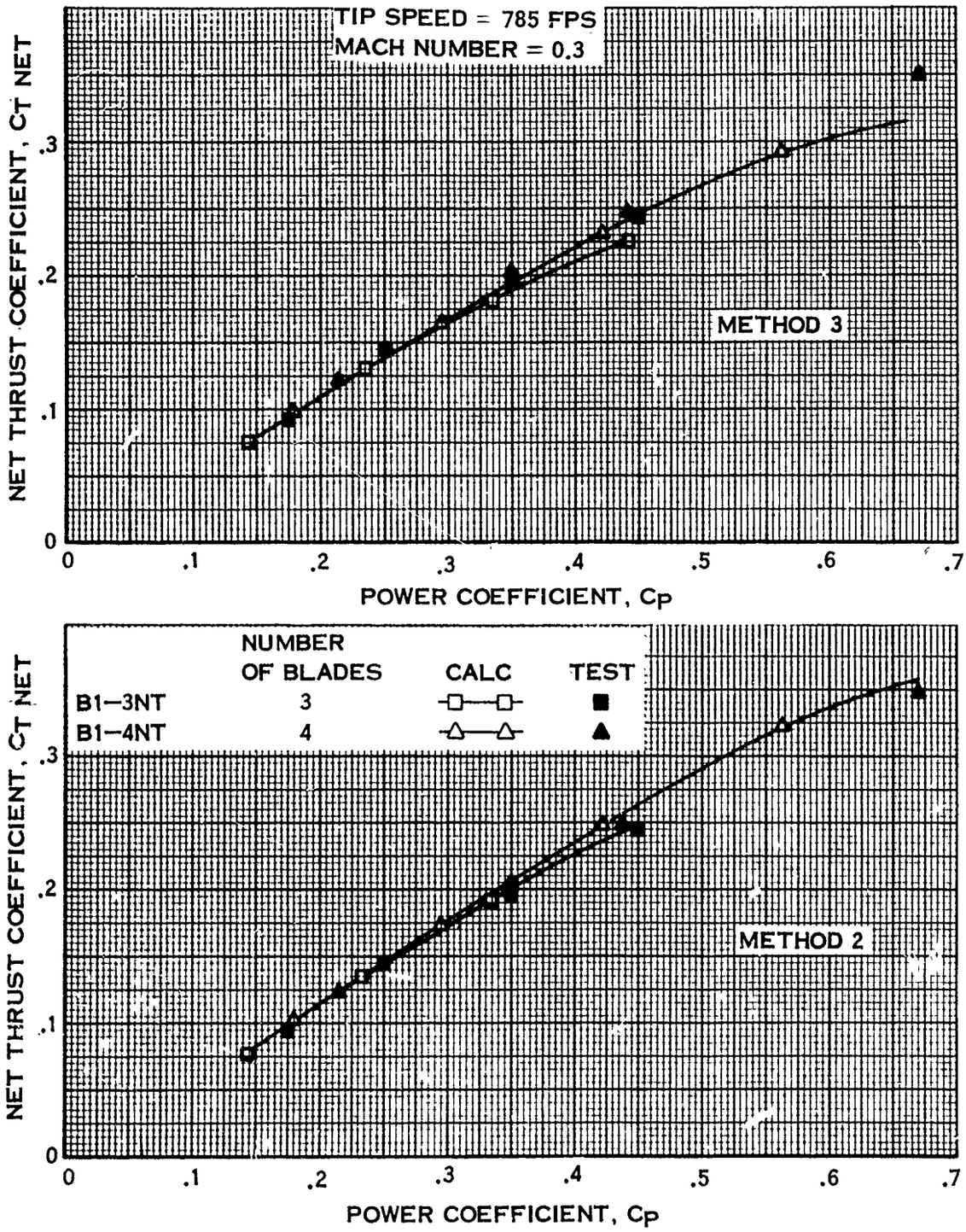

FIGURE 77.

SHROUD PERFORMANCE COMPARISON OF CALCULATION AND TEST—
EFFECT OF SHROUD LIP SHAPE

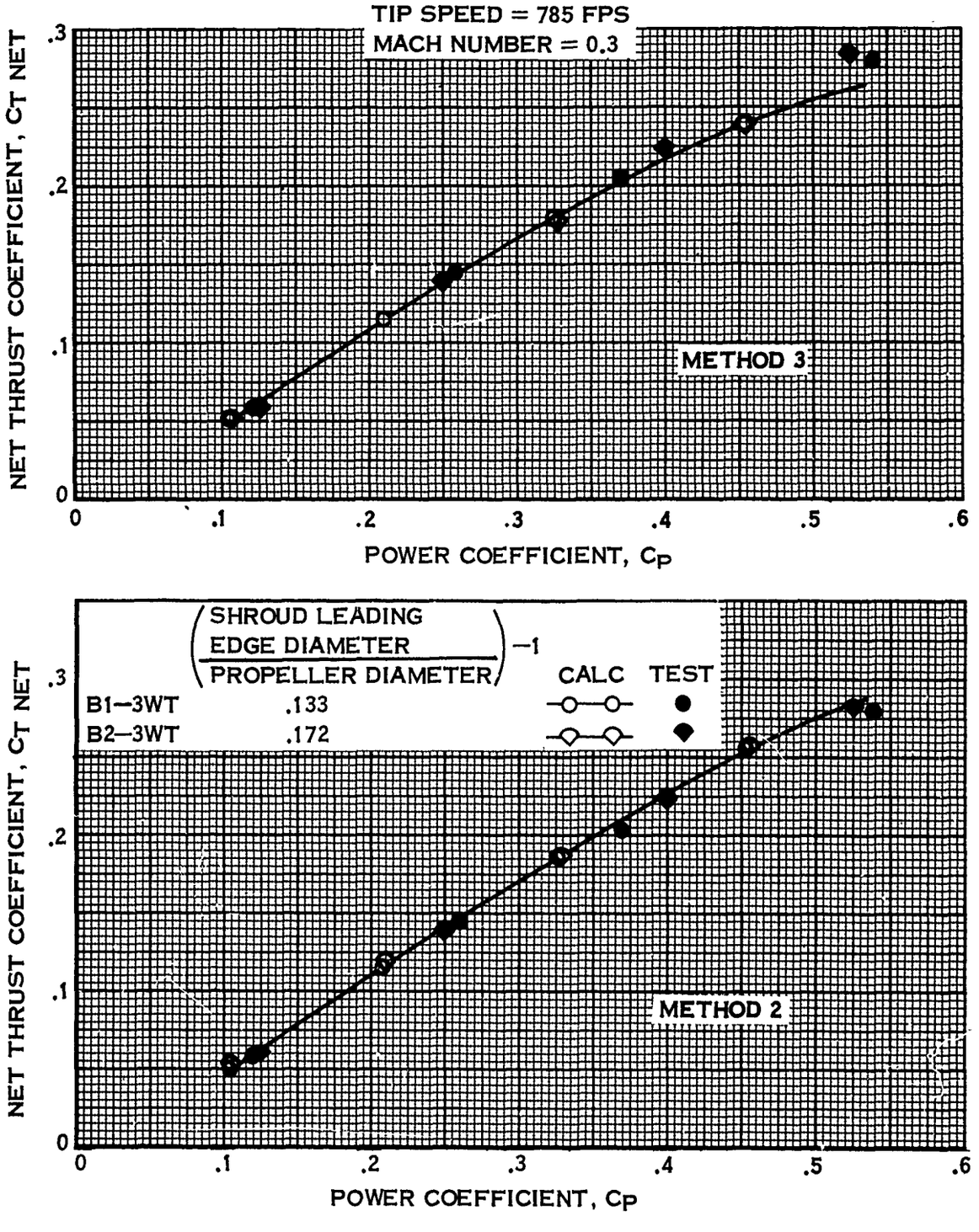

FIGURE 78.

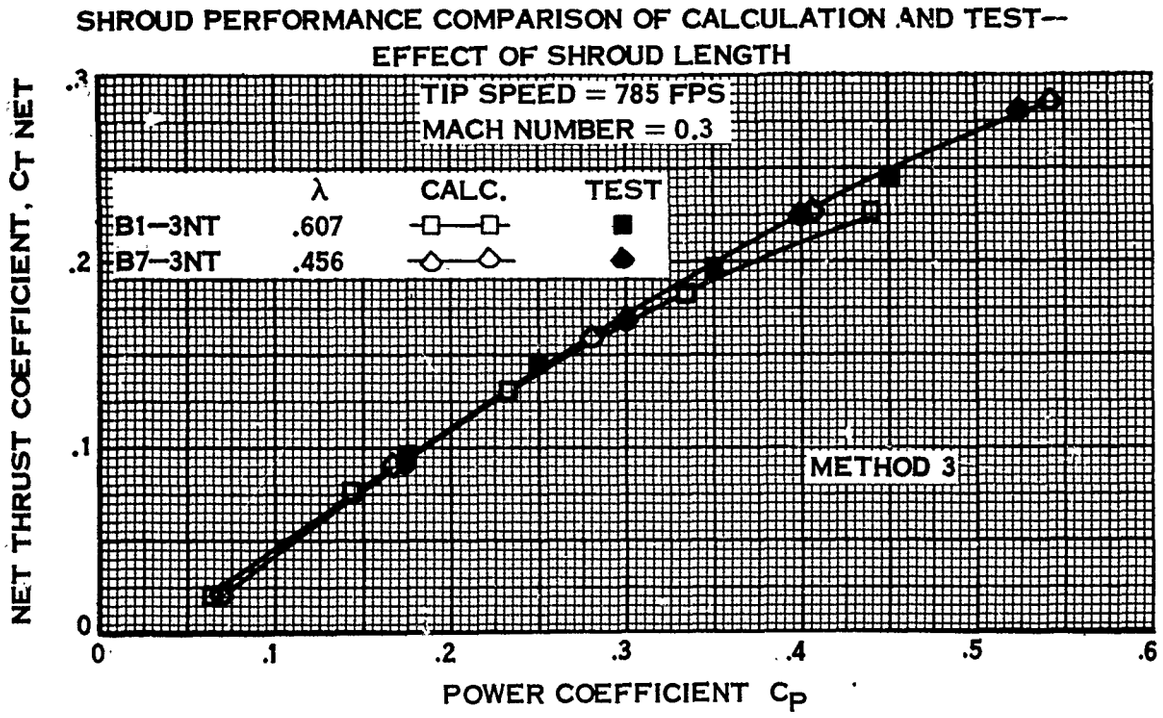
SHROUD PERFORMANCE COMPARISON OF CALCULATION AND TEST--
EFFECT OF SHROUD LENGTH
TIP SPEED = 785 FPS
MACH NUMBER = 0.3
λ
CALC.
TEST
B1—3NT .607
B7—3NT .456
METHOD 3
NET THRUST COEFFICIENT, C_T NET
POWER COEFFICIENT C_P
0
.1
.2
.3
.4
.5
.6

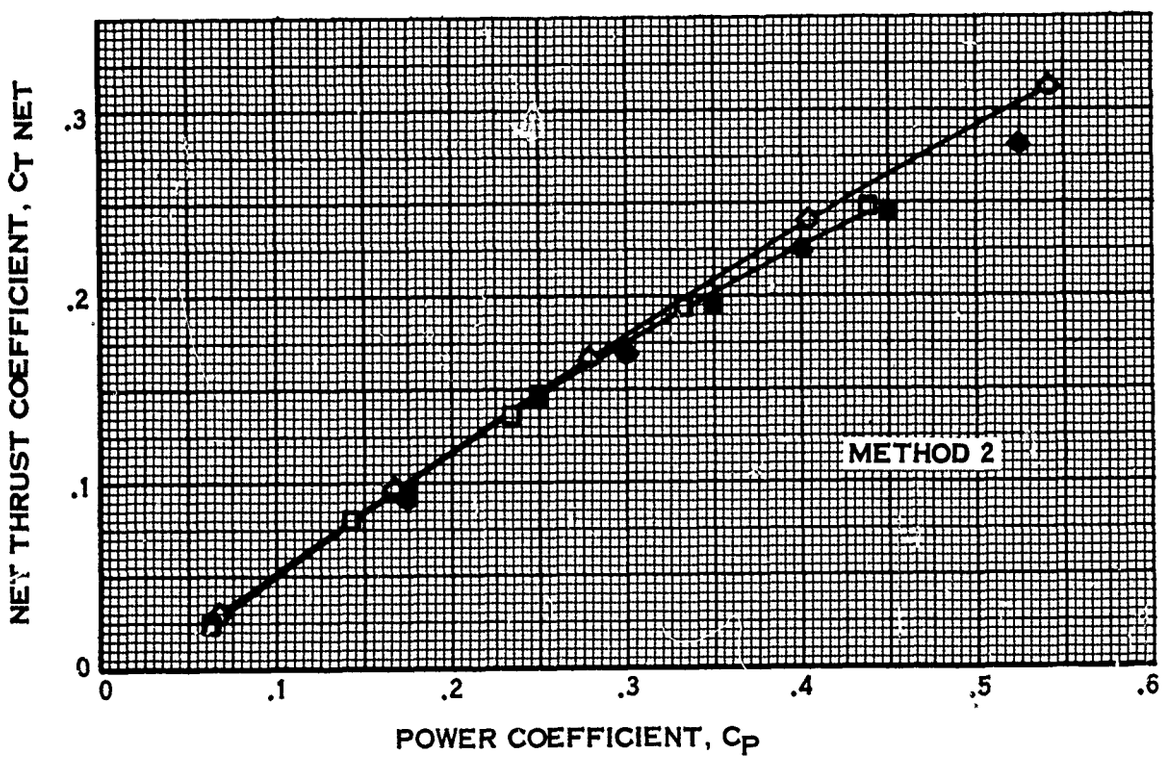
METHOD 2
NET THRUST COEFFICIENT, C_T NET
POWER COEFFICIENT, C_P
0
.1
.2
.3
.4
.5
.6

FIGURE 79.

SHROUD PERFORMANCE COMPARISON OF CALCULATION AND TEST
EFFECT OF SHROUD EXTERNAL SHAPE
TIP SPEED = 785 FPS
MACH NUMBER = 0.30

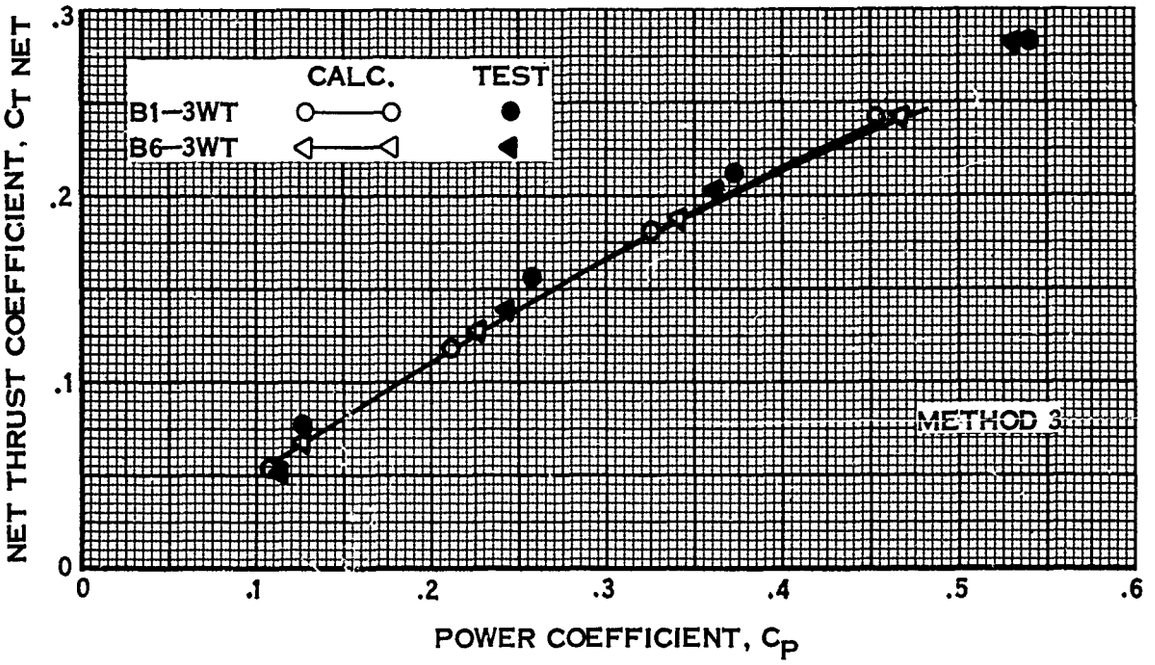

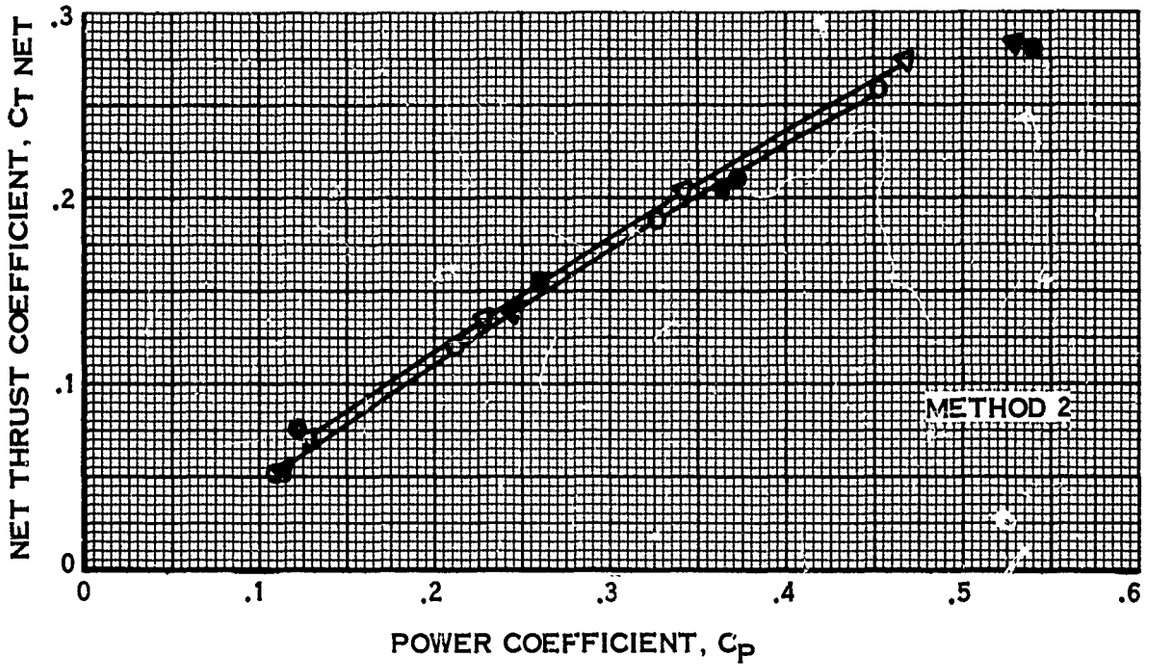

FIGURE 80.

7.4.4c Summary

Comparison of the theoretically predicted total thrusts with experimental results indicated that a clear choice between Method 2 and Method 3 was not possible. Method 3 was superior in the low Mach number range, as expected from theoretical considerations. However, for the higher Mach numbers, neither method appeared totally adequate. The reason for the descrepancies at the higher Mach numbers is threefold. First, both methods require simplifying assumptions for the calculation of the jet velocity: Method 2 requiring the assumption of negligible wake contraction and Method 3 the assumption of one dimensional flow. Second, the total thrust in either case is based on the knowledge of the axial velocity in the plane of the propeller and either the propeller total thrust or its circulation distribution. Both of these are subject to the same inherent errors of the T. A. R. theory, and when used in the same equation compound the errors. Finally, the shroud drag is estimated theoretically and is itself subject to error.

The performance changes due to changes in the secondary parameters were small, as expected, and on the whole properly accounted for by both methods.

7.4.5 Discussion of Centerbody Effects

In Phase I, there was some uncertainty as to whether the parametric variation effects on performance might be clouded by the effect of the propeller test rig centerbody. Therefore, performance comparisons were made of calculations based on the propeller test rig centerbody (PTR) and a slender centerbody (SB) with tests. Fig. 81 shows the centerbody physical differences. The performance comparisons for area ratio are shown on Fig. 82 and for propeller position on Fig. 83 for propeller thrust coefficient and net thrust coefficient versus power coefficient for a .3 Mach number.

Figure. 82 shows that there is a difference in propeller performance due to centerbody. To better understand what is happening, the propeller performance variation at $\bar{C}_P = 0.30$ was investigated and the results are tabulated in the following table.

	Test $C_{T_{prop}}$	Calc. $C_{T_{prop}}$ (PTR)	Calc. $C_{T_{prop}}$ (S.B.)
B1-3WT	0.177	0.181	0.171
B4-3WT	0.150	0.153	0.146
B1/B4	1.180	1.182	1.170

From the table above, it can be seen that propeller performance changes of 5-6% are computed due to the two centerbodies. The PTR representation better matches test results which were tested with such a centerbody. However, the changes in area ratio which are represented in the table by B1/B4 (A.R. = 1.1/A.R. = 1.3) show that the PTR computations agree well with test and that the SB differential computation only differs 1% from test. The net thrust comparisons show very slight differences

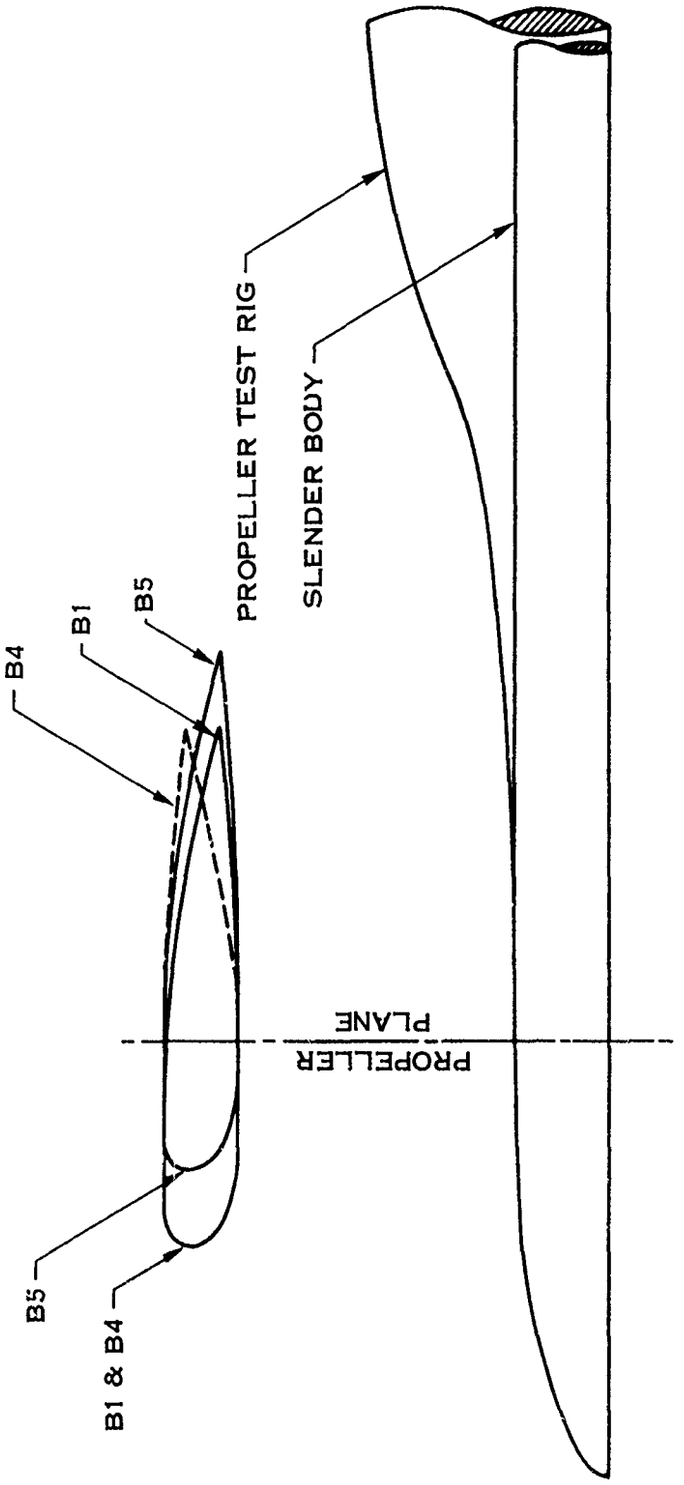

SKETCH OF SHROUD CONFIGURATIONS B1, B4, B5

FIGURE 81.

PERFORMANCE COMPARISON OF CALCULATION AND TEST — EFFECT OF CENTERBODY ON AREA RATIO

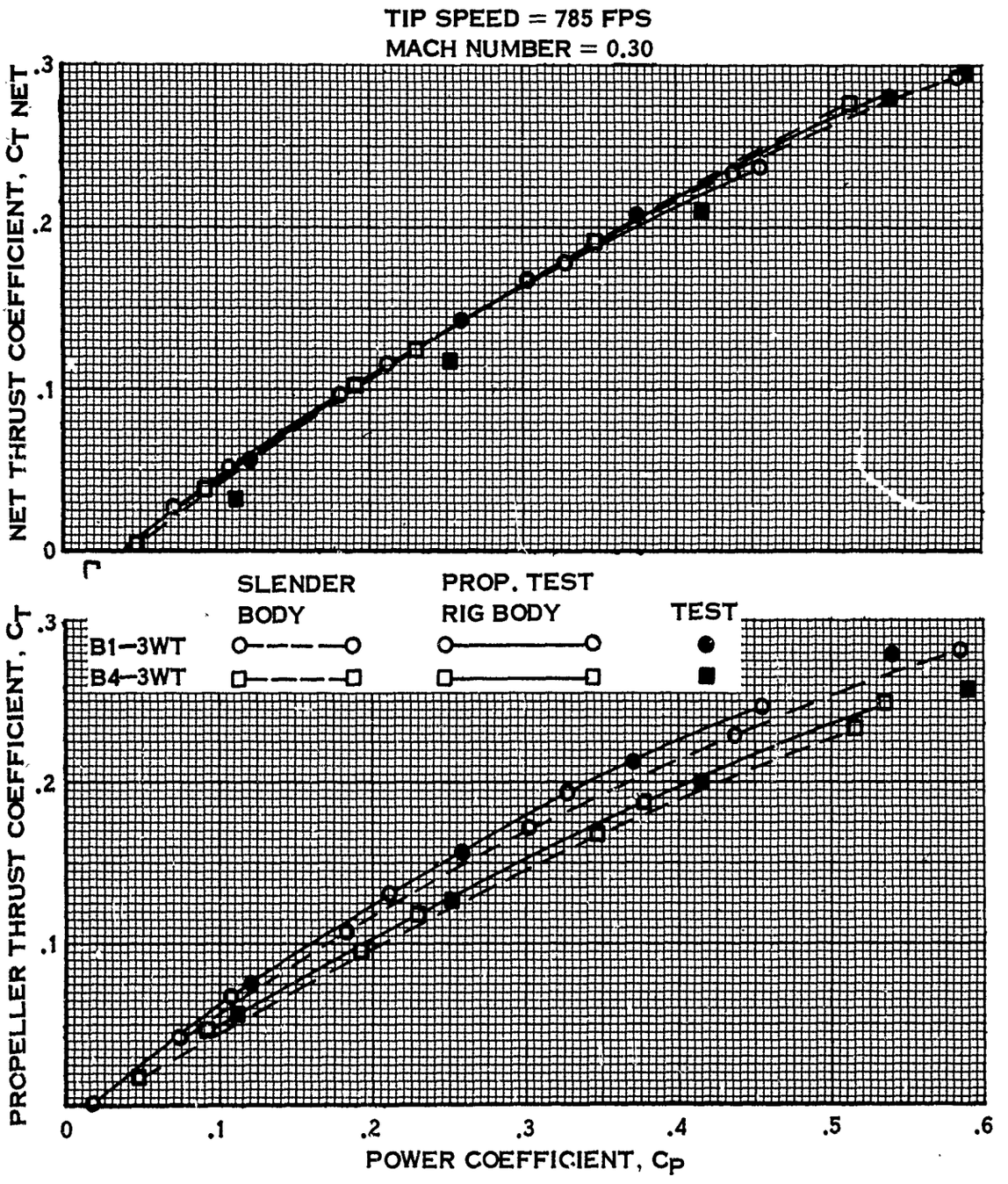

FIGURE 82.

7.4.5 (Continued)

with neither centerbody representation well defining the area ratio effect. The validity of the net thrust computational procedure has been discussed in paragraph 7.4.4. The net thrust results for the two centerbodies are comparable because of the compensating changes in Eq. (42) due to $\bar{V}_a/V_o$ and $C_{T\ prop}$ as shown in the table below:

	$\bar{V}_a/V_o$		$C_{T\ prop}$	
	PTR	S B	PTR	S B
B1	1.089	1.111	0.181	0.171
B4	1.289	1.356	0.153	0.146
B5	1.124	1.159	0.181	0.171

The effect on propeller position is shown in Fig. 83. Again, the PTR computation of propeller performance better matches test data and both methods show the same effect of parameter variation with the SB computations showing a lower level of performance. The net thrust comparison is similar to that seen for the area ratio variation.

In summary, the computational procedure does show a difference in performance due to centerbody configuration. The computations based on the PTR centerbody better match test data which is based on such a centerbody. The incremental parameter variation of area ratio and propeller position do not appreciably vary with centerbody configuration and only the performance level changes.

7.5 SUMMARY - COMPARISONS OF CALCULATION AND TEST

The comparisons of test and theory indicate that for the higher Mach numbers, the T.A.R. theory modified to include the corrections discussed in paragraph 6.2 predicts propeller performance that is in excellent agreement with experiment. At the lower Mach numbers, the comparison is poorer, and is attributed to inadequacies in the T.A.R. model and at static the propeller theory also. The good agreement between the theoretical and experimental axial velocity distributions and $d\bar{C}_T/dx$ distributions further substantiate the validity of the method for the higher Mach numbers.

The shroud total thrust calculation method presents a problem. The two methods investigated both gave fair agreement at the higher Mach numbers, whereas Method 3, as expected, was better at the lower Mach numbers. The agreement between test and theory was not as good as that exhibited by the propeller, indicating the need for further refinements in both the inviscid and viscous portions of the thrust calculation. Definite choice of one of the methods is unjustified at this point, and further investigation is warranted. For purposes of uniqueness in the computer program, however, Method 3 has been incorporated along with the shroud drag calculation method based on the flat plate friction drag.

PERFORMANCE COMPARISON OF CALCULATION AND TEST— EFFECT OF CENTERBODY ON PROPELLER POSITION

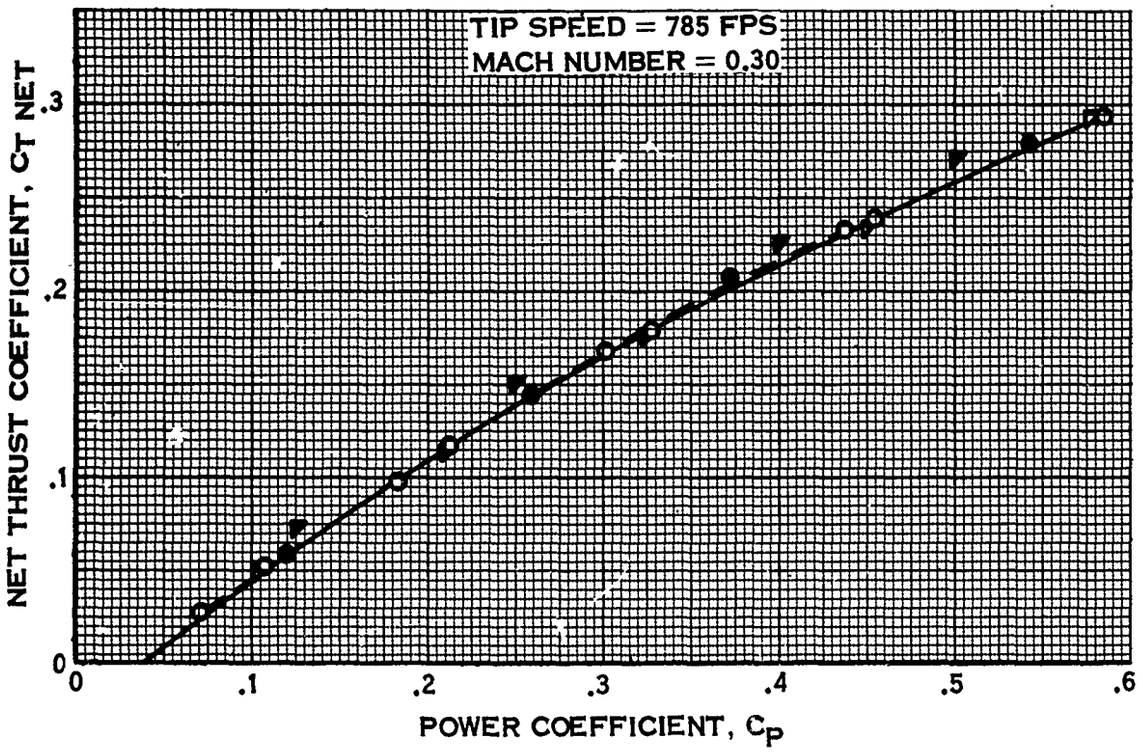

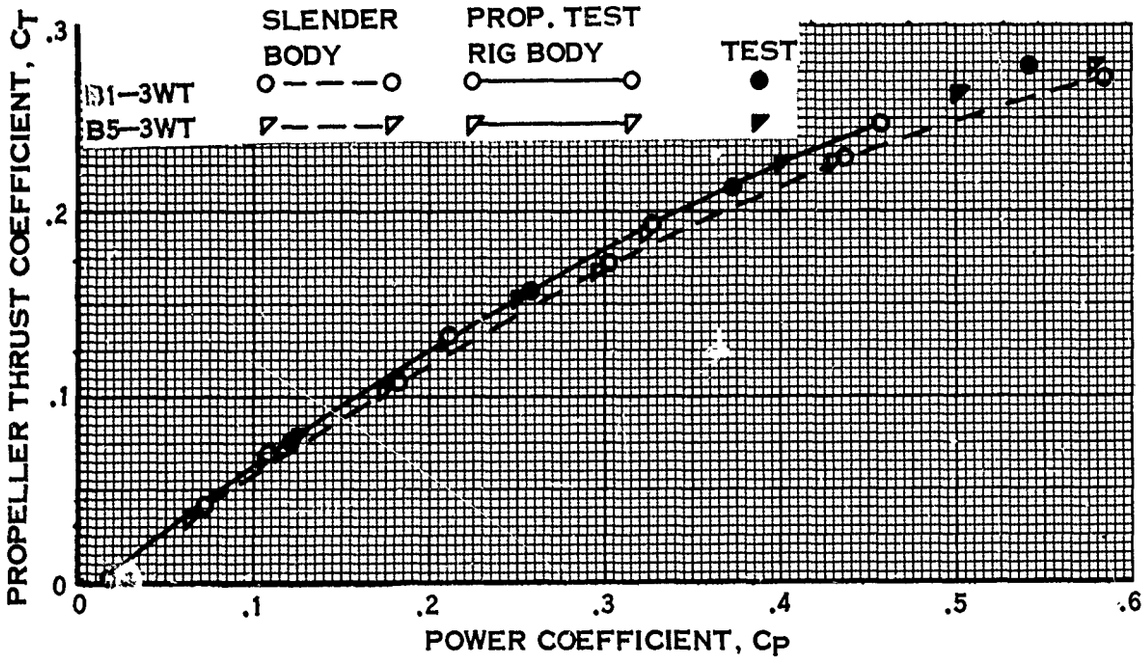

FIGURE 83.

7.5 (Continued)

The shroud pressure distribution was well predicted everywhere but near the leading edge at the higher Mach numbers. The singularities inherent in the theory give rise to infinite velocities there, which are partially corrected by application of the Riegels factor. The leading edge discrepancies are in part due to this and in part may be due to the inadequate prediction of the propeller velocities along the shroud reference line.

At the lower Mach numbers, the theoretical pressure distributions and performance predictions deviate significantly from the experimental values, due to the inapplicability of the theory at these lower Mach numbers.

The effect of centerbody on performance is properly predicted as shown by the comparisons in paragraph 7.4.5 for the PTR and the SB.

8.0 EXTENSION TO STATIC

Extension of the T.A.R. theory to include the static and low speed flight regime has not been successful. In view of its formulation, this is not surprising. In fact, it is impressive that it remains valid to as low a forward speed as it does. The purpose of this section is therefore to recommend the use of a temporary alternate calculation method for the low speed regime and to delineate the boundaries within which it is applicable.

To summarize, the various corrections applied to the theory improved the performance comparisons at the higher Mach numbers, but did not improve the lower Mach number agreement.

The propeller and net thrust predictions were in closest agreement with test data for values of $M \geq .2$. The shroud pressure distributions at $M = .3$ and $.5$ were good, but very poor for $M = .05$. A cutoff of $M = 0.2$ for the pressure distribution is also chosen since good comparison between test and theory still exists at this Mach number as shown in Fig. 84 for the B4-3WT. Below 0.2 Mach number the method loses accuracy and recourse to an alternate method is necessary. Hamilton Standard experience has been to use a less sophisticated theory based on the work of Patterson, discussed in Ref. 16. The application of this theory has been reduced to a convenient cook-book technique which is contained in Ref. 17. This theory does not account for the effects of such parameters as shroud shape, tip clearance, and propeller location, but is valid for the zero and low Mach number range. Since it does not account for shroud shape it is incapable of predicting shroud pressure distribution although it does account for the effect of area ratio. In addition, the method requires that the shroud exit plane static pressure be specified. This requires a-priori knowledge of the pressure field, which must be obtained experimentally. A value of this pressure equal to the free stream ambient value is found to be valid for shrouds with reasonable chord to diameter ratio (0.3 or greater). It is therefore recommended that the method of Ref. 17 be used in lieu of the T.A.R. method for values of M below 0.2 with a value of exit plane static pressure equal to the free stream ambient. It is also recommended that a method be derived for the low speed and static regime which has the sophistication to account for the effects of tip clearance, shroud shape, area ratio and also to predict shroud pressure distribution. The method must eliminate the shortcomings of the theory discussed herein, such as the invalid representation of the shroud thickness form, and should incorporate the corrections developed during this contract. The initial static regime work of T.A.R. (Ref. 18) based on the assumption of an infinitely thin shroud with small camber and a uniformly loaded propeller serves as a starting point for this effort. The inclusion of the effects of large camber and thickness and variable propeller circulation would result in a method that had the degree of sophistication required and when coupled with the forward flight method reported on herein, would provide a tool which is uniformly valid over the complete flight regime.

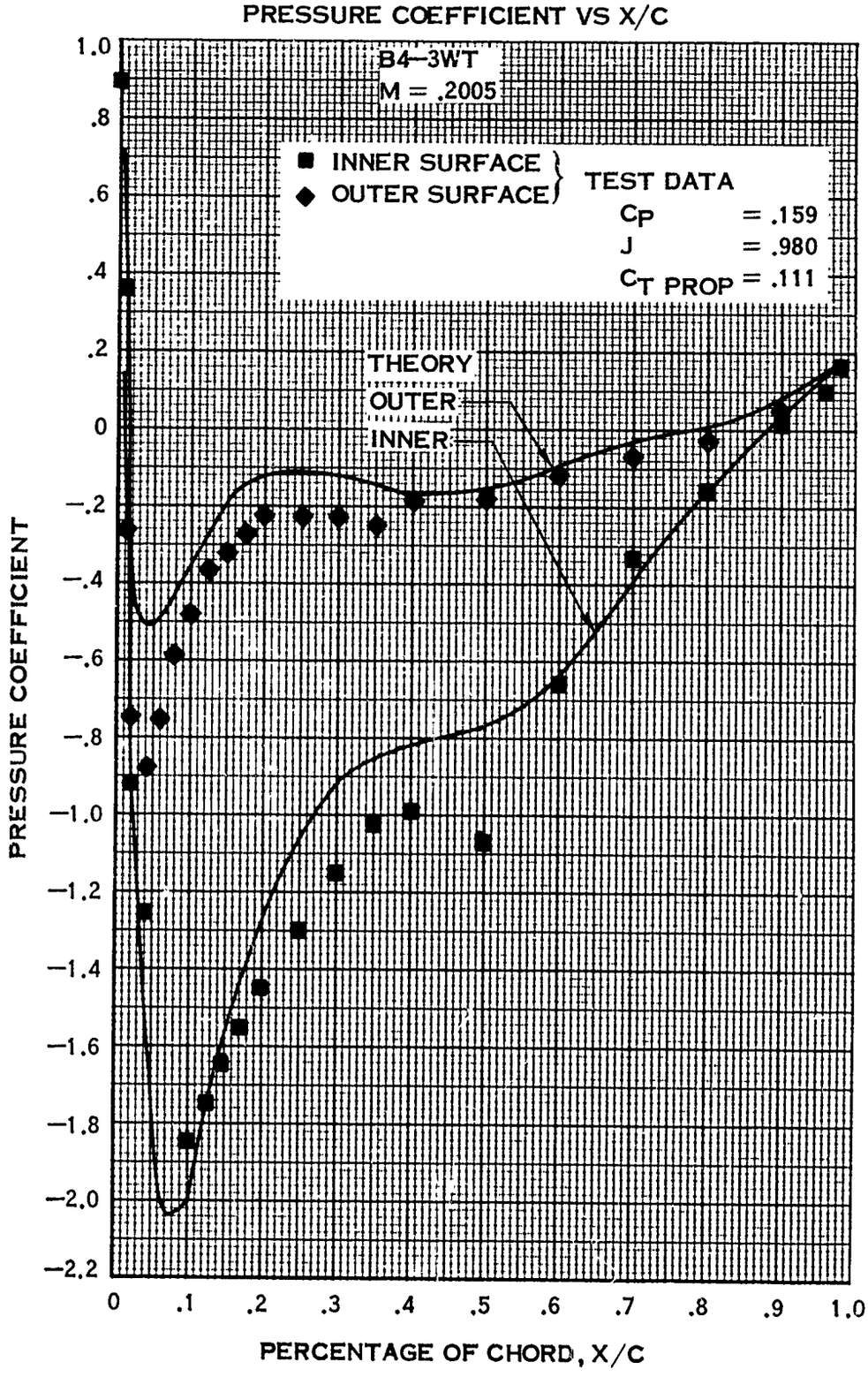
PRESSURE COEFFICIENT VS X/C
B4-3WT
M = .2005
INNER SURFACE
OUTER SURFACE
TEST DATA
CP = .159
J = .980
CT PROP = .111
THEORY
OUTER
INNER
PRESSURE COEFFICIENT
1.0
.8
.6
.4
.2
0
-.2
-.4
-.6
-.8
-1.0
-1.2
-1.4
-1.6
-1.8
-2.0
-2.2
0
.1
.2
.3
.4
.5
.6
.7
.8
.9
1.0
PERCENTAGE OF CHORD, X/C

FIGURE 84.

8.0 (Continued)

The limit beyond which the forward flight T.A.R. theory is invalid has been shown to correspond to a value of M = 0.2. This lower limit represents the point at which the assumption that the induced velocity U be small compared to V_0 is violated. Rather than use Mach number as the delineating parameter, a parameter more directly related to the assumption $U << V_0$ is desirable. Such a parameter is the ratio of the average axial velocity at the propeller plane to the free stream value $\overline{V}_a/V_0$. A value of this parameter around 1 implies that the induced velocity is small compared to V_0. A value much greater than 1 implies the induced velocity is of the same order as V_0. This parameter is readily calculated and is printed out by the program under the label "ratio of average duct velocity to free stream velocity". To determine at what value of $\overline{V}_a/V_0$ the theory becomes invalid, the information on Fig. 47 and 48 is replotted as percentage error in propeller thrust coefficient versus V_a/V_0. Fig. 85 represents this data for the 1.1 and 1.3 area ratio shrouds for power coefficients of 0.15, 0.25, and 0.35. The error, on the average, increases as $\overline{V}_a/V_0$ increases, as expected. A value of $\overline{V}_a/V_0$ of 1.35 or less results in a maximum error on the order of 5% and corresponds approximately to a Mach number of 0.2. Use of the program should thus be limited to cases in which the printed value of $\overline{V}_a/V_0$ is less than 1.35 or so. For values greater than 1.35, the method of Ref. 17 should be used.

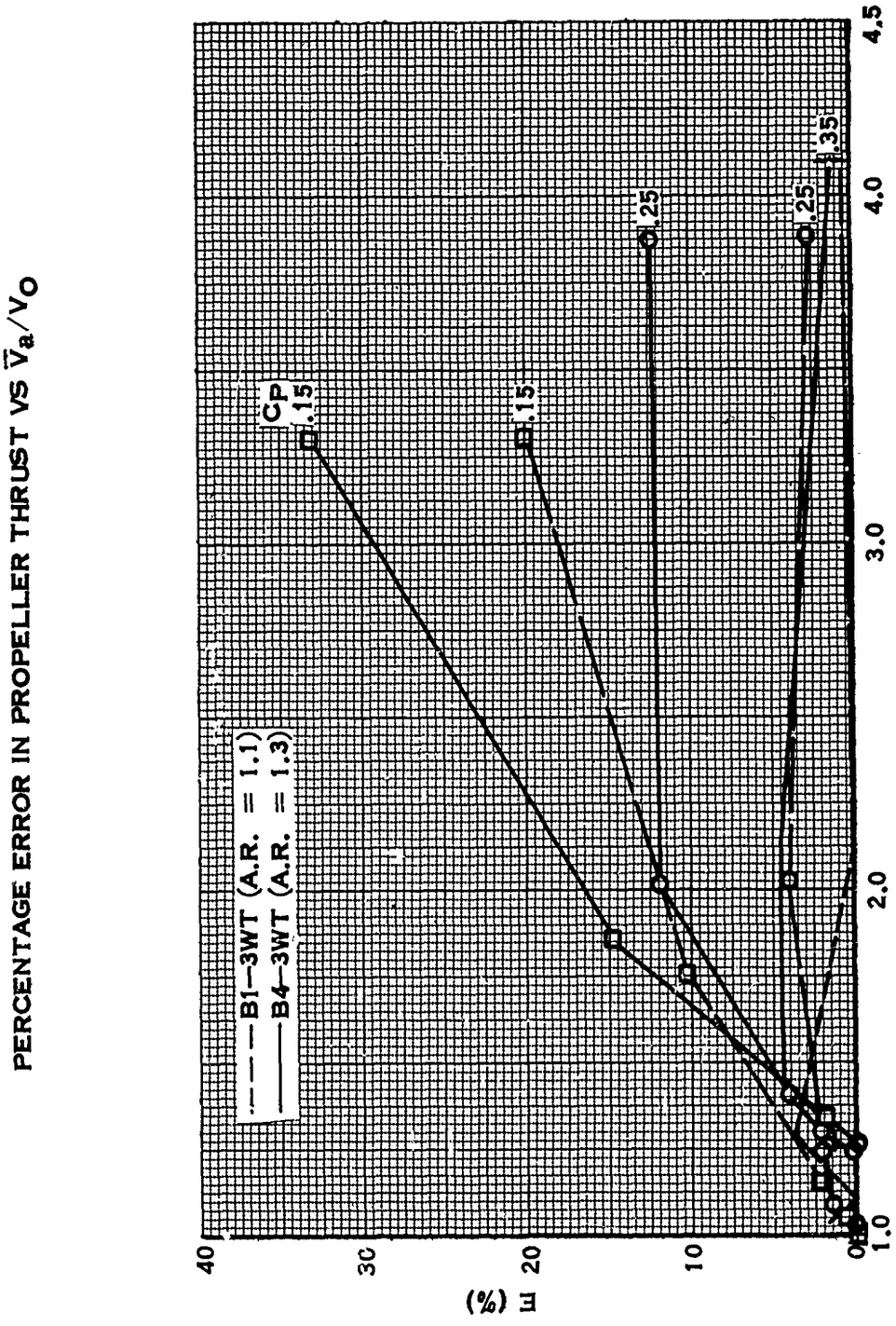
PERCENTAGE ERROR IN PROPELLER THRUST VS $\bar{V}_a/V_O$
B1—3WT (A.R. = 1.1)
B4—3WT (A.R. = 1.3)
C_P
.15
.15
.25
.25
.35
E (%)
40
30
20
10
0
1.0
2.0
3.0
4.0
4.5
$\bar{V}_a/V_O$

FIGURE 85.

9.0 LISTS OF SYMBOLS, SUBSCRIPTS AND SUPERSCRIPTS

Principal Nomenclature

A_j - propeller wake area

A_n - coefficients of thickness distribution expansion (Eq. 18)

A_p - propeller area at propeller plane

a_n - coefficients of source distribution expansion related to A_n (See Appendix 11.1)

B - number of blades

b/D - propeller chord/diameter ratio

$bo\nu$ - coefficients of Glauert Series

$bo\nu^{2-D}$ - two dimensional Glauert coefficients

C - shroud chord

C_D' - drag coefficient (Eq. 56)

C_{D_F} - shroud friction drag coefficient (Eq. 53)

C_D/C_L - propeller lift/drag ratio

$_nC_i$ - binominal coefficients

C_L - propeller lift coefficient

C_{f_e} - external shroud surface friction drag coefficient

C_{f_i} - internal shroud surface friction drag coefficient

C_P - power coefficient $= \dfrac{\text{power}}{\rho n^3 D^5}$

C_p - pressure coefficient $= \dfrac{p - p_\infty}{q_0}$

C_{po} - peak negative value of shroud surface pressure coefficient

C_{ps} - partial pressure coefficient

9.0 (Continued)

$$C_T = \frac{\text{Thrust}}{\rho n^2 D^4}$$

$$C'_{T\ prop} = \frac{\text{Thrust}}{1/2\ \rho V_o^2\ \pi R_p^2}$$

$$C_{Tnet} = C_{T_{tot}} + \text{drag}$$

$$C_{T\ tot} = \frac{\text{Total Thrust}}{\rho n^2 D^4}$$

$$C'_{T\ tot} = \frac{\text{Total Thrust}}{q_o\ A_p}$$

$C_{TS} = F_s\left(2\ \pi \rho R_p^2 V_o^2\right)^{-1}$ thrust coefficient due to shroud vorticity

$C_{T_V} = F_V\left(2\ \pi \rho R_p^2\ V_o^2\right)^{-1}$ thrust coefficient due to shroud vorticity

D - propeller diameter

dC_P/dx - sectional non-dimensional power derivative

dC_T/dx - sectional non-dimensional thrust derivative

Des C_L - airfoil design lift coefficient

F - tip correction

F_D - total friction drag force = $F_{D_i} + F_{D_e}$

F_{D_e} - external surface friction drag force

F_{D_i} - internal surface friction drag force

F_s - shroud axial force due to shroud thickness

F_t - f_t/V_o

F_V - shroud force due to shroud vorticity

f_t - strength of shroud source-sink distribution

9.0 (Continued)

[I] - unit matrix

J - advance ratio = $\frac{V_o}{nD}$

$J'_o = \frac{V_o}{R_p \Omega}$

$J_2 = \frac{\overline{V}_a}{nD}$

$J'_2 = \frac{\overline{V}_a}{R_p \Omega}$

M - free stream Mach number

M/M_{crit} - ratio of sectional Mach number to critical Mach number

N - propeller speed (rpm)

n - propeller speed (rps)

p - static pressure

p_∞ - free stream static pressure

[P] - matrix of curvature coefficients

P_g - propeller geometric pitch

P_t - true pitch of propeller wake

$Q_{1/2}(w)$ - Legendre function with respect to argument w

$q_a = 1/2 \ \rho \overline{V}_a^2$

r - radius

r_j - radius of wake at infinity

r_v - radial location on propeller

$\bar{r}_v = r_v/R$

9.0 (Continued)

R – shroud reference cylinder radius

R_{cb} – radius of the centerbody at the propeller plane

R_{eo} – Reynolds number = $\frac{V_o C}{\nu}$

R_p – propeller radius (ft.)

T_{prop} – propeller thrust

t – 1/2 shroud thickness

t/b – propeller sectional thickness ratio

u – axial induced velocity along shroud surface

U – axial induced velocity along camber line

u_o – maximum velocity on shroud surface

u_p – axial component of the propeller bound vortex velocity

u_e – axial velocity at propeller plane due to all singularities except the propeller bound vorticity

$\bar{U} = U/V_o$

V_a – axial velocity at propeller plane

$\bar{V}_a$ – average total axial velocity in propeller plane

$\bar{V}_j$ – average total velocity in far wake

V_o – free stream velocity (ft/sec)

V_{CB} – centerbody induced radial velocity along shroud surface

v_e – tangential velocity at propeller plane due to all singularities except the propeller bound vorticity

v_p – tangential component of the propeller bound vorticity velocity

V_r – radial velocity along the mean camber line

$\bar{V}_r = V_r/V_o$

9.0 (Continued)

$V_{r_{\bar{\Gamma}'}}$ - propeller wake induced radial velocity along shroud surface

w - velocity relative to a point in the propeller fixed coordinate system

$w_s = \sqrt{w_\theta^2 + w_x^2}$

w_θ - tangential component of w exclusive of propeller bound vortex velocity

w_x - axial component of w exclusive of propeller bound vortex velocity

x - blade sectional r/R_p

$\bar{X}$ - location on shroud reference cylinder normalized with respect to R.

x/c - nondimensional shroud chord location measured from the leading edge.

X_p - propeller location measured from the shroud mid chord position

$\bar{X}_p = Xp/R$

$\Delta \bar{X}_p = (\bar{X}_s - \bar{X}_p)$

X_s - field point on shroud at which radial velocity is computed

$\bar{X}_s = X_s/R$

X_v - position of shroud vortex ring

$\bar{X}_v = Xv/R$

$\Delta \bar{X}_v = \bar{X}_s - \bar{X}_v$

y - shroud thickness form

$\bar{y} = y/R$

α - blade sectional angle of attack

α_n - coefficients defined by Eq. (32)

β - sectional blade induced angle of attack

$\beta_{\theta''} = bov^{2\text{-}D(C.B.)} + bov^{2\text{-}D(\bar{\Gamma}')}$

Γ - strength of bound blade vortex

9.0 (Continued)

$\bar{\Gamma} = \Gamma / R_p V_o$

γ - shroud vorticity distribution

ϵ_e - effective camber

ϵ_L - slope of shroud lower surface (Eq. 21b)

ϵ_u - slope of shroud upper surface (Eq. 21a)

$\epsilon(X)$ - slope of the shroud camber line

Θ - angular variable defined in Fig. 1

Θ_p - blade sectional twist

$\Theta_{3/4}$ - blade angle at 3/4 radius

$\Delta\Theta$ - sectional twist change from 3/4 radius

Θ_t - momentum thickness

λ - shroud chord/diameter ratio = C/2R

μ - tip clearance R_p/R

ν - kinematic viscosity of air

ρ - density

$\phi = \phi_o + \beta$

ϕ_o - sectional advance angle

ϕ_s - Glauert variable

ϕ_v - Glauert variable

Ω - rotational speed (radius/sec)

$\omega_3 = 1 + \left| \Delta\bar{X}^2_p + (1-\bar{r}_v)^2 \right| / 2\bar{r}_v$

9.0 (Continued)

Subscripts and Superscripts

c - continuous velocity

C.B. - due to centerbody

D - discontinuous velocity

jp - due to propeller wake at propeller plane

jp_{∞} - due to propeller wake at infinity

L - lower surface of shroud

S - due to shroud

u - upper surface of shroud

$\bar{\Gamma}'$ - due to propeller wake

10.0 REFERENCES

1. Ordway, D. E., Sluyter, M. M., and Sonnerup, B. O. U., "Three-Dimensional Theory of Ducted Propellers", Therm Advanced Research Report TAR-TR602, August 1960.

2. Ordway, D. E. and Greenberg, M. D., "General Harmonic Solutions for the Ducted Propeller", Therm Advanced Research Report TAR-TR613, August 1961.

3. Hough, Gary R. "The Aerodynamic Loading on Streamlined Ducted Bodies", Therm Advanced Research Report TAR-TR625, December 1962.

4. Goldstein, M. A., "On the Vortex Theory of Screw Propellers", Proceedings of the Royal Society, A123, 440, 1929.

5. Lock, C. N. H., "Application of Goldstein's Airscrew Theory to Design", Aeronautical Research Committee Reports and Memoranda, No. 1377, November 1930.

6. Kuethe, A. M. and Schetzer, J. D., "Foundations of Aerodynamics", John Wiley & Sons, Inc., 1950.

7. Csanady, G. T., "Theory of Turbomachines", McGraw-Hill Book Company, 1964.

8. Goodman, T., "The Tip Correction for Wind-Tunnel Tests of Propellers", Journal of Aeronautical Sciences, December 1956.

9. Kaskel, A. L., Ordway, D. E., Hough, G. R., and Ritter, A., "A Detailed Numerical Evaluation of Shroud Performance for Finite-Bladed Ducted Propellers", Therm Advanced Research Report TAR-TR639, December 1963.

10. Milne-Thomson, L. M., "Theoretical Hydrodynamics", The MacMillan Company, 1960.

11. Shapiro, A. H., "The Dynamics and Thermodynamics of Compressible Fluid Flow", The Ronald Press Company, 1953.

12. Küchemann, D., and Weber, J., "Aerodynamics of Propulsion", McGraw-Hill Book Company, Inc., 1953.

13. Schlichting, H., "Boundary Layer Theory", McGraw-Hill, 1960.

10.0 (Continued)

14. Kriebel, A. R., and Mendenhall, M. R., "Predicted and Measured Performance of Two Full-Scale Ducted Propellers", NASA CR-578, September 1966.

15. Black, D. M., Wainauski, H. S., and Simmonds, A. W., "Shrouded Propeller Test Program", Hamilton Standard HSER 4348, May 1967.

16. Patterson, G. N., "Ducted Fans of High Efficiency", Australia Council of Aeronautics, Report No. A-7, July 1944.

17. Anonymous, "Generalized Method of Shrouded Propeller Performance Estimation," Hamilton Standard Report PDB 6220.

18. Greenberg, M. D., and Ordway, D. E., "The Ducted Propeller in Static and Low Speed Flight," Therm Advanced Research Report TAR-TR6407, October 1964.

11.0 APPENDICES

Each appendix includes its own curves, references and nomenclature.

11.1 INCORPORATION OF CENTERBODY INTO THERM ADVANCED RESEARCH THEORY

11.1.1 Introduction

The centerbody of the shrouded propeller is represented by a distribution of sources and sinks along the shroud centerline. The effect of this distribution on the shroud vorticity distribution is derived, and the expressions for the axial velocity at any field point are presented.

11.1.2 Incorporation Into Therm Advanced Research Theory

To insure that the flow is everywhere tangent to the shroud, the boundary condition equation is written as follows.

$$\epsilon = \left(\frac{v_{ri}}{V_o}\right)_{\text{propeller}} + \left(\frac{v_{ri}}{V_o}\right)_{\text{shroud}} + \left(\frac{v_{ri}}{V_o}\right)_{\text{centerbody}}$$

where ϵ is the slope of the shroud camber line. The contribution of the propeller is given by Eq. 20 of the text. The shroud camber is known and the contribution of the centerbody will be derived. This leaves the contribution of the shroud itself as the only unknown, which is written in terms of the known quantities as follows

$$\left(\frac{v_{ri}}{V_o}\right)_{\text{shroud}} = \epsilon - \left(\frac{v_{ri}}{V_o}\right)_{\text{propeller}} - \left(\frac{v_{ri}}{V_o}\right)_{\text{centerbody}}$$

Multiplying both sides of the equation by 2, the following expression for the effective camber ϵ_e results,

$$2\left(\frac{v_{ri}}{V_o}\right)_{\text{shroud}} - 2\,\epsilon_e = 2\left[\epsilon - \left(\frac{v_{ri}}{V_o}\right)_{\text{centerbody}} - \left(\frac{v_{ri}}{V_o}\right)_{\text{propeller}}\right]$$

The two-dimensional Glauert coefficients are related to the effective camber ϵ_e by the following equations, as discussed in paragraph 6.1.2 of the text,

$$b_{oo}^{2\text{-D}} = \frac{2}{\pi}\int_0^{\pi} \epsilon_e \, d\phi_s$$

$$b_{o\nu}^{2\text{-D}} = -\frac{4}{\pi}\int_0^{\pi} \epsilon_e \cos\nu\,\phi_s \, d\,\phi_s$$

11.1.2 (Continued)

Thus, the centerbody is accounted for by incorporating $v_{ri}/V_o)_{centerbody}$. The centerbody source-sink distribution is considered next.

11.1.3 Derivation of Velocity Equations

In this section the expression for $v_{ri}/V_o)_{centerbody}$ will be derived, assuming that the centerbody is represented by a source-sink distribution along the shroud centerline as illustrated below.

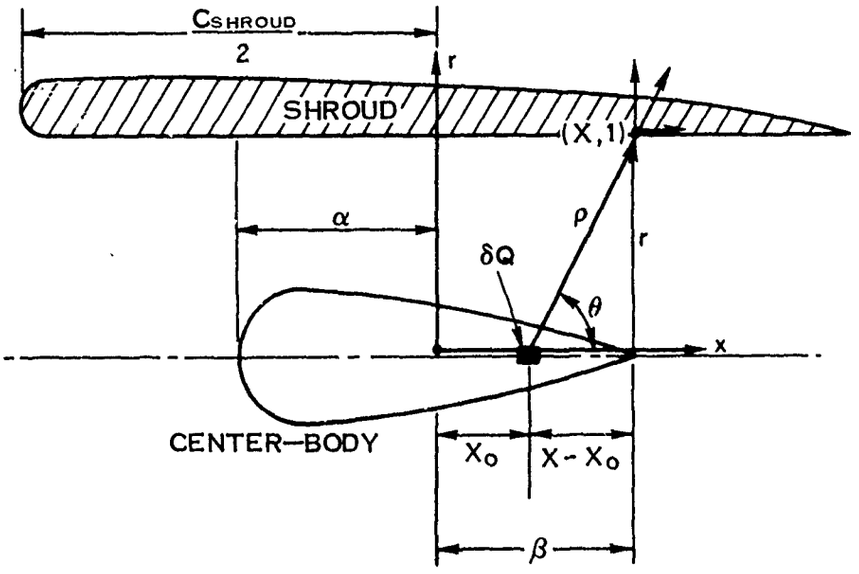

Figure A-1. Source-sink Distribution Along Shroud Centerline

The vector velocity at a distance ρ from a source element of strength δQ is given by the following equation.

$$\delta.\bar{v} = \frac{\delta Q \bar{1}_\rho}{4\pi\rho^2}$$

where δQ is the volume of fluid per unit time emitted by the source. The origin of the (x, r) coordinate system is located at the center of the shroud centerline. Expressing the distance ρ in terms of its coordinates, the following equation results

$$\rho = \left([x-x_o]^2 + r^2 \right)^{1/2}$$

11.1.3 (Continued)

The cosine of the angle θ is given by $(x-x_0)/\rho$ and the sine is given by r/ρ . A unit vector in the ρ direction can be expressed by its components, i.e.,

$$\bar{i}_\rho = \cos\Theta\ \bar{i}_x + \sin\Theta\ \bar{i}_r = \frac{X-X_0}{\rho}\ \bar{i}_x + \frac{r}{\rho}\ \bar{i}_r$$

Upon substitution of these terms, the vector velocity $\delta\ \bar{v}$ is given by Eq. (1).

$$\delta \bar{v} = \frac{\delta Q}{4\pi} \frac{(X-X_0)\ \bar{i}_x + r\ \bar{i}_r}{\left[(X-X_0)^2 + r^2\right]^{3/2}} \qquad (1)$$

Since the sources and sinks are distributed along the chord line of the centerbody, a function $S(X_0)$ is defined which represents the strength of the source per unit length of the chord line. Thus δQ can be expressed as follows.

$$\delta Q = S(X_0)\, d X_0$$

where $d X_0$ is an element of length along the centerbody chord line. The velocity $\bar{v}$ due to the complete distribution of sources and sinks then becomes

$$\bar{v} = \int_{-\alpha}^{\beta} \frac{S(X_0)\ \left[(X-X_0)\ \bar{i}_x + r\ \bar{i}_r\right] d X_0}{4\pi\ \left[(X-X_0)^2 + r^2\right]^{3/2}}$$

The radial component of this velocity at any point (x, r) is given by

$$v_r = \bar{v} \cdot \bar{i}_r = \int_{-\alpha}^{\beta} \frac{S(X_0)\, r\, d X_0}{4\pi \left|(X-X_0)^2 + r^2\right|^{3/2}} \qquad (2)$$

The axial component is given by

$$v_a = \bar{v} \cdot \bar{i}_x = \int_{-\alpha}^{\beta} \frac{S(X_0)\,(X-X_0)\, d X_0}{4\pi \left[(X-X_0)^2 + r^2\right]^{3/2}} \qquad (3)$$

11.1.3 (Continued)

These equations can be put into more compact form by nondimensionalizing with respect to R, where R is the duct reference radius, as follows.

Let $\bar{r} = \frac{r}{R}$, $\bar{x} = \frac{x}{R}$, $\bar{X}_o = \frac{X_o}{R}$, $\bar{\alpha} = \frac{\alpha}{R}$, and $\bar{\beta} = \frac{\beta}{R}$

Then

$$\left(\frac{v_{ri}}{V_o}\right)_{CB} = \int_{-\bar{\alpha}}^{\bar{\beta}} \frac{S(\bar{X}_o)\ \bar{r}\ d\bar{X}_o}{4\pi\ RV_o \left[(\bar{X}-\bar{X}_o)^2 + \bar{r}^2\right]^{(3/2)}}$$

$$\left(\frac{Va}{V_o}\right)_{CB} = \int_{-\bar{\alpha}}^{\bar{\beta}} \frac{S(\bar{X}_o)\ (\bar{X}-\bar{X}_o)\ d\bar{X}_o}{4\pi\ RV_o \left|(\bar{X}-\bar{X}_o)^2 + \bar{r}^2\right|^{3/2}}$$

Next define a non-dimensional source distribution as follows.

$$S'(\bar{X}_o) = \frac{S(\bar{X}_o)}{4\pi\ R\ V_o}$$

The equation for the radial velocity then becomes

$$\left(\frac{v_{ri}}{V_o}\right)_{CB} = \int_{-\bar{\alpha}}^{\bar{\beta}} \frac{S'(\bar{X}_o)\ \bar{r}\ d\bar{X}_o}{\left[(\bar{X}-\bar{X}_o)^2 + \bar{r}^2\right]^{3/2}} \qquad (4)$$

11.1.4 Assumption of Power Series for Source-Sink Distribution

In order to facilitate evaluation of Eq. (4), $S'(\bar{X}_o)$ is expanded into a power series as follows.

$$S'(\bar{X}_o) = \sum_{n=1}^{8} a_n \bar{X}_o^{\,n-1}$$

11.1.4 (Continued)

The expression for the radial velocity now becomes

$$\left.\frac{v_{ri}}{V_o}\right)_{CB} = \int_{-\bar{\alpha}}^{\bar{\beta}} \frac{\bar{r} \sum a_n \bar{X}_o^{n-1} d\bar{X}_o}{\left[(\bar{X}-\bar{X}_o)^2 + \bar{r}^2\right]^{3/2}} \qquad (5)$$

The following substitutions reduce further the complexity of the integration.

Let $\eta = \bar{X}_o - X$, $\bar{X}_o = \eta + \bar{X}$, $d\bar{X} = d\eta$ and $\left|\begin{matrix}\bar{\beta}\\ \bar{X}_o\\ -\bar{\alpha}\end{matrix}\right. \Rightarrow \left|\begin{matrix}\bar{\beta}-\bar{X}\\ \eta\\ -\bar{\alpha}-\bar{X}\end{matrix}\right.$

Then

$$\left.\frac{v_{ri}}{V_o}\right)_{CB} = \int_{-\bar{\alpha}-\bar{X}}^{\bar{\beta}-\bar{X}} \frac{\bar{r} \sum a_n (\eta+\bar{X})^{n-1} d\eta}{(\eta^2 + \bar{r}^2)^{3/2}} \qquad (6)$$

The expression $(\eta+\bar{X})^{n-1}$ can be expanded by the binomial theorem and results in

$$(\eta+\bar{X})^{n-1} = \sum_{m=o}^{n-1} d_m^{n-1} \bar{X}^{n-1-m} \eta^m,$$

where d_m^{n-1} are the coefficients afforded by the binomial theorem as given in Dwight, "Tables of Integrals and Other Mathematical Data", page 1. Substituting the above expression in Eq. (6), the radial velocity can now be expressed as follows.

$$\left.\frac{v_{ri}}{V_o}\right)_{CB} = \bar{r}\left(\sum_{n=1}^{8} a_n \sum_{m=o}^{n-1} d_m^{n-1} \bar{X}^{n-1-m}\right) \int_{-\bar{\alpha}-\bar{X}}^{\bar{\beta}-\bar{X}} \frac{\eta^m d\eta}{(\eta^2+\bar{r}^2)^{3/2}} \qquad (7)$$

11.1.4 (Continued)

Let $$I_n = \sum_{m=o}^{n-1} d_m^{n-1} \bar{X}^{n-1-m} \int_{-\bar{\alpha}-\bar{X}}^{\bar{\beta}-\bar{X}} \frac{\eta^m \, d\eta}{(\eta^2 + \bar{r}^2)^{3/2}} \qquad (8)$$

and $$L_m = \int_{-\bar{\alpha}-\bar{X}}^{\bar{\beta}-\bar{X}} \frac{\eta^m d\eta}{(\eta^2 + \bar{r}^2)^{3/2}} \qquad (9)$$

Eq. (9) can be integrated analytically and yields the following results (for locations on the shroud reference radius, i.e., $\bar{r} = 1$).

$$L_o = \frac{N}{Y} - \frac{M}{Z}$$

where $N = \bar{\beta} - \bar{X}$, $M = \bar{\alpha} - \bar{X}$, $Y = ([\bar{\beta}-\bar{X}]^2+\bar{r}^2)^{1/2}$, $Z = ([\bar{\alpha} + \bar{X}]^2+\bar{r}^2)^{1/2}$ and $\bar{r} = 1$.

$$L_1 = \frac{1}{Z} - \frac{1}{Y}, \quad L_2 = \ln\left[\frac{N+Y}{M+Z}\right] + \frac{M}{Z} - \frac{N}{Y}$$

$$L_3 = Y + \frac{1}{Y} - Z - \frac{1}{Z}, \quad L_4 = \frac{NY}{2} + \frac{N}{Y} - \frac{MZ}{2} - \frac{M}{Z} + \frac{3}{2} \ln\left[\frac{M+Z}{N+Y}\right]$$

$$L_5 = \frac{Y^3}{3} - 2Y - \frac{1}{Y} - \frac{Z^3}{3} + 2Z + \frac{1}{Z}$$

$$L_6 = \frac{N^5}{4Y} - \frac{5N^3}{8Y} - \frac{15N}{8Y} - \frac{M^5}{4Z} + \frac{5M^3}{8Z} + \frac{15M}{8Z} + \frac{15}{8} \ln\left[\frac{N+Y}{M+Z}\right]$$

$$L_7 = \frac{Y^5}{5} - Y^3 + 3Y + \frac{1}{Y} - \frac{Z^5}{5} + Z^3 - 3Z - \frac{1}{Z}$$

11.1.4 (Continued)

The radial velocity is then given by the following equation.

$$\left(\frac{v_{ri}}{V_o}\right)_{CB} = \sum_{n=1}^{8} a_n \sum_{m=o}^{n-1} d_m^{n-1} \bar{X}^{n-1-m} L_m \qquad (10)$$

The methods employed thus far have allowed for an analytical integration of Eq. (5) rather than a cumbersome numerical method. The problem has now been reduced to the evaluation of the coefficients a_n of the power series representing the shroud source-sink distribution.

11.1.5 Relationship Between the Body Shape and the Source-Sink Distribution

The relationship between the body shape and the source-sink distribution can be derived as follows, assuming that the axial velocity induced by the source distribution is small compared to V_o.

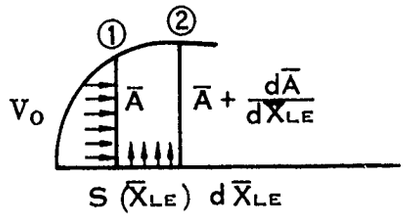

Figure A-2. Derivation of Relationship Between Body Shape and Source-Sink Distribution

With this assumption the flow at point (1) is $V_o \bar{A} R^2$, where $\bar{A}$ is the area divided by R^2. The flow at point (2) is $V_o R^2 (\bar{A} + \frac{d\bar{A}}{d\bar{X}_{LE}} d\bar{X}_{LE})$

The difference in the flow between points (2) and (1) is the flow added by the source, i.e.,

$$V_o R^2 (\bar{A} + \frac{d\bar{A}}{d\bar{X}_{LE}} d\bar{X}_{LE}) - V_o \bar{A} R^2 = RS(\bar{X}_{LE})\, d\bar{X}_{LE}$$

and $$V_o R \frac{d\bar{A}}{d\bar{X}_{LE}} = S(\bar{X}_{LE})$$

11.1.5 (Continued)

In terms of the non-dimensional source distribution $S'(X_{LE}) = \frac{S(\bar{X}_{LE})}{4\pi R V_0}$, this equation becomes

$$\left(\frac{1}{4\pi} \quad \frac{d\bar{A}}{d\bar{X}_{LE}}\right) = S'(\bar{X}_{LE}) \tag{11}$$

and relates the source distribution to the physical shape of the centerbody.

11.1.6 Evaluation of Coefficients, a_n, of Power Series for S'

The coefficients of the power series can be directly related to the body shape by use of Eq. (11), i.e.,

$$\sum_{n=1}^{8} a_n \bar{X}_0^{n-1} = S'(\bar{X}_0) = \frac{\overline{r_{CB}}}{2} \quad \frac{d\overline{r_{CB}}}{d\bar{X}}$$

There are two other constraining conditions that will be used in evaluation of the coefficients. The first of these is that the leading edge radius is related to the coefficients of the series as is shown in the following section. The second condition is that the body close on itself, or that the sum of sources and sinks be zero. Utilizing these three conditions, the relationship between the coefficients, a_n, and the body shape will be derived in this section.

For the purpose of simplifying the derivations it is advantageous to relate the power series to a coordinate system originating at the leading edge of the centerbody. The non-dimensional source distribution is thus given by

$$S'(X_{LE}) = \sum_{n=1}^{8} A_n \bar{X}_{LE}^{n-1}$$

where A_n represents the coefficients for the expansion about the leading edge. The leading edge radius of the centerbody is related by the following expression (as shown in paragraph 11.1.7)

$$\overline{R_{LE}} = -2A_1 \tag{12}$$

to A_1, the first coefficient of the power series.

The method of sources and sinks requires that the sum of the sources and sinks be zero so that the body closes on itself, i.e.,

$$\int_0^{\bar{C}} S'(\bar{X}_{LE})\, d\bar{X}_{LE} = 0$$

where $\bar{C}$ is the non-dimensional centerbody chord length. Evaluation of the above integral in terms of the power series expansion of $S'(\bar{X}_{LE})$ yields the following expression.

11.1.6 (Continued)

$$\sum_{n=1}^{8} A_n \, \bar{C}^{\,n-1} \, \bar{C}^{\,n} = 0 \qquad (13)$$

Eq. (13) makes it possible to represent A_2 in terms of the other coefficients, i.e.,

$$A_2 = -2\left[A_1 \bar{C}^{-1} + \sum_{n=3}^{8} \frac{A_n}{n} \bar{C}^{n-2}\right]$$

By utilizing the above equation to eliminate A_2 the non-dimensional source-sink distribution can now be represented by the following equation:

$$S'(\bar{X}_{LE}) = A_1 - \frac{2A_1}{(\bar{\beta} + \bar{\alpha})} \bar{X}_{LE} - 2\bar{X}_{LE} \sum_{n=3}^{8} \frac{A_n}{n} (\bar{B} + \bar{\alpha})^{n-2} + \sum_{n=3}^{8} A_n \bar{X}_{LE}^{\,n-1} \qquad (14)$$

Since A_1 is known (Eq. 12), it remains to solve for the other six coefficients of Eq. (14) and to relate them to the $\bar{X}_o$ coordinate system. The method employed to determine these coefficients is a curve-fitting technique known as the "Method of Least Squares." This method derives the coefficients of a polynomial such that the sum of the squares of the differences between the actual data points and their representation by the polynomial will be a minimum. This insures that in the case of a series of plotted points the best representative curve in the least squares sense will pass as closely as possible to all points.

Recall that the source-sink distribution is related to the body shape in the following manner.

$$\bar{r}_{CB} \frac{d\bar{r}_{CB}}{d\bar{X}_{LE}} = 2S'(\bar{X}_{LE})$$

Knowing the variation of centerbody radius with chord, it is possible to obtain the value of $S'(\bar{X}_{LE})$ at any number of points along the chord. This information will represent the series of plotted points for which the "Method of Least Squares" will afford the six A_n's which give the best representative polynomial.

With the coefficients A_n of the power series being given by the method described above, the only remaining task is to relate the coefficients to the $\bar{X}_o$ coordinate system.

Making use of the fact that

$$S'(\bar{X}_o) = \sum_{n=1}^{8} a_n \bar{X}_o^{\,n-1} = \sum_{n=1}^{8} A_n (\bar{X}_o + \bar{\alpha})^{n-1}$$

11.1.6 (Continued)

and of the binomial expansion it can be shown that

$$a_1 = A_1 + A_2\bar{\alpha} + A_3\bar{\alpha}^2 + A_4\bar{\alpha}^3 + A_5\bar{\alpha}^4 + A_6\bar{\alpha}^5 + A_7\bar{\alpha}^6 + A_8\bar{\alpha}^7$$

$$a_2 = A_2 + 2A_3\bar{\alpha} + 3A_4\bar{\alpha}^2 + 4A_5\bar{\alpha}^3 + 5A_6\bar{\alpha}^4 + 6A_7\bar{\alpha}^5 + 7A_8\bar{\alpha}^6$$

$$a_3 = A_3 + 3A_4\bar{\alpha} + 6A_5\bar{\alpha}^2 + 10A_6\bar{\alpha}^3 + 15A_7\bar{\alpha}^4 + 21A_8\bar{\alpha}^5$$

$$a_4 = A_4 + 4A_5\bar{\alpha} + 10A_6\bar{\alpha}^2 + 20A_7\bar{\alpha}^3 + 35A_8\bar{\alpha}^4$$

$$a_5 = A_5 + 5A_6\bar{\alpha} + 15A_7\bar{\alpha}^2 + 35A_8\bar{\alpha}^3$$

$$a_6 = A_6 + 6A_7\bar{\alpha} + 21A_8\bar{\alpha}^2$$

$$a_7 = A_7 + 7A_8\bar{\alpha}$$

$$a_8 = A_8$$

11.1.7 Relationship Between the Leading Edge Radius and the Coefficients of the Power Series

The relationship between the leading edge radius and A_1 is now derived. The non-dimensional source distribution is represented by the following polynomial.

$$S'(X_{LE}) = \sum_{n=1}^{8} A_n \bar{X}_{LE}^{n-1} = \frac{S(\bar{X}_{LE})}{4\pi R V_o}$$

Substituting into Eq. (11) there results

$$\frac{d\bar{A}}{d\bar{X}_{LE}} = 4\pi \sum_{n=1}^{8} A_n \bar{X}_{LE}^{n-1} \qquad (15)$$

Normalizing the equation for the area in the following manner

$$A = \pi r_{CB}^2;\ R^2\bar{A} = R^2\pi r_{CB}^2 \ :\frac{d\bar{A}}{d\bar{X}_{LE}} = 2\pi\bar{r}_{CB}\ \frac{d\bar{r}_{CB}}{d\bar{X}_{LE}}$$

Eq. (15) becomes

$$2 \sum_{n=1}^{8} A_n \bar{X}_{LE}^{n-1} = \bar{r}_{CB}\ \frac{d\bar{r}_{CB}}{d\bar{X}_{LE}} \qquad (16)$$

11.1.7 (Continued)

Integrating Eq. (16) yields the following results.

$$2\sum \frac{A_n}{n} \bar{X}_{LE}^{n} = \frac{\bar{r}_{CB}^{2}}{2}$$

$$\bar{r}_{CB}^{2} = 4 \sum_{n=1}^{8} \frac{A_n}{n} \bar{X}_{LE}^{n}$$

$$\bar{r}_{CB} = 2\left(\sum_{n=1}^{8} K_n \bar{X}_{LE}^{n}\right)^{1/2} \tag{17}$$

where $K_n = A_n/n$.

The leading edge radius in terms of r_{CB} is given by the following equation

$$R_{LE} = \lim_{X_{LE} \to 0} \frac{\left[1 + \left(\frac{dr_{CB}}{dX_{LE}}\right)^2\right]^{3/2}}{\frac{d^2 r_{CB}}{dX_{LE}^2}} \tag{18}$$

Changing to the barred coordinate system,

$$\bar{r}_{CB} = \frac{r_{CB}}{R} \; ; \frac{d\bar{r}_{CB}}{d\bar{X}_{LE}} = \frac{1}{R}\frac{dr_{CB}}{d\bar{X}_{LE}} = \frac{1}{R}\frac{dr_{CB}}{dX_{LE}}\frac{dX_{LE}}{d\bar{X}_{LE}} \; ; \bar{X}_{LE} = \frac{X_{LE}}{R} \; ; d\bar{X}_{LE} = \frac{1}{R}\, dX_{LE}$$

so

$$\frac{d\bar{r}_{CB}}{dX_{LE}} = \frac{dr_{CB}}{dX_{LE}}$$

$$\frac{d^2\bar{r}_{CB}}{d\bar{X}_{LE}^2} = \frac{d}{d\bar{X}_{LE}}\left(\frac{dr_{CB}}{dX_{LE}}\right) = R\frac{d}{dX_{LE}}\left(\frac{dr_{CB}}{dX_{LE}}\right)$$

and

$$\frac{d^2\bar{r}_{CB}}{d\bar{X}_{LE}^2} = R\frac{d^2 r_{CB}}{d\bar{X}_{LE}^2}$$

Substituting these expressions into Eq. (18), there results.

11.1.7 (Continued)

$$\bar{R}_{LE} = \lim_{\bar{X}_{LE} \to 0} \frac{\left[1 + \left(\frac{d\bar{r}_{CB}}{d\bar{X}_{LE}}\right)^2\right]^{3/2}}{\frac{d^2\bar{r}}{d\bar{X}^2_{LE}}}$$

From Eq. (17)

$$\bar{r}_{CB} = 2\left(\sum_{n=1}^{8} K_n \bar{X}_{LE}^{\,n}\right)^{1/2}$$

Differentiating the above expression,

$$\frac{d\bar{r}_{CB}}{d\bar{X}_{LE}} = \left(\sum_{n=1}^{8} K_n \bar{X}_{LE}^{\,n}\right)^{-1/2}\left(\sum_{n=1}^{8} nK_n \bar{X}_{LE}^{\,n-1}\right)$$

$$\left(\frac{d\bar{r}_{CB}}{d\bar{X}_{LE}}\right)^2 = \frac{\left(\sum_{n=1}^{8} nK_n \bar{X}_{LE}^{\,n-1}\right)^2}{\left(\sum_{n=1}^{8} K_n \bar{X}_{LE}^{\,n}\right)}$$

Taking the second derivative,

$$\frac{d^2\bar{r}_{CB}}{d\bar{X}^2_{LE}} = \left(\sum_{n=1}^{8} K_n \bar{X}_{LE}^{\,n}\right)^{-1/2}\left(\sum_{n=1}^{8} n(n-1) K_n \bar{X}_{LE}^{\,n-2}\right) + \left(\sum_{n=1}^{8} nK_n \bar{X}_{LE}^{\,n-1}\right)^2 \left(-\frac{1}{2}\left(\sum_{n=1}^{8} K_n \bar{X}_{LE}^{\,n}\right)^{-3/2}\right)$$

$$\frac{d^2\bar{r}_{CB}}{d\bar{X}^2_{LE}} = \frac{\left(\sum_{n=1}^{8} K_n \bar{X}_{LE}^{\,n}\right)\left(\sum_{n=1}^{8} n(n-1) K_n \bar{X}_{LE}^{\,n-2}\right) - \frac{1}{2}\left(\sum_{n=1}^{8} nK_n \bar{X}_{LE}^{\,n-1}\right)^2}{\left(\sum_{n=1}^{8} K_n \bar{X}_{LE}^{\,n}\right)^{3/2}}$$

11.1.7 (Continued)

Substituting the first and second derivatives into Eq. (18),

$$\bar{R}_{LE} = \lim_{\bar{X}_{LE} \to 0} \frac{\left[\left(\sum_{n=1}^{8} K_n \bar{X}_{LE}^{\,n}\right) + \left(\sum_{n=1}^{8} nK_n \bar{X}_{LE}^{\,n-1}\right)^2\right]^{3/2}}{\left(\sum_{n=1}^{8} K_n \bar{X}_{LE}^{\,n}\right)\left(\sum_{n=1}^{8} n(n-1) K_n \bar{X}_{LE}^{\,n-2}\right) - \frac{1}{2}\left(\sum_{n=1}^{8} nK_n \bar{X}_{LE}^{\,n-1}\right)^2}$$

on taking the required limit, the desired relationship between $\bar{R}_{LE}$ and A_1 results,

$$\bar{R}_{LE} = \frac{K_1^{\,3}}{-\frac{1}{2} K_1^{\,2}} = -2K_1 = -2A_1.$$

11.2 APPLICATION OF PROPELLER TIP CORRECTION

11.2.1 Introduction

The application of the tip correction discussed in Ref. 1 to the circulation distribution of the shrouded propeller is investigated. This investigation is carried out in two parts. The first concerns itself with a study of Ref. 1 and the generation of curves which defined the tip correction factor as a function of number of blades, advance ratio, etc. The second part concerns itself with the incorporation of this correction into both the Vortex and Goldstein propeller performance prediction methods.

11.2.2 Discussion of Tip Correction Factor

The optimum propeller sheds a wake that is a rigid helicoid at downstream infinity moving with constant velocity. The radial velocity in the wake is small, except at the edge of the helical surfaces. It was shown by Prandtl (Ref. 3) that this radial flow has the effect of reducing the propeller circulation near the tip.

The model used by Prandtl first replaces the helical vortex sheet by a series of parallel disks. Since the flow around the edges is being investigated, the circular shape of the disks can be neglected, and semi-infinite vortex sheets used instead. The three dimensional flow is thus replaced by the two dimensional model shown below in Fig. A-3.

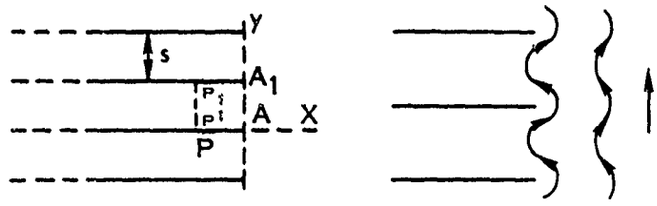

Figure A-3. Two-dimensional Model

11.2.2 (Continued)

The gap is related to the pitch angle ϕ by the following equations.

$$\lambda = \tan \phi \qquad (1)$$

$$S = \frac{2 \pi R_p}{B} \sin \phi \qquad (2)$$

where R_p is the propeller radius, B is the number of blades, and ϕ is defined by the velocity diagram of Fig. A-6.

Using complex variables, Prandtl solved this two-dimensional potential flow problem. The propeller circulation is related to the line integral of the velocity around the edge of the vortex sheet by Helmholtz' laws. Carrying out this integration, Prandtl obtained the following propeller circulation drop-off factor F_∞,

$$F_\infty = \frac{2}{\pi} \cos^{-1} (e^{-f}) \qquad (3)$$

where

$$f = (1 - \frac{r}{Rp}) \frac{B \sqrt{1 + \lambda^2}}{2\lambda} \qquad (4)$$

r is radial distance, and Rp and λ were previously defined. The factor F_∞ varies from 1 inboard to 0 at the tip as shown in Fig. A-5.

Goodman (Ref. 1) took a similar approach, but now put a wall near the vortex sheets as shown below.

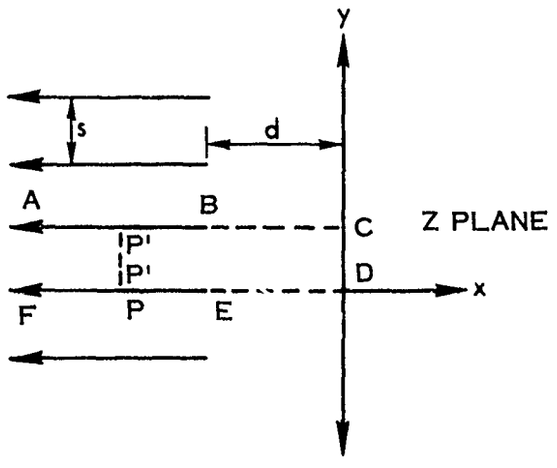

Figure A-4. Placement of Wall Near Vortex Sheets

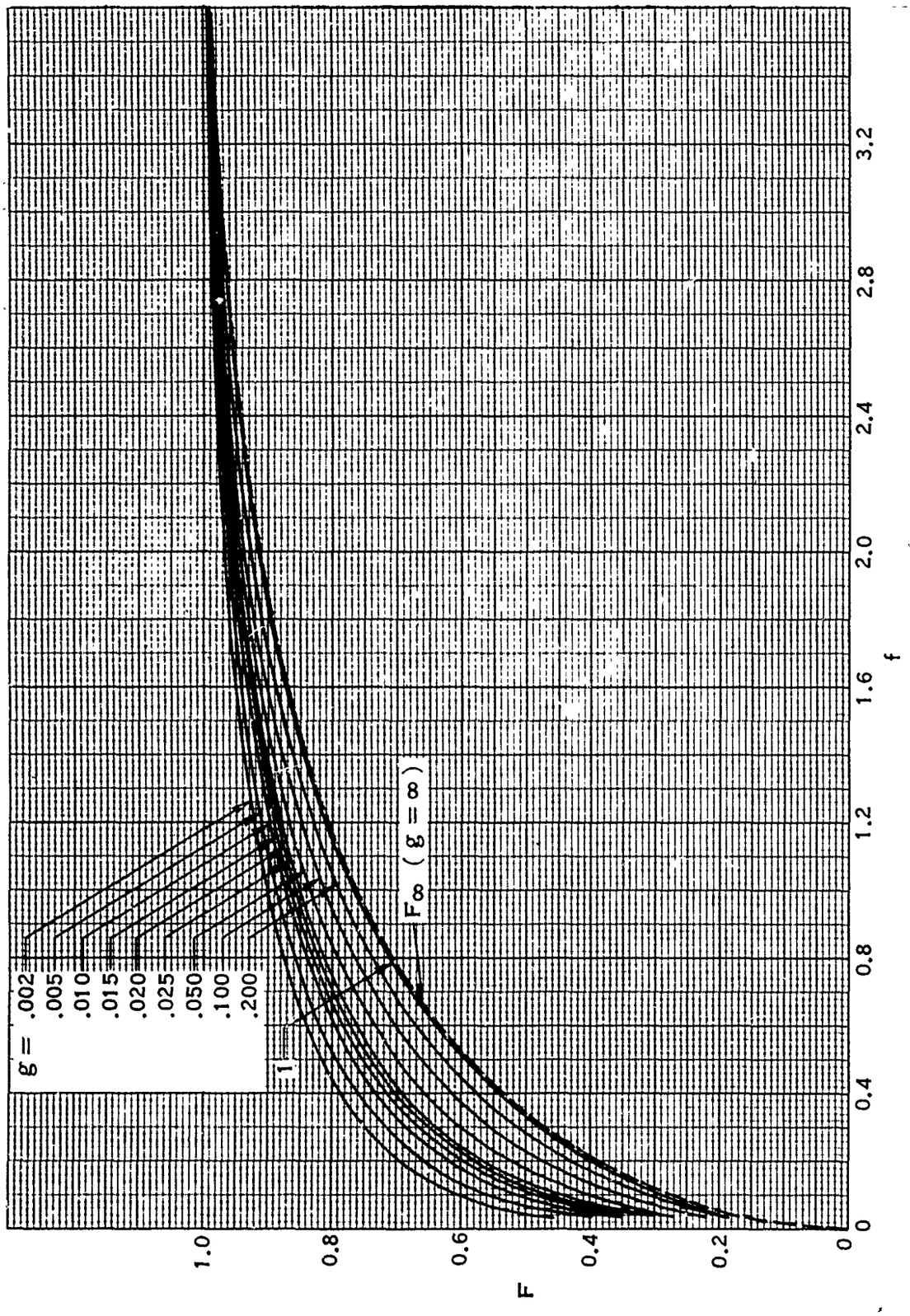

Figure A-5. Goodman Tip Correction.

11.2.2 (Continued)

The distance d represents the difference between tunnel (shroud) radius and propeller radius. Again solving for the flow, and integrating around the vortex sheet, the circulation drop-off is

$$F = 1 - \frac{u \left\{ \sin^{-1} \left[\cosh g / \cosh (f+g)\right] / \sin^{-1} (1/\cosh g) \right\}}{K \left[\sin^{-1} (1/\cosh g)\right]} \qquad (5)$$

where f is the same as before and

$$g = \frac{d}{Rp} \frac{B\sqrt{1+\lambda^2}}{2\lambda} \qquad (6)$$

K is the complete elliptic integral as a function of g, and u is the elliptic integral of the first kind and is a function of both f and g.

From the sketch, it can be seen that $d = \infty$ represents the wall at infinity, and from Eq. (6) it can be seen that $g = \infty$. If this value is put into the circulation reduction factor F, Prandtl's F_∞ for no wall results. The factor F is shown in Fig. A-5.

Since $F > F_\infty$, it can be seen that the presence of the wall increases the reduction factor (the circulation does not drop off as much). This is because less air can flow around the tips, and must therefore flow around the blade section in a manner approaching the two-dimensional case, resulting in increased circulation and increased thrust.

11.2.3 Application of Tip Correction Factors

The theory of Ref. 1 represents the edge of the propeller wake by an infinite number of stacked plates adjacent to an infinitely long wall. The drop off in circulation in the presence of this wall is then computed using the tip correction factor discussed in paragraph 11.2.2. In the shrouded propeller, the wall of the shroud does not extend to infinity, so that the analogy between the model in Ref. 1 and the shrouded propeller is not exact. However, the shroud is adjacent to the propeller wake in a region just downstream of the propeller. Since this portion of the propeller wake has the greatest influence on the induced velocity field, it is desirable to represent it as accurately as possible. Therefore, the errors incurred by using the model of Ref. 1, (with its infinite wall) should be small since only that portion of the wake which lies beyond the shroud exit is improperly represented, and this portion has only a small effect on induced velocity.

The application of this correction factor to vortex theory and the Goldstein theory will be discussed in the following paragraphs. Since in vortex theory the velocity diagram is representative of the circumferential average, or actuator disk, and since the wake flow as discussed in paragraph 11.2.2 is representative of a finite bladed propeller, the

11.2.3 (Continued)

solution for the wake flow will be used to correct the average velocity diagram for a finite number of blade effects. The application to Goldstein is more straightforward since the infinite tip clearance solution for F(F = F∞) is analogous to the Goldstein solution, and the effects of tip clearance can thus be incorporated by taking the ratio F/F∞ as the correction.

Considering now, the application of F to the vortex theory, the expressions for the average axial and tangential velocities, subject to the assumption of negligible wake contraction, are given by Eq. (7) and (8).

$$\bar{U}_z = \frac{\Gamma B}{4\pi r \ \mathrm{Tan}\ \bar{\phi}} \tag{7}$$

$$\bar{U}_\theta = -\frac{\Gamma B}{4\pi r} \tag{8}$$

where

Γ = blade circulation distribution
B = number blades
$\bar{\phi}$ = pitch angle of helix (based on vortex theory)
r = radius

Note that vortex theory represents the propeller by an actuator disk, so that the velocities given by Eq. (7) and (8) actually represent the circumferentially averaged velocities of a finite bladed propeller whose product of circulation and number of blades is $B\Gamma$. The actual velocity field varies circumferentially, and in particular, the actual three-dimensional values of $\bar{U}_z$ and $\bar{U}_\theta$ at the blade differ from those given in Eq. (7) and (8). It is possible, however, to deduce the velocity diagram at the blades by use of the wake solution of paragraph 11.2.2.

The velocity diagram for a typical blade section is shown below.

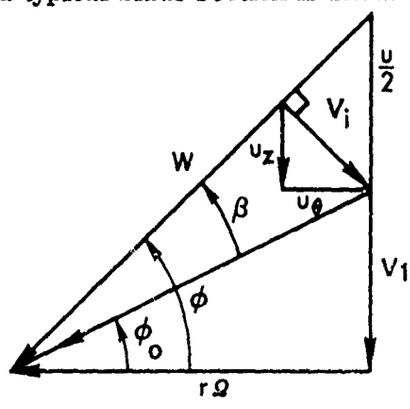

Figure A-6. Velocity Diagram for a Typical Blade Section.

11.2.3 (Continued)

where U is the displacement velocity of the far wake, that is, the velocity with which the far wake translates relative to stationary air. The velocity V_1 is made up of V_o plus the velocity due to the shroud and centerbody singularities. This diagram is based on the actual velocities at the blade, and not the circumferentially averaged velocities, which will be denoted by a bar. Under the assumption that the wake is a rigid helicoid, the wake induced velocity V_i is perpendicular to the surface of the helicoid as shown.

Now, it is also possible to draw the average velocity diagram for a given propeller radius, and this is shown below.

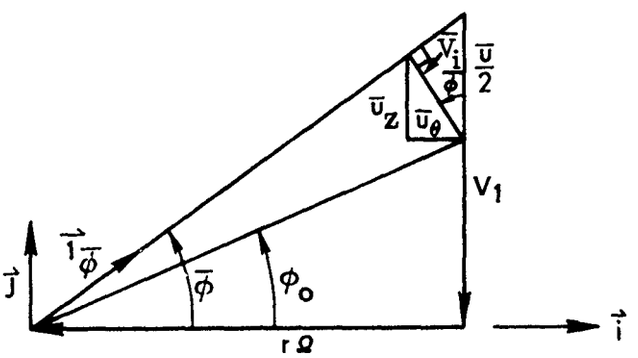

Figure A-7. Average Velocity Diagram For A Given Propeller Radius

where $\bar{U}$ represents the average of U and will be explained later. Note that $\bar{V}_i$ is also perpendicular to the wake surface, as can be shown from Eq. (7) and (8). If $\vec{1}_{\bar{\phi}}$ represents a unit vector in the $\bar{\phi}$ direction as shown above, then the condition that $\bar{V}_i$ be perpendicular to $\vec{1}_{\bar{\phi}}$ (or the wake surface) is that

$$\vec{\bar{V}}_i \cdot \vec{1}_{\bar{\phi}} = 0$$

But

$$\vec{1}_{\bar{\phi}} = \cos\bar{\phi}\,\vec{i} + \sin\bar{\phi}\,\vec{j}$$

and by Eq. (7) and (8)

$$\vec{\bar{V}}_i = \frac{-\Gamma B}{4\pi r}\left(\frac{1}{\tan\bar{\phi}}\right)\vec{i} + \frac{\Gamma B}{4\pi r}\vec{i}$$

Thus

$$\vec{\bar{V}}_i \cdot \vec{1}_{\bar{\phi}} = \frac{\Gamma B}{4\pi}\left(\cos\bar{\phi} - \frac{\sin\bar{\phi}}{\tan\bar{\phi}}\right) = 0$$

11.2.3 (Continued)

and $\bar{V}_i$ is in fact perpendicular to $1_{\bar{\phi}}$.

From Fig. A-7, the relation between $\bar{U}_z$, $\bar{U}_\theta$ and $\bar{U}$ is given as

$$\bar{U}_z^2 + \bar{U}_\theta^2 = \frac{U^2}{4} \cos^2 \bar{\zeta}$$

Substituting from Eq. (7) and (8) for $\bar{U}_z$ and $\bar{U}_\theta$, there results

$$\frac{\Gamma B}{4\pi} = \frac{\bar{U}}{2} \cos \bar{\phi} \sin \bar{\phi} \qquad (9)$$

Thus, Eq. (9) gives the circulation as a function of $\bar{U}$, the average displacement velocity of the three dimensional wake.

The meaning of $\bar{U}$ and the relationship between $\bar{U}$ and U can be seen more clearly if reference is made to the following illustration, which depicts the flow about the flat plate approximation to the propeller wake.

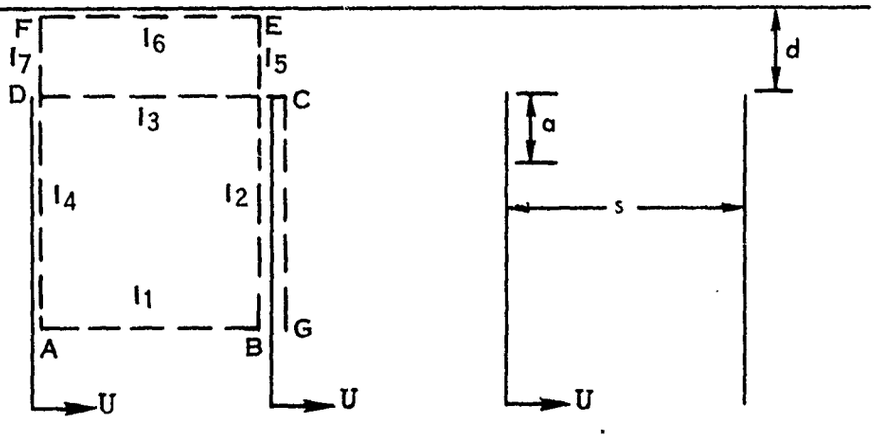

Figure A-8. Flow About Flat Plate Approximation

In the above, each plate is taken to move with the displacement velocity U. Thus the axial velocity of the fluid at the plate, say point A, is U. If a point between the plates is chosen, the axial velocity is different from U. If w is defined as the axial velocity, then on the surface of a plate w = U, and the average of w represents the average of the axial velocity between the plates, and is in fact the $\bar{U}$ referred to in Figure A-7, since this illustration represents the velocity diagram based on average velocities. Thus

$$\bar{U} = \frac{1}{s} \int_0^S w \, dx$$

11.2.3 (Continued)

Now, a relationship exists between $\bar{U}$ and U and is derived as follows: Consider the path ABCD in Figure A-8 above. The circulation about the path is zero and is given as

$$C = I_1 + I_2 + I_3 + I_4 = 0$$

where $I_1 = \int_o^s w dx$, $I_2 = \int_B^C v dy$, $I_3 = \int_C^D w dx$, $I_4 = \int_D^A v dy$

Now,

I_4 can also be written as

$$I_4 = \int_C^G v dy$$

since the flow is periodic. But $\int_B^C v dy + \int_C^G v dy$ is simply minus the circulation around the edge of the sheet and is equal to the potential jump $\Delta \psi$ across the sheet. Thus

$$I_2 + I_4 = \int_B^C + \int_C^G = \Delta\psi$$

and I_1 can be written as

$$I_1 = -I_3 - \Delta\psi$$

I_3 can be obtained as follows. Consider the path DCEF. Again, the circulation around the path is zero so that

$$I_3 + I_5 + I_6 + I_7 = 0$$

But due to the periodicity $I_5 = -I_7$, so

$$I_3 = -I_6$$

where $I_6 = -\int_F^E w dx$

11.2.3 (Continued)

Now $\frac{I_6}{S}$ represents the average axial velocity along the wall, and is taken to be zero

so that the solution physically represents the flow field of a wake translating relative to a fluid mass which is stationary with respect to the wall. With this condition imposed, I_6 and therefore I_3 are zero, and I_1, the average axial velocity between the plates becomes

$$S\,\bar{U} = I_1 = \int_0^S w\,dx = \Delta\psi$$

But $-\Delta\psi$ as shown in Ref. 1, also represents the circulation drop off near the tip. Thus from Eq. (19) of Ref. 1, which is the expression for $-\Delta\psi$

$$S\,\bar{U} = \frac{2SC}{\pi}\cosh\left(\frac{\pi d}{S}\right) cd^{-1}\left\{\left(\cosh\frac{\pi d}{S}\right)/\cosh\pi\left(\frac{d+a}{S}\right)\right\}$$

where the modulus of cd^{-1} is $\operatorname{sech}\frac{\pi d}{S}$ and where C is a constant that is determined by the condition that $\bar{U} = U$ when a, the inboard distance from the tip of the sheet becomes infinite. Upon evaluating C, in the manner described in Ref. 1 Eq. (19) and (20), the expression for $\bar{U}$ in terms of U becomes

$$\bar{U} = UF \tag{10}$$

Thus it turns out that F has two interpretations. The first, as discussed in Ref. 1, is that F represents the drop in circulation near the tip of the propeller. The second, as discussed here and in Ref. 3, that F represents the ratio of the average axial or displacement velocity to the actual three-dimensional displacement velocity.

Substitution of Eq. (10) into Eq. (9) gives the circulation distribution of a propeller based on vortex theory corrected for the three-dimensional effects of the flat plate wake. This theory will henceforth be referred to as the corrected vortex theory. The result of substituting Eq. (10) into Eq. (9) is given by Eq. (11),

$$\Gamma = \frac{\bar{U}F\cos\bar{\phi}\,\sin\bar{\phi}\,2\pi r}{B} \tag{11}$$

where it should be noted that $\bar{\phi}$ is obtained from the average velocity diagram. If the propeller is lightly loaded, in the sense that wake contraction is negligible, (an assumption which has been used implicitly throughout the discussion), then the displacement velocity U and therefore $\bar{U}$ is small compared to V_1, so it is reasonable to assume that $\bar{\phi} = \phi$. With this assumption Eq. (11) becomes

$$\Gamma = \frac{U F\cos^2\phi\,\tan\phi\,2\pi r}{B} \tag{12}$$

11.2.3 (Continued)

An expression similar to Eq. (12) can be obtained from the Goldstein theory. The velocity diagram at the propeller is that shown in Fig. A-6, so that U_Z and U_ρ are given in terms of U by the following expressions

$$U_Z = 1/2\ U \cos^2 \phi$$

$$U = -1/2\ U \cos \phi \sin \phi$$

In addition, Goldstein's solution to the flow about the wake of the propeller results in the following expression for circulation as a function of U, (See Ref. 2),

$$\Gamma = \frac{KU\ 2\ \pi r \tan \phi}{B} \qquad (13)$$

where K is the Goldstein K factor, which depends in part on r, and gives the drop in circulation at the tip. Thus the factor K is equivalent to the tip correction factor F of Ref. (1) for infinite tip clearance.

Thus, in order to correct the Goldstein theory for the effects of tip clearance, the ratio of F to F_∞ (see Fig. A-9) will be applied to the Goldstein K factor. This method of applying the tip clearance correction assumes that the ratio of circulation with finite tip clearance to circulation with infinite tip clearance is the same for both the flat plate representation of Ref. 1 and the actual geometry consisting of a rigid helicoid enclosed by a cylinder.

If F_r is defined as the ratio of the tip correction factor F at the given tip clearance to F_∞, (i.e., $F_r = F/F_\infty$), and then Eq. (13) becomes

$$\Gamma = \frac{U2\ \pi r \tan \phi}{B} \quad (K\ F_r) \qquad (14)$$

11.2.4 References

1. Goodman, T., "The Tip Correction for Wind-Tunnel Tests of Propellers", Journal of Aeronautical Sciences, December 1956.

2. Lock, C. N., "Application of Goldstein's Airscrew Theory to Design", British R&M 1377, November 1930.

3. Durand, W. F., "Aerodynamic Theory", Vol. IV, pages 261-269, Springer Press, 1938

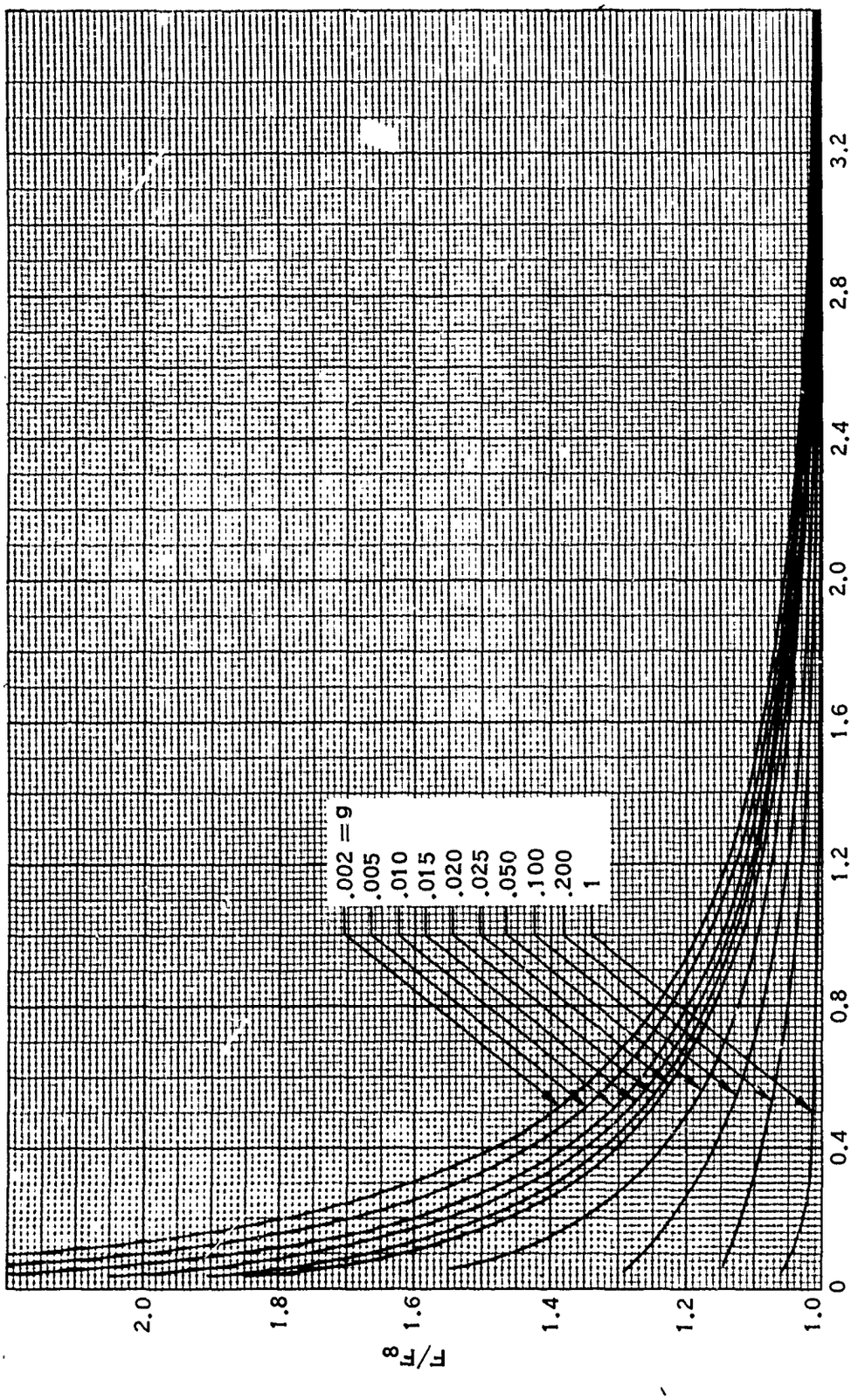

Figure A-9. Ratio Of Tip Correction To Tip Correction With No Wall.

11.3 THRUST DUE TO DISTRIBUTION OF SOURCES

11.3.1 Introduction

The force on the source and sink distribution representing the shroud thickness is calculated in terms of the velocity at the body due to external sources and sinks. In order to do this, a theorem from Ref. 1 is used that gives the force on an obstacle due to a source or sink in terms of the velocity at the singularity due to all causes except this singularity itself (See Fig. A-10).

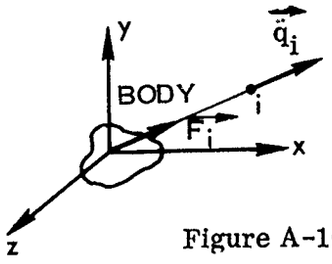

i = ith singularity
$\vec{F}_i$ = Force on body
$\vec{q}_i$ = vel. at singularity i due to other causes

Figure A-10. Force on Obstacle.

11.3.2 Preliminary Analysis

Ref. 1 gives the force on an obstacle due to a source i as

$$\vec{F}_i = 4\pi m_i \rho \vec{q}_i \tag{1}$$

where m_i is the strength of the source, ρ is the density of the fluid, and $\vec{q}_i$ is the velocity at i due to all causes except the source itself. If the body is in the presence of N sources or sinks, then the total force on the body is:

$$\vec{F} = \sum_{i=1}^{N} 4\pi m_i \rho q_i \tag{2}$$

Before Eq. (2) can be converted into the desired form, certain symmetry properties of the expression for the velocity at a point i due to a source at j must be developed. The velocity due to a source is:

$$\vec{q}_r = \frac{m}{R^2} \vec{U}_R \tag{3}$$

where m is the strength of the source, R is the distance between the source and the point at which the velocity is desired, and $\vec{U}_R$ is a unit vector in the direction from the source to the point (See Fig. A-11).

11.3.2 (Continued)

Writing Eq. (3) in rectangular coordinates:

$$\vec{Q}_{ji} = \frac{m_j \left| (X_i - X_j)\,\vec{i} + (Y_i - Y_j)\,\vec{j} + (Z_i - Z_j)\,\vec{k} \right|}{(X_i - X_j)^2 + (Y_i - Y_j)^2 + (Z_i - Z_j)^2} \tag{4}$$

where $\vec{Q}_{ji}$ represents the velocity at i due to a source at j. Eq. (4) can be written in the condensed form:

$$\vec{Q}_{ji} = m_j \vec{K}_{ji} \tag{5}$$

where

$$\vec{K}_{ji} = \frac{(X_i - X_j)\,\bar{i} + (Y_i - Y_j)\,\bar{j} + (Z_i - Z_j)\,\bar{k}}{(X_i - X_j)^2 + (Y_i - Y_j)^2 + (Z_i - Z_j)^2} \tag{6}$$

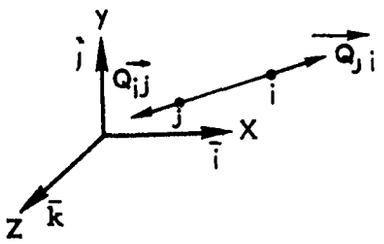

Figure A-11. Velocity Due to a Source

In a similar manner, the velocity at j due to a source at i can be written:

$$\vec{Q}_{ij} = m_i \vec{K}_{ij} \tag{7}$$

where

$$\vec{K}_{ij} = \frac{(X_j - X_i)\,\bar{i} + (Y_j - Y_i)\,\bar{j} + (Z_j - Z_i)\,\bar{k}}{(X_j - X_i)^2 + (Y_j - Y_i)^2 + (Z_j - Z_i)^2} \tag{8}$$

From Eq. (6) and (8), it can be seen that the influence coefficients $\vec{K}'_{ij}$ and K'_{ji} are of the same magnitude, but of opposite signs, i.e.,

$$\vec{K}_{ji} = -\vec{K}_{ij} \tag{9}$$

11.3.3 Force on a Source-Sink Distribution Due to External Sources and Sinks

Fig. A-12 shows the problem to be solved. The body is represented by a source-sink distribution, $f(\xi)$ with the x or ξ axis through the center of the body. External to the body are i sources and sinks. The force on the body due to the sources i is to be calculated.

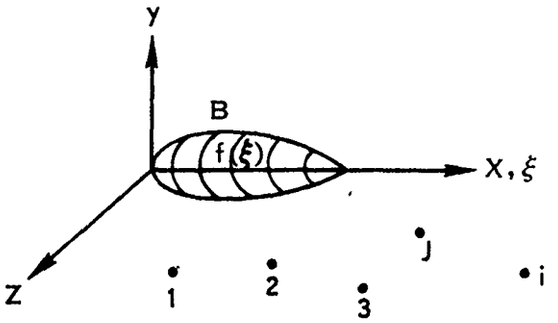

Figure A-12. Force on a Source-Sink Distribution Due to External Sources and Sinks.

Eq. (1) gives the force on the body due to source i in terms of the velocity at i. The velocity at i is due to the other discrete sources and the body B, and can be written as:

$$\vec{Q}_i = \sum_j \vec{Q}_{ji} + \vec{Q}_{Bi} \tag{10}$$

The velocity at i due to a source of strength m_j at j is, from Eq. (5)

$$\vec{Q}_{ji} = m_j \vec{K}_{ji} \tag{11}$$

where $\vec{K}_{ji}$ is given by Eq. (6). The velocity at i due to the body B is:

$$\vec{Q}_{Bi} = \int f(\xi) \vec{K}(\xi, X_i, Y_i, Z_i) \, d\xi \tag{12}$$

where $\vec{K}(\xi, X_i, Y_i, Z_i)$ represents the influence function for the velocity at (X_i, Y_i, Z_i) due to an elemental source at ξ. The total velocity due to all sources (except i) and the body B is therefore, from Eq. (11) and (12):

$$\vec{Q}_i = \sum_j m_j \vec{K}_{ji} + \int f(\xi) \vec{K}(\xi, X_i, Y_i, Z_i) \, d\xi \tag{13}$$

Putting Eq. (13) into (1), the expression for the force on the body becomes:

$$\frac{\vec{F}}{4\pi\rho} = \sum_j m_i m_j \vec{K}_{ji} \sum_i m_i \int f(\xi) \vec{K}(\xi, X_i, Y_i, Z_i) \, d\xi \tag{14}$$

11.3.3 (Continued)

Making use of Eq. (9), the first term of Eq. (14) becomes:

$$\sum_{ij} m_i m_j \frac{1}{2} \left(\vec{K}_{ji} + \vec{K}_{ij}\right) = \frac{1}{2}\left[\sum_{ij} m_i m_j K_{ji} - \sum_{ij} m_i m_j K_{ij}\right] \tag{15}$$

Since the order of summation can be changed without changing the sum,

$$\sum_{ij} m_i m_j \vec{K}_{ij} = \sum_{ij} m_i m_j \vec{K}_{ji} \tag{16}$$

Putting this into Eq. (15), it can be seen that the first term of Eq. (14) is zero. This means that the effect of the sources on each other cancels if the sources are taken two at a time.

Eq. (14) thus becomes:

$$\vec{F} = 4\pi\rho \sum_i m_i \int f(\xi)\ K\ (\xi, X_i, Y_i, Z_i,)\ d\xi \tag{17}$$

where $\bar{K}(\xi, X_i, Y_i, Z_i)$ is the influence function giving the velocity at i due to the source at ξ. For the ξ axis shown in Fig. A-12, which corresponds to the center line of the body,

$$\vec{K}\ (\xi, X_i, Y_i, Z_i) = \frac{(X_i - \xi)\ \bar{i} + Y_i\ \bar{j} + Z_i\ \bar{k}}{(X_i - \xi)^2 + Y_i^2 + Z_i^2} \tag{18}$$

By the argument given above, the influence function $\vec{K'}$ for the velocity at a point ξ due to a source at i is given as -K, so

$$\vec{K'}\ (\xi, X_i, Y_i, Z_i) = -\vec{K}\ (\xi, X_i, Y_i, Z_i) \tag{19}$$

Making the substitution into Eq. (17) there results:

$$\vec{F} = -4\pi\rho \int f(\xi)\left[\sum_i m_i \vec{K'}\ (\xi, X_i, Y_i, Z_i,)\right] d\xi \tag{20}$$

The velocity at ξ due to sources at i is:

$$\vec{Q}_R = \sum_i m_i \vec{K'}\ (\xi, X_i, Y_i, Z_i) \tag{21}$$

11.3.3 (Continued)

Substituting Eq. (21) into (20) the desired expression results, i.e.,

$$\bar{F} = -4\pi\rho \int f(\xi)\, Q_R^{\dagger}\, d\xi \qquad (22)$$

Eq. (22) thus gives the force on a body due to external sources and sinks in terms of the source-sink distribution of the body, $f(\xi)$, and the resultant velocity at ξ due to external sources and sinks, Q_R. Eq. (21), (19), and (18) give this velocity in terms of the strengths and locations of the external sources and sinks.

11.3.4 References

1. Milne-Thomson, L.M. "Theoretical Hydrodynamics", MacMillan, New York, 1960.

11.4 SHROUD THRUST BASED ON MOMENTUM THEOREM

11.4.1 Introduction

The thrust of the shrouded propeller is derived by application of the momentum theorem to a control volume surrounding the shroud. The velocities in the far wake are estimated by assuming negligible propeller wake contraction. All velocities are written in terms of their averages and perturbations from these averages. In this way the results can be used either in a one dimensional sense when only averages are known, or in a two-dimensional sense if the details of the distribution are known.

11.4.2 Discussion of Average Velocities and Wake Area

Before actually deriving the equation for shroud plus propeller thrust, it is necessary to define certain average velocities. Two average velocities will be defined, one at the propeller plane and one in the wake at infinity. At either point the average velocity is defined as that velocity, which when multiplied by the available flow area, results in actual mass flow passing through that area. In order to obtain this average, it is necessary to know the axial velocity distribution at the plane in question. The shroud-induced contribution to this velocity can be obtained from the T.A.R. theory whereas the propeller-induces portion is obtained from Eq. (15) which is derives in a later paragraph. The following model, including the effects of centerbody, is assumed in the theory,

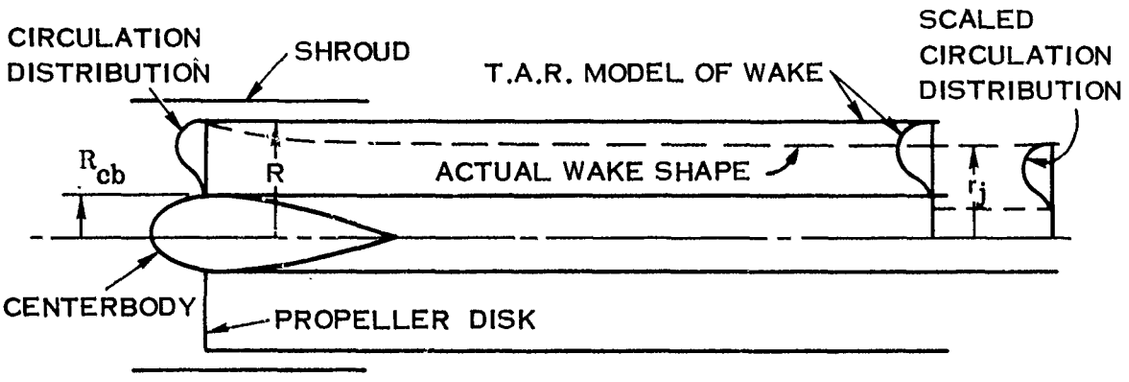

Figure A-13. Wake Model.

where the T.A.R. model of wake does not have any contraction. In reality, the wake will contract somewhat and it is assumed that the distribution of circulation in the wake is just a scaled version of the propeller circulation, that is

$$\Gamma_{wake}\left(\frac{r}{r_j}\right) = \Gamma_{prop}\left(\frac{r}{R}\right) \quad (1)$$

11.4.2 (Continued)

where r = the radius at which Γ is desired;
R = the propeller radius
r_j = the jet radius

With the assumption of Eq. (1), the axial velocity due to the propeller wake at infinity is given as (See Eq.(15)in paragraph 11.4.4)

$$\frac{v_{jp_\infty}}{V_\infty}\left(\frac{r}{r_j}\right) = \frac{N\Gamma\left(\frac{r}{r_j}\right)\Omega}{2\pi V^2_\infty} \qquad (2)$$

while the propeller wake axial induced velocity at the propeller plane is given as

$$\frac{v_{jp}}{V_\infty}\left(\frac{r}{R}\right) = \frac{1}{2}\,\frac{N\Gamma\left(\frac{r}{R}\right)\Omega}{2\pi V^2_\infty} \qquad (3)$$

where the parenthesis indicate functional variation with respect to the indicated variable. Having defined the axial velocity due to the propeller wake at the propeller and in the wake at infinity, the expressions for average velocity will be obtained next. Consider first the average at the propeller plane. At this point, the axial velocity has four components, i.e.,

$$V_a = V_\infty + v_s + v_{jp} + v_{cb}$$

where V_∞ = free stream velocity
v_s = velocity due to shroud - T.A.R. Theory
v_{jp} = velocity due to propeller wake - Eq. (3)
v_{cb} = velocity due to centerbody - T.A.R. Theory

The average velocity at the propeller plane is, by definition,

$$\frac{\overline{V}_o}{V_\infty}\left(1-\frac{R_{cb}^2}{R^2}\right) = 2\int_{\frac{R_{cb}}{R}}^{1}\left(1+\frac{v_s}{V_\infty}+\frac{v_{jp}}{V_\infty}+\frac{v_{cb}}{V_\infty}\right)\frac{r}{R}\,d\left(\frac{r}{R}\right)$$

Now define,

$$\frac{\overline{v_{ip}}}{V_\infty} = \frac{2}{\left(1-\frac{R_{cb}^2}{R^2}\right)}\int_{\frac{R_{cb}}{R}}^{1}\left(\frac{v_s}{V_\infty}+\frac{v_{jp}}{V_\infty}+\frac{v_{cb}}{V_\infty}\right)\frac{r}{R}\,d\left(\frac{r}{R}\right)$$

11.4.2 (Continued)

so in terms of $\overline{v}_{ip}$ (the average induced velocity at the propeller plane) $\overline{V}_o/V_\infty$ becomes

$$\frac{\overline{V_o}}{V_\infty} = 1 + \frac{\overline{v_{ip}}}{V_\infty} \tag{4}$$

Again applying the definition of the average velocity to the wake at infinity, where since there is no centerbody, the integration is taken from r=o to $r = r_j$, there results

$$\frac{\overline{V_j}}{V_\infty}\ \pi r_j^2 = 2\pi r_j^2 \int_o^1 (1 + \frac{v_{jp\infty}}{V_\infty})\ \frac{r}{r_j}\ d\ (\frac{r}{r_j})$$

since in the wake at infinity, the velocities due to the shroud and center-body are zero. Now, defining the wake average induced velocity as follows,

$$\frac{\overline{v}_{jp_\infty}}{V_\infty} = 2\int_o^1 \frac{v_{jp_\infty}}{V_\infty}\ \frac{r}{rj}\ d\ (\frac{r}{r_j}) \tag{5}$$

there results

$$\frac{\overline{V}_j}{V_\infty} = 1 + \frac{\overline{v}_{jp_\infty}}{V_\infty} \tag{6}$$

Thus Eq. (4) and (6) define the average velocities at the propeller and in the jet at infinity.

Having these average velocities defined, it is now possible to compute the slipstream area at infinity by applying continuity as follows

$$\overline{V_o}\ A_{PROP} = \overline{V_j}\ A_{WAKE}$$

or

$$\frac{\overline{V_o}}{V_\infty}\ \pi\ (1 - \frac{R^2_{cb}}{R^2}) = \frac{\overline{V_j}}{V_\infty}\ \pi\ (\frac{r_j}{R})^2$$

Solving for r_j/R, the equation for slipstream contraction becomes

$$\frac{r_j}{R} = \sqrt{\left|1 - \frac{R^2_{cb}}{R^2}\right|\ \frac{\overline{V}_o/V_\infty}{V_j/V_\infty}} \tag{7}$$

11.4.2 (Continued)

It is now possible to obtain the total thrust of the shroud and propeller combination by application of the momentum theorem and the wake radius defined above.

11.4.3 Derivation of Equation for Shroud and Propeller Thrust

The derivation is limited to the case of an actuato disk. Fig. A-14 shows the coordinate system and the control volume which were used in the analysis.

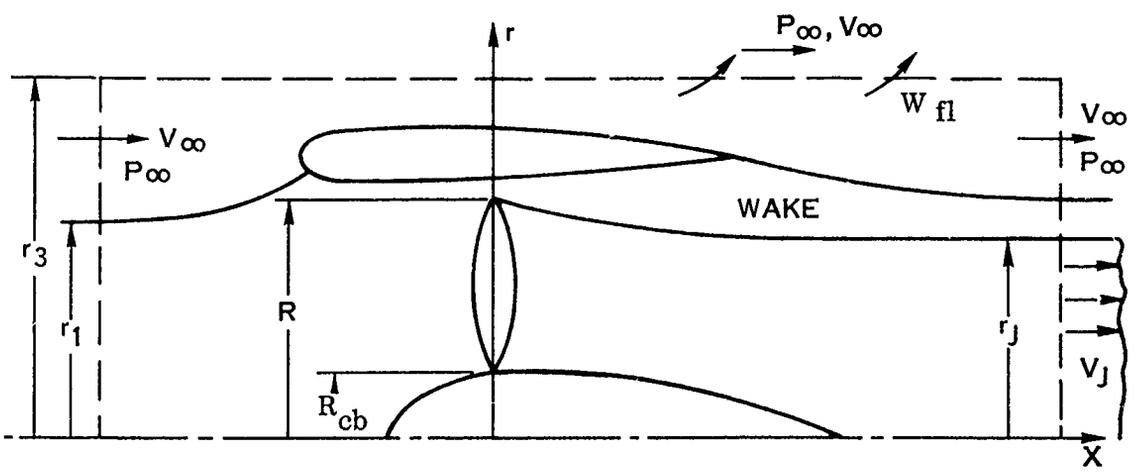

Figure A-14. Shroud Control Volume

The momentum equation can be stated as follows for the x direction,

SUM FORCES ON CONTROL VOLUME = MOMENTUM OUT - MOMENTUM IN

The control volume is taken so that all flow properties are uniform along its surfaces with the exception of the flow in the wake. With the control volume defined as such the momentum out can be written as,

$$\text{MOMENTUM OUT} = \rho V_\infty^{\,2} (A_3 - A_j) + \int_0^{r_j} 2\pi r \rho V_j^{\,2}\, dr + W_{fl} V_\infty \qquad (8)$$

where W_{fl} is the weight flow that passes through the cylindrical part of the control volume. The momentum in can be written simply as

$$\text{MOMENTUM IN} = \rho V_\infty^{\,2} A_3 \qquad (9)$$

11.4.3 (Continued)

The forces on the control volume arise from two sources, pressure forces on the control volume surface and the total thrust of the device. For the control volume configuration stipulated, the pressure forces in the X direction cancel out since at distances far downstream the wake pressure can be assumed constant and equal to the free-stream static. Thus the momentum equation for total thrust becomes upon substitution of Eq. (8) and (9).

$$T_{tot} = \int_0^{r_j} 2 \pi r \rho V_j (V_j - V_\infty) \, dr \qquad (10)$$

This equation is the desired result and relates total thrust to the jet velocity in the wake V_j. The relationship between this jet velocity and the propeller circulation distribution is considered next.

11.4.4 Relation Between Jet Velocity and Propeller Circulation

Within the framework of the T.A.R. theory for the zeroth harmonic the shroud is represented by a cylindrical distribution of vorticity whose length is equal to the shroud chord. The propeller is represented by a disk at the propeller plane and a semi-infinite constant radius cylinder of vorticity represents the propeller wake. At the downstream surface of the control volume the effect of shroud vorticity on jet velocity is negligible due to the fact that the velocity induced by a vortex element at a point is inversely related to distance between the point and the element. Therefore, the velocity in the far wake is made up of the free stream velocity V_∞ and the velocity induced by the propeller wake. The velocity induced at the propeller disk by the propeller wake is exactly one-half of that induced by the wake far downstream. This is because in the far jet, the propeller wake effectively extends from minus infinity to plus infinity. If the wake is divided at the point where the velocity is being evaluated, it consists of a semi-infinite section extending to plus infinity and a similar semi-infinite section extending to minus infinity. Each of these sections then contributes one-half of the total wake velocity (induced by the wake). If the section which extends to plus infinity is considered alone, it appears to be exactly the same as the wake extending from the propeller disk. Therefore, at the disk, the wake induced velocity is one-half of the total induced velocity at plus infinity.

Due to the preceeding discussion, the wake velocity V_j can be written as:

$$V_j = V_\infty + 2 v_{jp} = V_\infty + v_{jp\infty} \qquad (11)$$

where v_{jp} is the velocity induced by the propeller wake at the propeller disk, and is one half of the wake induced velocity at infinity $v_{jp\infty}$, i.e.,

$$v_{jp} = \frac{1}{2} v_{jp\infty}$$

11.4.4 (Continued)

The propeller induced velocity v_{jp} can be related to the propeller circulation by applying Stokes Theorem to the circulation around the far jet. In the far jet the velocity just outside the wake is V_∞ and all radial components of velocity are zero. In addition, the assumption of negligible wake contraction leads to the existence of a circulation in the far wake which is a scaled version of the propeller circulation.

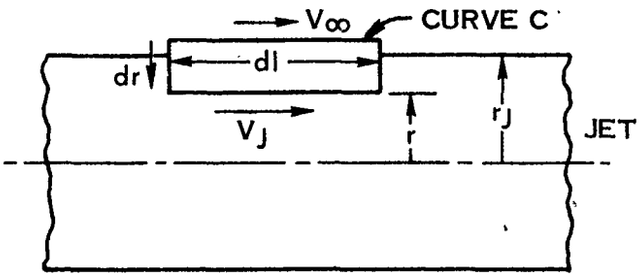

Figure A-15. Circulation Through the Cross Section of a Jet.

The circulation around a path C through the cross-section of the jet (Ref. Fig. A-15). can be written as:

$$V_j dl - V_\infty \, dl = \Gamma = \oint_c \bar{V} \cdot d\bar{l} \tag{12}$$

Now, Stokes Theorem permits $\oint_c \bar{V} \cdot d\bar{l}$ to be written as:

$$\oint_c \bar{V} \cdot d\bar{l} = \iint_A \bar{\nabla} \times \bar{V} \cdot d\bar{A}$$

but $\bar{\nabla} \times \bar{V}$ is by definition the circulation per unit area, so that is just the total circulation enclosed by the curve C. With these notions, Eq. (12) becomes:

$$V_j \, dl - V_\infty \, dl = \Gamma_{tot_c} \tag{13}$$

where Γ_{tot_c} is the total circulation within C. If dl is taken to be $2\pi r/\tan\theta$, in development the propeller and its wake for the radius r appears as follows:

11.4.4 (Continued)

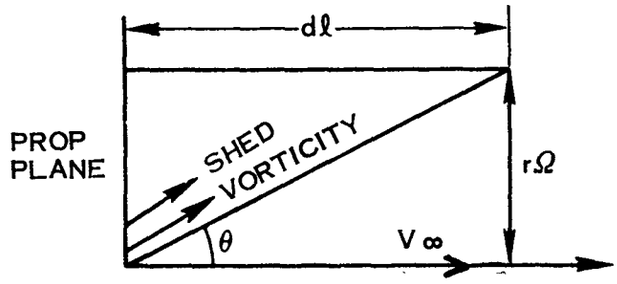

Figure A-16. Propeller and Wake Radius Diagram

where $\tan\theta = r\Omega/V_\infty$. Helmholtz's Theorem states that circulation must be conserved, so that the circulation shed from a propeller blade per unit length is $d\Gamma/dr$. For the curve c, with $dl = 2\pi r/\tan\theta$, the total circulation within c becomes, $\int N \frac{d\Gamma}{dr}\, dr$ where N is the total number of blades and Γ is the circulation distribution/blade. Eq. (13) now becomes

$$(V_j - V_\infty)\frac{2\pi r\, V_\infty}{r\Omega} = N\int_{r_j}^{r} \frac{d\Gamma}{dr}\, dr \qquad (14)$$

The right hand side of Eq. (14) integrates immediately to

$$(V_j - V_\infty)\frac{2\pi r\, V_\infty}{r\Omega} = N\left[\Gamma(r) - \Gamma(r_j)\right]$$

The circulation of the propeller tip $\Gamma(r_j) = 0$, so that this equation becomes in terms of v_{jp}

$$(V_\infty + 2v_{jp} - V_\infty)\frac{2\pi V_\infty}{\Omega} = N\Gamma(r)$$

or

$$v_{jp} = \frac{1}{2}\,\frac{N\Gamma(r)\Omega}{2\pi V_\infty} \qquad (15)$$

Eq. (15) relates v_{jp} to propeller circulation for the case of an actuator disk with a small amount of wake contraction.

Using the equations for the total thrust and propeller wake induced velocities, it is now possible to continue with the derivation of a total thrust coefficient for the shroud and propeller.

11.4.5 Expression for $C_{T_{tot}}$

By defining a total thrust coefficient as follows,

$$C_{T_{tot}} = \frac{T_{tot}}{\frac{1}{2}\rho V_\infty^2 \pi R^2}$$

Eq. (10) becomes upon substitution of Eq. (11) for V_j,

$$C_{T_{tot}} = 4\left(\frac{r_j}{R}\right)^2 \int_0^1 \frac{r}{r_j}\left[1 + \frac{v_{jp_\infty}}{V_\infty}\right] \frac{v_{jp_\infty}}{V_\infty}\, d\left(\frac{r}{r_j}\right) \qquad (16)$$

where v_{jp_∞}/V_∞ is given by Eq. (3).
Now v_{jp_∞}/V_∞ can be written in terms of $\bar{v}_{jp_\infty}/V_\infty$ as follows

$$\frac{v_{jp_\infty}}{V_\infty} = \frac{\bar{v}_{jp_\infty}}{V_\infty} + \frac{\delta_p}{V_\infty} \qquad (17)$$

where Eq. (17) is the definition of δ_p/V_∞. Now from the definition of v_{jp_∞}/V_∞ it follows that

$$\int_0^1 \frac{r}{r_j} \frac{\delta_p}{V_\infty}\, d\left(\frac{r}{r_j}\right) = 0 \qquad (18)$$

i.e., by applying continuity, there results,

$$\int_0^1 \frac{r}{r_j} \frac{v_{jp_\infty}}{V_\infty}\, d\left(\frac{r}{r_j}\right) = \frac{\bar{v}_{jp_\infty}}{V_\infty} \int_0^1 \frac{r}{r_j}\, d\left(\frac{r}{r_j}\right) + \int_0^1 \frac{\delta_p}{V_\infty} \frac{r}{r_j}\, d\left(\frac{r}{r_j}\right)$$

or

$$\int_0^1 \frac{r}{r_j} \frac{v_{jp_\infty}}{V_\infty}\, d\left(\frac{r}{r_j}\right) = \frac{1}{2} \frac{\bar{v}_{jp_\infty}}{V_\infty} + \int \frac{\delta_p}{V_\infty} \frac{r}{r_j}\, d\left(\frac{r}{r_j}\right)$$

Substituting for $\bar{v}_{jp_\infty}/V_\infty$ from Eq. (5), there results

$$\int_0^1 \frac{r}{r_j} \frac{v_{jp_\infty}}{V_\infty}\, d\left(\frac{r}{r_j}\right) = \int_0^1 \frac{r}{r_j} \frac{v_{jp_\infty}}{V_\infty}\, d\left(\frac{r}{r_j}\right) + \int_0^1 \frac{\delta_p}{V_\infty} \frac{r}{r_j}\, d\left(\frac{r}{r_j}\right)$$

11.4.5 (Continued)

or

$$\int_0^1 \frac{\delta_p}{V_\infty} \frac{r}{r_j} \, d\left(\frac{r}{r_j}\right) = 0$$

which is the desired result.

Substituting Eq. (17) into Eq. (16) for the thrust coefficient, and utilizing Eq. (18), there results

$$C_{T_{tot}} = 2\left(\frac{r_j}{R}\right)^2 \frac{\bar{V}_j}{V_\infty} \frac{\bar{v}_{jp_\infty}}{V_\infty} + 4\left(\frac{r_j}{R}\right)^2 \int_0^1 \left(\frac{p}{V_\infty}\right)^2 \frac{r}{r_j} \, d\left(\frac{r}{r_j}\right)$$

or using Eq. (7) for r_j/R

$$C_{T_{tot}} = 2\left[1 - \frac{R_{cb}^2}{R^2}\right] \frac{\bar{V}_o}{V_\infty} \frac{\bar{v}_{jp_\infty}}{V_\infty} + 4\left(\frac{r_j}{R}\right)^2 \int_0^1 \frac{\delta_p}{V_\infty} \frac{r}{r_j} \, d\left(\frac{r}{r_j}\right)$$

In terms of v_{jp} the wake induced velocity at the propeller, instead of v_{jp_∞} (the wake induced velocity at infinity) this equation becomes,

$$C_{T_{tot}} = 4\left[1 - \frac{R_{cb}^2}{R^2}\right] \frac{\bar{V}_o}{V_\infty} \frac{\bar{v}_{jp}}{V_\infty} + 4\left(\frac{r_j}{R}\right)^2 \int_0^1 \left(\frac{\delta_p}{V_\infty}\right)^2 d\left(\frac{r}{r_j}\right) \qquad (19)$$

where

$$\frac{\bar{v}_{jp}}{V_\infty} = 2\int_0^1 \frac{v_{jp}}{V_\infty} \frac{r}{r_j} \, d\left(\frac{r}{r_j}\right) = \frac{1}{2} \frac{\bar{v}_{jp_\infty}}{V_\infty}$$

The first term on the right of Eq. (19) represents the thrust that would result from simple one-dimensional momentum theory, whereas the second term represents the correction to the thrust due to the fact that there is in reality a velocity gradient.

11.5 ANALYSIS OF HIGHER HARMONICS

11.5.1 Introduction

Pressure traces yielding histories of pressure versus time were obtained during the test program. These traces were used to estimate the magnitude of the higher harmonics by subtracting the pressure history due to the rotating bound vortices representing the propeller blades. This appendix presents the derivation of the velocity field due to the bound vortices. The use of this velocity field is discussed in paragraph 6.2.2. of the text.

11.5.2 Mathematical Model

The model of the shrouded propeller used in this analysis is composed of an N-bladed propeller positioned in a right-circular cylindrical shroud of radius R_s and zero thickness (Fig. A-17A). The radius of the propeller blades is $R_p < R_s$ and the propeller plane is perpendicular to the axis of the shroud; the axis of the propeller coincides with the shroud axis. The plane of the propeller is located a distance A_0 from the leading face of the shroud and a distance B_0 from the trailing face.

As viewed from a laboratory, or earth-fixed, inertia frame of reference, the shroud and propeller have a transverse velocity V_∞ to the left; the propeller is rotating with angular velocity Ω, clockwise as seen from the rear (Fig. A-17B). A cylindrical coordinate system fixed to the propeller blades such that the x-axis coincides with the propeller-shroud axis, with the positive x-direction to the right, is set up. The positive radial direction is out from the axis; the positive tangential direction is defined in accordance with a right-handed screw advancing along the positive x-direction. In this frame the fluid is seen to have a transverse velocity V_∞ in the positive x-direction, and a tangential velocity Ω in the positive θ direction. The shroud is seen to have a similar angular velocity Ω, but, since the shroud is axisymmetric, the shroud may be viewed as stationary with respect to the propeller-fixed frame (Fig. A-17C).

In the propeller-fixed frame, the plane of the propeller lies at x = O, while the Nth blade defines the angular $\theta = O$. The leading face of the shroud lies at $-A_0$; the trailing face at B_0. Finally, positive circulation is defined in the right-handed sense; i.e., if the thumb of the right hand is placed in the direction of the vorticity vector, the flow circulates in the direction of the curled fingers.

11.5.3 Velocity Induced by a Line of Vorticity

Consider first the case of a single blade, which is represented by a radial circulation distribution function $\Gamma(\rho)$, oriented in the propeller plane at angle ϕ. It is necessary to determine the velocity induced at a field point P (X, r, θ), as shown in Fig. A-18. The velocity induced by an element of circulation $\Gamma d\bar{s}$ at ρ is given by the Biot-Savart Law.

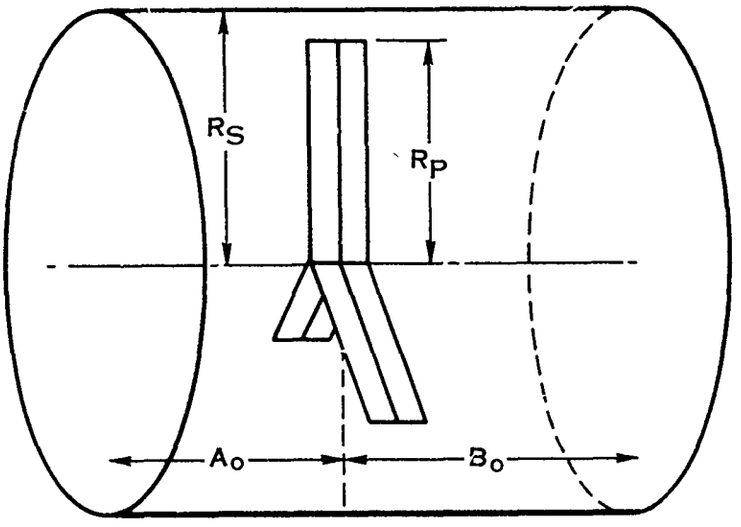

A. SHROUD & PROPELLER DIMENSIONS

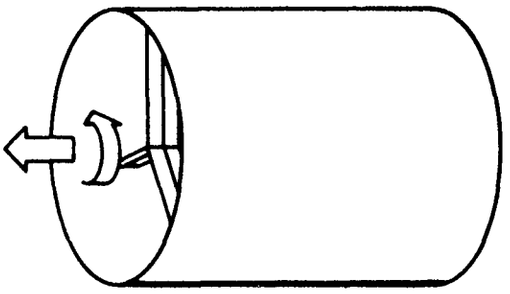

B. EARTH – FIXED FRAME

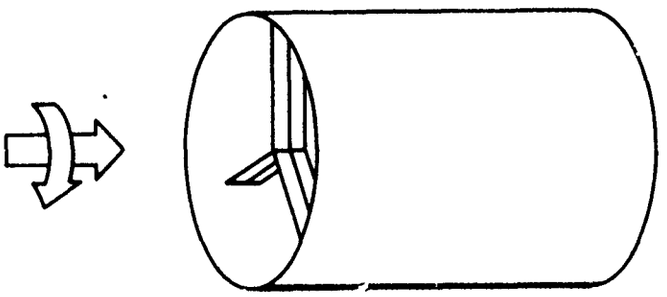

C. PROPELLER – FIXED FRAME

Figure A-17. Definition of Coordinate System

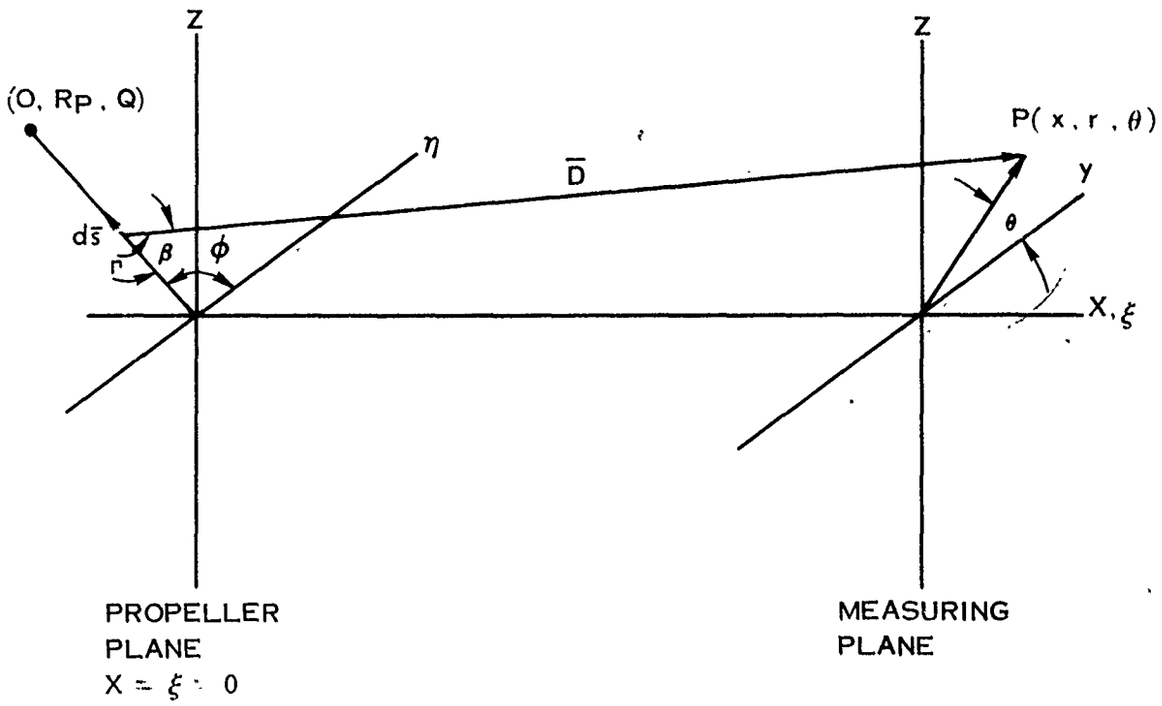

Figure A-18. Definition of Variables in Biot-Savart Law

11.5.3 (Continued)

$$d\bar{V} = \frac{\Gamma}{4\pi} \frac{d\bar{s} \times \bar{D}}{|\bar{D}|^3} \tag{1}$$

$$|d\bar{V}| = \frac{\Gamma(\rho)}{4\pi} \frac{\cos\beta \; |d\bar{s}|}{|\bar{D}|^2} \tag{2}$$

where β is defined in Fig. A-18. The following expressions for $|\bar{D}|$ and $\cos\beta$ result by use of the relations.

$X = X$	$\xi = 0$
$Y = r\cos\theta$	$\eta = \rho\cos\phi$
$Z = r\sin\theta$	$\neq = \rho\sin\phi$

Now

$$\bar{D} = (X-\xi)\,\bar{i} + (y-\eta)\,\bar{j} + (Z-\neq)\,\bar{k}$$

$$|\bar{D}| = \left[X^2 + (r\cos\theta - \rho\cos\phi)^2 + (r\sin\theta - \rho\sin\phi)^2\right]^{1/2}$$

$$|\bar{D}| = \left[X^2 + r^2 + \rho^2 - 2r\rho\cos(\theta-\phi)\right]^{1/2} \tag{3}$$

The derivation of $\cos\beta$ is much more involved and will not be shown here. In terms of the variables (X, r, θ, ϕ, D) it becomes,

$$\cos\beta = \frac{\left[X^2 + r^2\sin^2(\theta-\phi)\right]^{1/2}}{|\bar{D}|} \tag{4}$$

Finally,

$$|d\bar{s}| = d\rho \tag{5}$$

Substitution of Eq. (3), (4), and (5) into Eq. (2) for the velocity yields:

$$|d\bar{V}| = \frac{\Gamma(\rho)}{4\pi}\left[X^2 + r^2\sin^2(\theta-\phi)\right]^{1/2} \frac{d\rho}{|\bar{D}|^3} \tag{6}$$

Integration of Eq. (6) along the entire lifting line from $\rho = 0$ to $\rho = R_p$ yields

$$|\bar{V}| = \frac{1}{4\pi}\left[X^2 + r^2\sin^2(\theta-\phi)\right]^{1/2} \int_0^{R_p} \frac{\Gamma(\rho)\,d\rho}{\left[X^2 + r^2 + \rho^2 - 2r\rho\cos(\theta-\phi)\right]^{3/2}} \tag{7}$$

11.5.3 (Continued)

The axial, radial, and tangential components of this total velocity are desired so that they may be superposed with the corresponding components from the other blades. Note that the velocity induced by the given vortex line is perpendicular to the plane determined by that line and the field point in question. From this observation a unit vector in the direction of the induced velocity can be derived,

$$\bar{1}_V = U_X \bar{i} + U_r \bar{1}_r + U_\theta \bar{1}_\theta$$

where

$$U_X = \frac{r\sin(\theta-\phi)}{\left[X^2 + r^2 \sin^2(\Theta-\phi)\right]} 1/2 \tag{8a}$$

$$U_r = -\frac{X \sin(\theta-\phi)}{\left[X^2 + r^2 \sin^2(\theta-\phi)\right]} 1/2 \tag{8b}$$

and

$$U_\theta = -\frac{X \cos(\theta-\phi)}{\left[X^2 + r^2 \sin^2(\theta-\phi)\right]} 1/2 \tag{8c}$$

The signs are chosen to agree with our definition of positive circulation in the right-handed sense. $\bar{1}_r$ and $\bar{1}_\theta$ are unit vectors in the radial and tangential directions, respectively, and are given by

$$\bar{1}_r = \cos\theta\, \bar{j} + \sin\theta\, \bar{k}$$

$$\bar{1}_\theta = -\sin\theta\, \bar{j} + \cos\theta\, \bar{k}$$

Defining

$$I(X, r, \theta, \phi) = \int_0^{R_p} \frac{\Gamma(\rho)\, d\rho}{\left[X^2 + r^2 + \rho^2 - 2r\rho\cos(\theta-\phi)\right]^{3/2}}$$

and using the above expressions for the components of the unit vector, the velocity components induced by one blade, of radius R_p located at an angle ϕ become:

$$V_X = \frac{r\sin(\theta-\phi)}{4\pi} I(X, r, \theta, \phi) \tag{9a}$$

11.5.3 (Continued)

$$V_r = -\frac{X \sin(\theta - \phi)}{4\pi} I(X, r, \theta, \phi) \tag{9b}$$

$$V_\theta = -\frac{X \cos(\theta - \phi)}{4\pi} I(X, r, \theta, \phi) \tag{9c}$$

11.5.4 Velocity Induced by an N-Bladed Propeller

By the principle of superposition, the axial components of velocity due to the separate blades are summed to obtain the total axial velocity at the field point P (X, r, ϑ). A similar summation yields the radial and tangential components. The total velocity is then the vector sum of the component velocities.

For an N-bladed propeller with the Nth blade oriented at $\theta = 2\pi$, the angles of the separate blades are

$$\phi_i = 2\pi\left(\frac{i}{N}\right) \quad i = 1, 2, \ldots\ldots, N \tag{10}$$

The axial, radial, and tangential velocities induced at P (x, r, θ) by the N propeller blades are then given as

$$q_{bx} = \frac{r}{4\pi} \sum_{i=1}^{N} I(X, r, \theta, \phi_i) \sin(\theta - \phi_i) \tag{11a}$$

$$q_{br} = -\frac{X}{4\pi} \sum_{i=1}^{N} I(X, r, \theta, \phi_i) \sin(\theta - \phi_i) \tag{11b}$$

$$q_{b\theta} = -\frac{X}{4\pi} \sum_{i=1}^{N} I(X, r, \theta, \phi_i) \cos(\theta - \phi_i) \tag{11c}$$

The total velocity induced by the blade-bound vorticity is

$$\bar{q}_b = q_{bx}\,\bar{i} + q_{br}\,\bar{1}_r + q_{b\theta}\,\bar{1}_\theta \tag{12}$$

Eq. (11) and (12) give the velocity at any point in terms of the integral I. Evaluation of this integral is now considered. Recall that I is given as

$$I(X, r, \theta, \phi_i) = \int_0^{R_p} \frac{\Gamma(\rho)\, d\rho}{\left[X^2 + r^2 + \rho^2 - 2r\rho \cos(\theta - \phi_i)\right]^{3/2}} \tag{13}$$

11.5.4 (Continued)

The circulation distribution $\Gamma(\rho)$ is approximated by a series of straight lines as follows. The radial distance from $\rho = o$ to $\rho = R_p$ is broken into T half-open intervals

$$(O, \rho_2], (\rho_2, \rho_3], \ldots . (\rho_T, R_p]$$

and the approximating function $\Gamma^*(\rho)$ defined as

$$\Gamma^*(\rho) = C_k \rho + d_k \quad \text{for } \rho_k < \rho \leq \rho_{k+1} \tag{14}$$

for $k = 1, 2, \ldots, T$

C_k and d_k are evaluated from the values $\Gamma(\rho_1), \ldots . \Gamma(\rho_{T+1})$ of the blade circulation at the endpoints of the intervals (See Fig. A-19). The integration of Eq. (13) subject to the approximating function Γ^* is considered in the next section.

11.5.5 Integration of $I(X, r, \theta, \phi_i)$.

The function Γ^* has been defined in Eq. (14). The values of C_k and d_k are given in terms of the distribution $\Gamma(\rho)$ as

$$C_k = \left[\Gamma(\rho_{k+1}) - \Gamma(\rho)\right] \Big/ (\rho_{k+1} - \rho_k) \tag{15}$$

$$d_k = \frac{\rho_{k+1}\, \Gamma(\rho_k) - \rho_k \Gamma(\rho_{k+1})}{(\rho_{k+1} - \rho_k)} \tag{16}$$

Using Γ^* in place of Γ in Eq. (14), the integral I becomes

$$I(X, r, \theta, \phi_i) = \sum_{k=1}^{T} C_k \int_{\rho_k}^{\rho_{k+1}} \frac{\rho\, d\rho}{D^3} + \sum_{k=1}^{T} d_k \int_{\rho_k}^{\rho_{k+1}} \frac{d\rho}{D^3} \tag{17}$$

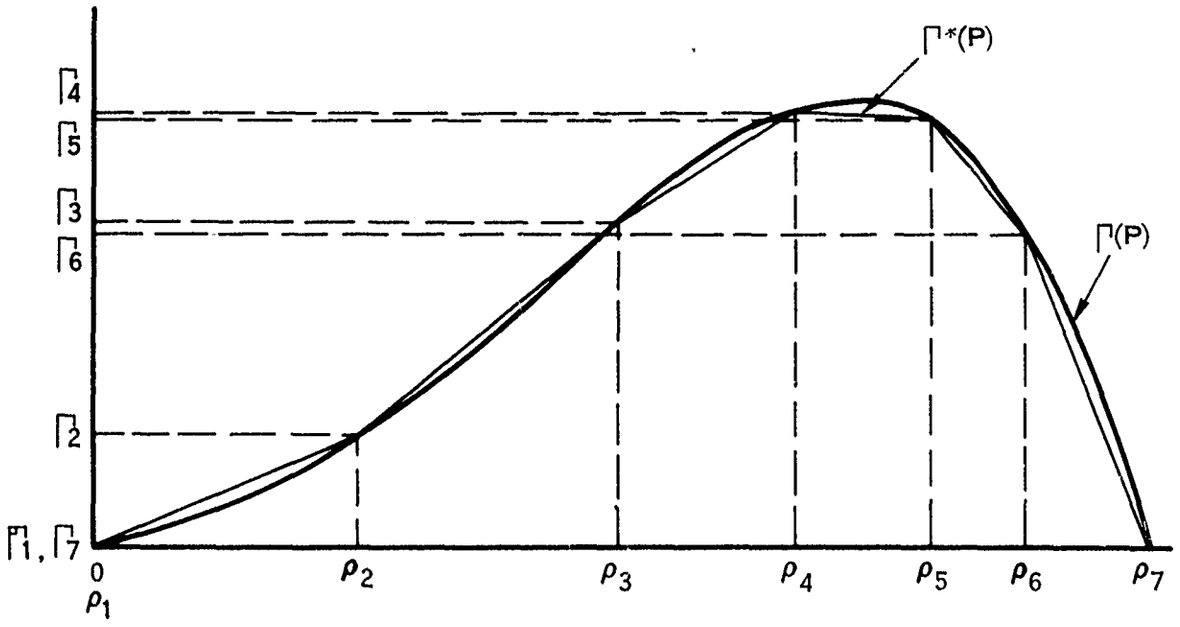

Figure A-19. Approximate Function for Γ.

11.5.5 (Continued)

where

$$D = \left|\vec{D}\right| = \left[X^2 + r^2 + \rho^2 - 2r\rho \cos(\theta - \phi_i)\right]^{1/2}$$

Integration of Eq. (17) over ρ is now possible. The first sum, defined as I_1, becomes

$$I_1(X, r, \theta, \phi_i) = \frac{1}{X^2 + r^2 \sin^2(\theta - \phi_i)} \quad x \tag{18}$$

$$\sum_{k=2}^{T+1} (C_k - C_{k-1}) \frac{X^2 + r^2 - r\rho_k \cos(\theta - \phi_i)}{\left[X^2 + r^2 + \rho_k^2 - 2r\rho_k \cos(\theta - \phi_i)\right]^{1/2}}.$$

The second sum I_2 is

$$I_2(X, r, \theta, \phi_i) = \frac{1}{X^2 + r^2 \sin^2(\theta - \phi_i)} \quad x \tag{19}$$

$$\sum_{k=2}^{T+1} (d_{k-1} - d_k) \quad \frac{\rho_k - r\cos(\theta - \phi_i)}{\left[X^2 + r^2 + \rho_k^2 - 2r\rho_k \cos(\theta - \phi_i)\right]^{1/2}}$$

The value of I is thus given as:

$$I = I_1 + I_2$$

11.5.5 (Continued)

Where I_1 and I_2 are known from Eq. (18) and (19) in terms of the coefficients C_k and d_k, defined by Eq. (15) and (16). The velocity at any point (X, r, θ), is then given by Eq. (11) and (12) in terms of I as defined above.

11.5.6 List of Symbols

C_k - slope of $\Gamma^*(\rho)$ in the k th interval

$\bar{D}$ - vector from vortex element to field point

d_k - y -intercept of $\Gamma^*(\rho)$ in the k th interval

$\bar{ds}$ - vector differential of distance along vortex element

N - number of blades

$\bar{q}_b$ - total velocity induced by all N blades at field point (X, r, θ)

q_{bx}, q_{br}, $q_{b\theta}$ - axial, radial, and tangential components of $\overline{q_b}$

R_p - radius of propeller

R_s - radius of shroud

T - number of intervals used to express $\Gamma^*(\rho)$

U_x, U_r, U_θ - axial, radial, and tangential components of $\overline{1_v}$

$\bar{V}$ - total velocity induced by one blade at a given field point (X, r, θ)

V_x, V_r, V_θ - axial, radial, and tangential components of $\bar{V}$

V_∞ - transverse velocity of propeller and shroud

(X, r, θ) - cylindrical coordinates of field point

(X, y, z) - Cartesian coordinates of field point

β - defined in Figure A-18

$\Gamma(\rho)$ - circulation at ρ

$\Gamma^*(\rho)$ - linearized function for $\Gamma(\rho)$

11.5.6 (Continued)

$\rho_1, \ldots, \rho_{T+1}$ - endpoints of the T intervals

ϕ_i - angular orientation of i th propeller blade

(ξ, ρ, ϕ) - cylindrical coordinates of vortex element

$(\xi, \eta, \neq)$ - Cartesian coordinates of vortex element

Ω - angular velocity of propeller

$\overline{1_V}$ - unit vector in direction of $\overline{V}$

11.6 DISCUSSION OF VELOCITY CALCULATION IN PROPELLER PLANE

11.6.1 Introduction

The axial velocity in the propeller plane utilized in the propeller velocity diagrams is made up of contributions from the propeller wake, the centerbody and the shroud thickness and vorticity distributions. The propeller wake contribution is obtained from the Hamilton Standard propeller design method. The centerbody contribution is obtained by numerical integration of the equation for axial velocity derived in Appendix 11.1 and is calculated by use of Hamilton Standard Deck H060. The axial velocities due to shroud vorticity and thickness are computed in Hamilton Standard Deck H194. This calculation utilizes the characteristic functions VELC (NU) and VELH (NU) which are derived below.

11.6.2 Derivation of VELC (NU). - Shroud Vorticity Characteristic Function

The velocity due to the shroud vorticity distribution is given by the Biot-Savart Law as

$$q_a(r_p) = \int_{-\lambda}^{\lambda} \gamma(\bar{x}_v) \left[\frac{1}{2\pi R^2} \left(\frac{R}{r_p} \right)^{3/2} \left\{ r_p Q'_{1/2} \left(1 + \frac{A^2}{2} \right) - R Q'_{-1/2} \left(1 + \frac{A^2}{2} \right) \right\} \right] dx_v \quad (1)$$

where

R = shroud radius

r_p = propeller radius at which q_a is desired

$$A^2 = R/r_p \left[1 + \left(\frac{x_p - x_v}{R} \right)^2 \right] + \frac{r_p}{R} - 2$$

x_p = propeller location

x_v = variable of integration

q_a = axial velocity

$\bar{x}_p = x_p/R$

$\bar{x}_v = x_v/R$

$\bar{r}_p = r_p/R$

11.6.2 (Continued)

$\gamma(\bar{x}_V)$ = shroud vorticity distribution

$$Q'_{1/2}(V) = \frac{d}{dV}\left(Q_{1/2}(V)\right)$$

$$Q'_{-1/2}(V) = \frac{d}{dV}\left(Q_{-1/2}(V)\right)$$

The term in square brackets represents the influence function for the velocity at ($\bar{x}_p$, $\bar{r}_p$) due to a vortex ring at $\bar{x}_V$ of unit strength. The vorticity distribution $(\bar{x}_V)$ is known from the T.A.R. solution in terms of the three dimensional Glauert coefficients, i.e. see paragraph 6.1.2 of text, and is

$$\frac{\gamma}{V_o} = \frac{b_{oo}}{2}\cot\phi_V + \sum_\nu \frac{b_{o\nu}}{2}\sin\nu\phi_V \qquad (2)$$

where ϕ_V is defined by

$$\bar{x}_V = -\lambda\cos\phi_V \qquad (3)$$

Substituting Eq. (2) into Eq. (1) and making the transformation Eq. (3) there results,

$$q_a = \frac{1}{4\pi}\frac{V_o}{R^2}\left(\frac{R}{r_p}\right)^{3/2}\left[b_{oo}\int_o^\pi (1+\cos\phi_V)\ \times\right.$$

$$\left. P\,\lambda R\,d\phi_V + \sum_\nu b_{o\nu}\int_o^\pi P\,\lambda R\sin\nu\phi_V\sin\phi_V\,d\phi_V\right] \qquad (4)$$

where

$$P \equiv r_p Q'_{1/2}\left(1+\frac{A}{2}\right)^2 - RQ'_{-1/2}\left(1+\frac{A}{2}\right)^2$$

The integrals in Eq. (4) can be evaluated since the integrands are known functions of ϕ_V. These integrals are evaluated numerically in the program and represent the VELC (NU) or shroud vorticity characteristic functions, $\bar{\Phi}_\nu$

11.6.2 (Continued)

Defining

$$\bar{\Phi}_o = \int_o^{\pi} \frac{P}{R} (1 + \cos \phi_v) \, d\phi_v$$

and

$$\bar{\Phi}_\nu = \int_o^{\pi} \frac{P}{R} \sin \phi_v \sin \nu\phi_v \, d\phi_v$$

the axial velocity becomes

$$\frac{q_a}{V_o} = \frac{\lambda}{4\pi} \left(\frac{R}{r_p}\right)^{3/2} \left[b_{oo} \bar{\Phi}_o + \sum_{\nu=1} b_{o\nu} \bar{\Phi}_\nu \right]$$

11.6.3 Derivation of VELH (NU) - Shroud Thickness Characteristic Functions

The velocity due to the shroud source-sink distribution is given by Eq. (5)

$$V_x = \frac{1}{2\pi} \int f(\bar{x}_o) \left[\frac{(\bar{x}_p - \bar{x}_o)}{\bar{r}_p^{3/2}} \, Q'_{-1/2} \left(1 + \frac{A^2}{2}\right) \right] d\bar{x}_o \qquad (5)$$

where

$$A^2 = \frac{1}{\bar{r}_p} \left[(\bar{x}_p - \bar{x}_o)^2 + \bar{r}_p^2 + 1 - 2\bar{r}_p \right]$$

$f(\bar{x}_o)$ = shroud source sink distribution

$\bar{x}_o$ - variable of integration

The remaining variables have already been defined and the quantity in brackets represents the influence function for the axial velocity at $(\bar{x}_p, \bar{r}_p)$ due to a unit source ring at $\bar{x}_o$.

11.6.3 (Continued)

The source-sink distribution f $(\bar{x}_o)$ is represented by a polynomial of the form

$$\frac{f(\bar{x}_o)}{V_o} = \frac{A_o}{\sqrt{\lambda + \bar{x}_o}} + \sum_n A_n (\bar{x}_o)^{n-1} \tag{6}$$

Substitution of Eq. (6) into Eq. (5) results in the following expression for the axial velocity due to shroud thickness,

$$\frac{V_x}{V_o} = \bar{V}_x = \frac{1}{2\pi \bar{r}^{3/2}} \left[A_o \int_\lambda^{-\lambda} \frac{(\bar{x}_p - \bar{x}_o)}{\sqrt{\lambda + \bar{x}_o}} Q'_{-1/2}\, d\bar{x}_o + \sum_\nu A_\nu \int_\lambda^{-\lambda} (\bar{x}_o)^{\nu-1} (\bar{x}_p - \bar{x}_o)\, Q'_{-1/2}\, d\bar{x}_o \right]$$

The integrals in the above equations can be evaluated since the integrands are known functions of $\bar{x}_o$. Defining the following characteristic functions due to shroud vorticity (VELH(NU)),

$$h_o = \int_\lambda^{-\lambda} \frac{(\bar{x}_p - \bar{x}_o)}{\sqrt{\lambda + \bar{x}_o}} Q'_{-1/2}\, d\bar{x}_o$$

$$h_\nu = \int_\lambda^{-\lambda} (\bar{x}_p - \bar{x}_o)\, (\bar{x}_o)^{\nu-1}\, Q'_{-1/2}\, d\bar{x}_o$$

the axial velocity due to the shroud source-sink distribution becomes

$$\bar{V}_x = \frac{1}{2\pi r_p^{3/2}} \left[A_o h_o + \sum_\nu A_\nu h_\nu \right]$$

11.7 CHI INTEGRALS

11.7.1 Introduction

The radial velocity at the shroud reference cylinder due to the propeller wake is given by Eq. (20) in the text in terms of the derivative of the propeller circulation distribution. In Ref. 1 of this Appendix this derivative is evaluated by expanding the propeller circulation into a Fourier series over the propeller radius. The details of the derivation are shown on pages 48 and 49 of Ref. 1. A brief description is given below.

11.7.2 Discussion

The expression for the radial wash in terms of the Fourier coefficients of the series expansions for circulation becomes,

$$\left(\frac{V_r}{V_o}\right)_{\substack{\text{prop}\\ \text{wake}}} = \frac{1}{2}\,\frac{N\Gamma}{2\pi J}\,m\mu^{1/2}\sum_{j=1}^{\infty} j\Gamma_j\,\chi_j\,(\Delta\bar{X}_p, \mu) \qquad (1)$$

where

N = number of blades

μ = tip clearance = R_p/R

J = advance ratio

$\Delta\bar{X}_p = \bar{X}_s - \bar{X}_p$

$$\chi_j = \int_0^1 \hat{r}_v^{1/2}\, Q_{1/2}(\tilde{\omega}_3)\cos j\pi\hat{r}_v d\hat{r}_v$$

$$\tilde{\omega}_3 = 1 + \frac{\Delta\bar{X}_p^2 + (1-\mu\hat{r}_v)^2}{2\mu\hat{r}_v}$$

$\hat{r}_v = r_v/R_p$

R = shroud radius

R_p = propeller radius

r_v = variable of integration (propeller radial variation)

11.7.2 (Continued)

The Γ_j's and I_m are best defined by noting the Fourier expansion for $\bar{\Gamma}$ i.e.,

$$\bar{\Gamma} = \Gamma_m \sum_{j=1}^{\infty} \Gamma_j \sin j\pi \hat{r}_v$$

where $\bar{\Gamma} = \Gamma / R_p V_o$

and where Γ_m is the maximum value of $\bar{\Gamma}$

The characteristic functions χ_j have been integrated and tabulated in Ref. 1 and are therefore known as functions of ΔX_p and μ.

The contribution of the propeller radial velocity to the two-dimensional Glauert coefficients is given by the following equations (See paragraph 6.1.2 of text.).

$$b_{oo_{\Gamma'}}^{2\text{-D}} = \frac{-4}{\pi} \int_o^{\pi} \left(\frac{V_r}{V_o} \right)_{\substack{\text{prop} \\ \text{wake}}} d\phi_s \qquad (2)$$

$$b_{o\nu_{\Gamma'}}^{2\text{-D}} = \frac{8}{\pi} \int_o^{\pi} \left(\frac{V_r}{V_o} \right)_{\substack{\text{prop} \\ \text{wake}}} \cos \nu\phi_s \, d\phi_s \qquad (3)$$

Substitution of Eq. (1) into Eq. (2) and (3) after making the substitutions

$$\bar{X}_p = -\lambda \cos\phi_p$$

$$\bar{X}_s = -\lambda \cos\phi_s$$

11.7.2 (Continued)

results in

$$b_{oo_{\Gamma'}}^{2\text{-D}} = -\frac{2}{\pi^2}\left(\frac{N\Gamma m\mu}{J}\right)^{1/2}\sum_j \frac{j\Gamma_j}{2}\int_o^{\pi} \chi_j(\phi_s)\,d\phi_s \qquad (4)$$

and

$$b_{o\nu_{\Gamma'}}^{2\text{-D}} = \frac{2}{\pi^2}\left(\frac{N\Gamma m\mu}{J}\right)^{1/2}\sum_j j\Gamma_j\int_o^{\pi} \chi_j(\phi_s)\cos\nu\phi_s\,d\phi_s \qquad (5)$$

The integrals in Eq. (4) and (5) are referred to as the "CHI" integrals in the program and are defined as follows:

$$\text{CHI}(j,0) = -\frac{1}{2}\int \chi_j\,d\phi_s = C_{j0}$$

$$\text{CHI}(j,\nu) = \int \chi_j \cos\nu\phi_s\,d\phi_s = C_{j\nu}$$

In terms of these integrals, the two-dimensional Glauert coefficients become:

$$b_{o\nu_{\Gamma'}}^{2\text{-D}} = \frac{2}{\pi^2}\left(\frac{N\Gamma m\mu}{J}\right)^{1/2}\sum_j \Gamma_j\ C_{j\nu}\ ;\ \nu = 0,\ 1,\ 2,\ldots..$$

11.7.3 References

1. Ordway, D. E., Sluyter, M. M., and Sonnerup, B. O. U.
"Three-Dimensional Theory of Ducted Propellers"
Therm Advanced Research Report TAR-TR602, August 1960.